Final technical report

The relationship between large-scale and convective states in the tropics - Towards an improved representation of convection in large-scale models

DE-SC0002731

Prepared by the Project PI: Prof. Christian Jakob

Summary

The project's goal was to exploit observations predominantly taken at the ARM CF site of Darwin to interrogate the relationship of small-scale tropical convection with larger-scale features of the tropical atmosphere. A second goal of the project was to use the findings from the observational analyses to inform the development of a new cumulus parametrisation that is being developed by the PI's group from other funding. The project made extensive use of the observational facilities at the ARM site and produced 8 publications. The main findings of the project are:

- Tropical convection occurs in four, instead of the previously reported three, distinct modes. These are: Shallow, congestus, deep and overshooting convection (Kumar et al., 2013a).
- Large-scale dynamical conditions are the primary driver for the existence, strength, and type of tropical convection with topographic features (e.g., coastlines) playing an important secondary role (Kumar et al., 2013b).
- There is a strong relationship of the strength of tropical convection with convergence-related large-scale measures (e.g., vertical motion), but only a very weak relationship with stability based measures (e.g., CAPE; Davies et al. 2013a).
- Area-averaged rainfall and its relationship to the large-scale dynamical conditions are largely controlled by the area coverage with convection, with no strong relationship to intensity (Davies et al., 2013a).
- The relationships between convective area coverage and the large scale can be reproduced by a stochastic multi-cloud model, which itself can form the basis for a new parametrisation (Peters et al., 2013).
- The growth of convection from moderate depth (congestus) to its deeper forms is not a simple thermodynamic transition but is strongly coupled to dynamical processes at large and mesoscales (Kumar et al., 2013a, 2014).
- Wind-profiler observations are suitable to derive area-averaged vertical profiles of convective mass-flux and its components of convective area fraction and vertical velocity. (Kumar et al., 2015).
- The vertical profile of convective mass-flux is dominated by the variations in convective area fraction with vertical motion being largely a function of convective type. This opens the door to developing estimates of convective mass-flux from a single radar (Kumar et al., 2015).

The behaviour of tropical convection as gleaned from observations

The main thrust of the research was to exploit the ARM observations at the Darwin location, in particular the data from the C-band polarimetric radar to discover relationships between the convective scale and larger scales. To do so we first extended our work to define the large-scale state from the TWP-ICE campaign (Davies et al., 2013b) to derive a three-year (wet-season only)

data set of the large-scale state of the atmosphere at Darwin using the standard ARM Variational Analysis tool (Davies et al., 2013a). We showed that using ECMWF data instead of radiosondes and combining this with the observed rainfall observations from the CPOL radar leads to a faithful reproduction of the TWP-ICE estimates of large-scale forcing (Fig 1).

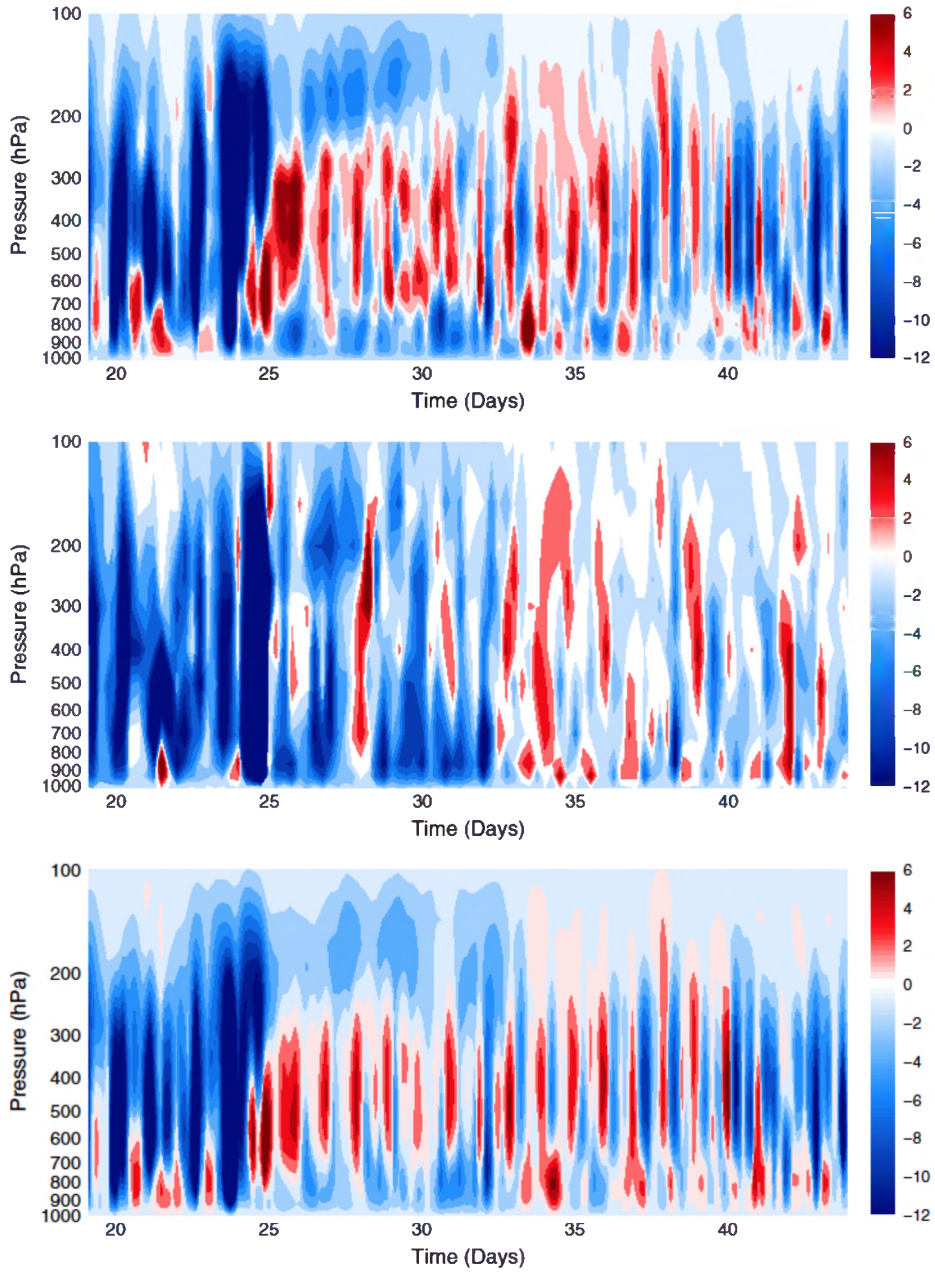

Fig 1: Time-series of vertical profiles of vertical velocity in pressure coordinates (omega) using all observations, i.e., (top panel) the best-estimate values, (middle panel) the direct ECMWF analysis, and (bottom panel) using ECMWF data as pseudo-radiosondes and combining it with radar-derived rainfall observations. Data are shown for the TWP-ICE period (19 January–14 February 2006) at Darwin, Australia.

We then focused on deriving properties of the convective-scale state, beginning with simple quantities, like the area fraction covered by convection. This was achieved using standard radar algorithms to define convective and/or stratiform rainfall areas. With both information on large and small scales concurrently available, we were able to investigate the relationship between the two scales (Fig. 2). We showed that there is a strong relationship between convergence-related (dynamic) measures of the large scale and the amount of convective rainfall, while the relationship

to stability (thermodynamic) measures were shown to be weak. We also showed that the relationship of convective precipitation to convergence, is largely one with the area that is precipitating, rather than one with the intensity of the convection. These relationships became instrumental in the development of ideas for a new cumulus parametrisation (see below).

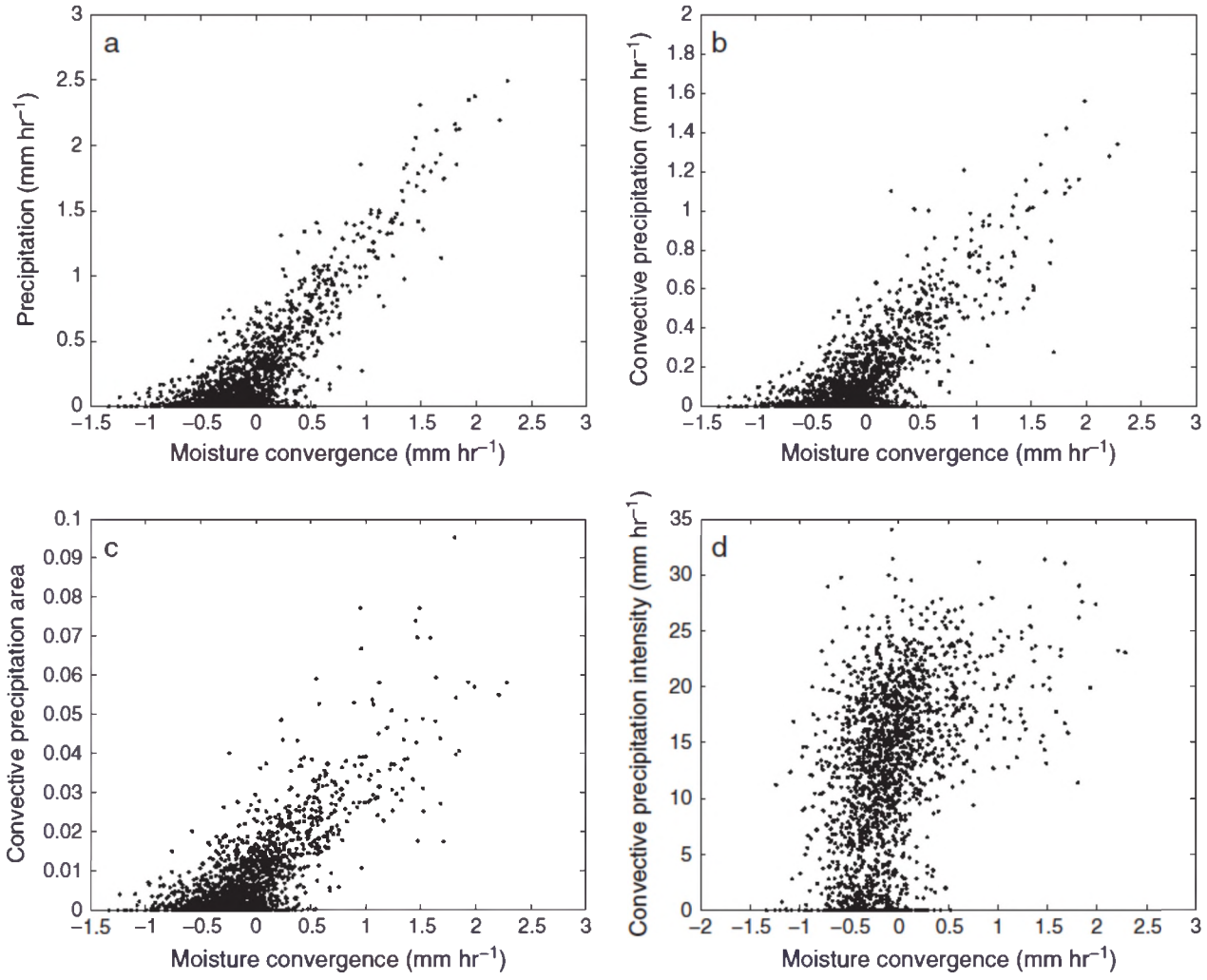

Fig 2: Relationship of moisture convergence with (a) precipitation, (b) convective precipitation, (c) convective precipitation area fraction, (d) convective precipitation intensity

Darwin is a coastal location. A very valid immediate next question was whether the relationships we found above were a result of the coastal character and if they are valid elsewhere. We tackled this problem with two separate approaches. One was to repeat our study at another location, in this case, Kwajalein. We found that while the range of large-scale conditions at Kwajalein is different from those at Darwin, the fundamental relationships discovered at Darwin also hold a Kwajalein (Peters et al., 2013). A second approach we took was to carry out an in-depth study of the relative roles of the large-scale conditions - as defined by objective weather regimes - and the land surface type on the characteristics of the convection in the Darwin region (Kumar et al., 2013b). The study found that the first order influence on the convective characteristics is the large-scale weather regime it occurs in. However, we also found that there was a non-negligible but secondary influence of the underlying surface.

Having identified simple relationships between the large scale and the “horizontal” structure of convection we turned our attention to identifying the relationship of the large-scale to the vertical extent and structure of convection. To begin this line of work we conducted a study that aimed at

identifying “typical” convective cloud types encountered in Darwin. We were able to identify three distinct modes of precipitating convection (in addition to the fourth mode of shallow convection not observable by the CPOL radar) by analysing the distribution of low-level (2.5 km) reflectivity as a function of echo top height (ETH; Fig. 3). By identifying two distinct regions of an increase of reflectivity (at 2.5 km) with ETH (below 7 km ETH, above 15 km ETH) and one region of constant reflectivity (at 2.5 km) with ETH, we were able to define a congestus mode (ETH<7 km), a deep convective mode (ETH between 7 and 15 km) and an overshooting mode (ETH>15km).

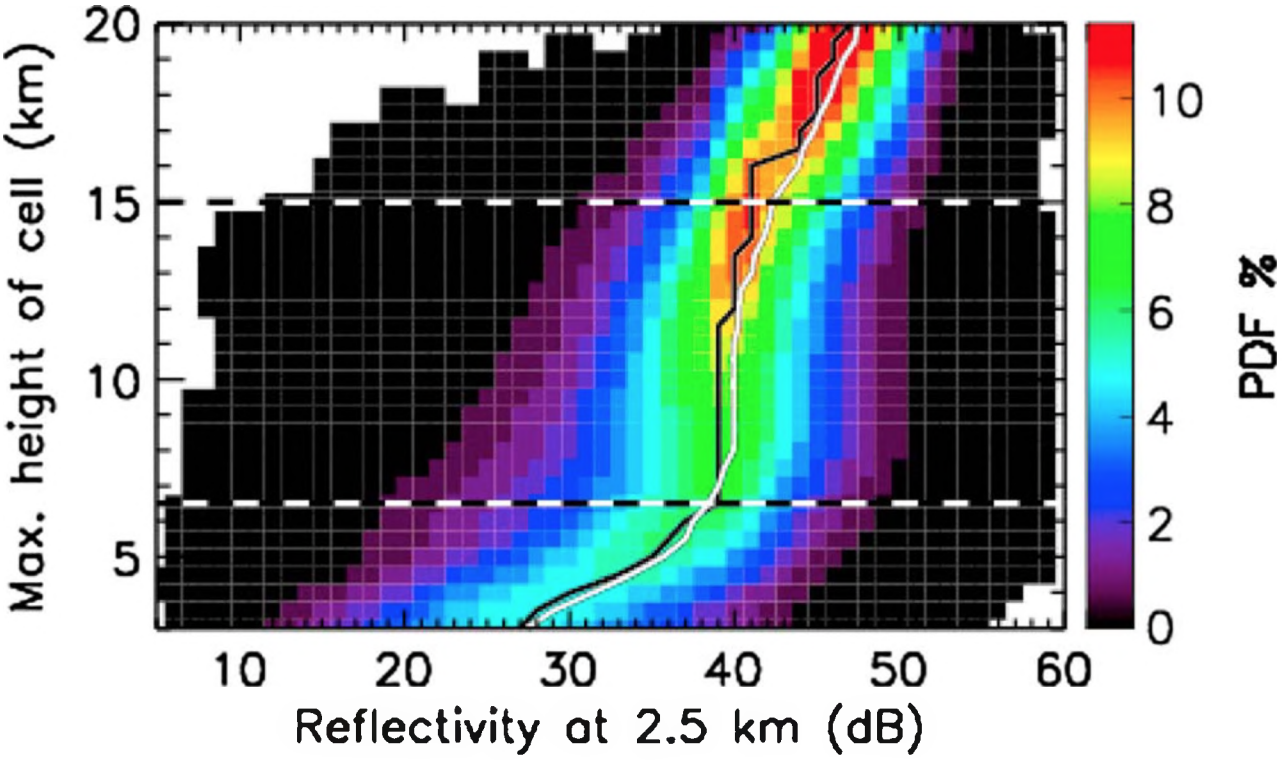

Fig 3: PDF of reflectivity using a bin size of 1 dB and as a function of ETH. One mean reflectivity was obtained per convective cell using reflectivity pixels that are bounded by the respective convective cells at the 2.5 km CAPPI level. The white curve is the overall mean reflectivity at each ETH level, and the black curve is the modal reflectivity. The dashed horizontal lines correspond to the breakpoints in the reflectivity trend indicating the lower (6.5 km) and the upper (15 km) ETH boundary for the “normal deep convection.”

We were able to use these cloud types in this and subsequent studies to show that the transition from congestus to deep convection has strong large- and mesoscale dynamical drivers and isn’t merely a thermodynamic cloud growth process (Kumar et al., 2013a, 2014). We also showed that the highest precipitation intensity (or extreme rainfall) is always associated with overshooting convection, a tantalising result that deserves follow-up in future work. Having been able to show the existence of four (compared to the previously shown three) types of convection has also influenced our decision making for building a new cumulus parametrisation (carried out under separate funding from the Australian Government), which will treat each of these four types, compared to the currently common distinction of shallow and deep convection only.

Our work to this point had highlighted the importance of the fractional area-coverage with convection, but it remained unclear how important the vertical distribution of in-cloud vertical velocity was to the convective transports, which are proportional to the product of fractional area and velocity, the convective mass-flux, which in turn underpins almost all convective parametrisation of convection in use today. While most of this work is the subject of a research

proposal recently submitted, we carried out a first foray into this area, by analysing several years of dual-frequency wind profiler observations at Darwin and combined with the CPOL radar (Kumar et al., 2015). We were able to show that the mass-flux profile is strongly shaped by the area fraction of convection with a weaker influence from vertical velocity (Fig 4, grey shading). We then

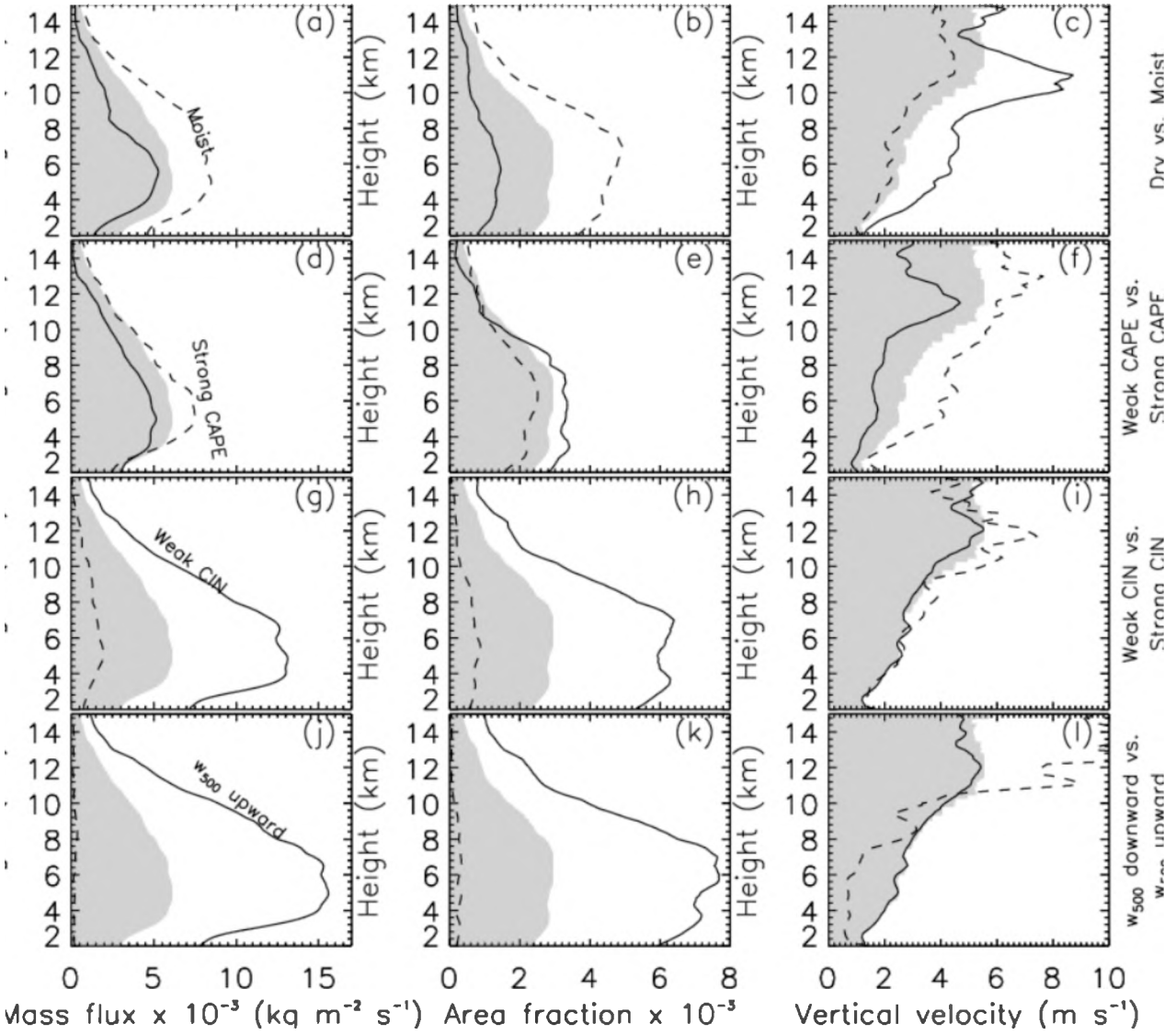

Fig 4: Effect of RH in the lowest 5 km (top panels), CAPE (second panels), CIN (third panels) and ω500 on updraft mass-flux (left column), upward area fraction (middle column) and upward vertical velocity intensities (right column). The shaded region is the overall updraft means without applying any environmental sorting. The solid and dotted line in each figure corresponds to lower and upper tercile of the environmental conditions.

investigated the influence of the large-scale environment on the mass-flux and its components. We found (not surprisingly) that higher mass-fluxes are found in moist atmospheres, but we were able to demonstrate once again that this a result of more widespread convection, with lower vertical motion rather than through more intense convection. As seen in earlier studies, we found that CAPE has relatively little effect on the mass-flux profile, in part due to a compensation of higher (lower) vertical velocity in high (low) CAPE conditions by lower (higher) area fractions. We also found that both vertical motion and CIN strongly affect convection once again through their effect

on the convective area fraction, with both having the expected strongly suppressing effect for high CIN and downward vertical motion.

The use of ARM observations in developing a cumulus parametrisation

A stated goal of our work was to analyse the observations in such a way that they can influence the design of cumulus parametrisations in general and help us to build a completely new scheme in our group in particular. The project was tremendously successful in achieving this in several ways.

First, we showed conclusively from the observations that by far the largest influence on the area-averaged (or grid-box averaged) convective rainfall (or mass-flux) is from the area that is convecting, with the vertical motion playing an secondary role. This opens the possibility to separate mass-flux - the variable commonly used in cumulus parametrisation - into area and velocity and to treat them independently, a decision we have already made for own developments.

Second, we showed that it might be useful to divide the rich spectrum of convective clouds into four major types and to allow for their coexistence in time, a feature none of the current cumulus parametrisation schemes allows for.

Third, we showed that commonly used stability measures, such as CAPE, are a poor predictor of area-average convective behaviour, as they do not seem to influence the convective area fraction much, whilst having a measurable effect on (the less important) vertical velocity.

We made use of these findings in evaluating a promising new technique for parametrisation, that of stochastic area-fraction modelling, using the observations at Darwin (and Kwajalein; Peters et al., 2013). In this study we demonstrated that an existing stochastic multi-cloud model can represent deep convection well if its predictors are vertical motion and mid-tropospheric humidity. We used the observations to change the model predictors and to retune its parameters to arrive at what will form the basis of our own new cumulus parametrisation. The findings of this study also enabled us to design a new closure for existing parametrisations, which is currently being tested in two GCMs.

Papers published from project funding

1. Kumar, V. V., C. Jakob, A. Protat, C. R. Williams, and P.T. May, 2015: Mass-flux characteristics of tropical cumulus clouds from wind profiler observations at Darwin, Australia J. Atmos. Sci., in press, accepted 24 January 2015.
2. Kumar, V. V., A. Protat, C. Jakob, and P.T. May, 2014: On the atmospheric regulation of the growth of moderate to deep cumulonimbus in a tropical environment J. Atmos. Sci. , 71, 1105-1120.
3. Petch, J., A. Hill, L. Davies, A. Fridlind, C. Jakob, Y. Lin, S. Xie, and P. Zhu, 2014: Evaluation of intercomparisons of four different types of models simulating TWP-ICE Quart. J. Roy. Meteorol. Soc., 140, 826–837, DOI: 10.1002/qj.2192.
4. Peters, K., C. Jakob, L. Davies, B. Khouider, and A. J. Majda, 2013: Stochastic behavior of tropical convection in observations and a multicloud model. J. Atmos. Sci. , 70, 3556–3575.
5. Davies, L., C. Jakob, P. May, V. V. Kumar, S. Xie, 2013a: Relationships between the large-scale atmosphere and the small-scale state for Darwin, Australia. J. Geophys. Res. , 118, 11534–11545, doi:10.1002/jgrd.50645

6. Kumar, V., A. Protat, P. T. May, C. Jakob, G. Penide, S. Kumar, and L. Davies, 2013b: On the effects of large-scale environment and surface conditions on convective cloud characteristics over Darwin, Australia. Mon. Wea. Rev., 141, 1358-1374.
7. Kumar, V. V., C. Jakob, A. Protat, P. May, L. Davies, 2013a: The four cumulus cloud modes and their progression during rainfall events: A C-band Polarimetric radar perspective. J. Geophys. Res. , 118, doi:10.1002/jgrd.50640.
8. Davies, L., C. Jakob, K. Cheung, A. DelGenio, A. Hill, T. Hume, R. J. Keane, T. Komori, V. E. Larson, Y. Lin, B. J. Nielsen, J. Petch, R. S. Plant, M. S. Singh, X. Shi, X. Song, W. Wang, M. A. Whitall, A. Wolf, S. Xie, G. Zhang, 2013b: A Single Column Model Ensemble approach applied to the TWP-ICE experiment. J. Geophys. Res. , 118, 6544-6563, doi:10.1002/jgrd.50450.

Mass-flux characteristics of tropical cumulus clouds from wind profiler observations at Darwin, Australia

Vickal V. Kumar
School of Earth, Atmosphere and Environment, Monash University, Australia

Christian Jakob
School of Earth, Atmosphere and Environment, Monash University, Australia and
ARC Centre of Excellence for Climate System Science, Monash University, Melbourne, Australia.

Alain Protat
Centre for Australian Weather and Climate Research: A partnership between the Bureau of Meteorology and CSIRO, Melbourne, Australia.

Christopher R. Williams
University of Colorado, and NOAA/Earth System Research Laboratory/Physical Sciences Division, Boulder, Colorado

Peter T. May
Centre for Australian Weather and Climate Research: A partnership between the Bureau of Meteorology and CSIRO, Melbourne, Australia.

Corresponding Author
Vickal V. Kumar
Centre for Australian Weather and Climate Research, Australian Bureau of Meteorology and CSIRO, GPO Box 1289, Melbourne 3001, Australia(E-mail: v.kumar@bom.gov.au)

Keywords: Wind profiler, congestus, deep clouds, overshooting clouds, relative moisture, cloud models

Abstract

Cumulus parameterizations in weather and climate models frequently apply mass-flux schemes in their description of tropical convection. Mass-flux constitutes the product of the fractional area covered by convection in a model grid box and the vertical velocity within cumulus clouds. However, vertical velocities are difficult to observe on GCM scales, making the evaluation of mass-flux schemes difficult. Here, we combine high temporal resolution observations of in-cloud vertical velocities derived from a pair of wind profilers over two wet-seasons at Darwin with physical properties of precipitating clouds (cloud top heights CTH, convective-stratiform classification) derived from the Darwin C-band polarimetric radar, to provide estimates of cumulus mass-flux and its constituents. The length of our data set allows for investigations of the contributions from different cumulus cloud types, namely congestus, deep and overshooting convection, to the overall mass-flux and of the influence of large-scale conditions on mass-flux. We found mass-flux was dominated by updrafts and, in particular, the updraft area fraction, with updraft vertical velocity playing a secondary role. The updraft vertical velocities peaked at above 10 km where both the updraft area fractions and air densities were small, resulting in a marginal effect on mass-flux values. Downdraft area fractions are much smaller and velocities are much weaker than those in updrafts. The area fraction responded strongly to changes in mid-level large-scale vertical motion and convective inhibition (CIN). In contrast, changes in the lower-tropospheric relative humidity and convective available potential energy (CAPE) strongly modulate in-cloud vertical velocities but have moderate impacts on area fractions. Although average mass-flux is found to increase with increasing CTH, it is the environmental conditions that seem to dictate the magnitude of mass-flux produced by convection through a combination of effects on area fraction and velocity.

1. Introduction

Cumulus clouds play an important role in weather and climate by maintaining the large-scale atmospheric circulation (e.g., Fritsch 1975; Emanuel et al. 1994), transporting heat, moisture, and momentum in the atmosphere (Yanai et al. 1973) and producing a multitude of clouds (e.g., Liu and Zipser 2005). Recent studies indicate the existence of distinct types of cumulus clouds in the tropics (e.g., Johnson et al. 1999; Kumar et al. 2013a). These are shallow cumulus with cloud-top heights (CTH) near the trade inversion layer 1–3 km above the surface, cumulus congestus clouds with CTH in the mid-levels between 3 and 7 km, deep cumulonimbus clouds with CTH between 7 km and the base of the tropopause layer (~15 km for the topics), and overshooting convection with tops extending into the tropopause layer.

Individual cumulus clouds, particularly deep and overshooting modes, are generally thought to contain convective-scale (1–10 km) updraft and downdraft cores. Observations reveal that cumulus updraft and downdraft flow characteristics differ in several ways (e.g., Knupp and Cotton 1985; Sun et al. 1993). Updrafts are triggered by convergence of environmental airflow and typically start near the cloud base. They dominate in the growing and mature phases of cumulus clouds (Paluch and Knight 1984). Entrainment processes and water loading reduce updraft strength, while latent heating (e.g., Zipser 2003) and precipitation (e.g., Fierro et al. 2009; Heymsfield et al. 2010) enhance updraft strength. In contrast, downdrafts commonly occur in the mature and decaying phases of cumulus clouds. Mature phase downdrafts generally occur above freezing level and they are forced by convergence of air detrained from the tops of the updrafts with slower moving ambient air (Smull and Houze 1987; Sun et al. 1993). While decay phase downdrafts typically occur below the freezing level and are forced by precipitation loading, evaporation and melting (May and Rajopadhyaya 1999).

In General Circulation Models (GCMs) convection cannot be represented by modelling individual convective clouds. Instead, simple representations of the collective effects of a cumulus cloud ensemble existing within a model grid box are applied. Amongst the most widespread of these cumulus parameterization approaches is the so-called mass-flux approach (see Arakawa (2004) for an overview). Here, the vertical transport by the cloud ensemble is directly related to the mass-flux through the clouds, itself a product of the air density, fractional area covered by and the vertical velocity within cumulus updrafts and downdrafts. While conceptually simple, the evaluation of mass-flux approaches from observations has proven difficult, as measurements of the area fraction and vertical velocities within updrafts and downdrafts on the scale of a GCM grid box are difficult to ascertain. As a result, much of the evaluation of mass-flux schemes has relied on the use of Cloud Resolving Models (e.g., Randall et al. 2003; Derbyshire et al. 2004; Petch et al. 2014).

The main motivation of this study is to close this obvious observational gap and to demonstrate the potential of using existing observational data set for evaluating model mass-flux schemes. In particular, we wish to address the following two questions: 1) What is the observed vertical structure of convective mass-flux and which of its constituents (area or velocity) dominates the overall structure? 2) How sensitive is mass-flux to changes in the environmental conditions?

There are previous observational studies that determined direct in-cloud mass-fluxes. Numerous in situ aircraft penetrations conventionally provide the best insights in convective cloud dynamics (e.g., Byers and Braham 1949; Marwitz 1973; LeMone and Zipser 1980; Jorgensen and LeMone 1989; Anderson et al. 2005). However, to facilitate evaluation of mass-flux schemes in GCM, longer temporal length of continuous convective profiling are needed, such as those from advanced remote sensing techniques. Examples of long-term in-

106 cloud mass-flux observations include the works of May and Rajopadhyaya (1999) and
107 Giangrande et al. (2013), where they used wind profiler retrievals from a tropical and
108 subtropical site, respectively. Both studies found the peaks in updraft speeds and updraft core
109 widths associated with deep convection occurred in upper levels, near 10 km altitude. In
110 contrast, downdrafts peaked near the cloud base. In the tropics, updraft cores have smaller
111 speeds, but are wider compared to the subtropics. Heymsfield et al. (2010), who investigated
112 deep convection in both tropics and subtropics using airborne Doppler radars, also reported
113 similar characteristics in vertical velocities for updrafts and downdrafts.

114 To extract mass-flux over a GCM size grid, we need direct measurements of vertical
115 velocities inside every cumulus cloud enclosed by the model grid box. Most commonly, this
116 is achieved using a dual-Doppler radar retrieval technique (e.g., Collis et al. 2013). However,
117 the dual-Doppler approach requires at least two radars, with the accuracy of retrieved vertical
118 velocity depending on the location within the radar domain. An alternative and more direct
119 approach to determine vertical velocity is to use a wind profiler (May and Rajopadhyaya
120 1999; Williams 2012). The current study will be using the latter approach using data
121 collected in Darwin, Australia, for the two wet seasons (Nov-Apr) of 2005/2006 and
122 2006/2007. The main difficulty in using wind profiler observations is they represent a single
123 atmospheric column and temporal aggregation is required to represent larger spatial areas. By
124 comparing the wind profiler cloud occurrences with volumetric radar data, we demonstrate
125 that the statistical aggregation of single column profiler measurements over a longer period
126 do depict convection comparable to that which will be observed in a GCM size grid box. We
127 then proceed to determine both the fractional area and in-cloud velocities in convective
128 updrafts and downdrafts using the profiler information and aggregate them into GCM-
129 equivalent mass-flux profiles.

Having determined profile of mass-flux from observations over a GCM size box, we evaluate the sensitivity of the vertical structure and strength of the mass-flux to environmental conditions (lower-troposphere (0–5 km) moisture, CAPE and CIN) and large-scale vertical motions. The Darwin wet season experiences a wide variety of convective systems due to the presence of two distinct convective regimes - active monsoon/oceanic conditions and build-up/break continental conditions (e.g., McBride and Frank 1999; Pope et al. 2009; Kumar et al. 2013b). This makes Darwin a good location to investigate the sensitivity of mass-flux to varying environmental conditions. Kumar et al. (2013b) showed that the main influence on convection in the Darwin area was the large-scale meteorological conditions. However, they also found underlying surface type also plays a role and as a result the effect of the surface type (coastal in this case) on the observed cumulus mass-flux characteristics cannot be ignored and will require a cautious approach when using these results for GCM evaluations.

Past studies have attempted similar sensitivity tests of mass-flux profiles (or the constituents of mass-flux) to the synoptic regimes and environmental conditions using both observations and simulations. Cifelli and Rutledge (1994; 1998) using wind profiler observed vertical velocity statistics found significant differences in the mean vertical motion between Darwin break and monsoon storms, with evidence of a bimodal peak in the vertical velocity profile for break cases, while the monsoon cases had a more uniform profile. Here we will extend these studies to more detail by contrasting the mass-flux and its constituents as a function of different large-scale environmental conditions. In particular, we will investigate the sensitivity of observed mass-flux to the low-level (0–5 km) tropospheric humidity and qualitatively compare the results to those of the idealized CRM simulations in Derbyshire et al. (2004). These simulations implied that in a dry environment, the mass-flux decreases monotonically with height above the cloud base leading to the formation of mostly shallow

154 convection. Moist environments, on the other hand, led to deep convection with the peak
155 mass-flux located at an elevated height in the mid-troposphere.

156 The paper is structured as follows. Section 2 will introduce the data sets used in the study.
157 Section 3 describes the method to retrieve velocity and area profiles from wind profiler
158 observations and establishes these single column observations when averaged in time provide
159 a good proxy for mass-flux in a GCM size grid box. Section 4 presents the main results of
160 the study, including the mean mass-flux profile and its variability, its sensitivity to
161 environmental conditions, and the contributions from different cumulus types to the overall
162 mass-flux. This is followed by a summary and discussion in Section 5.

163 ## 2. Data

164 The main goal of this study is to provide observational estimates of convective mass-flux and
165 its constituents at a scale relevant to the parameterisation of convection in GCMs as well as
166 its sensitivity to environmental conditions. This requires the use of a variety of data sets.
167 Specifically, we make use of a pair of wind profilers embedded in the field-of-view of
168 scanning C-band dual-polarization radar (CPOL; Keenan et al. (1998)) and combine those
169 with detailed estimates of the large-scale conditions provided by a variational analysis
170 algorithm. Each of these data sources is explained in turn below.

171 ### 2.1 The Darwin wind profiler radar pair

172 We use data collected by a 50- and 920-MHz wind profiler pair from two Darwin wet seasons
173 (October 2005 – April 2006 and October 2006 – April 2007), recorded at 1-min resolution.
174 The main advantage of using this data source is that wind profilers provide more accurate
175 estimates of in-cloud vertical velocity than other remote sensing techniques, including dual-
176 Doppler radar techniques (e.g., Collis et al. 2013). The disadvantage is that measurements are

177 taken at a single point, but frequently in time, and a time-space conversion is required to
178 make them useful to study the mass-flux behaviour on scales of a GCM grid box.

179 Here, vertical velocities are computed by applying the dual-frequency algorithm developed in
180 Williams (2012) to the Doppler returns from the vertical beams of the 50- and 920-MHz wind
181 profiler pair. The beam width of the vertical beam is approximately 0.2 km at 1 km height
182 and increases to 2 km by 10 km height. The wind profiler pair was synchronized to begin
183 their vertical beam observations every 1 min. The full description of the Darwin wind profiler
184 setting can be found in Williams (2012).

185 The 50-MHz profiler simultaneously observes both Bragg scatter from ambient air, which
186 provides a direct measurement of the vertical velocity of air parcels (wanted signal), and
187 Rayleigh scatter from hydrometeors (unwanted signal). If signals from the two scattering
188 processing are not properly separated, then the vertical air motion estimates will be biased
189 downwards because of contamination from falling hydrometeors. The Williams (2012)
190 method uses the spectra from the 920-MHz profiler, which are sensitive to mainly
191 hydrometeor returns, to remove the Rayleigh echo returns from the 50-MHz profiler spectra.
192 The filtered 50-MHz signal is then processed using the standard wind profiling processing
193 technique described in Carter et al. (1995) and is based on the profiler online processing
194 (POP) routine. The POP routine estimates the spectrum noise level, the spectrum signal start
195 and end integration points, and the first three moments—power, mean reflectivity-weighted
196 Doppler velocity and the spectrum width (equal to twice the spectrum standard deviation).
197 The mean Doppler velocity corresponds to the vertical air motion. The accuracy of the
198 vertical velocity retrieval by the Darwin wind profiler pair is estimated to be between 0.05 to
199 0.25 m s^{-1} using a Monte Carlo simulation design (Williams 2012). Further comparisons
200 between the Darwin wind profiler and statistical techniques for the separation of terminal fall

velocity and vertical air velocity also yielded an agreement to within 0.1-0.15 ms^{-1} (Protat and Williams 2011).

The profiler vertical velocity measurements are interpolated onto a vertical grid of 100 m resolution over an altitude range of 1.7 – 17 km. However, the highest quality data is thought to be limited to heights below 11 km (May and Rajopadhyaya 1999), because of the reduction in profiler sensitivity with height. Moreover, the spreading of the profiler beam leads to increase in velocity uncertainties with changing height. These uncertainties can be lowered by temporal averaging of the data.

Finally, the vertical velocity data from the wind profiler was further filtered to keep only measurements that were within cumulus clouds (see Section 3 form more detail). To achieve this, we need to know; i) if cumulus cloud occurred over the profiler, and ii) what is the CTH of these cumulus clouds. These two cloud properties are extracted from the CPOL radar, which contains the wind profilers within its field-of-view, roughly 24 km southwest from the radar location (see Fig. 1 of May et al. 2002). The CPOL measurements are introduced in more detail in the following subsection. Vertical velocities outside cumulus clouds are not considered here.

2.2 Darwin CPOL radar

We use measurements of reflectivity from the CPOL radar, which have been sampled onto a cubic grid with a horizontal grid size of 2.5 km x 2.5 km, and vertical resolution of 0.5 km. The horizontal scanning area of CPOL is approximately 70,000 km^2, sufficient enough to contain few GCM size grid boxes.

Specifically, this study makes use of two physical characteristics of precipitating clouds derived from the CPOL reflectivities:

i) We apply a convective vs. stratiform classification and use only those precipitating clouds identified as convective over the wind profiler to extract their mass-flux characteristics. Steiner algorithm (Steiner et al. 1995) is used to identify convective clouds at the CPOL pixel collocated with the wind profiler location. This algorithm has been successfully employed in previous studies (e.g., Kumar et al. 2013a-b; Penide et al. 2013a). As the CPOL radar takes 10 minutes to complete a full volume scan, all 1-min scans of the wind profiler falling into a 10-minute interval of convective cloud occurrence over the profiler are used as valid measurements of vertical velocity.

ii) As our focus is on convective mass-flux, we filter out any vertical velocity measurements taken in cirrus anvils and/or in clear air above active convective drafts. To do so we make use of the 0-dBZ echo top height (0-dBZ ETH) extracted from the CPOL reflectivity profile over the profiler site. Previous studies have shown that the 0-dBZ echo tops from C-band radar observations are usually within 1 km of cloud top heights estimated by millimetre cloud radars such as that on CloudSat (Casey et al. 2012) or on the ground at Darwin (Kumar et al. 2013a). To ensure that we study continuous updrafts or downdrafts we require that there is vertically continuous reflectivity signal between the lowest CPOL level of 2.5 km height and the 0-dBZ echo top. We also apply the echo top height to classify the observed precipitating cumulus cell as either congestus, deep and overshooting (Kumar et al. 2013a; 2014), allowing us to investigate the contribution to the total mass-flux from the various cumulus modes.

In summary, we use CPOL data for four purposes; 1) identify convective cloud incidences at the profiler site, 2) remove vertical velocity measurements taken in clear air above the convective towers, 3) separate the convective clouds into three cumulus modes and 4)

247 validate area fractions derived from vertically pointing measurements against that obtained
248 with volumetric data (more details in section 3).

249 ### 2.3 Background environmental conditions

250 Apart from providing overall mass-flux estimates we also aim to examine the effects of the
251 environmental conditions on the mass-flux behaviour. To do so requires reliable
252 observational estimates of key environmental parameters. Here we use 6-hourly information
253 on lower-tropospheric (0–5) km relative humidity ($RH_{0\text{-}5}$), CAPE (Convective Available
254 Potential Energy), CIN (Convective inhibition), and the large-scale vertical motion at 500
255 hPa (ω_{500}). We use two main sources to derive these parameters.

256 The $RH_{0\text{-}5}$ is extracted from the Darwin airport operational radiosoundings. We simply
257 average the relative humidity measurements between 0 and 5 km. The remaining three
258 parameters, CAPE, CIN and ω_{500}, are from a large-scale data set derived for the Darwin
259 region by Davies et al. (2013) by applying the variational budget analysis technique of Zhang
260 and Lin (1997) using Numerical Weather Prediction (NWP) analysis data as "pseudo-
261 radiosondes" and radar and satellite observations at the surface and top of the atmosphere, as
262 suggested by Xie et al. (2004). By comparing their approach to results from the Tropical
263 Warm Pool International Cloud Experiment field study (May et al. 2008), Davies et al.
264 (2013) showed that this technique provides much better estimates of the large-scale state of
265 the atmosphere than the direct use of analyses or reanalyses from NWP Centres.

266 The median over the two wet seasons for $RH_{0\text{-}5}$, CAPE, CIN and ω_{500}, respectively, were
267 74%, 548 J kg^{-1}, 43 J kg^{-1} and −0.38 hPa $Hour^{-1}$. Note that a negative value for vertical
268 motion represents upward motion. Likewise, the 90% interval (i.e., between 5 and 95% levels
269 about the medians) for $RH_{0\text{-}5}$ measurements were between 43 and 96%, for CAPE were

between 0 and 1410 J kg^{-1}, for CIN were 9 and 243 J kg^{-1}, and ω_{500} were between −6.67 and 3.81 hPa $Hour^{-1}$. These values set the range for which our results can likely be compared to GCMs.

3.0 Method

The main motivation of this study is to provide a statistical picture of mass-flux profiles using observations, which will then be useful to evaluate existing cumulus mass-flux scheme in models and assess the respective contributions of convective area fraction and vertical velocity to mass-flux. Ideally, this would require high resolution observations of vertical velocity both in time and space over a volume of 100 km x 100 km in the horizontal and 20 km in the vertical (typical GCM grid box). No such measurements exist. As outlined in the introduction, this study makes use of vertical velocity retrievals from dual-frequency wind profiler observations. However, we will combine the wind profiler information with that from the scanning CPOL radar to investigate the representativeness of the single site measurements for convection over a GCM size grid.

While our overall goal is to provide a statistical study of several hundred cumulus cells occurring over time in a GCM box we first illustrate our methodology to derive vertical motion and area fraction profiles using a snapshot of a deep convective case observed concurrently by both radar types shown in Figure 1. Figure 1a shows the time-height cross-section of reflectivity from the CPOL radar at the profiler site, which is available in 10 min time intervals and 0.5 km resolution in height. The remaining panels of Fig. 1 show the wind profiler measurements. The profiler observations are available at a much finer resolution of 1 min in time and 0.1 km in height. The red circles in Fig. 1a depict the 0-dBz ETH locations at those times where the Steiner classification finds a convective cloud over the profiler site (also indicated by the black line).

294 The differences between the CPOL reflectivities (Fig. 1a) and the 50-MHz (Fig. 1b) and 920-
295 MHz (Fig. 1c) wind profiler reflectivities are found to be quite large, with the CPOL
296 reflectivities in better agreement with the 920-MHz wind profiler reflectivities than with the
297 50-MHz wind profiler reflectivities. This is not surprising, as the 50-MHz wind profiler
298 reflectivities are a mixture of echoes from clear air and hydrometeors, while CPOL is only
299 sensitive to hydrometeors. The differences between CPOL and the 920-MHz reflectivities
300 likely reflect the high temporal evolution of the convective event within the sampling
301 resolution of CPOL (10 minutes), which is captured by the 920-MHz observations at 1-
302 minute resolution.

303 Examinations of CPOL radar loops for the event described in Fig. 1 revealed that the
304 overshooting convective system sampled in Figure 1 was embedded in widespread stratiform
305 clouds and the whole system was moving across the profiler from the southwest. The time-
306 height sections of vertical velocity (Fig. 1d) indicate that the storm was present over the
307 profiler location for approximately one hour. The regions with vertical motion exceeding 1.5
308 m s^{-1} (strong updrafts) and below −1.5 m s^{-1} (strong downdrafts) are shown by the black
309 contours. The upward motions first occur at the low-levels (3 km) around 0500 LT, which
310 appear to gradually shift to mid- and upper level. From between 0520–0550 LT, the updrafts
311 remain constantly strong between 5 and 15 km. After 0550 LT, there is a secondary increase
312 in upward motions at around 7 km. By this time, the main convective cell had passed over the
313 profiler and the profiler is now sampling the stratiform anvils of the storm as indicated by the
314 absence of convective clouds in Steiner classification applied to CPOL (Fig 1a).

315 While present in Figure 1, it is evident that downdrafts occur much less frequently and with
316 much weaker magnitudes than updrafts. This is well known and has been illustrated in other
317 studies using radar profiler measurements (e.g., see May et al. 2002; Heymsfield et al. 2010;

318 Giangrande et al. 2013). The observed regions of downdrafts, although short-lived (so
319 smaller spatial width), are consistent with the different downdraft types known to exist (e.g.,
320 Knupp and Cotton 1985; Sun et al. 1993). Downdrafts forming at low levels, which are more
321 frequent than downdrafts in upper levels, are likely to be associated with precipitation
322 loading, evaporation and melting and can be seen throughout the active storm phase. Several
323 downdrafts can be found above the freezing level, such as the observed strongest downdraft
324 around 0540 LT between 7 and 10 km and short-lived downdraft preceding the main updraft
325 shaft at 0500 LT. These upper-level downdrafts can occur both ahead and behind the
326 convective updrafts and their physical cause are suggested to be quite distinct from those
327 downdrafts that occur in lower-levels (Sun et al. 1993). These are thought to be air-forced,
328 initiated by convergence between air detrained from the tops of the updrafts and slower
329 moving ambient air (Smull and Houze 1987). There is tendency that these upper-level
330 downdrafts are positively buoyant, whereas the lower level downdrafts are negatively
331 buoyant (Sun et al. 1993). It is clear from the case study illustrated in Figure 1 that vertical
332 motions vary significantly over the storm lifetime, with cloud height and also between
333 convective and stratiform structures. We do not attempt to study the evolution of vertical
334 velocities as a function of storm lifetime because the profiler may be sampling only a section
335 of individual storms.

336 To be of use for model evaluation, the derived mass-flux profiles must be representative for
337 an area the size of a GCM grid box. To account for all cumulus clouds over the model size
338 grid requires computation of convective area fraction. The area fraction is typically defined as
339 the ratio of the size of all convective cells in the domain over the total domain size. Scanning
340 radars, such as CPOL, are most suitable to calculate area fraction using this spatially
341 sampling approach. Since we wish to compute mass-flux from a vertically pointing wind
342 profiler, which takes measurements over a column with a small cross-sectional area, the area

343 fraction cannot be directly estimated using these measurements. Instead, convective area
344 fraction is determined as the ratio of the time CPOL identifies convection above the profiler
345 over the total sampling time. We use a long total sampling time of two wet season with the
346 rationale that the convection, at a point, derived from this long time series is a good sample of
347 that occurring in the entire domain over the same sampling time.

348 To evaluate this approach, the area fractions were derived as described above using both the
349 scanning CPOL and vertically pointing wind profiler, respectively (Fig. 2). Recall that only
350 convective cloud columns from CPOL are used to calculate both the spatial statistics from
351 CPOL and the temporal statistics at the profiler site. The convective area fraction from CPOL
352 was calculated for various circular regions of radius ranging from 10 to 100 km centred on
353 the wind profiler site. The CPOL area fractions for three selected domain sizes shown in Fig.
354 2 are remarkably similar. This suggests that convection experienced at the profiler site is a
355 good approximation for convection experienced in a GCM size grid box centred on the wind
356 profiler location. Importantly, the convective area fraction derived from the wind profiler for
357 the whole time period (solid curve, $|w| \geq 0\,\mathrm{m\ s^{-1}}$) shows a similar structure as the area fraction
358 from CPOL in the lower and middle troposphere but drops off more rapidly above 8 km. The
359 CPOL radar takes 10 mins to complete each volumetric scan, so when present it is assumed
360 that the convection will last for the entire 10 mins. The example discussed in Fig. 1 shows
361 that the temporal variability is high within 10 minutes, with large differences observed
362 between CPOL and 920-MHz reflectivities. In contrast, the wind profiler samples every 1
363 min, so even though a 10-min window is classified as convective by CPOL, the individual ten
364 1-min profiles from the wind profiler does not always contain valid vertical velocity
365 measurements. Inevitable instrumental problems may have further contributed to this. Also,
366 at higher altitude, the profiler area fraction begins to drop relatively rapidly compared to the

CPOL fractions due to the drop in profiler sensitivity with altitude. The CPOL sensitivity does not change much with height.

We further evaluate the area fraction estimates from the profiler by applying consecutively larger thresholds to the vertical velocity measurements. The thresholds of $|v| > 0.5$, 1.0 and 1.5 m s^{-1} are chosen as they have been employed by previous investigators to identify updraft/downdraft cores with profiler observations (e.g., LeMone and Zipser 1980; May et al. 2002; Giangrande et al. 2013). Increasing the velocity selection threshold leads to larger difference in area fractions from the two radars, particularly below the freezing level. Thus, to achieve convective area fractions with the profiler approach that is closest to the area fractions obtained with the CPOL radar, all vertical velocity data points (i.e. $|v| > 0$ m s^{-1}) from the identified convective intervals will be used from hereafter. This will likely result in values of mean vertical velocity that are much lower than those reported in previous studies, which generally used velocity thresholds to remove the low velocity values from their analysis.

Equipped with estimates of area fraction and in-cloud vertical velocity from the profiler measurements we can now calculate the mass-flux M_c (kg s^{-1} m^{-2}). Here, M_c is defined using the traditional GCM-type definition for mass-flux by considering all cumulus cloud occurring over a large area:

$$M_c = \rho \sigma_u v_u + \rho \sigma_d v_d \qquad (1)$$

where: ρ is the air density (kg m^{-3});

σ_u, is the area fraction of updraft cores in the grid box and is a dimensionless quantity. The σ_u can be further subdivided into the numbers of cores and the width of cores;

389 v_u is the mean velocity of updraft (m s^{-1}) ;

390 and σ_d and v_d is the area fraction and mean velocity of the downdraft cores,
391 respectively.

392 The vertical profile of air density is computed using standard textbook formulae, with input
393 temperature and pressure fields extracted from the Darwin radiosoundings. The mean profiles
394 of all remaining variables in Equation (1) are computed using the profiler vertical velocity
395 data from the convective intervals. We found that unlike the area fraction, the mean mass-
396 flux profile was largely independent of the different velocity threshold (result not shown).
397 This is because larger vertical velocity thresholds lead to smaller area fractions (Fig. 2) but
398 much larger mean vertical velocities, with the two effects compensating and leading to
399 similar mean mass-flux values.

400 **4. Results**

401 **4.1 Overall characteristics of convective mass-flux and its constituents**

402 a) Mean mass-flux profile

403 Precipitating convective clouds were identified by the CPOL radar over the profiler site for a
404 total of 283 10-minute scans during the two wet-seasons analysed here. This corresponds to a
405 convective area fraction near the surface of approximately 0.5 %. Note that this represents an
406 average including many instances with no convection present in the domain for significant
407 periods of time. It is therefore not comparable to convective area fractions found in previous
408 studies (e.g., Davies et al. 2013), which reach values up to 10 % but reflect instantaneous
409 conditions rather than long temporal averages. Going back to the overall time average, Table
410 1 summaries the contributions to the total convective area fraction from congestus (CTH < 7

411 km), deep (CTH between 7 and 15 km) and overshooting clouds (CTH> 15). It also shows
412 the variability of convective cloud frequency in different environment and large-scale
413 terciles. The results shown in Table 1 are discussed further in sections 4.2 and 4.3.

414 Mean profile of the overall mass-flux as well as upward and downward mass-flux profiles are
415 shown in Fig. 3. Here, the lower x-axis represents the overall mean over the entire two
416 seasons including the very frequent times (99.5%) of no convective clouds present over the
417 profiler site. To provide at least a rough estimate of the values of mass-flux "when present", a
418 value more useful to modellers, we average mass-fluxes over 3-hour windows and discard all
419 windows with no presence of convective clouds (~93 %). These results are indicated by the
420 upper x-axis in Figure 3. A 3-hour window translates to a grid size of roughly 60 km;
421 calculations based on 5 m s^{-1} average propagating speed of convective cells (Kumar et al.
422 2013b). Note that removing zeros will not affect the profile shape but only its magnitude. The
423 overall mean mass-flux (thick curve) increases steadily from near cloud base to peak at 6 km
424 just above the freezing level, and thereafter decreases gradually with height. At all height
425 levels, except at very high altitudes, mass-flux totals are dominated by updrafts (thin curve).
426 Importantly, these observational results also validate those reported in many studies using
427 cloud-resolving models (e.g., Derbyshire et al. 2004; Kuang and Bretherton 2006) and are
428 also in good agreement with previous attempts to retrieve mass-fluxes from profiler
429 observations (e.g., May and Rajopadhyaya 1999).

430 **b) Mean area fraction and vertical velocity**

431 Equation 1 indicates that updraft and downdraft mass-fluxes are affected by three
432 fundamental factors; the number of cores, the size of the cores and the vertical velocity in the
433 cores. The product of the number and size terms divided by domain size gives the area

434 fraction. We now examine the characteristics of these three fundamental factors with the aim
435 to understand the relative contributions of these factors to the mass-flux totals.

436 We begin by examining the variations in convective area fraction (thick solid line in Fig. 4a)
437 divided into upward area fraction (thin solid line) and downward area fraction (dashed line).
438 Once again we show the overall period averages with the lower x-axis and those for 3-hour
439 windows that contain convection with the upper x-axis. At low levels, updraft and downdraft
440 area fractions are nearly equal. The updraft fraction remains more or less constant from near
441 the surface to 8 km and then decreases steadily at higher levels. Starting from the top the
442 small downdraft fraction increases slightly to just above the freezing level, where a
443 significant increase in downdraft fraction occurs, indicating the potential importance of this
444 level in downdraft formation. In Fig. 4c and 4d, the upward and downward area fractions
445 (shaded) are subdivided into the number of cores (solid lines) and their size (dashed line).
446 The core width is measured in minutes, and represents the number of consecutive 1-min
447 periods with vertical motion $> 0\,\mathrm{m\ s^{-1}}$ for an updraft core. Downdraft cores are defined
448 analogously using downward motion.

449 The mean core spatial width associated with upward motion (dashed line in Fig. 4c) increases
450 gradually from an average of ~2 min at cloud base to a maximum average width of ~6 min at
451 a height of 8 km. Assuming a propagation speed of 5 m s^{-1}, this translates into a width of
452 ~600 m near cloud base and ~1.8 km at mid-levels. Above 8 km the updraft core width
453 decreases sharply. In contrast, the core frequency associated with updrafts is highest near
454 cloud base, decreasing monotonically with increasing height. The net effect of this pattern in
455 updraft width and frequency is that the upward area fraction (shaded region in Fig. 4c) is
456 highest and constant between cloud base and 8 km. Downdraft number increases downwards
457 with a particularly sharp increase near the freezing level. The average width of downdraft

458 cores is ~3 min and remains fairly constant with height. Once again assuming a 5 m s^{-1}
459 propagation speed, this translates into a size of ~900 m.

460 The mean vertical velocity (thick black curve in Fig. 4b) increases gradually with height and
461 peaks at ~4 m s^{-1} at 12 km. This mean profile is the sum of the velocities in updrafts (thin
462 black curve in Fig. 4b) and downdrafts (dashed black curve) weighted by the fractional area
463 of updraft and downdraft cores. The updraft velocity evolution with height is very similar to
464 the overall mean with a drop between 2 and 3 km followed by a steady increase to values of
465 ~5 m s^{-1} at high levels. In contrasts, the downdrafts show much weaker velocities of ~ 1 m s^{-1}
466 which are almost constant throughout the cloud layer with slightly large values near the tops
467 of very deep clouds.

468 The mean vertical velocity values shown in Fig. 4b are much lower than those reported
469 elsewhere (e.g., May and Rajopadhyaya 1999; Heymsfield et al. 2010; Giangrande et al.
470 2013). This is because we do not apply any threshold for the inclusion of the observed in-
471 cloud velocities in our sample of convective drafts, whose existence is instead determined by
472 the CPOL radar measurements over the profiler site (see section 2.2). To enable a more
473 meaningful comparison with previous studies, Fig. 4b shows not only the averages, but also
474 the full 2D histogram of vertical velocity distributions. The 90^{th} percentile of updraft and
475 downdraft velocities (white curves in Fig. 4b) reached up to 15 m s^{-1} and −6 m s^{-1},
476 respectively. The profile of the 90^{th} percentile velocities are consistent, both in magnitude and
477 in vertical structure, with the values for land-based deep convection reported in Heymsfield et
478 al. (2010), who only examined the profiles of the maximum updraft and downdraft velocity.
479 May and Rajopadhyaya (1999) and Giangrande et al. (2013) removed velocities between ±1.5
480 m s^{-1} from their analysis, but the strongest velocity profiles in those studies compare well
481 with our results. In-situ aircraft penetrations results reported in LeMone and Zipser (1980)

showed 90th percentile values of around 5 m s^{-1} in middle levels. These lower values are likely due to the more continental character of the convection sampled here as well as a possible undersampling of strong convection by aircrafts due to safety concerns.

Next, we reconcile the vertical structure of the mass-flux (Fig. 3) with area fraction (Fig. 4a, Fig.4c–4d) and vertical velocity (Fig. 4b). As it is difficult to mentally sum all contributing factors to the total mass-flux we compare the updraft and downdraft terms separately. The increase in updraft mass-flux between 2 and 5 km is largely a reflection of the vertical velocity increase combined with a small increase in area fraction. The large reduction in updraft mass-flux above 8 km is due to the strong decrease in area fraction, which is slightly offset by an increase in vertical velocity. Note that the decrease in density with height also affects the mass-flux profile, such that constant velocity and area fraction would still imply a reduction of mass-flux with height. As the downdraft velocities are small and relatively constant with height, the strong increase in downdraft mass-flux below 6 km (Fig. 3) is to first order driven by the corresponding increase in downdraft area fraction.

Overall, perhaps with the exception of increase in updraft mass-flux at low levels, the total mass-flux is governed to first order by the area fraction. If confirmed at other locations, this would provide the opportunity of estimating the first order characteristics of mass-flux from area fraction alone, a quantity that is much more easily measured using instruments both on the ground and in space than vertical motions.

4.2 Sensitivity of mass-flux to environmental and large-scale conditions

Of key relevance to cumulus parameterisation is the connection of mass-flux with the environmental conditions in which the convection is embedded. In this section, we examine the relationship between $RH_{0\text{-}5}$, CAPE, CIN and ω_{500} with the updraft mass-flux, upward

505 area fraction and upward velocity. As the downdraft contribution to overall mass-flux is
506 relatively small we focus on updraft behaviour only.

507 For the analysis shown in this section, the environmental conditions are grouped into terciles
508 of their respective probability density functions. This ensures that the wind profiler sampling
509 time in each tercile is identical. Note though that the amount of convective clouds observed in
510 each tercile can still vary significantly depending on how favourable the conditions in each
511 tercile are for convection. The tercile boundaries for each environmental variable, the amount
512 of time with which convective clouds occur in each tercile and their sub-division into
513 congestus, deep and overshooting modes are shown in Table 1.

514 a) Effect of 0-5 km Relative Humidity (RH_{0-5})

515 A moist environment, which is represented by the upper tercile of RH_{0-5}, is thought to be
516 important to support the formation of deep convection over its shallower counterparts (e.g.,
517 Redelsperger et al. 2002; Derbyshire et al. 2004; Takemi and Liu 2004). The results shown in
518 top panels of Fig. 5 reveal several interesting differences between dry (solid curves, $RH_{0-5}<68\%$)
519 and moist (dashed curve, $RH_{0-5}>82$ %) condition updraft mass-flux (left), area
520 fraction (middle) and velocity (right). The updraft mass-flux (Fig. 5a) in dry conditions
521 exhibits a sharp peak at the height of 6 km with a strong drop-off in mass-flux above that
522 level, while in moist conditions a smoother and deeper mass-flux profile is evident. The
523 behaviour in dry conditions likely indicates the prevalence of shallower clouds (see Section
524 4.3). The updraft area fraction is much smaller in dry conditions, indicative of a less frequent
525 occurrence of convection (see also Table 1). As seen before for the overall means (Fig. 3 and
526 4), area fraction increases from cloud base to mid-levels, followed by a decrease higher up.
527 Vertical velocity increases with height in both states of RH_{0-5}. Perhaps surprisingly, the
528 velocities are stronger in dry conditions than in moist conditions, partly compensating the

lower mass-flux strength induced by the lower area fractions in that state. The higher velocities can be understood by the need to produce stronger updrafts to penetrate through the dry atmosphere, while in moist conditions weaker updrafts occur more frequently and can penetrate higher into the moist troposphere more easily.

b) Effect of CAPE

Next we study the relationship of mass-flux to CAPE (Fig. 5d–f). The differences in the upper (> 747 J kg^{-1}; dashed) and lower tercile (<365 J kg^{-1}; solid) CAPE conditions are much smaller than those for $RH_{0\text{-}5}$. The mass-flux is slightly weaker in low CAPE conditions and it reaches higher levels in high CAPE conditions. Somewhat paradoxically, low CAPE conditions give rise to higher area factions. This is consistent with the findings of Kumar et al. (2013b) who showed that low CAPE conditions are associated with more frequent but shallower convective clouds over Darwin. The air parcels in the convective clouds are less buoyant in low CAPE conditions, leading to weaker updraft speed (Fig. 5f) and often shallower cloud. In contrast, in high CAPE condition, convection is much deeper because the air parcels have greater growth momentum. While less frequent in high CAPE conditions, convection that occurs exhibits significantly larger vertical velocities. The net effect is that the updraft mass-flux at all heights, except near cloud base, is higher in high CAPE conditions compared to low CAPE conditions.

c) Effect of CIN

In general, when the convective inhibition (CIN) of the atmosphere is low, more convective cloud systems are likely to form. This is confirmed by our analysis of mass-flux in the lowest (< 30 J kg^{-1}; solid) and highest (> 62 J kg^{-1}; dashed) CIN terciles (Fig. 5g–i). There is a large difference in mass-flux between high and low CIN conditions, which is entirely caused by

552 differences in area fraction, which is synonymous with the frequency of occurrence of
553 convection. The vertical velocity profiles are largely unaffected by the state of CIN,
554 indicating that CIN is more likely a predictor for the existence of convection than its strength.

555 d) Effect of large-scale upward motion at 500 hPa (ω_{500})

556 Similar to CIN, large-scale vertical motion is strongly related to the existence of convection
557 (Fig. 5j-l). Almost all convective events occur in the "lower" tercile, which comprises of
558 large-scale upward motion ($\omega_{500} \leq -1.82$ hPa Hour^{-1}, solid), while the upper tercile of large-
559 scale downward motion ($\omega_{500} \geq 1.24$ hPa Hour^{-1}, dashed) is more or less void of convection.
560 The very small fraction (7%) of convective systems that do form when there is large-scale
561 downward motion tend to have very high upward vertical velocities in the upper level,
562 although the poor sampling in this class prevents us from drawing any firm conclusions.

563 e) Summary of effects of environmental conditions on mass-flux

564 In its entirety Fig. 5 provides an important set of lessons about convective behaviour that can
565 potentially be used in the construction of cumulus parameterisations. It is clear that different
566 environmental parameters, many of which have been used in constructing elements of
567 existing cumulus schemes, have different effects on the mass-flux because they affect its two
568 constituents, area and velocity, in different ways. Large-scale vertical motion and CIN are
569 strongly related to area fraction. These conditions strongly influence the existence and
570 prevalence of convection and through the area fraction exerts a strong control on the
571 convective mass-flux. In addition, $RH_{0\text{-}5}$ is strongly related to vertical motion in the clouds,
572 although it is likely that there is no direct causality in that relationship. Instead, we speculate
573 that the higher velocities in dry conditions are a result of weaker updrafts not being able to
574 penetrate the dry atmosphere. Changes in CAPE have the least impact on the convective area

fraction but instead show a strong relationship with cloud growth dynamics. In low CAPE conditions, the convective systems tend to be moderately more frequent but with weak updraft speeds while high CAPE conditions support stronger vertical motions, leading to slightly higher overall mass-fluxes in high CAPE conditions. In summary, there is some evidence from Fig. 5, that the constituents of mass-flux are responding differently to different environmental conditions, making it difficult to relate mass-flux itself to only one of them. This may indicate a potential benefit from treating area and velocity separately in future cumulus parameterisation approaches.

4.3 Contributions of each cumulus cloud type to the total mass-flux in different environmental conditions

Having investigated the overall mass-flux properties and their relationship to the state of the environment the convection is embedded in, we now investigate the contributions of individual precipitating cumulus cloud modes, namely congestus, deep and overshooting clouds, to the overall cumulus mass-flux. The three cloud modes are defined by tracking convective cells and identifying their 0-dBZ ETH (Kumar et al. 2013a, 2014). Cells that never exceed 7 km are classified as congestus, those that exceed 15 km are classified as overshooting and the rest as deep convection. Kumar et al. (2013a) noted that these three modes have remarkably different rainfall and drop size characteristics, and thus, it will be worthwhile to examine the mass-flux characteristics of these cumulus modes separately as well as quantify their overall effect.

The breakdown of the total time for which the three cumulus convective modes are found at the profiler site is shown in Table 1. We find that the most frequent type of convection sampled by the profiler is deep convection, with just over half of all cases in this category. The other two types contribute roughly one quarter each to the overall sample.

599 The mean profile of upward mass-flux associated with the three cumulus modes and the
600 constituents of these mass-flux profiles are displayed in Fig. 6. Given its high frequency the
601 highest contribution to the upward mass-flux in the lower 8 km of the troposphere is from the
602 deep mode. The mean vertical velocity intensity of this mode shows intermediate strength
603 updraft velocities of 2 to 4 m s^{-1} with a bimodal structure with peaks at 6 km and above 10
604 km. The congestus mode contributes about one quarter of the area fraction below 4 km, but
605 due to its relatively weak upward motion on the order of only 1 m s^{-1} makes a relatively small
606 contribution to the overall mass-flux. The overshooting mode contributes around one quarter
607 to the area fraction below 10 km and dominates the area fraction above 10 km. It shows the
608 strongest vertical motion of the three modes with average values increasing from around 4 m
609 s^{-1} at 5 km to 6 m s^{-1} above 10 km.

610 As the mass-fluxes were shown to be sensitive to the environmental conditions we next
611 investigate how the relative contribution from the three cloud modes may change with the
612 state of the environment. It was evident from Fig. 5 that ω_{500} and CIN mostly determined the
613 existence of convection, while $RH_{0\text{-}5}$ and CAPE had a more direct influence on its structure.
614 We therefore focus on the latter two parameters and contrast the contribution of the three
615 cumulus modes to mass-flux in changing $RH_{0\text{-}5}$ and CAPE conditions. These results are
616 shown in Fig. 7

617 The total time of each cumulus mode during the different environmental conditions are given
618 in Table 1. The most notable change in total time of individual cumulus modes with respect
619 to different environment conditions occurs for the overshooting mode when sorted with
620 respect to CAPE. While constant in overall terms (Fig. 7h and k), overshooting cloud forms
621 17% of all convection in low CAPE conditions but 37% in high CAPE conditions. This is a
622 result of the occurrence of both the congestus and deep mode decreasing as CAPE increases

623 (Fig. 7 h and k). As expected, the vertical velocities for the deep and in particular for the
624 overshooting mode increase with CAPE (Fig. 7i and l), leading to the overall larger mass-
625 fluxes in high CAPE conditions discussed earlier (Fig. 5). We now see that this increase is
626 predominantly driven by an increase in the velocities in the overshooting mode.

627 Changes in $RH_{0\text{-}5}$ (Fig. 7a–f) also strongly affect the overall mix of the occurrence of
628 convective modes. In dry conditions, 60% of the time convection is present is associated with
629 either the congestus or overshooting mode. In contrast, in moist conditions the deep mode
630 becomes the dominant mode occurring 54% of the time. The area of all three convective
631 modes increases significantly in moist conditions (Fig. 7b and e), while the velocities in the
632 deep modes decrease by about half with little change in the congestus mode. This once again
633 highlights that deep convection of both types is stronger but less frequent in dry conditions.

634 **4.4 Variability in mass-flux measurements**

635 The results shown so far have focused entirely on the mean behaviour of mass-flux and its
636 constituents, although some indication of variability is revealed by the breakdown into cloud
637 modes and by the 2D histogram of vertical velocity distributions (Fig. 4b). In this section we
638 aim to investigate the variability of mass-flux at the typical scale of a GCM grid box across
639 different events, as this is more readily comparable to what the mass-flux parameterization
640 produces. To enable this investigation we need to compute mass-flux over some discrete time
641 window rather than averaging over long periods of time. This once again requires finding a
642 compromise between representing the size of a GCM grid box and the results being affected
643 by the evolution of the convective systems over the time window. We choose a 3-hour time
644 averaging window (~60 km), but we will also contrast our results to those found using a
645 longer 6-hour window (~100 km). As most time-windows will have no convection at all in
646 them, we focus our investigation on the 95^{th}, 99^{th} and 99.5^{th} percentile of the respective

647 distribution functions. Figure 8 shows these percentiles for area fraction (top) and mass-flux
648 (bottom) for both the 3-hourly (green) and 6-hourly (red) time windows. For comparison, we
649 also include the area fractions measured by CPOL in a 50km radius around the profiler site in
650 Figure 8a.

651 While the length of the time window does not affect the mean profile of area fractions, it does
652 affect the variability. Shorter time windows will produce larger variability because there will
653 be increases in incidence of both very large and very small area fraction. Of the 2300 (1150)
654 available 3-hourly (6-hourly) time blocks, 93% (88%) had a convective area fraction of 0. As
655 expected, the upper percentiles of the area fraction distribution yields larger (smaller) values
656 for the 3-hourly (6-hourly) window ranging from 0.05 (0.03) for the 95^{th} percentile to 0.1
657 (0.08) for the 99^{th} percentile. The 6-hourly window is in closer agreement with the CPOL
658 area fractions.

659 The upper percentiles of the mass-flux distribution associated with the 3- and 6-hourly
660 windows are shown in Fig. 8b. This figure is in the same format as Fig. 8a, except the 98^{th},
661 not the 95^{th} percentile is shown, as the 95^{th} percentile mass-fluxes were too small to be seen
662 clearly. The 98^{th} percentile mass-flux has the vertical structure as the mean updraft and
663 downdraft mass-flux profile (Fig. 3), with peak updraft and downdraft mass-flux just above
664 the freezing level and close to cloud base, respectively. At higher percentiles very large
665 updraft mass-flux values occur at higher altitude and are linked with large vertical velocity
666 events occurring in deep and overshooting convection.

667 **5. Summary and Discussion**

668 The aim of this study was to derive convective mass-fluxes and their constituents on the scale
669 of a GCM grid box from wind profiler observations and thereby to provide a zeroth-order

observational reference for the evaluation of cumulus mass-flux schemes. The analysis conducted characterised the updrafts and downdrafts of precipitating convective clouds with continuous dual-frequency wind profiler observations taken over two wet-seasons at Darwin, Australia. We found the net mass-flux over the entire measurement period to be positive (upwards) between 2 and 14 km height with a peak at ~6 km. The downdraft cumulus mass-flux was found to be strongest close to cloud base associated with precipitation loading, with values of less than half of that seen in updrafts.

The separation of mass-flux into velocity and area fraction, the latter itself a product of core width and frequency, showed the mass-flux was most strongly regulated by the area fraction compared to the vertical velocity. While of secondary importance to overall mass-flux magnitude, the vertical velocity intensities revealed some crucial properties related to the cloud dynamics. The convective updraft velocity exhibited a dominant peak in upper-levels (>10 km), and a small secondary peak in lower level at 6 km particularly associated with the deep convective cloud mode. The observed structures in vertical velocity intensities associated with the deep convection (Fig. 4b and Fig. 6) matched well with the updraft profiles reported in previous studies (e.g., May and Rajopadhyaya 1999; Giangrande et al. 2013). The overshooting convective mode had more intense vertical velocity magnitudes than the deep mode at all height levels, increasing monotonically with height.

By separating the mass-flux into contributions from different precipitating cumulus types, we demonstrated that wide variety of vertical velocity intensities and cumulus sizes contribute to the mean mass-flux profile. This was shown to be due to a complex interplay of the frequency, size and strength of cumulus clouds with the environment. The analysis revealed that ~80% of the cumulus population over the two seasons formed when the large-scale vertical motions were strongly upwards (≤ -1.82 hPa Hour^{-1}) and/or when CIN was small

694 ($\leq$30 J kg^{-1}). Both low-level relative humidity ($RH_{0\text{-}5}$) and CAPE had a moderate effect on the
695 existence of cumulus clouds but these parameters had a significant impact on the vertical
696 velocity and hence the growth dynamics of clouds. Higher mean velocities were mainly
697 associated with deeper convection that formed in dry ($RH_{0\text{-}5}$ < 68%) and high CAPE
698 conditions (Fig. 5 and Fig. 7). While the latter is easily explained by energetic arguments, the
699 former is a less obvious result. We interpret this result as driven by the effects of entrainment
700 of dry air into the clouds limiting the vertical growth of clouds (e.g., Redelsperger et al.
701 2002). The very few deep cumulus clouds that do succeed to grow in the unfavourable dry
702 conditions need very strong vertical growth momentum and hence display very large vertical
703 velocities.

704 The downdraft vertical velocities and frequencies were significantly less than those for
705 updrafts at all height levels, except at cloud base and near cloud top, where they were similar.
706 This is consistent with the conceptual picture that a convective cloud is generally made up of
707 one or more dominant updraft cores, which are partly compensated by small and short-lived
708 downdrafts driven by precipitation loading in lower levels and air-forced processes in upper
709 levels (see Fig 1).

710 Our study has extended previous investigations of May and Rajopadhyaya (1999) for the
711 tropical Darwin region and Giangrande et al. (2013) for mid-latitude central plain of United
712 States by examining not only the overall mass-flux but its constituents at scales relevant to
713 GCM evaluation. Unlike these studies, we accepted all values of vertical motion in our
714 statistical analysis rather than setting a threshold value. This led to better agreement with
715 convective area fraction profile shapes derived from the CPOL scanning radar (Fig 2), likely
716 making our sample more representative. The mean updraft and downdraft vertical velocity
717 profiles found here are nevertheless in good agreement with earlier studies (e.g., Heymsfield

et al. 2010). The sensitivity of mass-flux to the environmental moisture conditions is in broad agreement with the modelling study of Derbyshire et al. (2004). Both the observational and model results show that during the moist conditions, the mass-flux has a broad peak at mid-levels, while in dry conditions, the mass-flux decreases monotonically with height albeit this decrease starts at higher levels in the observations (4 km) than in the model simulations (cloud base).

Despite the availability of two wet seasons of observations, perhaps the biggest limitation of our study remains the relatively small sample size. This once again highlights the difficulty of supporting the development of cumulus parameterizations with the relevant measurements. An obvious way to alleviate this problem is to use data from scanning radar systems. Such systems can provide frequent measurements of convective area fractions at GCM grid box scale (e.g., Davies et al. 2013) but the challenge is to derive long time series of reliable retrievals of in-cloud vertical velocity from them. This will be the next step of this work. We will use the computationally-efficient dual-Doppler retrieval technique from Protat and Zawadzki (1999), which will be evaluated first using the wind profiler vertical velocities as in Collis et al. (2013), but applied to a much longer dataset over Darwin. Our finding that mass-flux profiles tend to be dominated by the convective area fraction and that in-cloud velocities vary with cloud depth may also enable us to derive mass-flux estimates from scanning systems by statistically modelling, rather than measuring, vertical motion and combining those with more easily observed area fractions. This will be the subject of a further study that will extend the first useful foray into supporting cumulus parameterization development more directly with long-term observations presented in this paper.

References

741 Anderson, N. F., C. A. Grainger, and J. L. Stith, 2005: Characteristics of strong updrafts in
742 precipitation systems over the central tropical Pacific Ocean and in the Amazon. *J. Appl.*
743 *Meteor.*, **44**, 731–738.

744 Arakawa, A., 2004: The Cumulus Parameterization Problem: Past, Present, and Future. *J. of*
745 *Climate*, **17**, 2493–2525.

746 Byers, H. R., and R. R. Braham, 1949: The Thunderstorm—Report of the Thunderstorm
747 Project. U.S. Weather Bureau, 287 pp.

748 Casey, S. P. F., E. J. Fetzer, and B. H. Kahn, 2012: Revised identification of tropical oceanic
749 cumulus congestus as viewed by CloudSat. *Atmos. Chem. Phys.*, **12**, 1587–1595.

750 Carter, D. A., K. S. Gage, W. L. Ecklund, W. M. Angevine, P. E. Johnston, A. C. Riddle, J.
751 Wilson, and C. R. Williams, 1995: Developments in UHF lower tropospheric wind profiling
752 at NOAA's Aeronomy Laboratory. *Radio Sci.*, **30**, 977–1001.

753 Cifelli, R., and S. A. Rutledge, 1994: Vertical motion structure in Maritime Continent
754 mesoscale convective systems: Results from a 50-MHz profiler. *J. Atmos. Sci.*, **51,** 2631–
755 2652.

756 Cifelli, R., and S. A. Rutledge, 1998: Vertical motion, diabatic heating, and rainfall
757 characteristics in N. Australia convective systems. *Quart. J. Roy. Meteor. Soc.*, **124,** 1133–
758 1162.

759 Collis, S., A. Protat, P. T. May, and C. Williams, 2013: Statistics of storm updraft velocities
760 from TWP-ICE including verification with profiling measurements, *J. Appl. Meteorol.*
761 *Climatol.*, **52,** 1909–1922.

762 Davies, L., C. Jakob, P. T. May, V. V. Kumar, and S. Xie, 2013: Relationships between the
763 large-scale atmosphere and the small-scale state for Darwin, Australia. *J. Geophys.* Res., **118**,
764 11534–11545.

765 Derbyshire, S. H., I. Beau, P. Bechtold, J.-Y. Grandpeix, J.-M. Piriou, J.-L. Redelsperger, and
766 P. M. Soares, 2004: Sensitivity of moist convection to environmental humidity. *Quart. J.*
767 *Roy. Meteor. Soc.*, **130**, 3055–3080.

768 Emanuel, K. A., J. D. Neelin, and C. S. Bretherton, 1994: On large-scale circulations in
769 convecting atmospheres. *Quart. J. Royal Meteor. Soc*, **120**, 1111–1143.

770 Fierro, A. O., J. M. Simpson, M. A. LeMone, J. M. Straka, and B. F. Smull, 2009: On how
771 hot towers fuel the Hadley cell: An observational and modelling study of line-organized
772 convection in the equatorial trough from TOGA COARE. *J. Atmos. Sci.*, **66**, 2730–2746.

773 Fritsch, J. M., 1975: Cumulus dynamics: Local compensating subsidence and its implications
774 for cumulus parameterization, *Pure Appl. Geophys.*, **113**, 851-867.

775 Giangrande S. E., S. Collis, J. Straka, A. Protat, C. Williams, and S. Krueger, 2013: A
776 summary of convective-core vertical velocity properties using ARM UHF wind profilers in
777 Oklahoma, *J. Appl. Meteor. Climatol.*, **52**, 2278–2295.

778 Heymsfield, G.M., L. Tian, A. J. Heymsfield, L. Li, and S. Guimond, 2010: Characteristics of
779 deep tropical and subtropical convection from nadir-viewing high-altitude airborne Doppler
780 radar. *J. Atmos. Sci.*, **67**, 285–308.

781 Johnson, R. H., T. M. Rickenbach, S. A. Rutledge, P. E. Ciesielski, and W. H. Schubert,
782 1999: Trimodal characteristics of tropical convection. *J. Climate*, **12**, 2397–2418.

783 Jorgensen, D. P., E. J. Zipser, and M. A. LeMone, 1985: Vertical motions in intense
784 hurricanes. *J. Atmos. Sci.*, **42**, 839–856.

785 Keenan, T. D., K. Glasson, F. Cummings, T. S. Bird, J. Keeler, and J. Lutz, 1998: The
786 BMRC/NCAR C-band polarimetric (CPOL) radar system. *J. Atmos. Oceanic Technol.*, **15**,
787 871–886.

788 Kuang Z., and Bretherton C. S., 2006: A Mass-Flux Scheme View of a High-Resolution
789 Simulation of a Transition from Shallow to Deep Cumulus Convection. *J. Atmos. Sci.*, **63**,
790 1895–1909.

791 Kumar, V. V., C. Jakob, A. Protat, P. T. May, and L. Davies, 2013a: The four cumulus cloud
792 modes and their progression during rainfall events: A C-band polarimetric radar perspective.
793 *J. Geophys. Res.*, **118**, 8375–8389.

794 Kumar, V. V., A. Protat, P. T. May, C. Jakob, G. Penide, S. Kumar, and L. Davies, 2013b:
795 On the effects of large-scale environment and surface conditions on convective cloud
796 characteristics over Darwin, Australia. *Mon. Wea. Rev.*, **141**, 1358–1374.

797 Kumar V.V., Protat, A., Jakob, C., and May P. T., 2014: On atmospheric regulation of the
798 growth of moderate to deep cumulonimbus in a tropical environment. *J. Atmos. Sci.*, **71**,
799 1105–1120.

800 Knupp K. R., and W. R. Cotton, 1985: Convective cloud downdraft structure' an interpretive
801 survey, *Rev. of Geophy.* **23**, 183-215.

802 LeMone, M. A., and E. J. Zipser, 1980: Cumulonimbus vertical velocity events in GATE.
803 Part I: Diameter, intensity and mass-flux. *J. Atmos. Sci.*, **37**, 2444–2457.

804 Liu, C., and E. J. Zipser, 2005: Global distribution of convection penetrating the tropical
805 tropopause. *J. Geophys. Res.*, **110**, D23104, doi:10.1029/2005JD006063.

806 Marwitz, J. D., 1973: Trajectories within the weak echo regions of hailstorms. *J. Appl.*
807 *Meteor.*, **12**, 1174–1182.

808 May, P. T., and D. K. Rajopadhyaya, 1999: Vertical velocity characteristics of deep
809 convection over Darwin, Australia. *Mon. Wea. Rev.*, **127**, 1056–1071.

810 May, P. T., A. R. Jameson, T. D. Keenan, P. E. Johnston, and C. Lucas, 2002: Combined
811 wind profiler/polarimetric radar studies of the vertical motion and microphysical
812 characteristics of tropical sea breeze thunderstorms. *Mon. Wea. Rev.*, **130,** 2228–2239.

813 May, P. T., J. H. Mather, G. Vaughan, C. Jakob, G. M. McFarquhar, K. N. Bower, and G. G.
814 Mace, 2008: The Tropical Warm Pool International Cloud Experiment. *Bull. Amer. Meteor.*
815 *Soc.*, **89**, 629–645.

816 Paluch, I. R., and C. A. Knight, 1984: Mixing and evolution of cloud droplet size spectra in a
817 vigorous continental cumulus, *J. Atmos. Sci.*, **41**, 1801-1815.

818 Penide, G., V. V. Kumar, A. Protat, and P. T. May, 2013: Statistics of drop size distribution
819 parameters and rain rates for stratiform and convective precipitation during the North
820 Australian wet season. *Mon Wea. Rev.*, **141**, 3222–3237.

821 Petch, J., A. Hill, L. Davies, A. Fridlind, C. Jakob, Y. Lin, S. Xie, and P. Zhu, 2014:
822 Evaluation of intercomparisons of four different types of models simulating TWP-ICE *Quart.*
823 *J. Roy. Meteorol. Soc.*, **140**, 826–837.

824 Pope, M., C. Jakob, and M. Reeder, 2009: Regimes of the North Australian Wet Season. *J.*
825 *Climate*, **22**, 6699–6715.

826 Protat, A., and C. R. Williams, 2011: The accuracy of radar estimates of ice terminal fall
827 speed from vertically pointing Doppler radar measurements. *J. Appl. Meteor. Climatol.,* **50**,
828 2120–2138.

829 Protat, A., and I. Zawadzki, 1999: A variational method for real-time retrieval of three-
830 dimensional wind field from multiple-Doppler bistatic radar network data. *J. Atmos. Oceanic*
831 *Technol.*, **16**, 432-449.

832 Randall, D. A., and Coauthors, 2003: Confronting models with data - The GEWEX Cloud
833 Systems Study. *Bull. Amer. Meteor. Soc.*, **84**, 455–469.

834 Redelsperger, J. -L., D. B. Parsons, and F. Guichard, 2002: Recovery processes and factors
835 limiting cloud-top height following the arrival of a dry intrusion observed during TOGA
836 COARE. *J. Atmos. Sci.,* **59**, 2438–2457.

837 Roode, S. R.D., A.P. Siebesma, H. J. J. Jonker and Y. D. Voogd, 2012: Parameterization of
838 the vertical velocity equation for shallow cumulus clouds. *Mon. Wea. Rev.*, **140**, 2424–2436.

839 Smull, B. F., and R. A. Houze Jr., 1987: Dual-Doppler radar analysis of a midlatitude squall
840 line with a trailing region of stratiform rain. *J. Atmos. Sci.,* **44**, 2128-2148.

841 Steiner, M., R. A. Houze Jr., and S. E. Yuter, 1995: Climatological characterization of three-
842 dimensional storm structure from operational radar and rain gauge data. *J. Appl. Meteor.*, **34**,
843 1978–2007.

844 Sun, J., S. Braun, M. I. Biggerstaff, R. G. Fovell, and R. A. Houze Jr., 1993: Warm Upper-
845 Level Downdrafts Associated with a Squall Line. *Mon. Wea. Rev.*, **121**, 2919-2927.

846 Takemi, T., O. Hirayama, and C. Liu, 2004: Factors responsible for the vertical development
847 of tropical oceanic cumulus convection. *Geophys. Res. Lett.*, **31**, L11109, doi:10.1029/
848 2004GL020225.

849 Williams, C. R., 2012: Vertical air motion retrieved from dual-frequency profiler
850 observations. *J. Atmos. Oceanic Technol.*, **29,** 1471–1480.

851 Xie, S., R. T. Cederwall, and M. Zhang, 2004: Developing long-term single-column
852 model/cloud system - resolving model forcing data using numerical weather prediction
853 products constrained by surface and top of the atmosphere observations. *J. Geophys. Res.*,
854 **109**, DOI: 10.1029/2003JD004045.

855 Yanai, M., S. Esbensen, and J. Chu, 1973: Determination of bulk properties of tropical cloud
856 clusters from large-scale heat and moisture budgets. *J. Atmos. Sci.*, **30**, 611–627.

857 Zhang, M. and J. Lin, 1997: Constrained variational analysis of sounding data based on
858 column-integrated budgets of mass, heat, moisture, and momentum: Approach and
859 application to ARM measurements. *J. Atmos. Sci.*, **54**, 1503–1524.

860 Zipser, E. J., 2003: Some view on ''hot towers'' after 50 years of tropical field programs and
861 two years of TRMM data. *Cloud Systems, Hurricanes, and the TRMM. Meteor. Monogr., No.*
862 *51, Amer. Meteor. Soc.*, 49–58.

863

864

865 **Acknowledgements**

866 This work has been supported by the US Department of Energy ARM Program (DE-FG02-
867 09ER64742). We would like to acknowledge the contributions of Brad Atkinson and Michael
868 Whimpey in supporting the Darwin observatory and data management. V. Kumar thanks Ed
869 Zipser and two other referees for reviewing this paper.

870

871

872

873

874

875

876

877

878

879

880

881

882

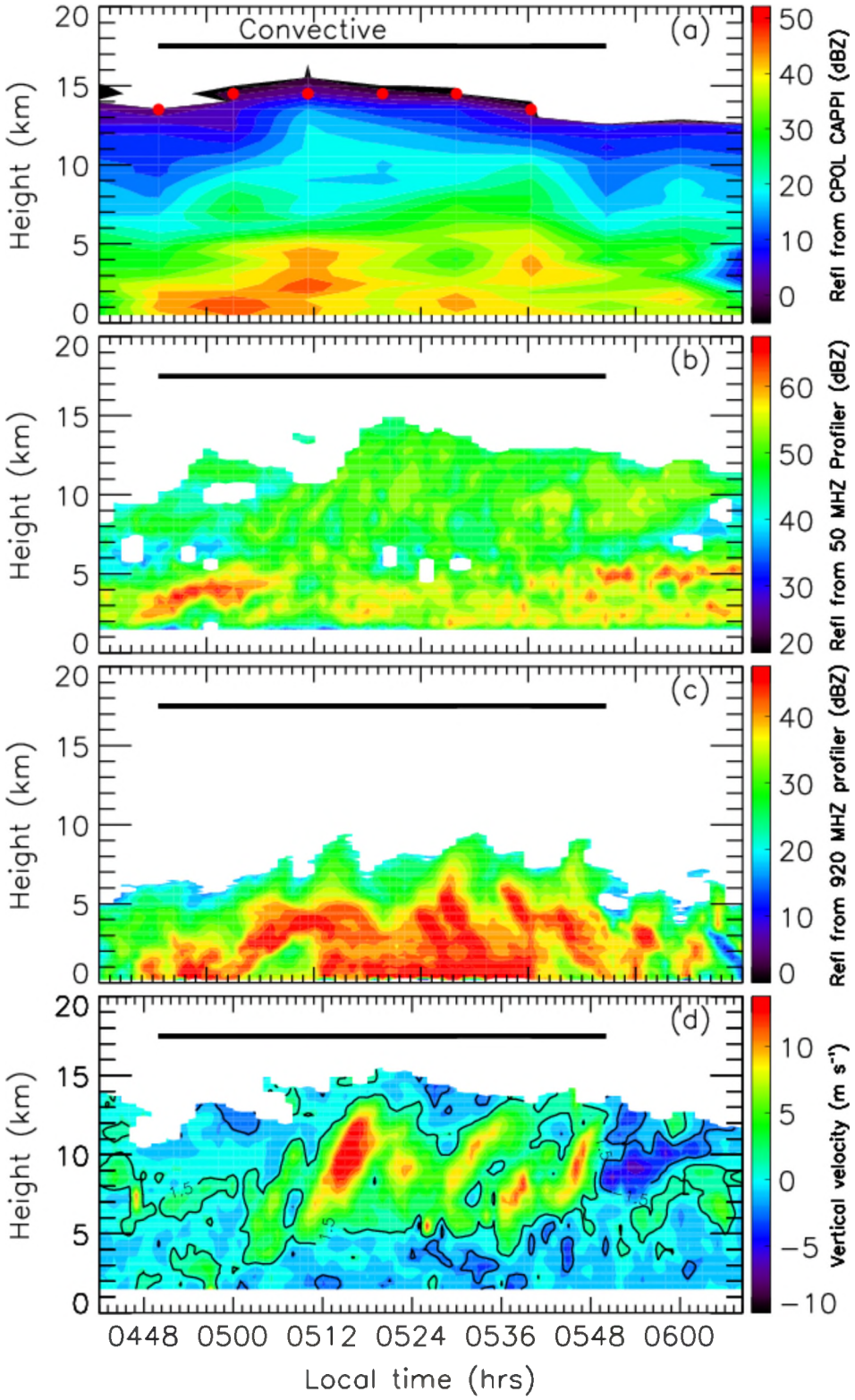

Figure 1: Overshooting convection captured by the wind profiler around 0500 LT on 21st March 2006. a) Time-height section of CPOL reflectivity collocated with the profiler in bins of 10 mins in time and 0.5 km in height. *The red dots are the 0-dBZ ETH* of Steiner classified convective columns. b)-d) Reflectivity from the 50- and 920-MHz profilers, and retrieved profiler vertical velocities, respectively. The profiler data are displayed in finer bins of 1 min in time and 0.1 km in height.

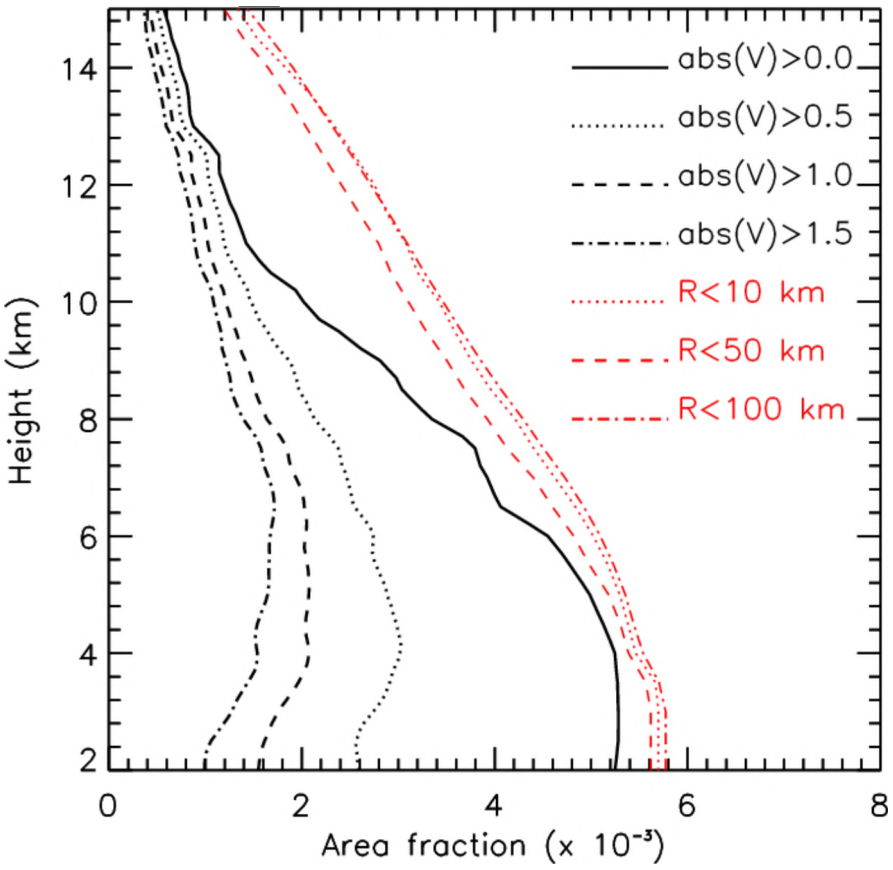

Figure 2: The two wet-season mean profile of convective area fractions using vertically pointing observations from the profiler (black) and volumetric observations from CPOL (red). As explained in the text, profiler area fractions were extracted by applying the "time approach" on different absolute vertical velocity thresholds ranging from 0 to 1.5 m s^{-1}. The area fractions from CPOL is extracted using the "space approach" for different circular region of radius ranging from 10 to 100 km, centred over the profiler.

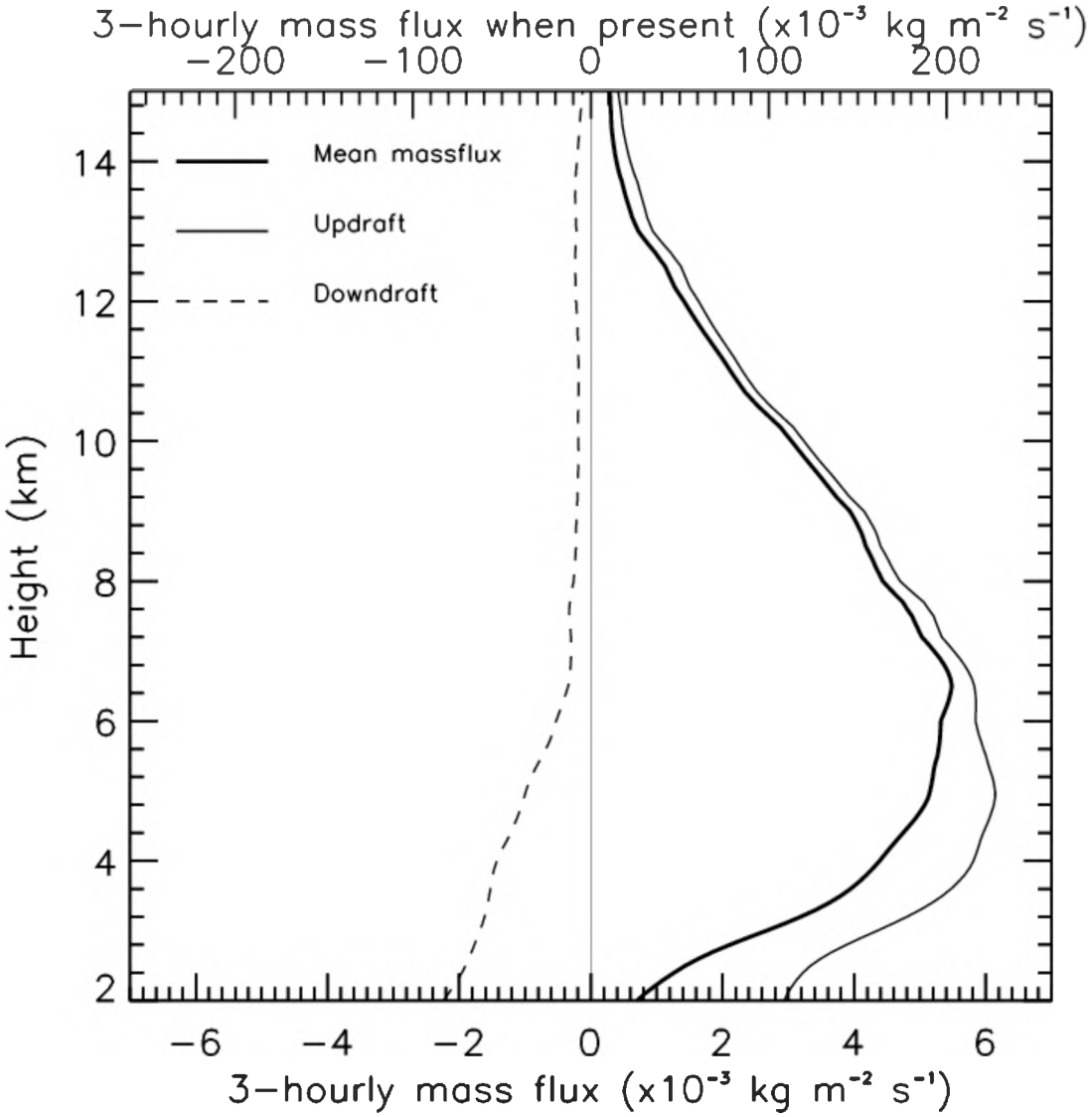

920

921

922 Figure 3: The two wet-season mean vertical profile of overall mass-flux (thick curve), updraft
923 mass-flux (thin curve) and downdraft mass-flux (dashed curve). As explained in the text,
924 mass-flux values were computed using the traditional GCM definition. The secondary x axis
925 represents mass-flux values provided there was at least one cumulus cloud in the 3-hourly
926 window (~60 km in spatial width).

927
928
929
930

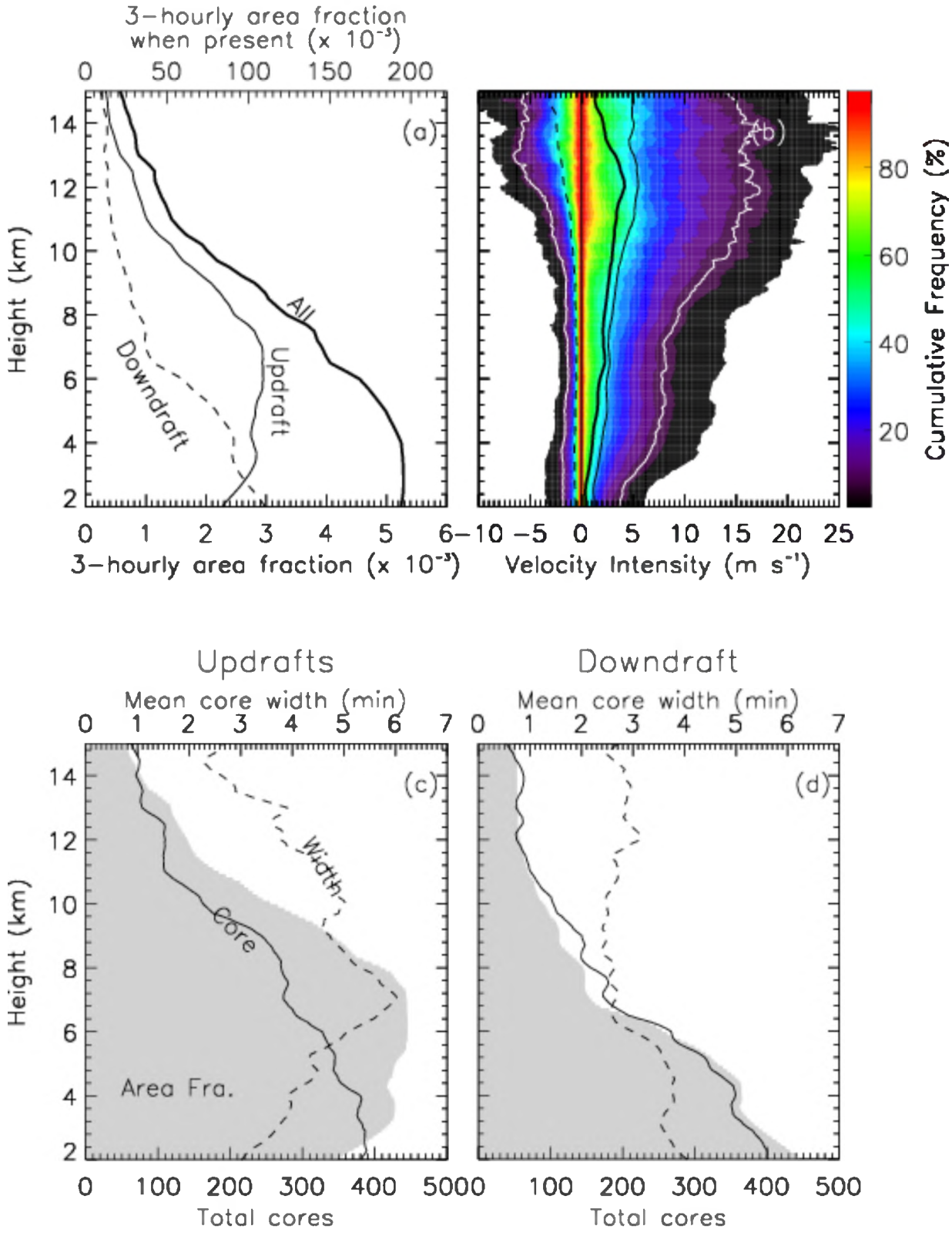

931 Figure 4: The same format as Fig. 3 and shows profiles of (a) mean area fraction, (b) mean
932 vertical velocity, c) cumulative count of updraft cores and mean spatial width and d) is the
933 downdraft core and width characteristics. The coloured plot in b) is the full 2D cumulative
934 histogram of vertical velocity distributions using bins of 0.5 km in height and 0.2 m s^{-1} in
935 velocity. The 90^{th} percentiles in updrafts and downdraft are the white curves.

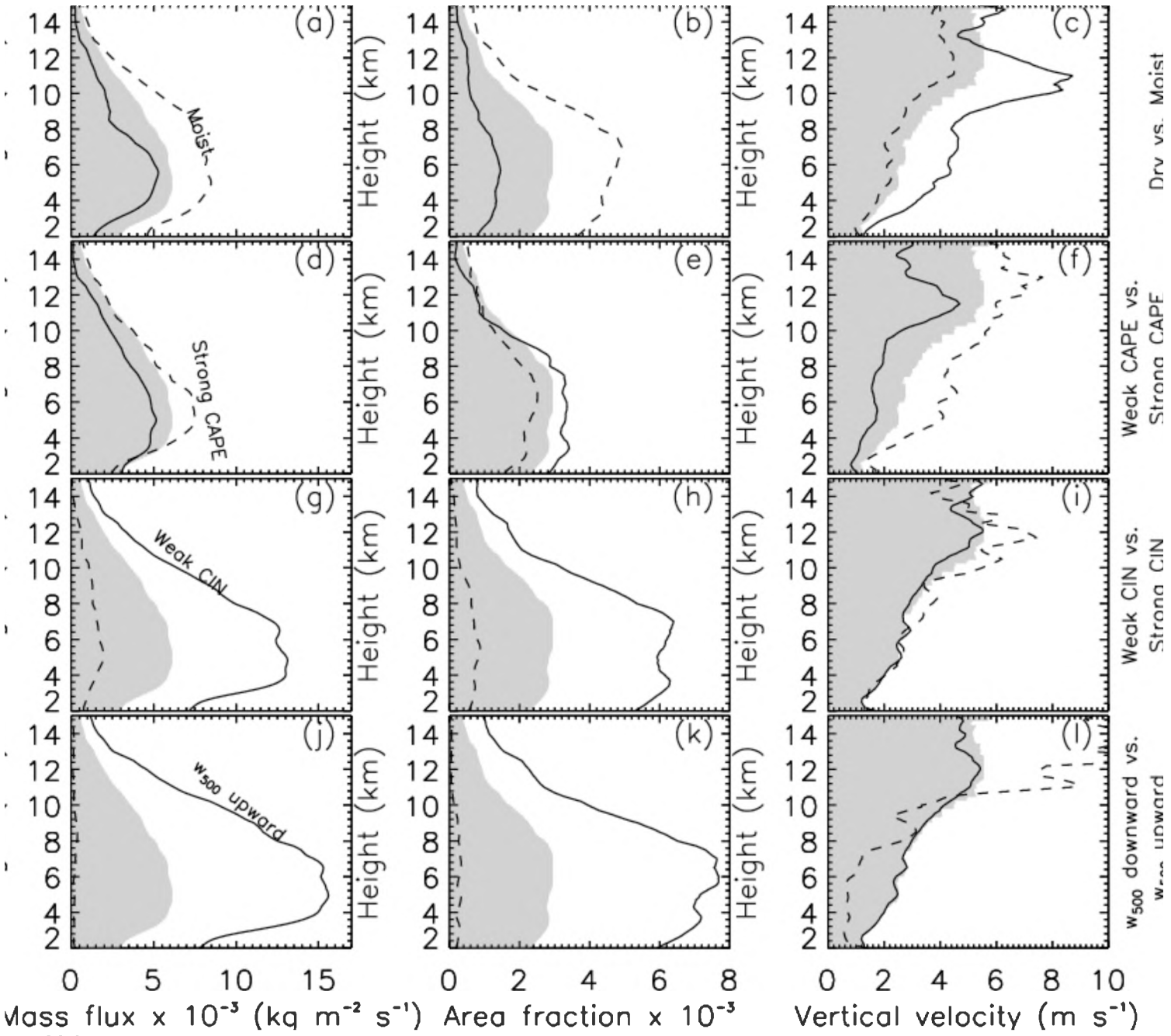

Figure 5: Effect of $RH_{0\text{-}5}$ (top panels), CAPE (second panels), CIN (third panels) and ω_{500} on updraft mass-flux (left column), upward area fraction (middle column) and upward vertical velocity intensities (right column). The shaded region is the overall updraft means without applying any environmental sorting. The solid and dotted line in each figure corresponds to lower and upper tercile of the environmental conditions. The tercile boundaries are in table 1.

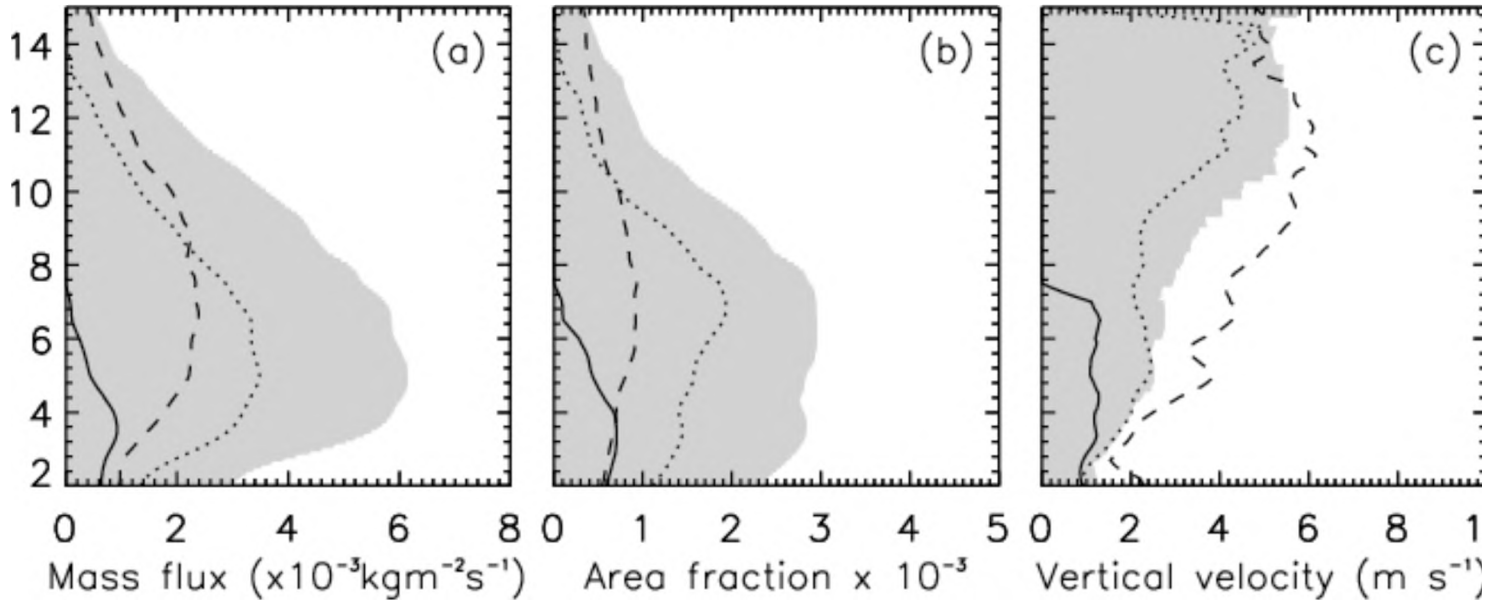

947
948

949

950 Figure 6: Contribution to (a) updraft mass-flux, (b) upward area fraction, and (c) upward
951 vertical velocity from congestus (solid), deep (dotted) and overshooting (dashed) cumulus
952 clouds. Once again, the shaded region represents all cumulus clouds.

953

954
955

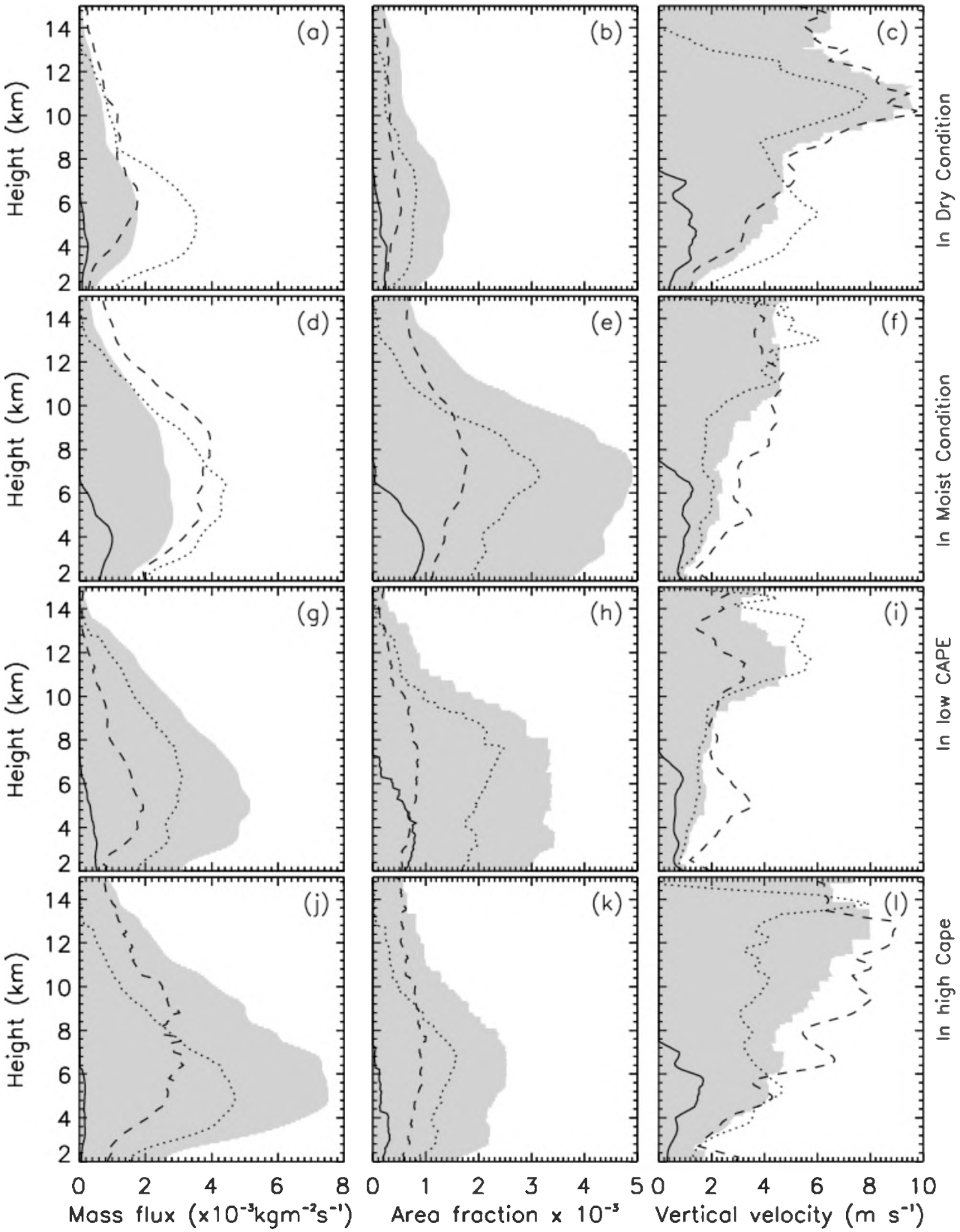

Figure 7: The same format as Fig. 6 and shows the mean response of the three precipitating cumulus modes in dry (top panels), moist (second panels), low CAPE (third panels) and high CAPE (bottom panels) conditions.

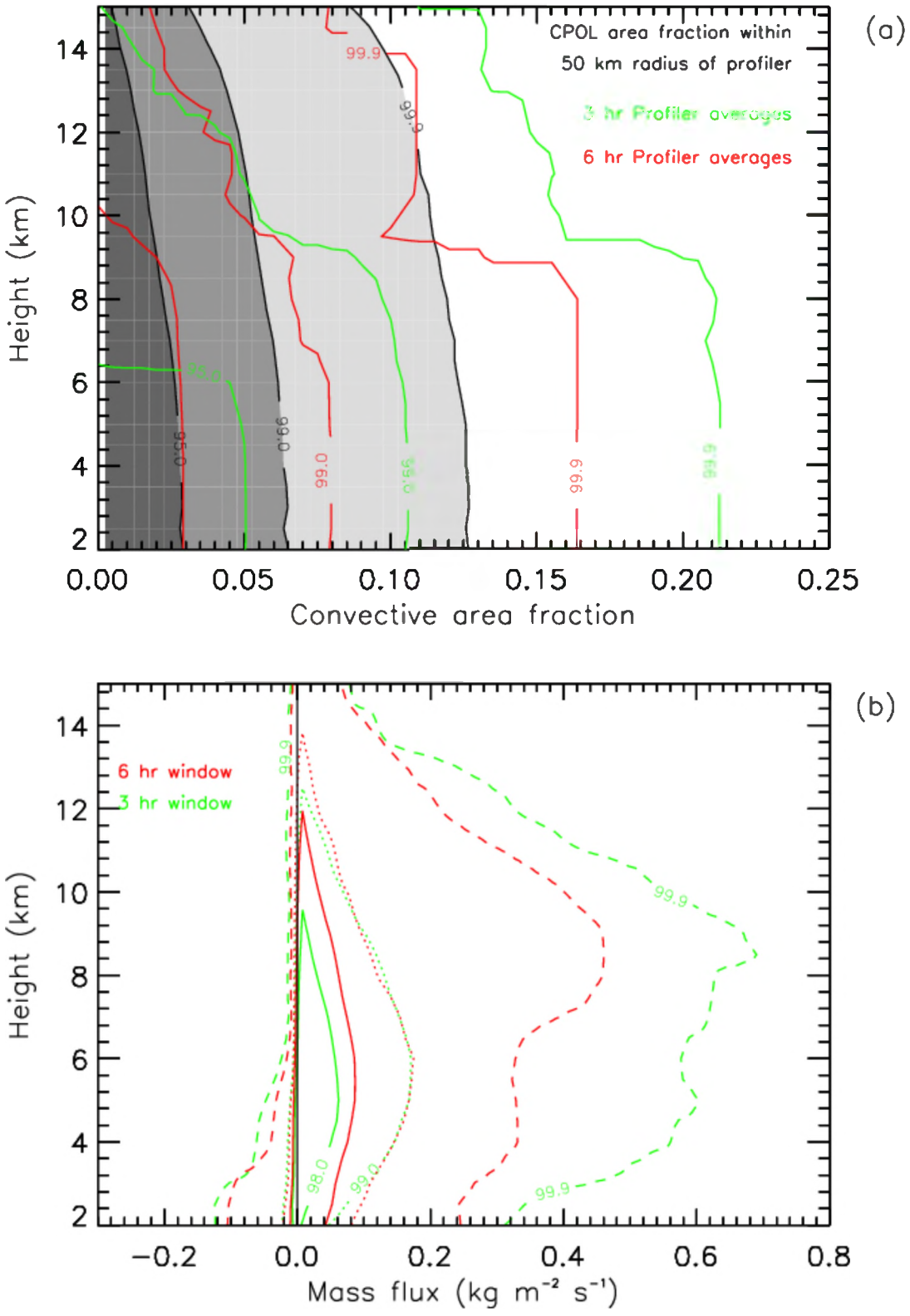

Figure 8: a) 2D cumulative histogram of convective area fraction from CPOL over a circular region of radius 50 km centred at the profiler site (shaded) and convective area fraction from wind profiler observations over 3- (green) and 6-hourly (red) time windows. b) The same as a) and shows the mass-flux.

991
992 Table 1: The two wet-season occurrence frequency of congestus, deep and over-shooting
993 clouds, and separately for the four environmental conditions
994

Environmental Conditions	**Total of the 1-min wind profiler scans**			
	Congestus (CTH < 7 km)	Deep (7 km < CTH < 15 km)	Over-shooting (CTH > 15 km)	All cumulus clouds
0-5 km RH ≤68%	145	196	148	489
0-5 km RH 68%-82%	228	557	184	969
0-5 km RH ≥82%	292	741	337	1370
CAPE ≤365 J kg^{-1}	251	620	184	1055
CAPE 365 – 747 J kg^{-1}	305	540	222	1067
CAPE ≥747 J kg^{-1}	109	334	263	706
CIN ≤30 J kg^{-1}	527	1030	512	2069
CIN 30 – 62 J kg^{-1}	78	346	127	551
CIN ≥62 J kg^{-1}	60	118	30	208
ω_{500} ≤−1.82 hPa $Hour^{-1}$	485	1232	649	2366
ω_{500} −1.82 to 1.24 hPa $Hour^{-1}$	109	176	10	295
ω_{500} ≥1.24 hPa $Hour^{-1}$	71	86	10	167
All	665	1494	669	2828

995
996

On the Atmospheric Regulation of the Growth of Moderate to Deep Cumulonimbus in a Tropical Environment

VICKAL V. KUMAR

School of Mathematical Sciences, Monash University, and Centre for Australian Weather and Climate Research, Melbourne, Victoria, Australia*

ALAIN PROTAT

Centre for Australian Weather and Climate Research, Melbourne, Victoria, Australia*

CHRISTIAN JAKOB

School of Mathematical Sciences, and ARC Centre of Excellence for Climate System Science, Monash University, Melbourne, Victoria, Australia

PETER T. MAY

Centre for Australian Weather and Climate Research, Melbourne, Victoria, Australia*

(Manuscript received 26 July 2013, in final form 29 October 2013)

ABSTRACT

Some cumulus clouds with tops between 3 and 7 km ($Cu_{3km-7km}$) remain in this height region throughout their lifetime (congestus) while others develop into deeper clouds (cumulonimbus). This study describes two techniques to identify the congestus and cumulonimbus cloud types using data from scanning weather radar and identifies the atmospheric conditions that regulate these two modes. A two-wet-season cumulus cloud database of the Darwin C-band polarimetric radar is analyzed and the two modes are identified by examining the 0-dBZ cloud-top height (CTH) of the $Cu_{3km-7km}$ cells over a sequence of radar scans. It is found that ~26% of the classified $Cu_{3km-7km}$ population grow into cumulonimbus clouds. The cumulonimbus cells exhibit reflectivities, rain rates, and drop sizes larger than the congestus cells. The occurrence frequency of cumulonimbus cells peak in the afternoon at ~1500 local time—a few hours after the peak in congestus cells. The analysis of Darwin International Airport radiosonde profiles associated with the two types of cells shows no noticeable difference in the thermal stability rates, but a significant difference in midtropospheric (5–10 km) relative humidity. Moister conditions are found in the hours preceding the cumulonimbus cells when compared with the congestus cells. Using a moisture budget dataset derived for the Darwin region, it is shown that the existence of cumulonimbus cells, and hence deep convection, is mainly determined by the presence of the midtroposphere large-scale upward motion and not merely by the presence of congestus clouds prior to deep convection. This contradicts the thermodynamic viewpoint that the midtroposphere moistening prior to deep convection is solely due to the preceding cumulus congestus cells.

1. Introduction

Johnson et al. (1999) and Kumar et al. (2013a) provided observational evidence that convective clouds in the tropics could be grouped into three main modes: shallow cumulus with cloud-top heights (CTH, by which we mean 0-dBZ maximum top height determined with a C-band radar) near the trade inversion layer, 1–2 km above the surface; midlevel cumulus clouds with a CTH

* A partnership between the Bureau of Meteorology and the Commonwealth Scientific and Industrial Research Organisation.

Corresponding author address: Vickal V. Kumar, Centre for Australian Weather and Climate Research, Australian Bureau of Meteorology and CSIRO, GPO Box 1289, Melbourne 3001, Australia.
E-mail: v.kumar@bom.gov.au

DOI: 10.1175/JAS-D-13-0231.1

near the 0°C freezing level; and deep clouds with a CTH near the tropopause. These cumulus modes have vastly different impacts on the water and energy budgets, as well as the circulation (e.g., Tao et al. 2003; Arakawa 2004). So to improve the parameterization of convective and cloud processes in the tropics, we need to better understand the characteristics of each of these cumulus modes, atmospheric factors that determine the type of cumulus mode that will occur, and how these cumulus modes may be linked with each other (e.g., Jensen and Del Genio 2006; Jakob 2010). This study will focus on the cumulus clouds with a CTH between 3 and 7 km ($Cu_{3km-7km}$), which has been hypothesized to precondition the atmosphere for deep convection by moistening it (e.g., Sherwood and Wahrlich 1999; Derbyshire et al. 2004; Mapes et al. 2006; Holloway and Neelin 2009; Nuijens et al. 2009; Powell and Houze 2013). A separate viewpoint is that the tropospheric moistening preceding deep convection is caused by large-scale dynamics (e.g., Hohenegger and Stevens 2013; Kumar et al. 2013a). In short, the fundamental question we want to address is as follows: What causes some $Cu_{3km-7km}$ cells to stay shallow throughout their lifetime, and promotes others to grow into deep convective cells?

In this study, the observed $Cu_{3km-7km}$ cells are separated into two modes: those that cease their growth in the lower stable layer near the freezing level, referred to here as congestus (Cg) cells, and those that continue to ascend to greater altitudes to become deep convective cells at a later time, referred to here as cumulonimbus (Cb) cells. This was achieved by examining the CTH of the $Cu_{3km-7km}$ cells in a sequence of the Darwin C-band polarimetric (CPOL; Keenan et al. 1998) radar scans. We hypothesize that combining the Cg and Cb modes into the single $Cu_{3km-7km}$ category could be a reason for the limited success in understanding the possible connection between the congestus cells and deep convection. Luo et al. (2009) separated the Cg (which they referred to as "terminal") and Cb (referred to as "transient") modes using estimates of the convective buoyancy of clouds from satellite observations and Numerical Weather Prediction (NWP) analyses and found that approximately 30%–40% of the cells are Cb while the rest are Cg. However, Casey et al. (2012) noted that the method proposed by Luo et al. (2009) may be missing up to 70% of the cells compared to the criteria of cloud-top heights lying between 3 and 9 km, where there is continuous radar echo from the near ground to the cloud top (Jensen and Del Genio 2006). The Luo method detects fewer cells compared to cells detected using cloud radar (e.g., Jensen and Del Genio 2006; Casey et al. 2012) because Luo's method was applied to convective cells only. The current study also focuses on convective cells and uses new height boundaries, as proposed in Kumar et al. (2013a), to identify the various cumulus modes in the tropics. Based on an objective analysis of the behavior of radar reflectivity as a function of CTH in the Darwin region, they found a major transition of the microphysical behavior of cells once they reached a CTH of 7 km. Thus, a 7-km height threshold is used here to separate shallow cells (aka $Cu_{3km-7km}$) from deep convection.

A major motivation of this paper is not only to separate the $Cu_{3km-7km}$ cells' population into Cg and Cb modes, but also to identify the atmospheric processes that regulate the occurrence of these nongrowing and growing cumulus clouds. Several studies (e.g., Lin and Johnson 1996; Kemball-Cook and Weare 2001; Redelsperger et al. 2002; Derbyshire et al. 2004; Kikuchi and Takayabu 2004; Takemi et al. 2004; Jensen and Del Genio 2006; Nuijens et al. 2009) have noted that presence of dry air at midtroposphere can effectively limit the vertical extent of convection. Thus, if there is sufficient moistening preceding a $Cu_{3km-7km}$ cell, then it increases the likelihood for it to develop into a deep Cb tower. Early studies hypothesized that the source of the midtropospheric moistening is due to congestus cells (e.g., Sherwood and Wahrlich 1999; Mapes et al. 2006; Holloway and Neelin 2009). However, a recent study has shown that the congestus cells alone would require too long a time to produce significant moistening of the midtroposphere, which would seem to rule out the potential role of the $Cu_{3km-7km}$ moistening as a dominant process for the transition to deep convection (e.g., Hohenegger and Stevens 2013). Their findings suggested that dynamical processes, potentially related to the heating from the $Cu_{3km-7km}$ cells, are likely an important ingredient in promoting the transition to deep convection. Another possible mechanism that has been found to promote the transition from shallow cumulus to deep convection over midlatitude continental surface types is greater low-level humidity, stronger large-scale updrafts in the midtroposphere, and boundary layer inhomogeneity (e.g., Zhang and Klein 2010).

This paper is organized along two major sections. The first section outlines and evaluates two new approaches to identify the Cg and Cb cells using CTH statistics from the scanning mode of the Darwin CPOL radar observations. The difference in microphysical rainfall properties of the Cg and Cb modes is also fully characterized. The second section highlights the difference in atmospheric conditions preceding the Cg and Cb modes using both observational and derived datasets.

2. Distinguishing congestus and cumulonimbus cells in radar data

This study uses a two-wet-season dataset (October 2005–April 2006 and October 2006–April 2007) of convective

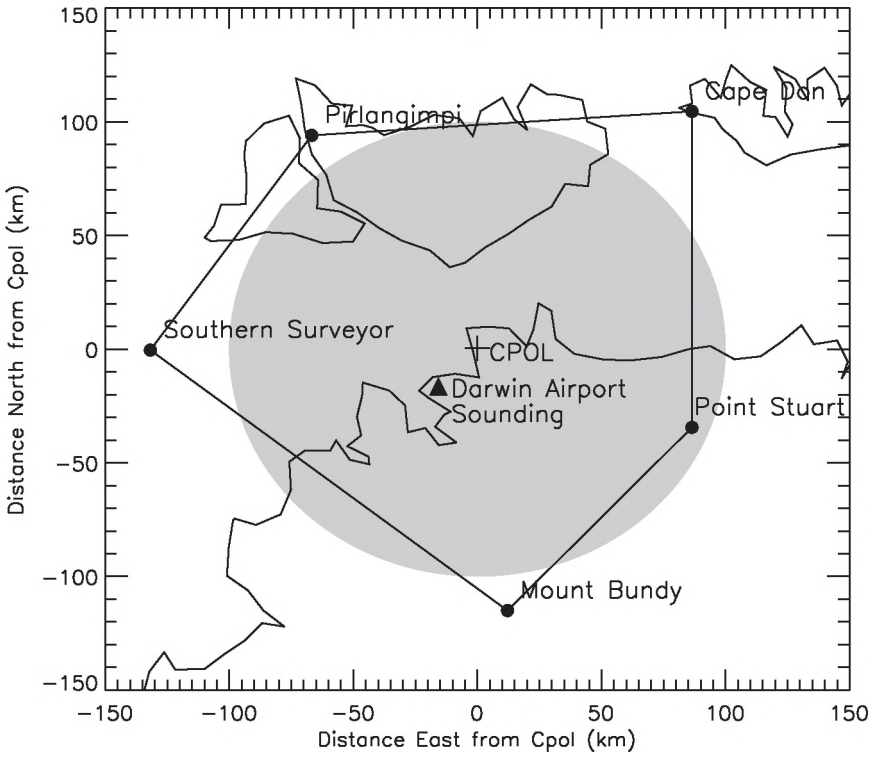

FIG. 1. The shaded gray circular region is the Darwin CPOL sampling domain. It is 100 km in radius from the radar location. The location of the operational Darwin airport radiosonde station and radiosonde stations that only operated during the TWP-ICE period are represented by a black triangle and black circles, respectively. The enclosed pentagon represents the domain for the large-scale dataset used in this study (see text for more details).

cells occurring within a radius of 100 km from the Darwin CPOL radar (12.25°S, 131.04°E; see Fig. 1). A convective cell is defined as consisting of one or more adjoining convective pixels (2.5 km × 2.5 km) using the 2.5-km radar constant altitude plan position indicators (CAPPI) data. The convective pixels are identified using the "Steiner" convective–stratiform classification algorithm (Steiner et al. 1995). For each convective cell, the maximum height reached by the 0-dBZ echoes above the cell is computed using reflectivity profiles to provide an estimate of the CTH. Note there must be continuous reflectivity fields in the vertical direction from the base of the cell at 2.5-km CAPPI level to the CTH (also see Kumar et al. 2013a,b). In most cases, the true cloud-top height will extend higher than the 0-dBZ CTH from a C-band radar. The difference between the C-band 0-dBZ top height and *CloudSat* CTH has been found to often be within 1 km (Casey et al. 2012). Similarly, Kumar et al. (2013a) noticed good matches between 0-dBZ cloud tops from the C-band and near −20-dBZ cloud tops from a millimeter-wavelength cloud radar (MMCR; Moran et al. 1998). Having retrieved one CTH per cell, we also calculate a single mean reflectivity, rain rate, drop size diameter (D_0) and number concentration of small hydrometers (N_W) for each convective cell. These mean values were calculated using the radar pixels at the 2.5-km level that are bounded by the horizontal cross-sectional area of the cell.

Descriptions of the algorithm used to retrieve drop size distributions (DSD) parameters and rain rates from the CPOL observations are given in Bringi et al. (2009). The algorithm assumes a normalized gamma DSD form (Testud et al. 2001) described by the median drop size diameter (D_0, mm) and the "generalized" intercept parameter (N_w). For simplicity, N_w can be thought as the number concentration of small hydrometers and has units of meters cubed per millimeter (the number concentration of hydrometeors per unit diameter). The parameter N_w is the same as the intercept parameter of an exponential DSD with the same D_0 and liquid water content as the gamma DSD. This algorithm uses a multiparameter approach to take advantage of the complementary information contained in the polarized backscattered signals. First, D_0 is retrieved from the differential reflectivity using polynomial fits [e.g., $D_0 = f(Z_{dr})$], then N_w is estimated using a power law of

the form $Z_h/N_w = c(D_0)^d$, and finally the rain rate is estimated using either a function of the form $R = f(K_{dp})$, $R = f(Z_h, Z_{dr})$, or $R = f(Z_h)$, depending on various thresholds and a decision tree (Bringi et al. 2009).

The Darwin CPOL radar operates at wavelength of 5.3 cm, with a minimum detectable reflectivity of −1.25 dBZ up to a radar range of 100 km. At this wavelength and radial distance, the radar will not be able to detect clouds made of drops of sizes less than 0.5 mm. Such clouds, which normally are classified as nonprecipitating clouds, are typically studied using millimeter wavelength cloud radars. Kumar et al. (2013a) have carried out a comparison between the cloud occurrence frequency detected by the Darwin CPOL and the Darwin MMCR radars. They found that the CPOL radar has a detection efficiency of 30% compared to MMCR for shallow cumulus clouds (CTH < 3 km; e.g., Zhang and Klein 2010) increasing to a 64% detection efficiency when the CTH is between 3 and 7 km (also known as $Cu_{3km–7km}$). Since CPOL misses most of the shallow cumulus cells, statistics associated with shallow cumulus category were removed from the subsequent analysis.

Over the two-wet-season study interval, CPOL detected a total of 207 871 cells with a CTH between 3 and 7 km—the $Cu_{3km–7km}$ cells. A 7-km CTH threshold is used instead of the often-used 9-km cutoff (e.g., Jensen and Del Genio 2006) because convective cell reflectivities and the DSD parameters exhibit clear microphysical differences when the CTH of the cells are less than 7 km compared to those that extended beyond 7 km (e.g., Takemi et al. 2004; Kumar et al. 2013a). Having identified the $Cu_{3km–7km}$ cells, the next task is to distinguish cells that will continue to rise above 7 km during their lifetime (Cb cells) from those that will not (Cg cells). Here, we employ two different methods.

Method 1 is a "nearest neighbor" approach. It employs the same logic as that used in the automated Thunderstorm Identification Tracking Analysis and Nowcasting (TITAN) radar analysis tool (Dixon and Wiener 1993). Note the current TITAN settings of a minimum volume requirement of 30 km^3 and the reflectivity threshold of 35 dBZ are fine tuned to identify deep convection. The tool has not been optimized to detect the less intense $Cu_{3km–7km}$ cells, and so cannot be used directly for our purpose. We therefore only use the TITAN cell speed and direction products to assist in establishing the potential search area to find the nearest neighbor for the test $Cu_{3km–7km}$ cells in the subsequent scan. The TITAN tool tracks the cloud cells in space at discrete times (every 10 min in this case) and so the velocity vectors of cloud cells through their lifetime were determined from relative motion of the cells. During times when the TITAN tool does not detect any cell track, the cell speed and direction is determined through an interpolation process of neighboring TITAN cell statistics.

The search area used in method 1 has a rectangular layout as highlighted in Fig. 2. This rectangle is positioned in such a way that the enclosed test $Cu_{3km–7km}$ cell is 5 km from its nearest two edges. The overall length of the north–south edge of the search rectangle is equal to twice the product of the meridional component of the 10-min median TITAN cell speed and the time to next scan (10 min) plus the offset of 5 km. The length of the east–west edge is calculated in the same way except using the zonal component of the TITAN cell speed. Note that some of the choices to establish the search area are somewhat arbitrary and have been selected as a compromise between having a sensible search area (not too large) while keeping a good chance of tracking the cell over its entire lifetime. Sensitivity studies changing those settings produced similar results to the ones used here.

Figure 2 shows the three different scenarios that could occur in the search area. Cell A is flagged as Cg cell since its subsequent stage has lower CTH compared to the previous scan. Cell B highlights the scenario where its nearest neighbor has a higher CTH compared to previous scan. In such situations, the $Cu_{3km–7km}$ cell is tracked over several subsequent scans until its CTH has been found to have either exceeded 7 km (thus flagged as Cb cell) or its CTH never exceeded 7 km throughout its lifetime (flagged as Cg cell). Cell C had no neighbor but is still flagged as Cg cell because there is a possibility that the test cell decayed by the time the subsequent radar scan was completed.

Method 2 is based on a probabilistic approach. The search area is defined in the same way as in method 1, except we examine up to six subsequent radar scans before making a decision. Here a cell is flagged as Cg cell if over the next six subsequent radar scans, at least 80% of the convective cells have CTH < 9 km; that is, the test $Cu_{3km–7km}$ cell has a high probability of never growing into a deep convective cell. Similarly, a cell is flagged as Cb when at least 50% of the convective cells over the next three radar scans are deep convective cells (CTH > 9 km); that is, the test $Cu_{3km–7km}$ has a high probability of growing further. We deliberately used a higher probability threshold of 80% for Cg cells and a moderate one of 50% for Cb cells because at any given time one would expect that there will be more Cg cells than deep convective ones. Other settings, such as height thresholds of 7–9 km, CTH occurrence ratios of 20%–90%, as well as different area multiplication factors (2–6 times) and lead times (20–120 min), have been tested and the results are similar.

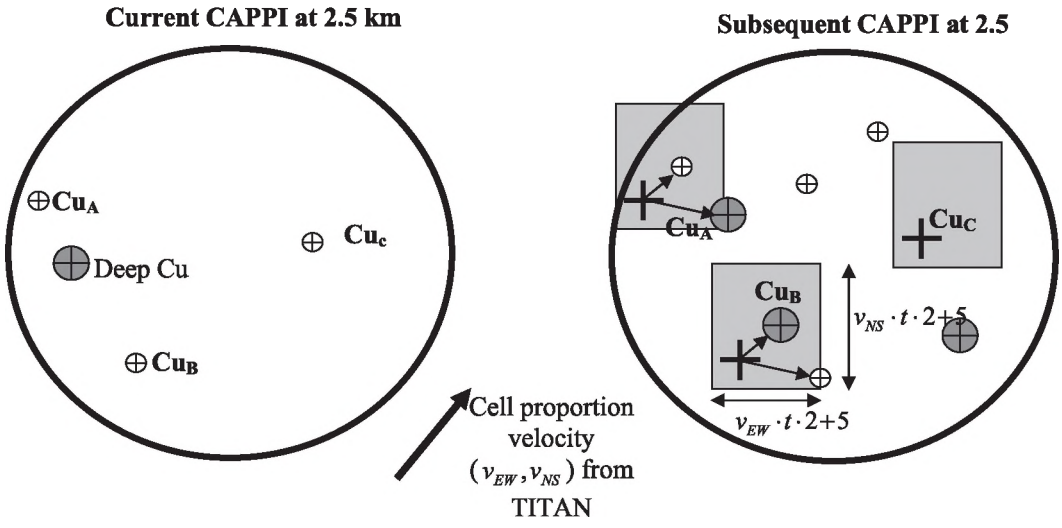

FIG. 2. Schematics for identification of congestus (Cg) and cumulonimbus (Cb) cells using the nearest neighbor approach (method 1). (left) Current radar CAPPI snapshot at 2.5-km level with three $Cu_{3km–7km}$ cells (Cu_A, Cu_B, Cu_C, smaller circles with crosses) and one deep cell (large circle with cross and gray filling). (right) Subsequent CAPPI snapshot after a scanning time of 10 min; the gray shaded rectangle is the search area (see text) and the large dark crosses represent the initial location of the cumulus cells. The nearest neighbor of Cu_A has a lower CTH than that of Cu_A; thus, it is an example of a Cg cell. The nearest neighbor of Cu_B has a higher CTH and represents the scenario where Cu_B can be classified as Cg or Cb depending on maximum CTH reached by this cell as it is tracked further through its entire lifetime. The cell Cu_C has no appropriate neighbor and is considered a Cg cell.

Figure 3 shows the overall results for all $Cu_{3km–7km}$ cells described above. The shaded gray region is the probability distribution function (PDF) for reflectivity at the 2.5-km CAPPI level associated with all the 207 871 $Cu_{3km–7km}$ cells in the sample. The solid and dashed curves represent the PDFs associated with Cg and Cb cells, respectively. The black and red curves are using data points detected by the two different methods discussed above. The bars plotted along the PDF curve in this figure represent the scatter in reflectivity PDFs arising from the sensitivity to parameter settings in the search algorithms. Note the current choices for each method are determined through a trial and error approach such that the difference between the Cg and Cb cells are most clear.

Both methods show that the Cg cells (solid lines) have a higher probability of having low reflectivity values compared to the overall distribution (shaded gray region). Similarly, the Cb cells (dashed lines) have a higher probability of having larger reflectivities. The modal reflectivity bin for the Cg cells is 35 dBZ with both methods and that of Cb cells is around 40 dBZ, with a slightly broader distribution in method 1.

Out of the more than 200 000 $Cu_{3km–7km}$ cells detected over the two wet seasons, method 1 flagged 82% as Cg cells and 18% as Cb cells. Fifty-one percent of the Cg cells had no subsequent nearest neighbor, indicating that they were very short lived. Note that because of the radar wavelength, we only detect the precipitating stage of the cells. Removing these short-lived cells from the analysis leads to a drop in reflectivity probabilities, particularly in the lower reflectivity bins (<25 dBZ; Fig. 3). Method 2 identifies 51% of the $Cu_{3km–7km}$ population

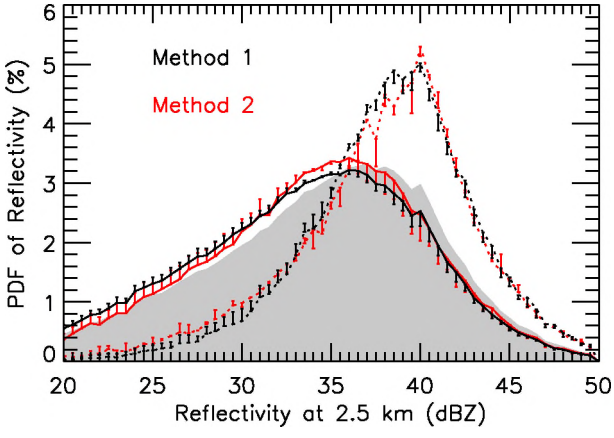

FIG. 3. Distribution of reflectivity using a bin size of 1 dBZ for the Cg (solid line) and Cb (dotted line) cells. The reflectivity is taken at the 2.5-km CAPPI level, where one mean reflectivity value is obtained per convective cell. The gray shaded region represents the PDF obtained using all $Cu_{3km–7km}$ cells (top height < 7 km). The black and red curves are the PDF values obtained using two different methods of classifying the Cg and Cb cells. The bars plotted along each curve represent the sensitivity to parameter settings in each method (see text for more details).

as Cg and 18% as Cb. The remaining 31% of the $Cu_{3km-7km}$ cells are not classified because the ratio of the number of $Cu_{3km-7km}$ to deep convective cells is within the uncertain range of 50%–80%, showing a limitation of this methodology.

The excellent agreement in the frequency of occurrence of Cb cells indicates that both methods are robust and not unduly sensitive to the thresholds used in each method. However, the Cg cell occurrence counts do show a significant discrepancy. The extra 30% Cg cells identified using method 1 are predominantly of the short-lived type (cell C in Fig. 2). Visual inspection of radar loops around several of the Cg cells that were classified by method 1 but not with method 2 confirms that these cells often occur in a single image only, hence indicating a lifetime of 10 min or less. To avoid biasing our results to those short-lived cells, we will only use data from the more conservative method 2 for the rest of our discussion. The 18:51 ratio between Cb and Cg found using method 2—that is, for every Cb cell there will be 2.8 Cg cells—is comparable with the 30:70 ratio (1 Cb is to 2.3 Cg cells) found in Luo et al. (2009). This provides a good test since the cell identification method used in this paper and the method used in Luo et al. (2009) are both looking at only genuine convective cells.

3. The basic properties of the congestus and cumulonimbus cells

The rainfall and cloud properties over the Darwin region have been shown to be strongly regulated by the large-scale environment (May et al. 2012; Kumar et al. 2013b; Penide et al. 2013). Pope et al. (2009) identified an effective way to divide the synoptic conditions in Darwin into five physically meaningful states. We first use this synoptic classification to study the effect of these large-scale states on the Cg:Cb ratio. The ratios of Cb to Cg cells were found to be largely insensitive to the large-scale regimes, with ratios of 25:75 during all five large-scale regimes. Overall, the deep westerly (DW) regime, which is associated with active monsoon conditions, contributed the most to the overall two season Cg and Cb cell totals. The second highest contribution was from the moist easterly (ME) regime. This regime is associated with the typical monsoon break conditions, and was the most frequent (157 out of 293 days) of all the regimes. The combined contribution from the remaining three regimes to the $Cu_{3km-7km}$ totals was less than 15%. Hence, these three regimes will not be discussed further.

Figure 4 shows the normalized diurnal variations of the relative occurrence of the Cg (solid lines) and Cb (dashed lines) modes for all cases and separately for the DW (crosses, 59 days) and ME (diamonds, 157 days) regimes. The overall pattern of the $Cu_{3km-7km}$ population shows a late morning to midday peak in all regimes (not shown). In the ME regime, this peak is contributed by a relative increase in Cg cells around midday, followed by relative increase in Cb cells in the afternoon and evening hours. The afternoon peak of Cb cells is indicative of the well-known often sea-breeze-driven diurnal cycle of deep convection in Darwin during monsoon buildup and break conditions. In contrast, the diurnal variability in the DW regime is weak. As the DW regime represents monsoon conditions, this is likely the result of the presence of continuous cloud cover reducing daytime heating and thus suppressing sea-breeze-driven convection (e.g., May et al. 2012; Kumar et al. 2013b).

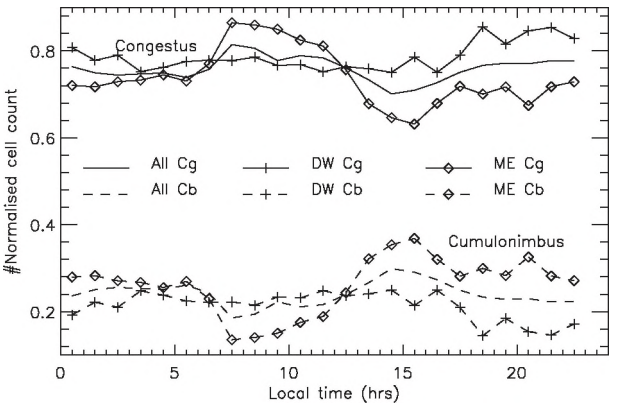

FIG. 4. Diurnal variations of the relative Cg (solid line) and Cb (dashed line) cell counts over the two-wet-season study interval for the DW (crosses) and ME (diamonds) regimes. A bin size of 1 h in local time is used here. In each local time bin, the occurrence frequency of the Cg and Cb cell are normalized such that their sum is always 1.

We now investigate some of the rainfall properties of the Cg and Cb modes making use of the polarimetric capabilities of the CPOL radar (e.g., Zrnić and Ryzhkov 1999; Bringi et al. 2009). Figure 5 shows the distribution of the reflectivity, rain rate, median raindrop volume diameter (D_0), and the number concentration of small hydrometers (N_w) as function of CTH using box–whisker plots. The CTH varies from 3 to 7 km in steps of 0.5 km. Recall that each $Cu_{3km-7km}$ cell is assigned a single mean rainfall parameter, obtained using radar data from the 2.5-km CAPPI level bounded by the horizontal cross-section area of the cell. In Fig. 5, the boxes represent the 25th and 75th percentiles with the thick gray box indicating all $Cu_{3km-7km}$ cells, the thin black box the Cg cells, and the thin striped box the Cb cells. The curves represent the median value for each $Cu_{3km-7km}$ cloud-top group, and the whiskers are the 5th and 95th percentiles

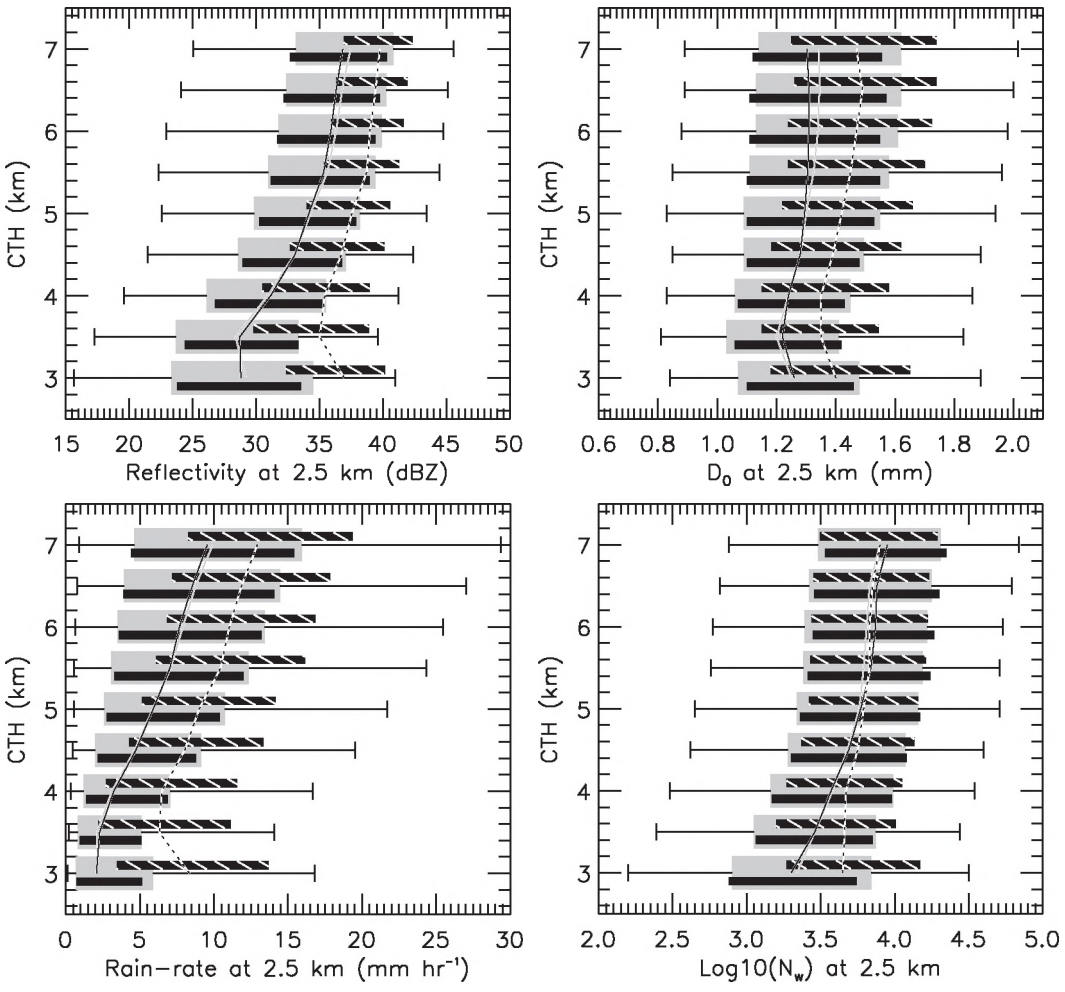

FIG. 5. Box–whisker plots in 0.5 km steps of CTH of (top) (left) reflectivity and (right) median drop size diameter (D_0); and (bottom) (left) rain rate and (right) number concentration of small hydrometers [log10(N_w)]. As in Fig. 3, a single mean value is obtained per cloud cell. The thick gray box (25th and 75th percentiles) with whiskers (5th and 95th percentiles) represents results using all the data. The thin black rectangle shows results for the Cg cells only. Similarly, the striped rectangles show the results for the Cb cells. The curves (solid gray for all cells; solid black for Cg; dashed for Cb) are the median values for each CTH level.

associated with all the $Cu_{3km–7km}$ cells. The whiskers for the Cg and Cb cells are omitted.

For the $Cu_{3km–7km}$ populations as the whole, the median reflectivity at 2.5 km shifts toward higher values (top panel) as the CTH increases while the distribution gets narrower. A positive correlation between near ground cell reflectivity and maximum height reached by cloud cell is typical since larger reflectivities generally correspond to stronger growth momentum (e.g., Zipser and Lutz 1994). In accordance with these results, the cell rain rate increases with CTH. The median raindrop size D_0 is almost invariant with CTH showing a very small increase as the cloud depth increases. The concentration of small hydrometeors increases by almost an order of magnitude as the cells deepen.

The behavior of the cloud properties shows some distinct differences between the Cg and Cb classes. Overall, for any given CTH the Cg cells have smaller mean reflectivity, lower rain rate, and smaller drop size at 2.5-km height than the Cb cells with the same CTH. The median reflectivity, rain rate, and drop size in the Cb cells exceed that of the Cg cells by 5 dBZ, 3 mm h^{-1}, and 0.18 mm, respectively. However, the N_w, parameter exhibited no obvious difference between the Cg and Cb cells, except in the shallowest $Cu_{3km–7km}$ cells with CTH below 4 km.

Despite the large mean (or median) differences between the Cg and Cb modes, there is a large overlap of the distributions of the rainfall properties. In other words, the radar parameters here cannot be used easily

to predict how an emerging $Cu_{3km-7km}$ cell will develop and in which class it will ultimately fall. However, it appears that the 25th percentile reflectivity level in the Cb cells is often very close to the overall median of all the $Cu_{3km-7km}$ cells. The largest separation between the Cg and Cb distribution occur when the CTH is small. We also investigated potential differences in the vertical profile of reflectivity lapse rate (e.g., Zipser and Lutz 1994) for the Cg and Cb modes (not shown). As before, the differences in this parameter did not serve as a confident proxy for separating the Cg and Cb cells. We hypothesize that the updraft speeds in the convective core, which can be obtained using Doppler radar techniques, may be a better criterion to distinguish between the Cg and Cb cells. Presumably, the Cb cells are likely to have a stronger updraft speed since they grow into deep convective clouds at a later time.

4. Atmospheric factors affecting the growth of convective cloud cells

The goal of this section is to identify key atmospheric processes that may determine the growth or suppression of $Cu_{3km-7km}$ cells and hence regulate if clouds will fall into the Cg or Cb classes defined above. Several hypotheses to explain the shallow to deep cloud transition in tropical convection have been put forward in the recent literature:

1) Moistening of the midtroposphere by $Cu_{3km-7km}$ cells precedes the onset of deep convection (e.g., Sherwood and Wahrlich 1999; Mapes et al. 2006; Holloway and Neelin 2009).
2) The moistening of the midtroposphere is caused by large-scale dynamical processes leading to ascent. The ascent is potentially related to heating from $Cu_{3km-7km}$ cells, causing moisture convergence (e.g., Hohenegger and Stevens 2013; Kumar et al. 2013a).
3) Increased boundary layer inhomogeneity in the thermodynamic and wind fields causes the rising cloud parcels to have more momentum, which increases the probability of clouds reaching the level of free convection and develop into deep convection (e.g., Zhang and Klein 2010).

Hypothesis 3 focuses largely on the transition from shallow, nonprecipitating convection to deep convection. Therefore, it cannot be reliably tested in this study, since we cannot reliably detect fair-weather shallow cumulus clouds. Both the Cg and Cb modes have already grown past the trade inversion layer. We will therefore focus on evaluating hypotheses 1 and 2 in what follows.

Hypothesis 1 and 2 are based on the premise that moistening of the midtroposphere occurring prior to deep convection is crucial for the formation of deep convection—often referred to as preconditioning. So we begin the analysis by testing this preconditioning requirement using the relative humidity and temperature measurements from radiosonde observations at Darwin airport (see Fig. 1 for the sounding location). The radiosondes operated typically at 6-h intervals. Since the Cg and Cb modes as well as the subsequent deeper mode rarely occur in complete isolation, special care has to be taken in establishing the link between the variations in atmospheric conditions and the growth of the two $Cu_{3km-7km}$ modes.

To do so, two procedures are applied here: The first step identifies times where one of the $Cu_{3km-7km}$ modes is dominant over the other. To achieve this, the ratio of the Cb cell count to the total (Cb + Cg) is calculated in bins of 6 h. A 6-h data block is flagged as dominated by the Cg mode if the ratio of the Cb to the total is below 12%—the lower tercile of the 6-hourly Cb to total ratio distribution. Similarly, if the 6-hourly ratio exceeded 38%, the upper tercile of the Cb to total ratio distribution, the data block is flagged as dominated by the Cb mode. Only Cg cells (Cb cells) that formed in the 6-hourly Cg dominated data blocks (Cb dominated data blocks) are kept for further analysis. This filtering process leaves ~42 000 Cg cells (40% of the original Cg population) and ~16 600 Cb cells (44% of the Cb population).

The second step of our analysis procedure aims to filter out atmospheric environments that may have already been modified by deep convection. Because of the high time resolution of the radar observations, the timing of the radiosonde ascents relative to the occurrence of the $Cu_{3km-7km}$ modes is random. It can be as little as 10 min and as much as 6 h before or after the cloud observations. As we wish to focus on the effects of the environment on the $Cu_{3km-7km}$ clouds, rather than the other way around, only radiosonde data with an occurrence time between 0 and 6 h prior to the detection time of the Cg and Cb cells are included in the analysis.

Figure 6 shows the joint frequency distributions of relative humidity (top panels) and temperature lapse rate (bottom panels) as a function of height for the Cg (left column) and Cb (right column) cells derived from radiosonde ascents 0–6 h before the radar image as described above. These two atmospheric parameters were chosen as they have been previously deemed to play a role in limiting the vertical extent of cumulus clouds (e.g., Derbyshire et al. 2004; Takemi et al. 2004). The difference between the distributions of relative humidity (Fig. 6, top panels), in particular above the altitude of 5.0 km, in the Cg and Cb modes is quite remarkable. The midtroposphere is clearly much drier in periods with

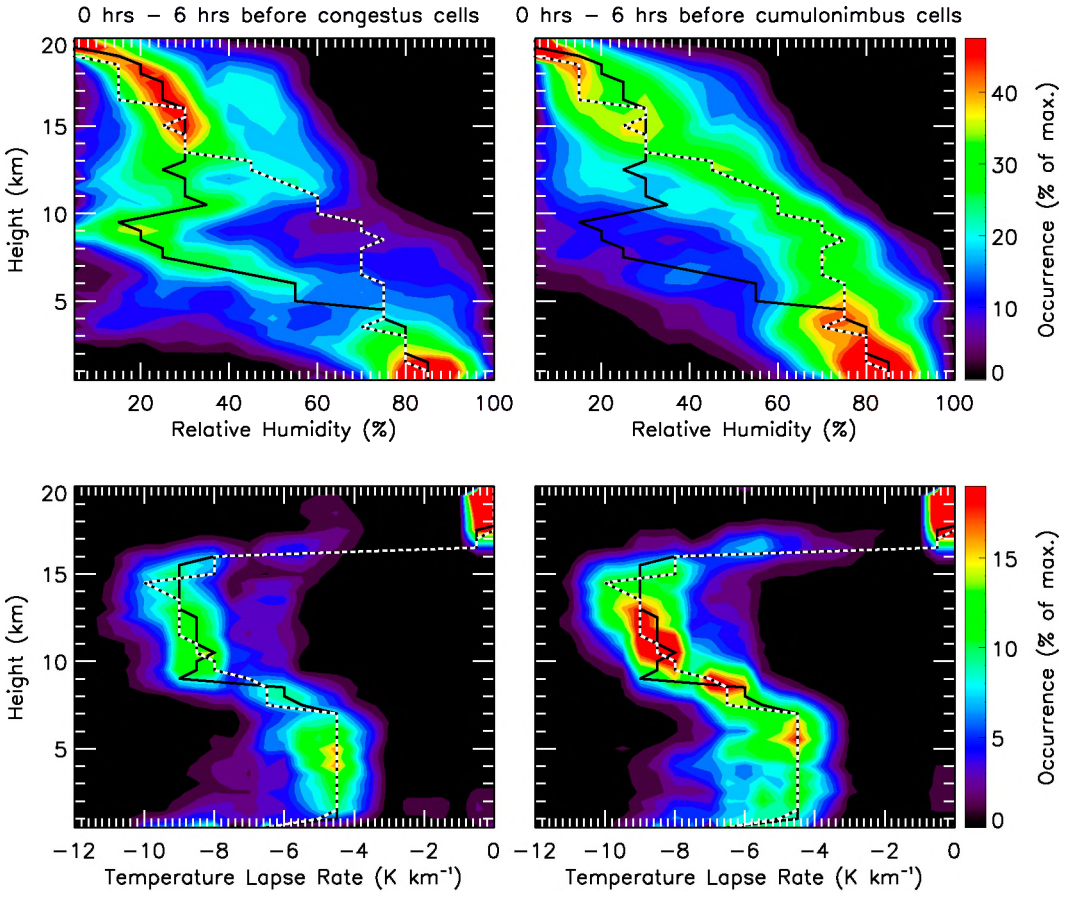

FIG. 6. (top) The vertical profile of relative humidity using of 5% size bins and (bottom) temperature lapse rate using 0.5 K km^{-1} size bins for (left) Cg and (right) Cb cells. The solid and dashed lines represent the values for the Cg and Cb modes, respectively; these have been overlaid for easier comparison.

predominantly Cg cells than in those with large numbers of Cb cells. The most notable feature is the abrupt drop in relative humidity from a modal value of 72% at 5 km to only 30% at 7.0 km associated with the Cg cells. The temperature lapse rate distributions associated with the two $Cu_{3km–7km}$ modes are found to be very similar (Fig. 6, bottom panels), except that the temperature lapse rates distributions are slightly broader for the Cb cells. The results shown in Fig. 6 are consistent with the viewpoint that entrainment of dry ambient air into the cells can play a key role in limiting the vertical extent of convection (e.g., Redelsperger et al. 2002; Derbyshire et al. 2004; Takemi et al. 2004; Jensen and Del Genio 2006). A key question remaining is to identify the source of the moistening preceding the Cb cells or drying preceding the Cg cells.

5. Sources of midtroposphere moistening preceding the development of cumulonimbus cells

In this section we aim to investigate what processes are involved in moistening the midtroposphere in the hours leading up to the onset of the predominantly Cb cell population. It is worth recalling that the two main processes are a moistening by $Cu_{3km–7km}$ cells (hypothesis 1) and moistening that involves large-scale dynamical processes (hypothesis 2).

Hypothesis 1 is tested by performing a composite analysis of relative humidity and occurrence frequency of two $Cu_{3km–7km}$ modes for the 6 h preceding the onset of the Cg and Cb cells. The results are shown in Fig. 7. For this analysis, the radiosonde data used are the same as those employed in Fig. 6, except that now we show the temporal evolution of relative humidity. The radiosonde data are divided into 1-h bins of time and 0.5-km bins of height, and the median is calculated separately for each bin and displayed in Fig. 7. The short vertical lines (which appear nearly continuous) above the humidity panels represent the actual timestamps of the radiosonde data used in this analysis. It is clear from this illustration that the radiosonde data is drawn from nearly all times leading up to the cell identification, providing confidence that the results are robust on an hourly scale

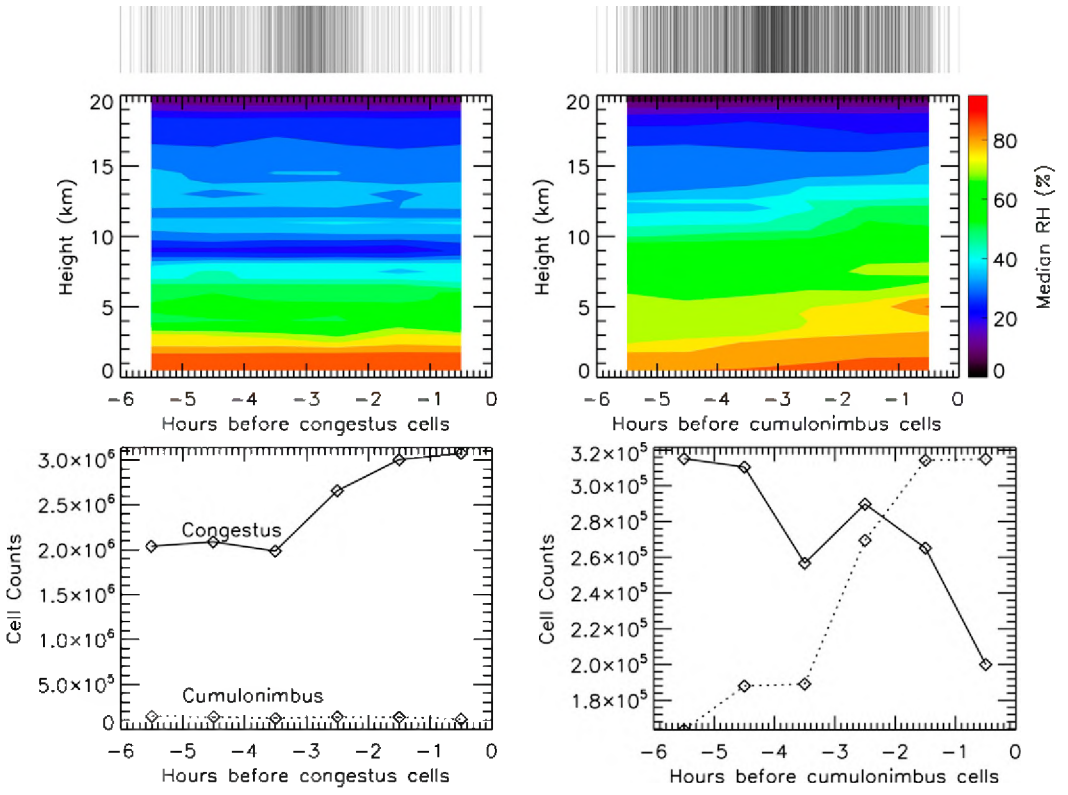

FIG. 7. Composite evolution of the (top) 6-hourly relative humidity and (bottom) radar cell occurrence frequency for the 6 h preceding the onset time of (left) terminal and (right) transient cells. The vertical black lines above the relative humidity tendency panels indicate the actual radiosonde times used in the composite analysis.

despite using the 6-hourly radiosonde data. The bottom panels show the composite count of the all Cg (solid curve) and Cb (dashed curve) cells.

The top panels of Fig. 7 show that conditions in the time leading up to Cg cells are distinctly different to those for Cb cells. In the case of Cg cells, the atmosphere above the boundary layer (but not the boundary layer itself) is significantly drier and this structure does not change in the 6 h leading up to the Cg cell event. The Cb cell cases are generally characterized by moister conditions even 6 h before the event, indicating an important difference in the meteorological background state associated with the two $Cu_{3km-7km}$ modes. Consistent with both hypotheses of preconditioning, the relative humidity, especially in the midtroposphere, increases before the onset of Cb cell events. The increase appears particularly rapid about 3 h before the event.

The bottom panels of Fig. 7 show that there is a large population of Cg cells leading up to both Cg and Cb cell events. Within 3 h preceding the Cg events, the incidence of Cg cells increases without any significant change in the vertical relative humidity distribution. This is interesting as it indicates that the increased number of Cg cells is not able to moisten the midtroposphere by itself, implying either strong compensating drying processes or a lack of efficiency in the moistening from $Cu_{3km-7km}$ cells alone. Similar to the findings in Fig. 4, it is evident that Cb cell events are preceded by a high occurrence of Cg cells a few hours before the transition to deeper cells. Thus, on face value the Cg cells appear to be a key ingredient to precondition the troposphere for the subsequent development of Cb cells, which eventually leads to the development of deep convection. However, a significant population of Cg cells also exists in the hours leading up to the occurrence of mostly Cg events. This clearly indicates that other processes must also be important in regulating the formation of Cg and Cb cells (hypothesis 2). This is explored next.

The investigation of the relative role of large- and small-scale processes in determining cloud depth requires reliable estimates of the large-scale state concurrent with the radar observations. Such datasets are typically derived from radiosonde arrays deployed during field campaigns or are simply derived from operational NWP analysis or reanalyses performed with

NWP systems. Using data from the Tropical Warm Pool International Cloud Experiment (TWP-ICE; May et al. 2008), Davies et al. (2013) have demonstrated that the use of NWP analysis at high time frequency is not justified owing to the poor quality of the divergent wind, and hence vertical motion field, in these analyses. However, they also showed that long records of reliable estimates of the large-scale budgets around Darwin can be derived by applying the variational budget analysis technique of Zhang and Lin (1997) using NWP analysis data as "pseudo radiosondes" and observations at the surface and top of the atmosphere, as suggested by Xie et al. (2004). The resulting large-scale dataset used here, which is often referred to as the forcing analysis, includes vertical profiles of heat and moisture budgets as well as thermodynamic and dynamic variables at 40-hPa vertical and 6-h temporal resolutions. The domain represented by this dataset is shown by the pentagon shape in Fig. 1 and is comparable to the CPOL domain used here (shaded gray circle).

The large-scale forcing dataset contains several parameters relevant to convection. Table 1 provides an overview of some of those parameters showing the 95% confidence intervals of their mean.[1] Note that the forcing dataset has been processed in the same manner as the radiosonde dataset above in that only profiles from the preceding 6 h relative to cell identification as Cg and Cb dominated are used in the analysis. Results shown in Table 1 reveal that the mean convection inhibition (CIN), surface evaporation, and midtroposphere (300–600 hPa) temperature preceding the two congestus modes are similar at the 95% confidence level. Thus, these factors are unlikely a cause for congestus clouds to grow in deep convection. In contrast, both the large-scale vertical motion (omega) in the midtroposphere and thus the vertical advection of moisture, as well as the convective available potential energy (CAPE), are clearly larger in the intervals preceding Cb cell than in those ahead of Cg cells. Similarly, the low-level horizontal winds and thus potentially the horizontal advection of moisture are also significantly different between the two $Cu_{3km-7km}$ modes. One possible explanation for these differences is that the different cell modes occur in different meteorological regimes, such as the Darwin monsoon (the DW regime) and break (the ME regime) conditions, which are known to have very different thermodynamic and wind profiles (Pope et al. 2009). This is further explored next.

[1] A set of 100 different mean values are generated using a randomly selected samples from the main batch of data. Then the 95% confidence interval is extracted from probability distribution function of the means (e.g., Chu and Wang 1997).

TABLE 1. Mean atmospheric conditions associated with the Cg and Cb cells. The data ranges represent the 95% confidence intervals about the mean (see text for details).

	Cg cells	Cb cells
Total number of cells analyzed	42 028	16 613
CAPE ($J\,kg^{-1}$)	267.3–292.3	570.9–603.3
CIN ($J\,kg^{-1}$)	22.4–25.1	23.8–25.2
Surface evaporation ($mm\,h^{-1}$)	0.38–0.40	0.34–0.35
300–600-hPa water mixing ratio ($g\,kg^{-1}$)	4.27–4.61	4.44–4.79
300–600-hPa RH (%)	60.3–62.4	63.9–65.5
300–600-hPa temp (K)	272.9–274.4	272.7–274.2
300–600-hPa omega ($hPa\,h^{-1}$)	−0.92 to −0.52	−2.82 to −2.44
600–1015-hPa HADV ($g\,kg^{-1}\,h^{-1}$)	−0.049 to −0.037	−0.021 to −0.016
600–1015-hPa horizontal advection of temperature ($K\,h^{-1}$)	0.049–0.061	0.027–0.037
600–1015-hPa westerly (u, $m\,s^{-1}$)	5.32–6.00	1.71–2.17
600–1015-hPa southerly (v, $m\,s^{-1}$)	−0.71 to −0.47	−1.40 to −1.14
600–1015-hPa wind speed ($m\,s^{-1}$)	7.41–8.13	4.89–5.42
600–1015-hPa wind shear ($m\,s^{-1}\,hPa^{-1}$)	0.024–0.030	0.030–0.032

We begin this by examining the vertical profiles of all the four terms in the large-scale moisture budget expression (Fig. 8). This expression can be defined as

$$\frac{\partial q}{\partial t} = \nu_H \cdot \nabla_H q + \omega \frac{\partial q}{\partial p} + Q2.$$

In the above, most of the notations are convectional; $\partial q/\partial t$ is the moisture tendency, which for sake of simplicity will be referred to as q tend. The q tend term arises from contributions from large-scale horizontal advection ($\nu_H \cdot \nabla_H q$ or simply HADV), vertical advection ($\omega \partial q/\partial p$ or VADV), and the residual term (Q2). The Q2 term represents the collective effects of all subdomain-scale processes (see Yanai et al. 1973). All terms are scaled to the same units of humidity change with time (i.e., $g\,kg^{-1}\,h^{-1}$).

The top panels of Fig. 8 show the mean profiles of large-scale moisture budget using all data points occurring within 6 h preceding the 42 000 Cg and 16 600 Cb cells. The middle and bottom panels separate these results into the DW and ME regimes, respectively. Note that ~50% of the 42 000 Cg cells used in these calculations occurred during the DW regime; thus, the mean behavior in the top left panel of Fig. 8 associated with all Cg cells will be strongly influenced by the DW regime.

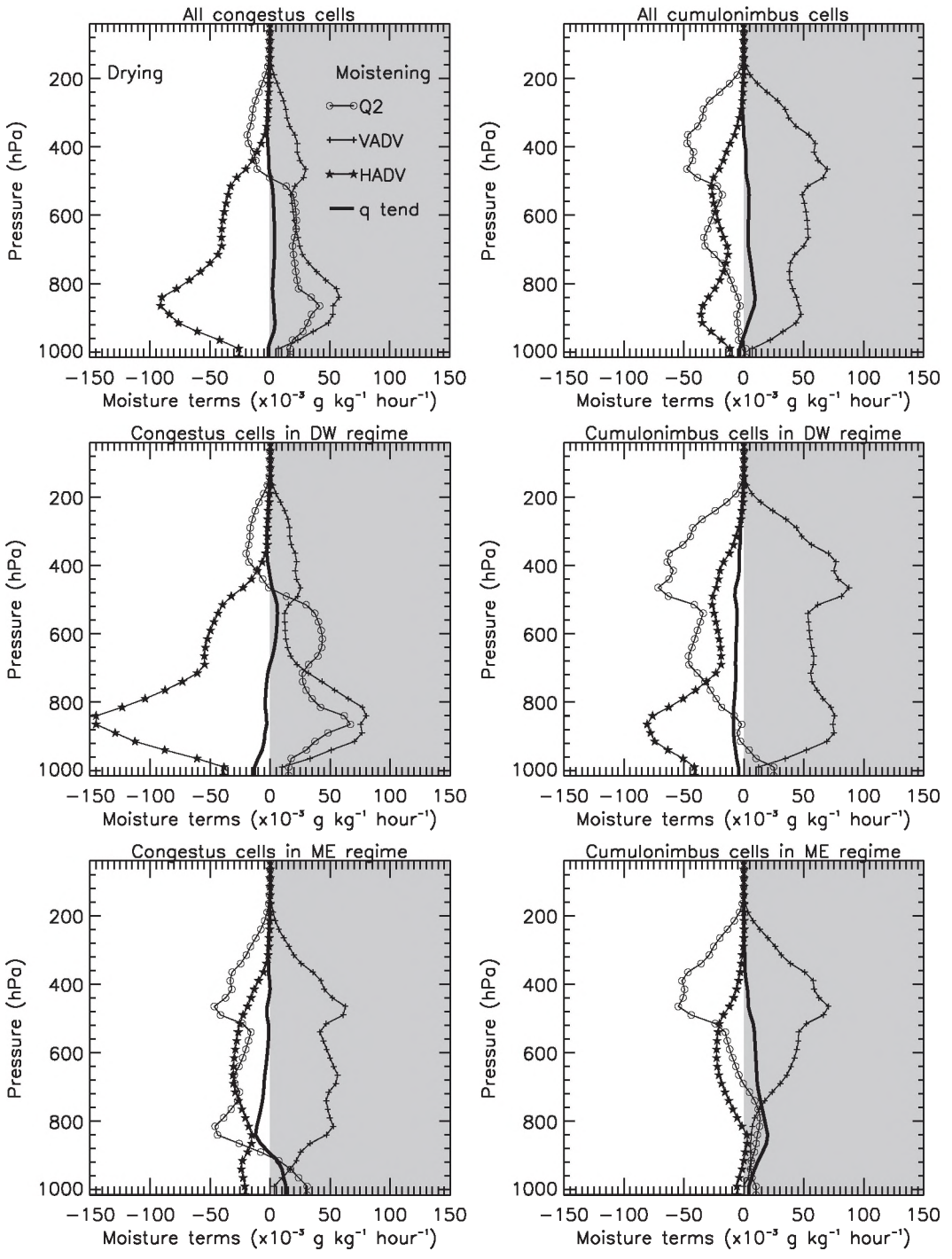

FIG. 8. Mean vertical profiles of the moisture budget terms preceding the (left) Cg and (right) Cb cells. (top) Results for all data, (middle) DW regime, and (bottom) ME regime. The shaded gray region represents moistening, while the white area indicates drying.

The Cb cells (right panels of Fig. 8) were most frequent in the ME regime (~42% of the 16 600 cells), followed by the DW regime (35% of the cells). Two features are found to be different between the Cg and Cb modes and these were reproducible regardless of the atmospheric regimes (hence can be considered genuine factors in regulating the growth of Cg and Cb cells) included:

1) The large-scale vertical advection causes moistening of the midtroposphere (300–600 hPa) preceding both cloud modes. However, this moistening is larger preceding the Cb cells than preceding the Cg cells.
2) Greater drying by large-scale horizontal advection in the low levels (600–1015 hPa) preceding the Cg cells than preceding the Cb cells.

In contrast, the Q2 and q tend terms associated with the different large-scale regimes are found to exhibit different signatures. For example, the subgrid processes (Q2) moisten the troposphere between 600 and 1000 hPa preceding the Cg cells only during the DW regime (thus also shows in overall average; Fig. 8) and not during the other conditions. This moistening by Q2 has been linked to evaporation of precipitation from stratiform clouds, which are widespread in the DW regimes (Kumar et al. 2013a,b). Thus, the responses in Q2 term and so in q tend are thought to be a result of different synoptic environments of the two regimes themselves and are less likely to explain why some $Cu_{3km-7km}$ cells grow and others remain shallow throughout their lifetime.

It is clear from the discussion above that there is a strong relationship between the growth of Cb cells into deep convection and the moistening of the midtroposphere in the hours preceding the onset of Cb cells. The moistening preceding the Cb cells appears to be linked to either one or both of the following causes: the preceding Cg cells and/or large-scale vertical advection (as the horizontal advection terms are almost always negative, so leads to drying). We now investigate the competing contributions of these two factors in increasing the moisture of the midtroposphere.

It is tempting at first glance to ascribe the midtroposphere moistening associated with the growth of Cb cells to the occurrence of Cg cells, which peaks a few hours before the Cb cells (Figs. 4 and 6). However, this is inconsistent with the findings for the Cg cell events themselves, which show Cg cells existing for long periods of time with no effect on the midtroposphere relative humidity and with few Cb and deep cells forming in the subsequent period. To study this further, we first identify peak Cg cell occurrence events, characterized by a Cg cell frequency larger than 42 cells per hour. This value corresponds to the upper tercile of all hourly Cg cell counts. A total of 275 such events were identified from our two wet-season database.

The top panel of Fig. 9 shows the results of a composite analysis of the mean Cg cell (solid) and Cb cell (dashed) frequencies around these events, separated into three bins of the midtroposphere large-scale vertical advection of moisture. The vertical advection values are taken at the 500-hPa level, $VADV_{500}$, and at the nearest time to the onset of events. There are 75 events with $VADV_{500} < 0\,g\,kg^{-1}\,h^{-1}$, indicating drying in the midtroposphere by vertical advection (diamonds); 64 events with $VADV_{500}$ between 0 and $0.03\,g\,kg^{-1}\,h^{-1}$, indicating moderate moistening (crosses); and 136 events with $VADV_{500} > 0.03\,g\,kg^{-1}\,h^{-1}$, indicating strong moistening (triangles). It is evident from Fig. 9 that the mean frequency of the Cg cells (solid lines) is independent of $VADV_{500}$. In contrast, the mean frequency of the Cb cells increases strongly with increasing $VADV_{500}$. Notably, there are 75 events with at least 42 Cg cells per hour, but very few Cb cells occurring in the subsequent hours because the vertical advection term associated with these events is negative (drying). The second and third panels of Fig. 9 repeat the composite analysis of the mean Cg cell (solid) and Cb cell (dashed) frequencies around events for the DW and ME regimes, respectively. While there is some effect of the large-scale regime on the evolution of the cell modes, qualitatively the two regimes behave very similarly to each other and the overall behavior. Independent of synoptic regime it is the increased moistening in the midtroposphere by vertical advection and not with the existence of Cg cells that explains the difference in the number of Cb cells.

6. Summary

This study used C-band radar data in the Darwin region to identify two types of convective cloud cells with a 0-dBZ cloud-top height (CTH) between 3 and 7 km ($Cu_{3km-7km}$). These two modes are the congestus (Cg) clouds, which terminate their growth around the freezing level, and the cumulonimbus (Cb) clouds, which grow into deeper convection at a later time. This was achieved by examining the statistical properties of cell top heights in a sequence of radar scans. Based on this approach, we were able to classify 70% of the entire $Cu_{3km-7km}$ population (CTH < 7 km) during two wet seasons at Darwin as either Cg or Cb cells. Of the classified $Cu_{3km-7km}$ cells, 26% are found to be Cb cells that will ascend to greater altitude at a later time, while 74% of the $Cu_{3km-7km}$ cells were found to never grow deeper than 7 km. This Cb to Cg splitting ratio is found to be invariant of the five large-scale Darwin regimes. Note there is a third cumulus cloud type with tops between 3 and 7 km: the nonprecipitating cumulus cloud. However, this cloud type cannot be easily detected by the C-band radar and is estimated to be as much as one-third of cumulus populations with tops between 3 and 7 km.

The cells classified as Cb are observed to have larger radar reflectivities, rain rates, and drop size at the lowest radar level (2.5 km) compared to the Cg cells. If the

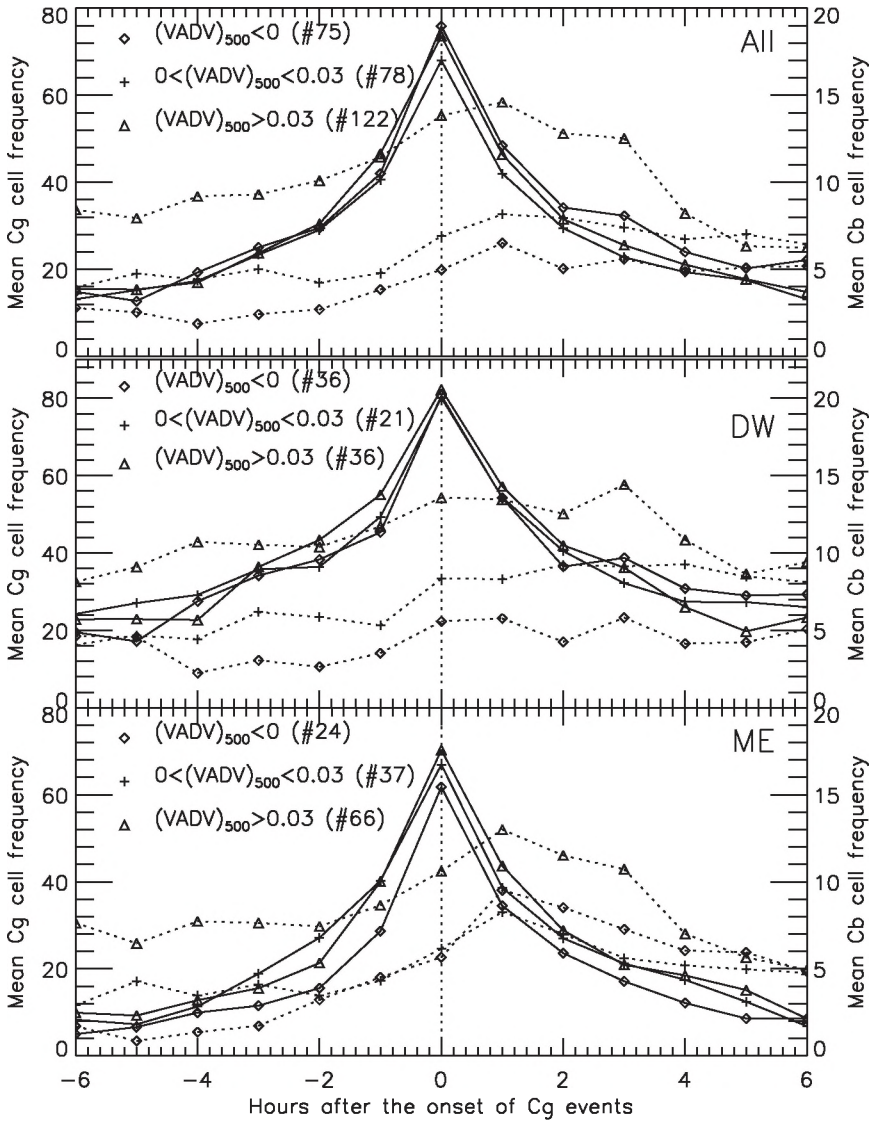

FIG. 9. Composite evolution of the Cg (solid lines) and Cb (dashed lines) cell occurrence frequency for 6 h on either side of the Cg cell peak occurrence events ($t = 0$). Mean cell occurrence frequencies in three different bins of the midtroposphere large-scale vertical advection of moisture ($VADV_{500}$): (top) all events, and events in the (middle) DW and (bottom) ME regime.

atmospheric conditions during both modes were similar, then it could be argued that it is the microphysical properties of Cb cells themselves that lead to stronger growth. However, the atmospheric conditions between the two $Cu_{3km-7km}$ modes were found to differ and are likely to play a significant role in determining which $Cu_{3km-7km}$ cell will be able to grow.

Combining the cell attributes from the radar analysis with radiosonde observations and results from the derived large-scale budget analyses in the Darwin region allowed the investigation of the relationship of the dynamic and thermodynamic state of the atmosphere with the two $Cu_{3km-7km}$ modes. In particular, we were able to investigate the conditions leading up to the occurrence of Cb cells, thereby shedding more light on the processes involved in the transition from shallow to deep convection. In the hours preceding the Cb cells, strong, well-defined enhancement in humidity occurs in the midtroposphere (5–10 km). In contrast, the midtroposphere is significantly drier prior to high occurrences of Cg cells. So, consistent with several previous studies, the moisture profiles of the midtroposphere have a strong impact on the vertical development of tropical cumulus clouds, and the presence of moisture in the midtroposphere

appears strongly related to the development of deep convective clouds. However, this study has shown that large numbers of $Cu_{3km-7km}$ cells exist prior to the development of both Cg and Cb cell populations, making it less likely that Cg moistening alone can explain the transition to deeper convection. Instead, it was shown that it is the presence of moistening by large-scale vertical advection, or simply the presence of large-scale upward motion, that is crucial to the development of Cb cells in relatively large proportions after the existence of the Cg cells. In contrast, when the large-scale motion is found to be downward very few Cb cells can form even though large numbers of Cg cells are present in the vicinity. While the overall number of Cb cells showed some dependence on the synoptic regime, the mechanisms for the transition from $Cu_{3km-7km}$ to deep convection were found to be independent of the large-scale regimes, lending additional confidence to the results. These results confirm the crucial importance of dynamical processes and their interplay with the convective cloud population in the transition from shallow to deep convection in the tropics.

Acknowledgments. This work has been supported by the U.S. Department of Energy ARM Grant DE-FG02-09ER64742. We would like to acknowledge the contributions of Brad Atkinson and Michael Whimpey in supporting the Darwin observatory and data management. V. Kumar thanks Rodney Potts, Joshua Soderholm, and Chris Chambers for their discussion on cell selection criteria.

REFERENCES

Arakawa, A., 2004: The cumulus parameterization problem: Past, present, and future. *J. Climate,* **17,** 2493–2525.

Bringi, V. N., C. R. Williams, M. Thurai, and P. T. May, 2009: Using dual-polarized radar and dual-frequency profiler for DSD characterization: A case study from Darwin, Australia. *J. Atmos. Oceanic Technol.,* **26,** 2107–2122.

Casey, S. P. F., E. J. Fetzer, and B. H. Kahn, 2012: Revised identification of tropical oceanic cumulus congestus as viewed by CloudSat. *Atmos. Chem. Phys.,* **12,** 1587–1595.

Chu, P. S., and J. Wang, 1997: Tropical cyclone occurrences in the vicinity of Hawaii: Are the differences between El Niño and non–El Niño years significant? *J. Climate,* **10,** 2683–2689.

Davies, L., C. Jakob, P. T. May, V. V. Kumar, and S. Xie, 2013: Relationships between the large-scale atmosphere and the small-scale state for Darwin, Australia. *J. Geophys. Res.,* **118,** 11 534–11 545, doi:10.1002/jgrd.50645.

Derbyshire, S. H., I. Beau, P. Bechtold, J.-Y. Grandpeix, J.-M. Piriou, J.-L. Redelsperger, and P. M. Soares, 2004: Sensitivity of moist convection to environmental humidity. *Quart. J. Roy. Meteor. Soc.,* **130,** 3055–3080.

Dixon, M., and G. Wiener, 1993: TITAN: Thunderstorm identification, tracking, analysis, and nowcasting—A radar-based methodology. *J. Atmos. Oceanic Technol.,* **10,** 785–797.

Hohenegger, C., and B. Stevens, 2013: Preconditioning deep convection with cumulus congestus. *J. Atmos. Sci.,* **70,** 448–464.

Holloway, C., and J. Neelin, 2009: Moisture vertical structure, column water vapor, and tropical deep convection. *J. Atmos. Sci.,* **66,** 1665–1683.

Jakob, C., 2010: Accelerating progress in global atmospheric model development through improved parameterizations: Challenges, opportunities, and strategies. *Bull. Amer. Meteor. Soc.,* **91,** 869–875.

Jensen, M. P., and A. D. Del Genio, 2006: Factors limiting convective cloud-top height at the ARM Nauru Island climate research facility. *J. Climate,* **19,** 2105–2117.

Johnson, R. H., T. M. Rickenbach, S. A. Rutledge, P. E. Ciesielski, and W. H. Schubert, 1999: Trimodal characteristics of tropical convection. *J. Climate,* **12,** 2397–2418.

Keenan, T. D., K. Glasson, F. Cummings, T. S. Bird, J. Keeler, and J. Lutz, 1998: The BMRC/NCAR C-band polarimetric (CPOL) radar system. *J. Atmos. Oceanic Technol.,* **15,** 871–886.

Kemball-Cook, S. R., and B. C. Weare, 2001: The onset of convection in the Madden–Julian oscillation. *J. Climate,* **14,** 780–793.

Kikuchi, K., and Y. N. Takayabu, 2004: The development of organized convection associated with the MJO during TOGA COARE IOP: Trimodal characteristics. *Geophys. Res. Lett.,* **31,** L10101, doi:10.1029/2004GL019601.

Kumar, V. V., C. Jakob, A. Protat, P. T. May, and L. Davies, 2013a: The four cumulus cloud modes and their progression during rainfall events: A C-band polarimetric radar perspective. *J. Geophys. Res.,* **118,** 8375–8389, doi:10.1002/jgrd.50640.

——, A. Protat, P. T. May, C. Jakob, G. Penide, S. Kumar, and L. Davies, 2013b: On the effects of large-scale environment and surface conditions on convective cloud characteristics over Darwin, Australia. *Mon. Wea. Rev.,* **141,** 1358–1374.

Lin, X., and R. H. Johnson, 1996: Heating, moistening, and rainfall over the western Pacific warm pool during TOGA COARE. *J. Atmos. Sci.,* **53,** 3367–3383.

Luo, Z., G. Y. Liu, G. L. Stephens, and R. H. Johnson, 2009: Terminal versus transient cumulus congestus: A CloudSat perspective. *Geophys. Res. Lett.,* **36,** L05808, doi:10.1029/2008GL036927.

Mapes, B. E., S. Tulich, J. Lin, and P. Zuidema, 2006: The mesoscale convection life cycle: Building block or prototype for large-scale tropical waves? *Dyn. Atmos. Oceans,* **42,** 3–29.

May, P. T., J. H. Mather, G. Vaughan, C. Jakob, G. M. McFarquhar, K. N. Bower, and G. G. Mace, 2008: The Tropical Warm Pool International Cloud Experiment. *Bull. Amer. Meteor. Soc.,* **89,** 629–645.

——, C. Long, and A. Protat, 2012: The diurnal cycle of the boundary layer, convection, clouds, and surface radiation in a coastal monsoon environment (Darwin Australia). *J. Climate,* **25,** 5309–5326.

Moran, K. P., B. E. Martner, M. J. Post, R. A. Kropfli, D. C. Welsh, and K. P. Widener, 1998: An unattended cloud-profiling radar for use in climate research. *Bull. Amer. Meteor. Soc.,* **79,** 443–455.

Nuijens, L., B. Stevens, and A. Siebesma, 2009: The environment of precipitating shallow cumulus convection. *J. Atmos. Sci.,* **66,** 1962–1979.

Penide, G., V. V. Kumar, A. Protat, and P. T. May, 2013: Statistics of drop size distribution parameters and rain rates for stratiform and convective precipitation during the North Australian wet season. *Mon. Wea. Rev.,* **141,** 3222–3237.

Pope, M., C. Jakob, and M. Reeder, 2009: Regimes of the north Australian wet season. *J. Climate,* **22,** 6699–6715.

Powell, S. W., and R. A. Houze Jr., 2013: The cloud population and onset of the Madden-Julian Oscillation over the Indian Ocean during DYNAMO-AMIE. *J. Geophys. Res.,* **118,** 11 979–11 995, doi:10.1002/2013JD020421.

Redelsperger, J.-L., D. B. Parsons, and F. Guichard, 2002: Recovery processes and factors limiting cloud-top height following the arrival of a dry intrusion observed during TOGA COARE. *J. Atmos. Sci.,* **59,** 2438–2457.

Sherwood, S. C., and R. Wahrlich, 1999: Observed evolution of tropical deep convective events and their environment. *Mon. Wea. Rev.,* **127,** 1777–1795.

Steiner, M., R. A. Houze Jr., and S. E. Yuter, 1995: Climatological characterization of three-dimensional storm structure from operational radar and rain gauge data. *J. Appl. Meteor.,* **34,** 1978–2007.

Takemi, T., O. Hirayama, and C. Liu, 2004: Factors responsible for the vertical development of tropical oceanic cumulus convection. *Geophys. Res. Lett.,* **31,** L11109, doi:10.1029/2004GL020225.

Tao, W.-K., D. Starr, A. Hou, P. Newman, and Y. Sud, 2003: A cumulus parameterization workshop. *Bull. Amer. Meteor. Soc.,* **84,** 1055–1062.

Testud, J., S. Oury, P. Amayenc, and R. A. Black, 2001: The concept of "normalized" distributions to describe raindrop spectra: A tool for cloud physics and cloud remote sensing. *J. Appl. Meteor.,* **40,** 1118–1140.

Xie, S., R. T. Cederwall, and M. Zhang, 2004: Developing long-term single-column model/cloud system–resolving model forcing data using numerical weather prediction products constrained by surface and top of the atmosphere observations. *J. Geophys. Res.,* **109,** D01104, doi:10.1029/2003JD004045.

Yanai, M., S. Esbensen, and J. Chu, 1973: Determination of bulk properties of tropical cloud clusters from large-scale heat and moisture budgets. *J. Atmos. Sci.,* **30,** 611–627.

Zhang, M., and J. Lin, 1997: Constrained variational analysis of sounding data based on column-integrated budgets of mass, heat, moisture, and momentum: Approach and application to ARM measurements. *J. Atmos. Sci.,* **54,** 1503–1524.

Zhang, Y., and S. A. Klein, 2010: Mechanisms affecting the transition from shallow to deep convection over land: Inferences from observations of the diurnal cycle collected at the ARM Southern Great Plains site. *J. Atmos. Sci.,* **67,** 2943–2959.

Zipser, E. J., and K. R. Lutz, 1994: The vertical profile of radar reflectivity of convective cells: A strong indicator of storm intensity and lightning probability? *Mon. Wea. Rev.,* **122,** 1751–1759.

Zrnić, D. S., and A. V. Ryzhkov, 1999: Polarimetry for weather surveillance radars. *Bull. Amer. Meteor. Soc.,* **80,** 389–406.

 Q. J. R. Meteorol. Soc. 140: 826–837, April 2014 DOI:10.1002/qj.2192

RMetS
Royal Meteorological Society

Evaluation of intercomparisons of four different types of model simulating TWP-ICE

Jon Petch,[a]* Adrian Hill,[a] Laura Davies,[b] Ann Fridlind,[c] Christian Jakob,[d] Yanluan Lin,[e] Shaoecheng Xie[f] and Ping Zhu[g]

[a]*Met Office, Exeter, UK*
[b]*University of Melbourne, Victoria, Australia*
[c]*NASA Goddard Institute for Space Studies, New York, NY, USA*
[d]*School of Mathematics, Monash University, Melbourne, Victoria, Australia*
[e]*Center for Earth System Science, Tsinghua University, Beijing, China*
[f]*Lawrence Livermore National Laboratory, CA, USA*
[g]*Department of Earth and Environment, Florida International University, Miami, FL, USA*

*Correspondence to: J. C. Petch, Met Office, FitzRoy Road, Exeter EX1 3PB, UK. E-mail: jon.petch@metoffice.gov.uk

Four model intercomparisons were run and evaluated using the TWP-ICE field campaign, each involving different types of atmospheric model. Here we highlight what can be learnt from having single-column model (SCM), cloud-resolving model (CRM), global atmosphere model (GAM) and limited-area model (LAM) intercomparisons all based around the same field campaign. We also make recommendations for anyone planning further large multi-model intercomparisons to ensure they are of maximum value to the model development community. CRMs tended to match observations better than other model types, although there were exceptions such as outgoing long-wave radiation. All SCMs grew large temperature and moisture biases and performed worse than other model types for many diagnostics. The GAMs produced a delayed and significantly reduced peak in domain-average rain rate when compared to the observations. While it was shown that this was in part due to the analysis used to drive these models, the LAMs were also driven by this analysis and did not have the problem to the same extent. Based on differences between the models with parametrized convection (SCMs and GAMs) and those without (CRMs and LAMs), we speculate that that having explicit convection helps to constrain liquid water whereas the ice contents are controlled more by the representation of the microphysics.

Key Words: convection; microphysics; numerical modelling

Received 7 January 2013; Revised 7 May 2013; Accepted 17 May 2013; Published online in Wiley Online Library 18 July 2013

1. Introduction

Weather and climate prediction relies on numerical models designed to represent our best understanding of the relevant components of the Earth system. One critical component of both weather and climate prediction systems is the representation of the atmospheric processes, both dynamical and physical. Global atmospheric models (GAMs) represent the whole globe and generally use coarse grid lengths which rely on the representation (or parametrization) of many physical processes whose scales are sub-grid, with convection and clouds being a key example. Regional or limited-area models (LAMs) are a key tool for weather prediction, and are increasingly used in climate research and prediction to dynamically downscale global climate predictions to add better understanding of the regional impacts of climate change (e.g. Kendon *et al.*, 2010). LAMs are an attractive tool because they cover smaller regions and are thus able to use smaller grid lengths for the same computational costs, and this allows a more explicit representation of the local orography as well as convective processes and the associated cloud.

The continuous development and improvement of atmospheric models is of critical importance to the weather and climate community (Randall *et al.*, 2003). Two further modelling systems which are valuable tools supporting the development of LAMs and GAMs are cloud-resolving models (CRMs) and single-column model (SCM) versions of the GAMs (Randall *et al.*, 1996). CRMs are very similar to LAMs in that they also represent a limited area and utilise shorter grid lengths to explicitly resolve key processes. They differ in that they have generally been developed to understand the physical processes of the atmosphere rather than as a prediction system. They are also often run at much higher resolution than LAMs and include more complex and computationally expensive representations of the physical processes such as microphysics. In this article, as is quite often the case, the CRMs

also differ from the LAMs in the way they are forced. The LAMs include the real land surface boundaries and use open boundary conditions provided by analysis of global forecasts. In contrast, the CRMs use a uniform ocean surface, employ cyclic boundary conditions and are driven by a uniform forcing consistent with the SCMs. SCMs, while they have their limitations, allow us to isolate the behaviour of GAM parametrizations from dynamical feedbacks and also prove a computationally efficient method for quickly evaluating parametrization changes (e.g. Randall *et al.*, 2003). In this work, they also use a uniform ocean and are essentially driven in the same way as the CRMs.

A framework to test all the models types discussed above and confront these with observations is the intercomparison. An intercomparison is where various models of the same type are run for the same case and their results compared. The benefits of this collaborative activity to model developers go beyond the ability to compare their model with many other models and identify their key deficiencies (as discussed in Petch *et al.*, 2006) because they also bring the community together to jointly discuss and tackle key challenges in model development. The GEWEX (Global Energy and Water Exchanges) project Global Atmospheric System Studies (GASS) acknowledge the importance of these activities and thus focus much of their work on coordinating these activities. This article describes the lessons we can learn from bringing together the results of four model intercomparisons involving GAMs, LAMs, CRMs and SCMs.

The intercomparisons were all based around the Tropical Warm Pool–International Cloud Experiment (TWP-ICE) which took place in and around Darwin, Australia, from 20 January to 13 February 2006. Its focus was to describe the evolution of tropical convection, including the large-scale heat, moisture, and momentum budgets at 3 h time resolution, while at the same time obtaining detailed observations of cloud properties and the impact of the clouds on their environment (May *et al.*, 2008). A field campaign of this kind provides an ideal test-bed for driving and evaluating a range of atmospheric models used in weather and climate research and prediction.

Under the umbrella of GASS and with the support of the US Department of Energy (DOE) Atmospheric System Research (ASR) program, observations made during the TWP-ICE campaign have been used to drive and evaluate multiple models of four different types. The resulting collaboration and articles describing model intercomparisons provide an important reference for various institutions to carry out further experiments which support their model development processes. The articles describing their comparisons using the TWP-ICE data are:

- CRMs: Cloud-resolving models (Fridlind *et al.*, 2012)
- LAMs: Limited-area models used in regional weather and climate prediction (Zhu *et al.*, 2012)
- GAMs: Global atmospheric models for predicting on weather or climate time-scales (Lin *et al.*, 2012)
- SCMs: Single-column models (Davies *et al.*, 2013).

In Fridlind *et al.* (2012), observations made during TWP-ICE were used to perform the most comprehensive evaluation of a cloud-resolving model intercomparison that has ever been carried out. The ability to challenge the models with such a range of observations, particularly those which describe the variability within the CRM domains, highlighted many challenges for both CRM development and for designing the frameworks in which the CRMs are run. Specific conclusions from the article noted that there was a wide spread in the prediction of cloud stratiform fraction and that all models systematically overestimated the areas with strong convective mean precipitation. While precipitation was constrained by the forcing, it was clear that the CRMs differed significantly in their prediction of the precipitation distribution. It was noted there was a large spread in predicted ice water path and, compared to observational estimates, it was overestimated in all models apart from those which were run in two dimensions. However, the existing estimates of uncertainty in ice water path retrievals also require further evaluation, as discussed by Fridlind *et al.* (2012).

Zhu *et al.* (2012) presented the first comparison of convective-scale LAMs carried out within GASS. The models produced realistic large-scale thermodynamic fields when compared to observations, although the locations of precipitation within the domains varied. As with the CRMs, ice water paths differed by large amounts between models. Stratiform cloud fractions showed large spread, especially high ice anvils, which can have large impacts on the radiative properties of the cloud systems. Both the water contents and the ice cloud fractions were seen to vary significantly between models.

In Lin *et al.* (2012), GAMs were compared over the TWP-ICE region and, while the models all captured the large-scale precipitation event seen in the observations, it was delayed by over a day. As with the CRMs, ice water contents had a very large spread (more than an order of magnitude) but it was also clear that in GAMs there was a large spread in liquid water paths. There were enough models involved in the comparison to identify that the models whose convection schemes were more responsive to mid-level moisture performed better during the less active periods.

Davies *et al.* (2013) described the first SCM intercomparison to use ensemble forcing which represented the observational uncertainty and provided a sensitivity study for the SCMs involved. It also included a single 2D and 3D CRM as a reference for the SCMs using the ensemble forcing. It was shown that, while the ensemble mean generally behaved like a single realisation using the mean forcing, this was not the case for all diagnostics or all models. The ensemble forcing was also shown to be of particular value for investigating how different models respond to changes in the forcing.

While the four articles described above each make conclusions relevant to evaluation and improvement of the individual model classes they address, the archive of all the modelling results and observations is also a key output of this project. Individual modelling centres can begin to make use of this for their model development work. The availability of different model types for this case makes this an even more valuable resource. For example, the ability of a weather or climate modelling centre to carry out sensitivity studies using both their SCM and GCM and place this into context by comparing against other models driven in the same way is very valuable. Petch *et al.* (2007) described a comparison using a single GCM, SCM and CRM driven and evaluated using observations made during the Tropical Ocean–Global Atmosphere Coupled Ocean–Atmosphere Response Experiment (TOGA-COARE) as a preparation for an intercomparison involving these model types. However, this work lacked the unique opportunity of having a completed intercomparison to allow us to study the spread and variation of the models. In this 'multi-model type intercomparison', we bring together the key findings of each of the separate modelling studies and diagnose some cross-model differences to learn more about both the models themselves and the experimental framework used.

This article analyses the results of all models used in the TWP-ICE intercomparison to identify what can be learnt from a multi-model type intercomparison. It also identifies and documents the key lessons learnt during this project which should help the planning of any similar work in the future. Section 2 describes the experimental frameworks and models used in these studies and how they differed for the different model types. Section 3 analyses the results of all model types and in section 4 we summarise our findings and make recommendations which should improve any further similar multi-model intercomparisons.

2. Experimental framework

The analysis of all the modelling carried out in this cross-comparison was based around the TWP-ICE field campaign.

Table 1. A summary of the models used in the four separate intercomparison articles.

Model type Reference	LES/CRM Fridlind *et al.* (2012)	LAM Zhu *et al.* (2012)	Global Lin *et al.* (2012)	SCM Davies *et al.* (2013)
Number of models	10	6	9	9
Horizontal domain size	200–300 km^2	400–500 km^2	Global	One column
Analysis area	Domain	Average of grid boxes overlapping with the TWP-ICE variational analysis domain	Average of grid boxes overlapping with the TWP-ICE variational analysis domain	One grid box
Horizontal grid length (km)	0.9–3	1–3	20–250	25–200
Vertical grid length (km) around 500 mb	0.18–0.6	0.3–0.5	0.3–1.0	0.3–1.0
Forecast lead time analysed	Free running for whole period	12–36 h	24–48 h	Free running for whole period
Forcing	Variational analysis	Nested in global models driven by EC analysis	ECMWF analysis	variational analysis
Deep convection	Explicit	Explicit	Parametrized	Parametrized
Shallow convection	Explicit	Mix of BL, shallow schemes numerical/explicit	Parametrized	Parametrized
Cloud fraction scheme	All or nothing	Some all or nothing, some parametrized	Parametrized	Parametrized

The periods simulated were designed to be a balance between covering a broad range of conditions at the site and the increasing computational costs of longer runs. As described in May *et al.* (2008), the Darwin region was influenced by a typical monsoonal circulation during TWP-ICE. It experienced three distinct regimes: active monsoon during 20 to 25 January, suppressed monsoon during 26 January to 3 February, and a monsoon break period during 3 to 13 February 2006. The active monsoon period was characterized by westerly monsoon flow, intensive mesoscale convective systems of mostly oceanic origin, and heavy surface precipitation. During the suppressed monsoon period, clouds were primarily associated with relatively shallow convection accompanied by much lower surface precipitation than in the preceding monsoon period. The break monsoon period was featured by intense afternoon thunderstorms with several squall lines crossing Darwin in the evening and early morning. Due to the high computational cost, the CRM study focused only on the active and suppressed periods and the LAMs were run only for the period 1200 UTC on 22 to 0000 UTC on 26 January. In contrast, both the SCMs and GAMs were run for the entire TWP-ICE period from 0000 UTC on 20 January to 0000 UTC on 13 February.

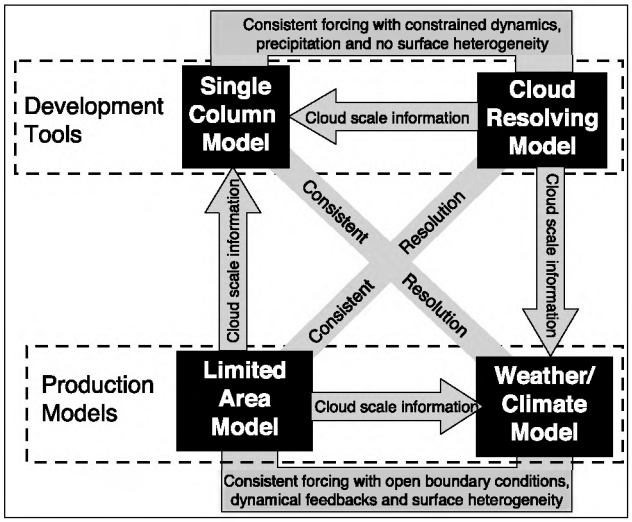

Figure 1. Schematic of the models used in the various comparisons with their relationships. Note that observations can be used in all components. CRMs and LAMs have resolved convection so provide additional information to convective parametrized models. SCMs are a tool to isolate climate model physics and keep consistent forcing.

2.1. *The models used*

A brief overview of the basic properties of all the models used and the runs carried out in the four intercomparisons are summarised in Table 1. As with any intercomparison project, there is a need to be pragmatic when specifying the design of the experiments. A balance is needed between constraining the components of the experiment such that the comparison is as clean as possible and the time it takes for the participants to adhere to any requirements. This is reflected in the ranges seen in properties such as the details of how the models are forced or how properties such as the land surface are initialised. While there would be benefit in having these set the same across all models, it is often more useful for centres to carry out the experiments with settings relevant to their typical use.

Table 1 shows that there are generally only a small number of models of each type. LAMs in particular only had six different models of which three were variants of WRF. The extent to which we should consider the variants of WRF as different models is quite subjective and through this article we will generally treat all model submissions equally. Full details of all the individual models used are available in the individual comparison articles and these will not be discussed here in any detail.

It is useful to consider the purpose of each model type in this cross-comparison article. Figure 1 depicts some of the key similarities and differences in the models used in this study, along with the way in which they are forced. The CRMs and SCMs are described here as development and research tools, i.e. they are not generally used to make operational predictions of weather or climate but more to understand atmospheric processes and support the development of other models. The CRMs can provide realistic cloud-scale motions to help diagnose how the processes should be parametrized in the larger-scale models. The SCMs allow us to isolate the model physics from the dynamics in a computationally inexpensive tool; in Davies *et al.* (2013), this efficiency has been exploited by carrying out an ensemble of forcing to learn about the behaviour of the physics in the SCMs as a function of the mean state and forcing. While there may be some exceptions, the GAMs and LAMs can be considered operational models as they are used to make predictions of weather and climate, often operationally as part of a national weather or climate service. It is the combination of all these model types which allows us to draw further general conclusions from this study. We are also able to identify key issues we should address when we organise future model intercomparisons involving SCMs, CRMs, GAMs and LAMs.

2.2. Comparing the different forcing and boundary conditions

Variational analysis is used to derive the domain-mean large-scale forcing dataset used to drive the SCMs and CRMs. The forcing data have a 10 mb vertical resolution and 3 h temporal resolution (centred in time) and were created using a combination of observations and the ECMWF analysis (Xie *et al.*, 2010). In both the SCM and CRM integrations, the models were initialised only once. The SCMs were then integrated for the entire length of the experiment, with no nudging towards observed profiles. In contrast, as described in Fridlind *et al.* (2012), the CRMs were free running below 16 km, while above 16 km the vapour and temperature profiles were nudged towards observed profiles. Thus, both the CRMs and SCMs simulations of the troposphere were free running for the entire period. There are pros and cons of running the entire period, but free runs are common in CRM and SCM intercomparisons (e.g. Xie *et al.*, 2002; Xu *et al.*, 2002). The SCM article (Davies *et al.*, 2013) focuses on the results from using an ensemble of forcing created using variational analysis with the precipitation perturbed within the observational uncertainties. However, in this article we focus on the deterministic forcing used as the basis for the CRM comparison; this forcing was also used in the SCM article for comparison to the ensemble forcing and was shown to give similar answers to the ensemble mean for most diagnostics.

A notable difference between the deterministic SCM forcing and the CRM forcing was the way in which the variational analysis was used. The horizontal advection term (which is generally much smaller than the vertical) is the same in both methods. However, for the SCM comparison, the vertical velocity from the analysis was used with the model predicted thermodynamic fields to give the vertical advection term to drive the model. In contrast, the CRM comparison used both the thermodynamic fields and vertical velocities from the analysis to derive vertical advection tendencies. Ghan *et al.* (2001) compared these two methods of forcing during the SCM comparison of midlatitude continental convection and it was concluded that there was no systematic dependence on the forcing method employed. Later, however, we will demonstrate that the different forcing method employed in the CRM and SCM intercomparison leads to a difference in the thermodynamic profile and is therefore a limitation of this cross-model comparison and a difference which should be avoided in future work. Hereafter we will refer to these methods as SCM forcing and CRM forcing, although we note that either forcing method can be applied to both SCMs and CRMs. A further difference between the SCM and CRM forcing was that the CRMs were transitioned from free-running below 15 km to nudging of model domain-mean water vapour and potential temperature towards observed domain-mean conditions with a 6 h time-scale above 16 km (specification and discussion in Fridlind *et al.* 2012). This was a pragmatic decision to better maintain a tropopause layer structure consistent with observations while not influencing total surface precipitation relative to a fully free-running simulation. This difference was much less significant for the results discussed in this article.

The GAMs wind, temperature, moisture, and surface pressure were initialized at 0000 UTC daily from the ECMWF operational analysis using the Cloud-Associated Parametrizations Testbed (CAPT) approach (Phillips *et al.*, 2004). Other fields, such as land surface properties (vegetation, soil moisture and temperature) were constrained to be as realistic as possible using a range of methods in the various models. The methods were chosen by the modelling centres themselves as the option they considered the best choice for their modelling system. The second day (24–48 h) of the forecasts was used for the comparisons made in this article. This was chosen to allow spin-up of the models but still keeping the large-scale dynamics close to the analysis. The different LAMs were constrained in somewhat different ways for the dynamics, thermodynamics and other fields such as land surface properties. This was an example where the various centres have typical or operational methods of driving their models and it was reasonable that they were driven using their own methods. However, the wind, temperature, moisture, and surface pressure in all models were essentially initialised and driven at the boundaries either by an analysis or by a short-range forecast initialised by the same ECMWF analysis that was used by the GAMs.

To understand the role of the different forcing from these experiments, it is useful to compare the ECMWF analysis to the variational analysis. Figure 2 shows vertical velocity from the ECMWF analysis (driving the LAMs and GAMs) and the variational analysis (driving the CRMs and SCMs). A key difference between the two forcings is that the strong upward motion in the wet period around 23–25 January has quite a different timing with the negative peak between 23 and 24 January for the variational analysis, but this occurs a whole day later in the ECMWF analysis. The mean vertical velocity from the wet and dry periods (defined in Figure 3(a)) shows that the upward velocities are typically stronger in the ECMWF analysis than they are in the variational analysis. In the dry period, there is also weak ascent in the ECMWF analysis while there is descent in the variational analysis. The implications of these mean and timing differences will be discussed during the evaluation of results from the different models in the next section.

3. Cross-model comparison

It is a challenge to show the vast number of results from various models in a simple set of plots. To do this we mainly focus on showing a selection of basic fields as the mean of each model type and the spread of those models. In plots used here we have focused on the use of the mean and standard deviation between models to describe the spread. It should be stressed that this potentially hides a great deal of information and can lead to somewhat misleading conclusions if more detailed analysis is not carried out. This is particularly true because of the relatively small sample sizes of models of each type (ten CRMs, six LAMs, nine SCMs and nine GAMs). Later we show the specific implication of the use of means and standard deviation for presenting the data.

By combining all models, we are removing the option for an individual centre to identify its own model and development needs. However, this level of detail would not be appropriate for an overview article and also near-impossible to present clearly. Instead we can highlight some basic interesting features from the models as a whole and thus allow any centre to carry out further work needed to review the performance of its model and any required sensitivity studies.

As shown in Table 1, different types of model were run over different sizes of experimental domain. To make an appropriate comparison with the observations and between different types of model, simulations from these four model types were all averaged over the variational analysis domain, which is the same as the TWP-ICE pentagonal sounding array. It should be noted that the actual domain size represented by the GAMs is slightly larger than the sounding array due to the coarse resolutions used in the GAMs. In addition, since different GAMs were run with different horizontal resolutions, model grid points used in the average vary from two for the coarsest model to over one hundred for models at 20 km resolution. As indicated in Lin *et al.* (2012), these differences are small compared to the variations between these GAMs. So we do not expect that they have large impact on our analysis.

3.1. Evolution of the models

Time series of some basic fields, such as precipitation, are important to give a basic guide to the evolution of the weather during the simulations, and these are shown in Figures 3 and 4. The period we focus on is 22 January to 3 February. The LAMs were only run for the period 0000 UTC on 23 to 0000 UTC on 26 January and the SCMs and GAMs were run for a longer period

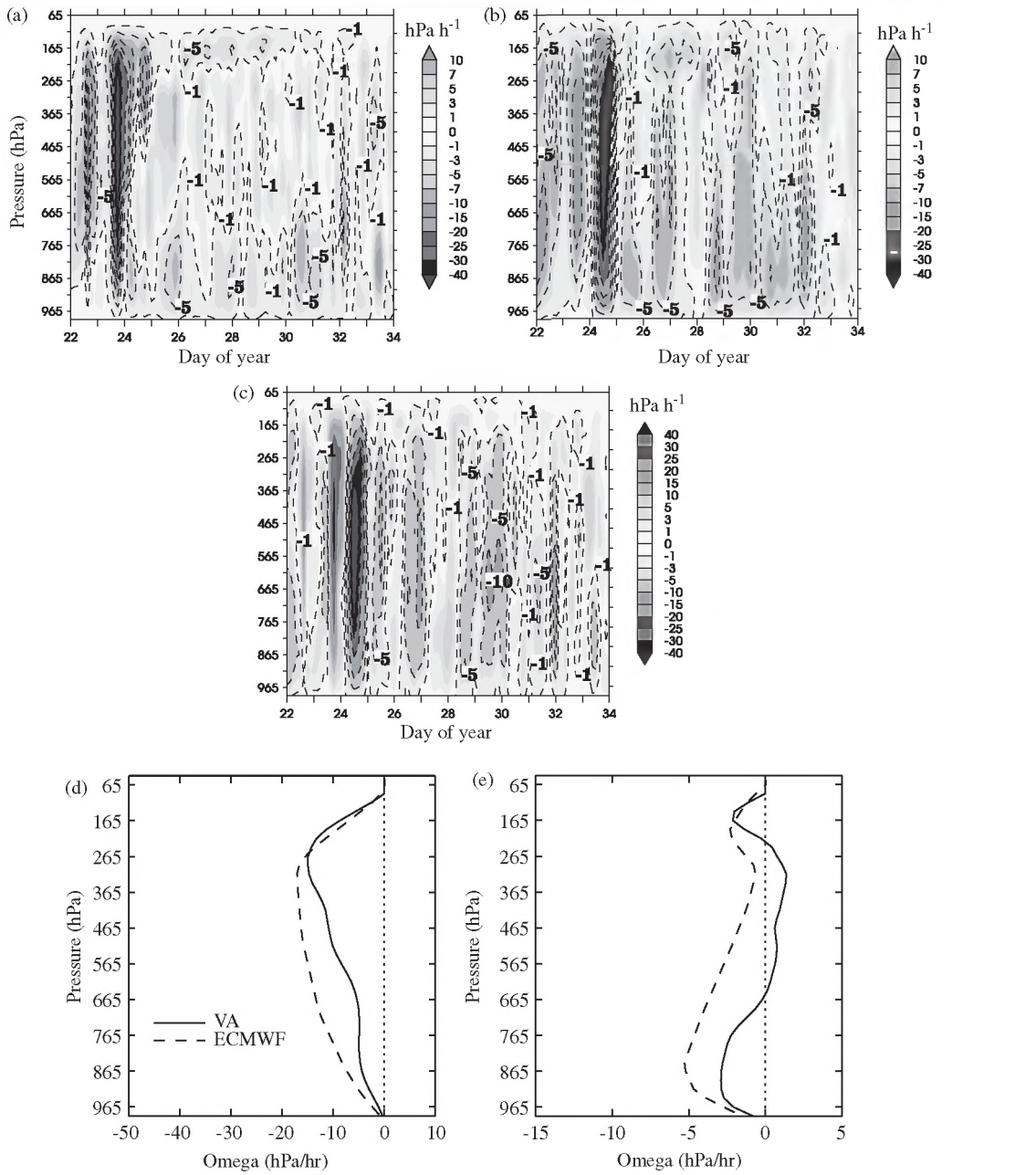

Figure 2. Comparison of the vertical velocity, ω, from the variational analysis (used to drive the CRMs and SCMs) and the ECMWF analysis (used to drive the GAMs and LAMs), showing time–height plots of 6 h mean ω from (a) the variational analysis, (b) the ECMWF analysis, and (c) the difference between the ECMWF analysis and the variational analysis. Also shown is the mean during the (d) wet and (e) dry periods (as defined in Figure 3).

than shown. The mean values use a 6 h averaging period. This was a pragmatic choice, balancing the removal of shorter temporal noise which makes the plot look too busy while maintaining useful information around the temporal variability. The standard deviations of the model spread were also calculated at these 6 h intervals but then averaged to 24 h to further remove noise. Standard deviation is shown normalised by the multi-model mean value. The spread was plotted separately from the mean, since plotting together (as is done in some later plots) led to too much clutter.

Figure 3(a) shows the time series of the multi-model mean surface rain rate along with observations. Also highlighted on this plot are two sub-periods we will describe as 'wet' and 'dry'. The wet period runs from 0000 UTC on 23 to 0000 UTC on 25 January and the dry period from 1200 UTC on 25 to 1200 UTC on 2 February (day of year 33.5). These are chosen to allow us to sample a period of organised convection producing heavy precipitation and then a more suppressed period characterised by mid-level and shallow convection or broken deep convection producing lighter domain-averaged precipitation. The LAM simulations covered only the wet period. One further point to note is that the periods are based on the observed surface precipitation and timing errors in some model types would influence results from this kind of averaging; where relevant this is discussed.

From Figure 3(a) we can see that the CRMs and SCMs produce very similar precipitation rates through the period, as we would expect, due to these models being mostly constrained on the longer time-scales by their forcing (as discussed in Fridlind *et al.*, 2012; Davies *et al.*, 2012). Perhaps of interest is that the highest peak rates are a little lower in the SCMs, something seen much more strongly in the GAMs. This may suggest that the SCM is trying to behave like the GAM but needs dynamical feedback to show the full response, although it could also be related to a low-level dry bias and the way the forcing is applied to the SCMs (discussed later).

The GAMs have a significant delay (of 1 to 2 days) and a reduced peak (by over 50%) in the large rain event on 23 January but have similar amounts of rain during the latter part of the period. The LAMs also show a reduced peak rain event, and heavier than observed rain after the peak. However, the timing of the peak event in the LAMs is much closer to the timing of the observed peak than we see in the GAMs. As discussed

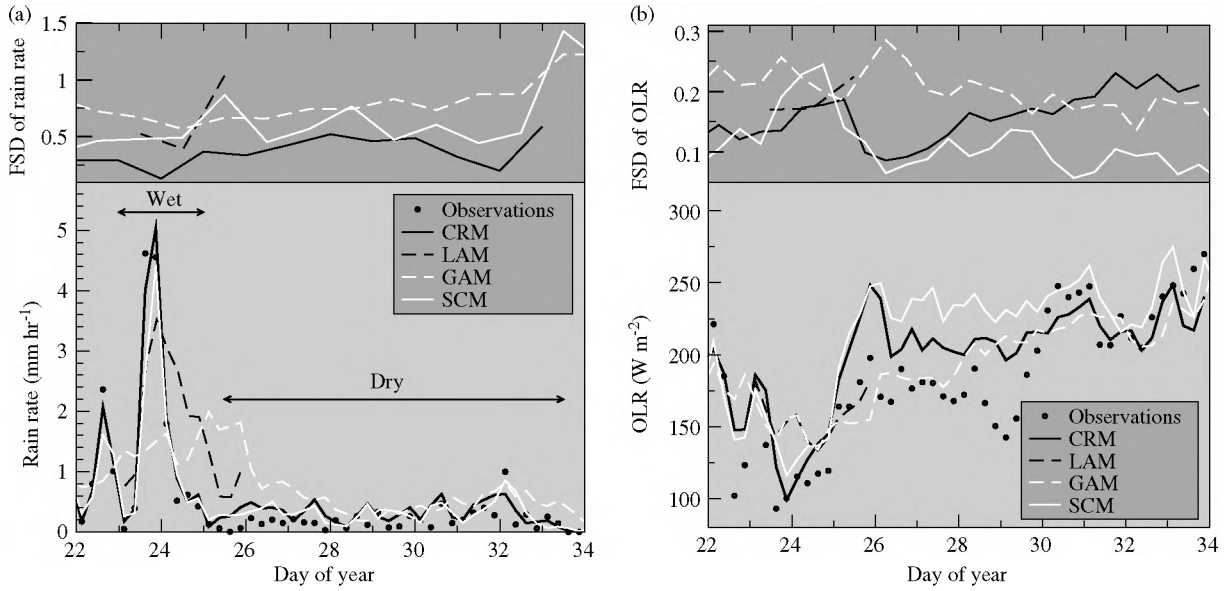

Figure 3. Time series of mean and fractional standard deviation (FSD, defined as standard deviation normalised by the mean value) of (a) rain rate and (b) outgoing long-wave radition (OLR). The time axis shows the day of the year at 0000 UTC.

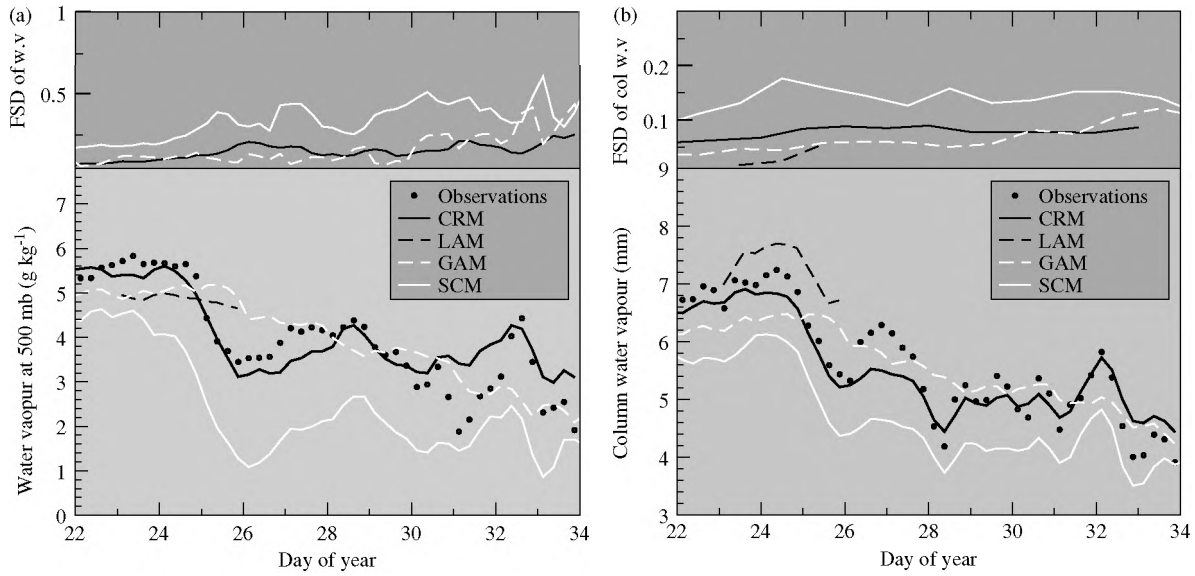

Figure 4. As Figure 3, but for (a) water vapour at 500 mb and (b) column water vapour.

in Zhu *et al.* (2013), the extended period of intense rain in the LAMs is the result of differences in mesoscale organisation in the inner model domain. For example, some models maintained the cyclone in the domain for longer than observed, which resulted in an increase in the period of intense precipitation. This issue is not seen in the CRMs and SCMs because these model types were constrained by the applied large-scale forcing. As the LAMs and GAMs are both run from the ECMWF analysis, this suggests that the large delay and reduction in the peak rain in the GAMs is, at least in part, due to the physics or dynamics in these models and not simply an issue with the forcing, which in Figure 2 was shown to have around a 1 day delay compared to the variational analysis. Issues with GAMs raining too frequently, producing too much lighter rain and not enough heavy rain events, has been noted before (Sun *et al.*, 2006; Wilcox and Donner, 2007; Stephens *et al.*, 2010) and this may be a useful case to study this. We also speculate here that the delay in the ECMWF analysis compared to the observationally based variational analysis may be due to the physics of the ECMWF model. The ECMWF physics will influence their analysis whereas the variational analysis uses precipitation observations directly to modify the divergent wind field. The SCM results highlight that this issue is not well studied in an SCM due to the need for a dynamical feedback.

The spread in the precipitation between models is shown in the top panel of Figure 3(a). The SCMs have larger spread than the CRMs, suggesting that, although precipitation is dynamically constrained on longer timescales, different SCMs can still produce quite different rain rates on a 6 h time-scale. The GAMs produce the largest spread between models on average, although it is clear that the LAMs vary a lot in their precipitation fields on 25 January as the large rain event moves away from the domain.

Figure 3(b) shows the time series and spread of outgoing long-wave radiation (OLR). The GAMs and LAMs lack of very intense precipitation, which is reproduced in the CRMs and SCMs, is also clear in the OLR with both model types missing the dip around 24 January. The CRM and SCM have larger than observed OLR between 25 and 30 January, suggesting a lack of cirrus cloud that was clearly seen in the observations and captured by the forcing data (Xie *et al.*, 2010). While the GAMs look better during the first half of this period, this is probably associated with the delay in the main convective event rather than them having a better cirrus representation. Overall, it appears that the GAMs and CRMs perform better than the SCMs. When we look at the spread of the models for OLR (Figure 3(b), top) it is clear that, although the GAMs do well in the multi-model mean, there is much larger spread than that exhibited by the CRMs and SCMs.

Figure 4 shows the mean and fractional standard deviation of (a) vapour on the model levels closest to 500 mb and (b) column integrated water vapour. In Figure 4 we see that in general the means of the CRMs compare well to observations. The good agreement between CRMs and observations in Figure 4(a) may suggest that the resolved convection is doing a good job of moistening the mid-troposphere. The GAMs and LAMs also capture the general water vapour trends, but seem to miss the steep drop in both column vapour and vapour at 500 mb around the heavy rain event. This is consistent with them delaying and reducing the peak in the precipitation during these events. We note here that we would expect the GAMs to remain reasonably close the observations as the analysis focuses on the 24–48 h period of the forecast, so long-term biases are not able to grow. On the other hand, the SCMs have already generated an obvious dry bias in both the column vapour and the mid-tropospheric vapour content at 500 mb by 22 January. This dry bias grows through the first half of the run. The dry bias at 500 mb in the SCMs may be a consequence of the convection schemes not responding to free tropospheric humidity and thus not producing an appropriate amount of mid-depth convection; this issue is reviewed in DelGenio *et al.* (2012). The causes of the overall dry bias exhibited by the SCMs are discussed in more detail in section 3.2. The spread in 500 mb water vapour and column vapour (Figure 4(a, b), top) in the GAMs and CRMs is similar through most of the period. The SCMs exhibit a larger spread than the other models which is in part because the mean is smaller but there is more absolute spread. This could be consistent with the fact that some convection schemes are more capable of moistening the free troposphere (as discussed in Lin *et al.*, 2012) and do not have such large biases.

Overall, Figure 3 shows the GAMs and CRMs simulate OLR better than the SCMs, presumably because the GAMs and CRMs do not exhibit the large dry bias and associated lack of mid- to high-level cloud seen in the SCMs. GAMs tend to produce the largest spread in OLR. This suggests that modelling centres should focus their attention on OLR and in particular its links with the behaviour of their convection schemes during both the wet and dry period. An SCM may be a useful tool for this; however, care must be taken since Figure 4 demonstrates large water vapour biases seen in this model type for these simulations, which have a strong influence on the OLR.

3.2. *The wet and dry periods*

Figure 5 shows the profiles of temperature and water vapour mixing ratio for the models and the ECMWF analysis differenced from the variational analysis averaged over the wet and dry periods (as indicated in Figure 3(a)). While not shown here, we note that the temperature and water vapour profiles taken directly from the radiosondes were a good match to the variational analysis, so the differences plotted are a true bias from observations. The first point to note from Figure 5 is that, particularly for temperature but also for water vapour, there are very large biases in the mean of the SCMs. The multi-model spread is large, but in the wet period there is no overlap between a standard deviation from the mean and the other models. As CRMs do not exhibit these same biases but are forced in a similar way, the biases are either related to the physics in the SCMs or to the different ways in which the forcing was applied in the two model types.

To investigate whether the method of forcing is leading to differences in the CRMs and SCMs, we carried out a sensitivity study using the Met Office CRM. Figure 6 shows the temperature and moisture bias from the wet period using the two methods for forcing the CRMs and SCMs. It is clear that the standard CRM forcing method and the SCM forcing method do lead to significantly different biases. In the lowest few kilometres, the temperature and water vapour bias in the Met Office CRM looks much more like the multi-model mean SCM bias, when the SCM forcing method is applied. However, above this the Met Office CRM appears to behave a little more like other CRMs, suggesting that the main influence of the forcing is in the lowest 5 km. This can be understood if we think about the convergence of water vapour with the two forcing methods, noting that during the wet periods there is a convergence of water vapour through much of the lower troposphere due to the vertical motion (Figure 2). In the CRM forcing method, the water vapour convergence is prescribed by the observations. However, in the SCM method of forcing the water vapour convergence is determined by the predicted water vapour in the model. Application of the SCM forcing to the CRM results in a 30% reduction in water vapour convergence due to the bias. As the SCMs and CRMs have a negative bias in water vapour in the lower troposphere, the convergent term of the forcing will give a positive feedback on this bias with the SCM style of forcing. Table 2 summarises the convergent term of the forcing feedback on the average bias.

Table 2. A summary of the feedback of the SCM-type forcing on the model bias.

Situation	Model bias	Feedback with SCM forcing
Convergence	Negative bias	Increased negative bias
Convergence	Positive bias	Increased positive bias
Divergence	Negative bias	Reduced negative bias
Divergence	Positive bias	Reduced positive bias

The sensitivity to the forcing method (Figure 6) suggests that the SCMs general cold/dry bias in the mid to upper troposphere (Figure 5) is not entirely an artifact of the forcing because the bias is much smaller in the CRM using identical forcing. Also, while we would expect the low-level dry bias also to contribute to such a bias (less moisture for latent heating in convection), this low-level dry bias is also present in the CRMs but the upper-level bias is much smaller. Therefore, this cold/dry bias may well be of interest to model developers as it is also evident in the full GAMs (although with a smaller magnitude for reasons discussed later).

The multi-model spread (of each model type) (Figure 5) is consistent with time series. The SCMs have a larger spread than the CRMs presumably because convection is parametrized in significantly different ways in the different SCMs. The GAMs have a larger spread than the LAMs for the same reason. The GAMs and LAMs both have lower spread than the CRMs and SCMs for two main reasons. Firstly, they are only 24–48 h into the forecast so very large biases do not have time to grow. Secondly, it is typical for large-scale dynamical feedbacks in the GAMs to prevent biases of the magnitude of those seen in the SCMs from developing.

Figure 7 shows profiles of the mean and spread of cloud fractions from the different models. During the wet period there are notable differences in the means, with the CRMs producing less cloud fraction below 5 km and more above. The GAMs and LAMs also have lower fractions than the SCMs. This may suggest there are issues around the forcing during this period leading to these differences but, given the very large multi-model spread, care should be taken into reading too much into this. It is also worth noting that the cloud fraction profiles are consistent with the OLR presented in Figure 3, namely, the CRMs produce the largest cloud fraction in Figure 7(a) and this corresponds to the lowest OLR during the wet period. Likewise the LAMs and GAMs simulate lowest cloud fractions, which is consistent with the largest OLR during the wet period. The mean of the cloud fractions during the dry period agree reasonably well across model types, particularly above the freezing level. However, again given the large spread of all model types, this would seem an area for all modellers to focus further attention on. We note here that the CRMs cloud fraction is produced from resolved cloud-scale motion whereas the SCMs and GAMs will all have a parametrization scheme to represent this. Above the freezing level, CRMs have as large a spread in cloud fraction as the SCMs and GAMs and this should be a focus for those who develop and evaluate CRMs. Fridlind *et al.* (2012)

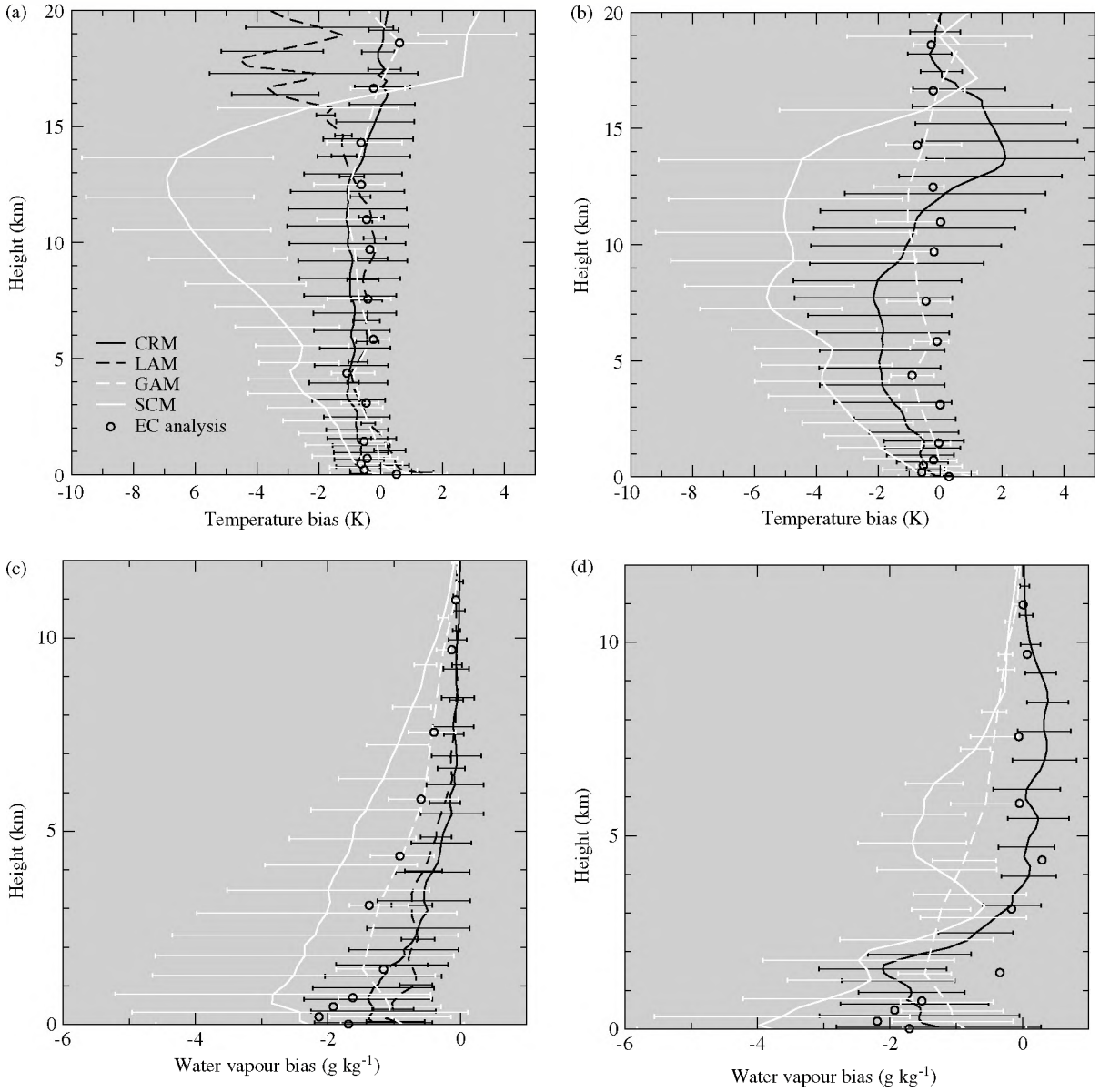

Figure 5. Mean temperature and water vapour mixing ratio biases (multi-model mean differenced from the variational analysis) and the multi-model spread shown as a standard deviation each side of the mean: temperature bias for (a) the wet period and (b) the dry period, and water vapour bias for (c) the wet period and (d) the dry period. Also included is the mean ECMWF analysis.

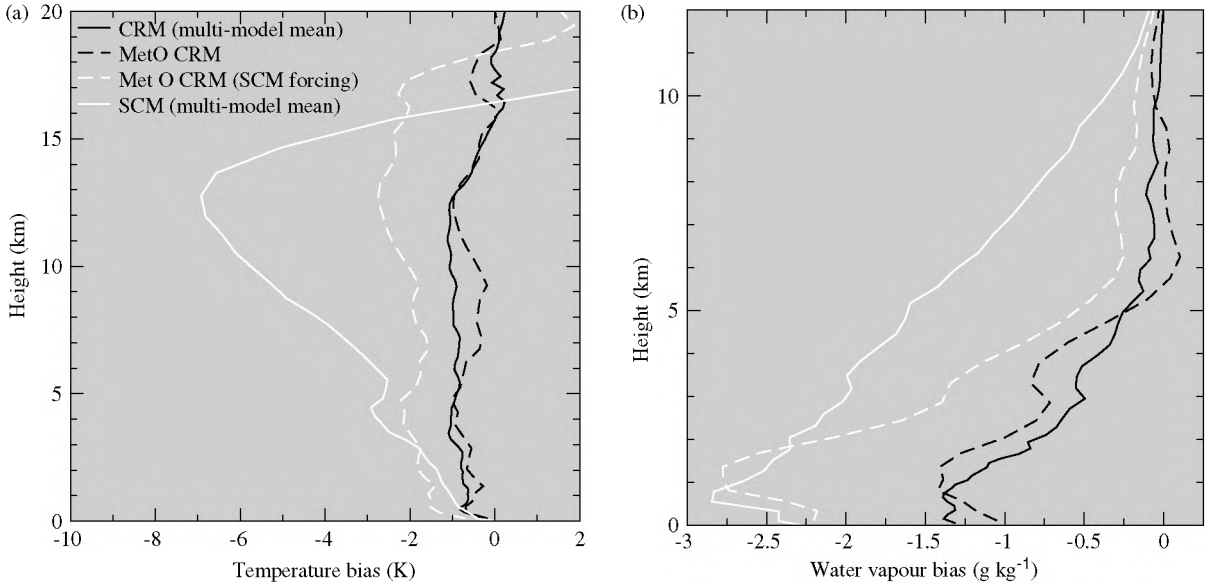

Figure 6. The sensitivity of the two forcing methods on (a) the temperature bias and (b) the moisture bias during the wet period using the Met Office CRM. Also included are the CRM and SCM multi-model means from Figure 5.

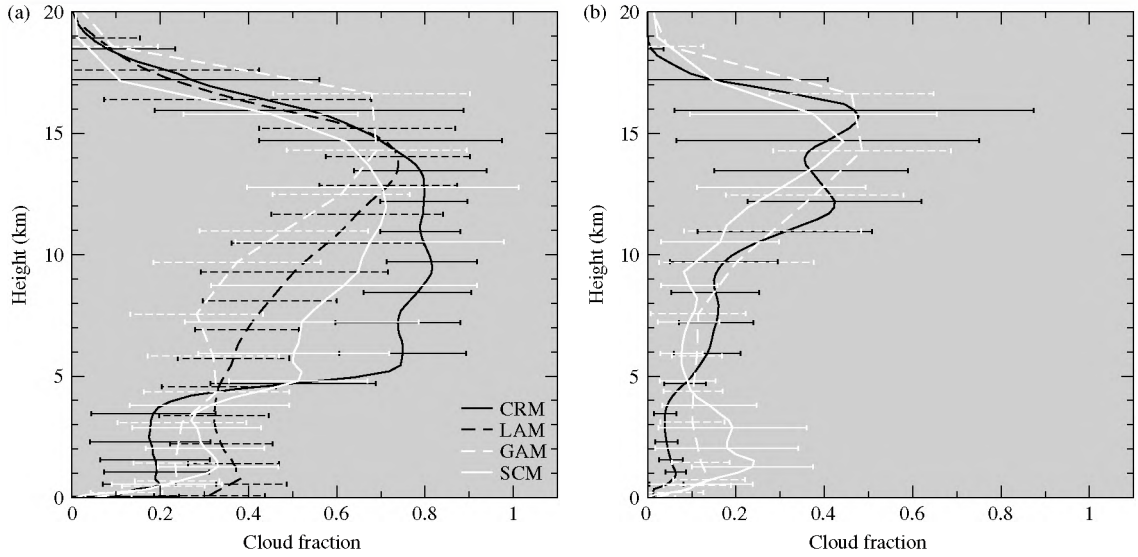

Figure 7. Domain-mean cloud fraction profiles and spread (shown as a standard deviation each side of the mean) for the (a) wet and (b) dry periods. In the CRM/LAMs, a point is considered cloudy if it has a water content greater than 10^{-3} g kg^{-1}.

suggest that CRM cloud fraction differences are attributable in part to differing ice nucleation schemes.

Figure 8 shows profiles of the domain mean and spread of ice and liquid water content. The liquid water shows that there is much lower spread in CRMs and LAMs and the means agree well with each other in the wet period (when the LAMs were run). This suggests that, for models which resolve cloud-scale motions, there is general agreement on the amount of cloud water which should be produced. On the other hand, the ice is a different story. In the wet period there are both large differences between the mean profiles for the model types and also large spread of ice for all model types. In the mean, perhaps of particular note are the low ice contents in the GAMs during this period; most of the SCMs had similarly low ice contents, although the mean does not show this and this is discussed later.

A potential reason for the differences in the mean ice contents in the CRMs and GAMs is related to what defines the ice water content. In the CRMs any solid hydrometeors (including snow and graupel) are included in Figure 8, whereas many GAMs and SCMs do not represent these species explicitly and therefore do not report them. While this difference may be a simple diagnostic issue, there are also potential modelling issues to consider. In particular, the snow and, to a lesser extent, graupel is important for radiative transfer (e.g. Petch, 1998) and if ignored in the GAMs there is likely to be compensating tuning to add in this missing cloud. While the CRM comparison did not request a breakdown of the ice into separate categories (owing to a lack of observation constraints for separate components), we do have this information from some models. As an example, Figure 9 shows the role of including all precipitating hydrometeors into the calculations of water content and cloud fraction for the Met Office CRM. While this impact will depend strongly on the microphysics scheme, it does highlight the need for significant care when we compare water contents and cloud fractions in convective situations.

Yet another issue to deal with when diagnosing and comparing water contents and cloud fraction is the role of the convection scheme in GAMs and SCMs. While convective schemes may detrain condensate into the large scale, they also have implied water content which are often not diagnosed and reported, not used in the radiation schemes, or both. We believe this should also be a focus for future comparisons.

3.3. *Presentational issues*

It was noted in the discussion about ice content that most of the SCMs had lower ice contents than the mean shown and that they were more similar to the GAMs. To highlight this, Figure 10 shows the ice content profiles from all the SCMs for the dry period; the wet period is not included but showed the same feature to a slightly lesser extent. It is clear from Figure 10 that there is a single outlier from other models and this is making a large contribution to the mean and spread. It would be possible to remove this outlier from the data, but there is not a good reason to do this and we noted that CRMs and LAMs had significantly higher ice contents than most of the SCMs. Another alternative would be to plot the median and interquartile range as shown on the figure. While this would be an entirely valid option, this is another way of downweighting outliers, and with relatively small samples (6–10 models) it may be preferable to plot both and ensure the true story is presented in any reporting of the results. For other issues discussed in this article, the averaging used in the plots did not influence the conclusions and therefore we have plotted mean values and standard deviations from this mean. However, when modelling centres use the data from this comparison, they should be aware of these issues.

4. Summary and discussion

In this article we have presented some basic fields from four intercomparisons of different model types, all simulating the TWP-ICE field campaign. This is the first example where there has been a coordinated effort to have CRMs, SCMs, GAMs and LAMs all evaluated for the same case. The large variety of observations and the high temporal sampling of atmospheric conditions, along with the availability of four separate model intercomparisons, make this a very good study for those developing their regional and global atmospheric models. The analysis in this article focused on comparing the multi-model means and the multi-model spread for each model type. When needed, we also performed some additional sensitivity studies using a single model. Conclusions from our analysis fall broadly into three categories. Firstly, there are the issues and lessons learnt about the design of multi-model type intercomparison experiments with recommendations for improvements in the future. Secondly, we highlight areas where most (or all) of the models of a given type are seen to perform poorly or have large spread, and therefore which require attention by model developers. Thirdly, we highlight where care needs to be taken when analysing and plotting model diagnostics.

Where possible the models were forced in a similar way. However, pragmatic choices were made, and, because it was not considered a key issue when the case was designed, the SCMs and CRMs applied their vertical forcing term differently. While both used the same observationally derived vertical velocity, SCMs were

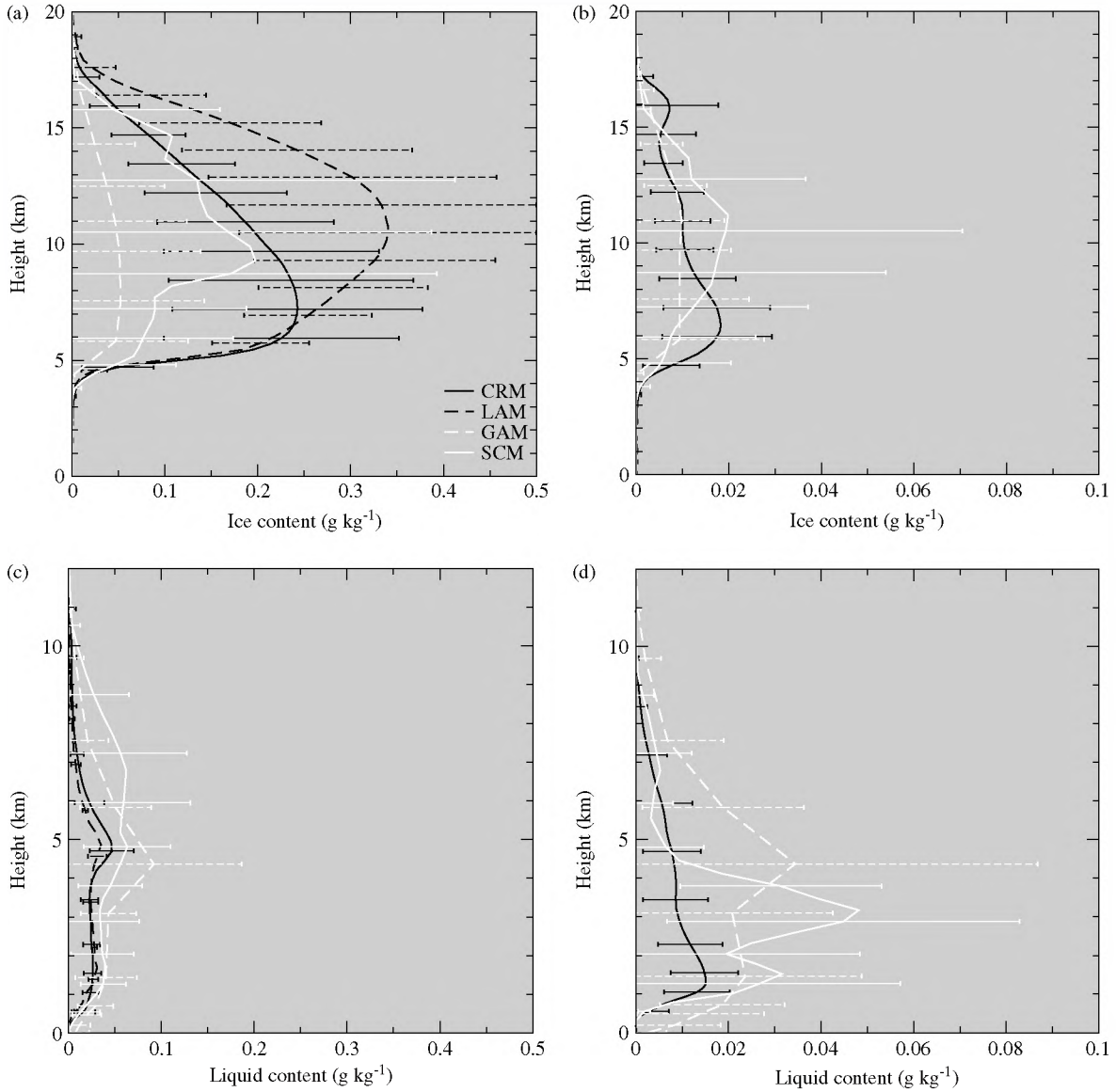

Figure 8. Domain-mean cloud water content profiles and spread (shown as a standard deviation each side of the mean). Included are ice mixing ratio for (a) the wet period and (b) the dry period, and liquid water mixing ratio for (c) the wet period and (d) the dry period. Note that the wet period has an x-axis range five times larger than the dry period.

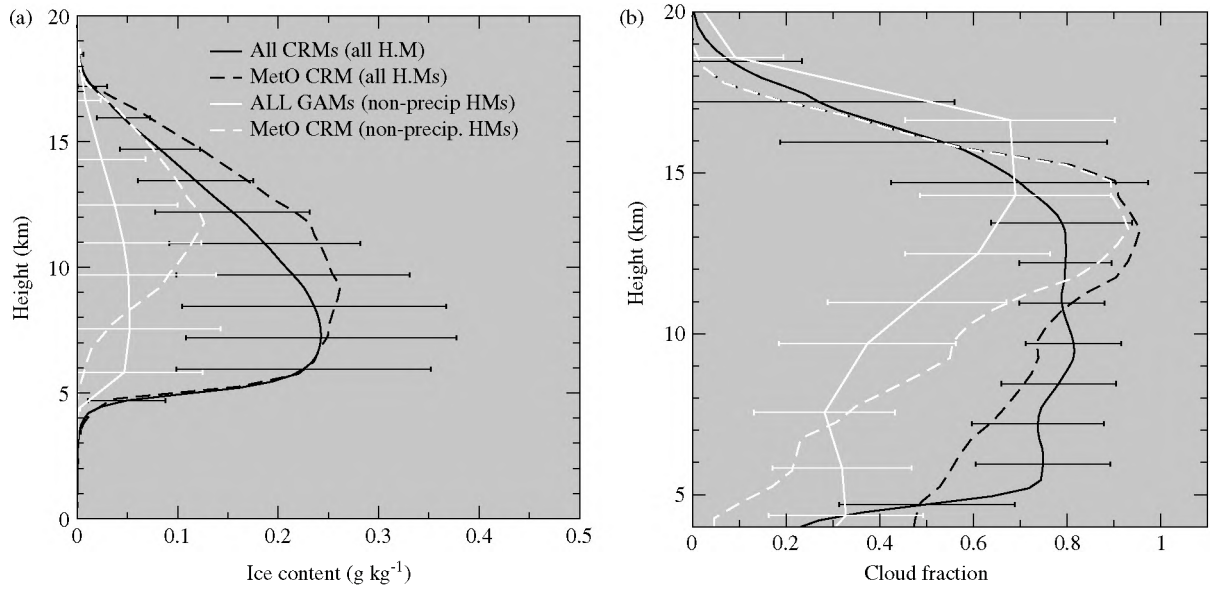

Figure 9. (a) solid water content and (b) fractional cloud cover for the wet period. Included are the profiles and spread from the CRMs and GAMs and a sensitivity study with the Met Office CRM where precipitating hydrometeors are included in the calculation.

forced by advecting their predicted temperature and moisture whereas CRMs were forced by advecting the observed temperature and moisture. This was shown to be important for our results with the SCMs growing a dry bias when there was convergence. While there is no obviously correct method for forcing SCMs and CRMs, it is important for future model comparisons such as this to use the same method (or both). The general strengths and weaknesses of both methods of forcing SCMs and CRMs used here are worth highlighting. The methods try to seperate the biases due to the physics from those due to the dynamics; however, such methods stop us from seeing how physical errors interact with the large scale. This is a reason why SCMs on their own cannot be used as a tool for developing parametrisations and why other methods such as weak temperature gradient have been employed in some studies (e.g. Sobel *et al.*, 2001). Also shown in this work is that the SCMs (and CRMs to some extent) generate large biases in their temperature or moisture profiles which are not seen in the GAMs or LAMs which used a series of short-range forecasts. As these biases may well influence many other physical aspects of the models, it is our recommendation that the SCMs are run as a series of short-range forecasts (as we do with the GAMs). As SCMs are computationally inexpensive to run, it should not be a problem for this to be done in addition to the longer free runs.

We also highlighted two key differences between the variational analysis and the ECMWF analysis. Firstly, there was stronger upward motion in the ECMWF analysis, although this was not linked with any specific differences between model types in our analysis. Secondly, the strongly forced rain event was of the order of a day later in the ECMWF analysis and this led to an expected delay in the peak rain produced in the LAMs and GAMs. Interestingly, the GAMs delayed the peak rain rate by a further day when compared to the LAMs and produced a weakened peak. As a reduced range of precipitation rates is a typical feature in many climate models (Stephens *et al.* 2010), we suggest that this may be a useful test case to study this despite the fact that there is already a signal for this in the driving analysis. The SCMs also produced a reduced peak in precipitation when compared to the CRMs.

A key finding of this study was that all model types had a lower tropospheric dry bias for this case and that the ECMWF analysis itself had a significant dry bias, particularly in the lowest levels. We speculated that, as all the GAMs had a tendency to produce a large dry bias, it was therefore the model contribution to the ECMWF analysis which led to bias in the analysis itself. It is possible that the dry bias which was seen most strongly in the SCMs and the GAMs could be the cause of the reduced precipitation intensity in the GAMs and the SCMs since they will have a reduced source of moisture for producing the precipitation.

This study also highlighted that there remains a great deal of uncertainty in ice microphysics across models. There was essentially a large spread in ice contents for all four model types which, given they all typically use similar bulk microphysical schemes, suggests that this remains an area for model developers on which to focus their attention. It also means there are no reference models for this kind of experiment, so observations to constrain the models remain a critical requirement. Liquid cloud was a somewhat different story. In the models which had explicit convection or cloud-scale dynamics (LAMs and CRMs), there was good agreement and small multi-model spread in liquid water profiles. However, for models with parametrized convection, there were notable differences from the CRMs and LAMs and large multi-model spread. The focus of those developing convection schemes tends to be on their impacts on the vertical transport of heat and water vapour, and on surface precipitation. The results shown here suggest that there also needs to be a focus on the clouds produced.

The challenges of comparing clouds and microphysical properties across model types were also highlighted in this paper. In particular, we noted that bulk microphysical schemes make

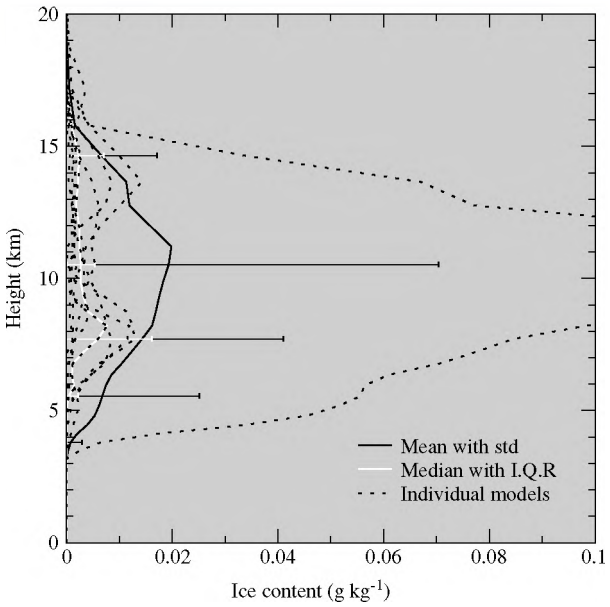

Figure 10. SCM ice contents averaged for the dry period.

different assumptions about how each category (e.g. snow, ice and graupel) is defined. However, often only the ice is prognostic and reported in many SCMs and GAMs, i.e. a precipitating ice hydrometeor content is not always diagnosed or reported. This makes a comparison with CRMs and LAMs difficult. An appropriate comparison may be to use the water content as seen in the radiation scheme, but it is quite possible that many models do not consider precipitating ice despite its significant contribution to optical depth (Petch, 1998). Therefore, to really understand how clouds compare across models of all types, we need to be very specific about the species in the model. While forward modelling and simulators can help (and this was used to compare CRMs with radar in Fridlind *et al.*, 2012), model developers would benefit from some clear comparisons of different hydrometeor types, clearly defining what they are, and how they influence radiative transfer. We acknowledge that it may be premature to focus solely on ice hydrometeor type, given that there is a lack of observational constraint. However, it is useful to understand how different treatments of the microphysics and their application within radiation schemes vary between models and to identify the impact of these differences. We therefore have a further recommendation for future multi-model type intercomparisons to clearly diagnose all hydrometeor types in their models separately and to define how they interact with radiation.

In summary, the TWP-ICE field campaign and the intercomparisons of four different model types provide an extremely valuable resource for those developing models. This article (along with the four individual intercomparison articles) highlights some interesting features which this experiment can be used to study further, but there are likely to be many more. We have also made recommendations for some changes to the forcing for those using this case for their model development, as well as various recommendations for those involved in coordinating future multi-model type intercomparisons.

Acknowledgements

A. Fridlind was supported by the NASA Radiation Sciences Program and the US DOE Office of Science, Office of Biological and Environmental Research, through contracts DE-AI02-06ER64173 and DE-SC0006712. The contributions of S. Xie to this work were performed under the auspices of the US Department of Energy (DOE), Office of Science, Office of Biological and Environmental Research by Lawrence Livermore National Laboratory under contract no. DE-AC52-07NA27344

and supported by the Atmospheric Radiation Measurement Program of the Office of Science at the US Department of Energy. Ping Zhu wishes to acknowledge his support by the DOE ASR program under grant DE-FG02-09ER64737. Yanluan Lin was supported by the Office of Science (BER), US Department of Energy. Laura Davies and Christian Jakob were supported by the US DOE ASR program under grant DE-FG02-09ER64742.

References

Davies L, Jakob C, Keane RJ, Whitall MA, Plant RS, Lin Y, Wang W, Wolf A, Del Genio AD, Larson VE, Nielsen BJ, Liu X, Shi X, Song X, Zhang G, Komori T, Hill AA, Petch JC, Hume T, Singh M, Cheung K. 2013. A single-column model ensemble approach applied to the TWP-ICE experiment. *J. Geophys. Res.* submitted.

Del Genio AD. 2012. Representing the sensitivity of convective cloud systems to tropospheric humidity in general circulation models. *Surv. Geophys.* **33**: 637–656. DOI: 10.1007/s10712-011-9148-9.

Fridlind AM, Ackerman AS, Chaboureau J-P, Fan J, Grabowski WW, Hill AA, Jones TR, Khaiyer MM, Liu G, Minnis P, Morrison H, Nguyen L, Park S, Petch JC, Pinty J-P, Schumacher C, Shipway BJ, Varble AC, Wu X, Xie S, Zhang M. 2012. A comparison of TWP-ICE observational data with cloud-resolving model results. *J. Geophys. Res.* **117**: D05204, DOI: 10.1029/2011JD016595.

Kendon LJ, Rowell D, Jones RG. 2010. Mechanisms and reliability of future projected changes in daily precipitation. *Clim. Dyn.* **35**: 489–509.

Lin Y, Donner LJ, Petch JC, Bechtold P, Boyle JS, Klein SA, Komori T, Wapler K, Willett M, Xie X, Zhao M, Xie S, McFarlane SA, Schumacher C. 2012. TWP-ICE global atmospheric model intercomparison: Convection responsiveness and resolution impact. *J. Geophys. Res.* **117**: D09111, DOI: 10.1029/2011JD017018.

May PT, Mather JH, Vaughan G, Bower KN, Jakob C, McFarquhar GM, Mace GG. 2008. The Tropical Warm Pool International Cloud Experiment. *Bull. Am. Meteorol. Soc.* **89**: 629–645.

Petch JC. 1998. Improved radiative transfer calculations from information provided by bulk microphysical schemes. *J. Atmos. Sci.* **55**: 1846–1858.

Petch JC, Willett M, Wong RY, Woolnough SJ. 2007. Modelling suppressed and active convection. Comparing a numerical weather prediction, cloud-resolving and single-column model. *Q. J. R. Meteorol. Soc.* **133**: 1087–1100.

Phillips TJ, Potter GL, Williamson DL, Cederwall RT, Boyle JS, Fiorino M, Hnilo JJ, Olson JG, Xie S, Yio JJ. 2004. Evaluating parameterizations in general circulation models: Climate simulation meets weather prediction. *Bull. Amer. Meteorol. Soc.* **85**: 1903–1915.

Randall DA, Xu K-M, Somerville RJC, Iacobellis S. 1996. Single-column models and cloud ensemble models as links between observations and climate models. *J. Climate* **9**: 1683–1697.

Randall DA, Khairoutdinov M, Arakawa A, Grabowski WW. 2003. Breaking the cloud-parameterization deadlock. *Bull. Amer. Meteorol. Soc.* **84**: 1547–1564.

Sobel AH, Nilsson J, Polvani LM. 2001. The weak temperature gradient approximation and balanced tropical moisture waves. *J. Atmos. Sci.* **58**: 3650–3665.

Stephens GL, L'Ecuyer T, Forbes R, Gettlemen A, Golaz JC, Bodas-Salcedo A, Suzuki K, Gabriel P, Haynes J. 2010. Dreary state of precipitation in global models. *J. Geophys. Res.* **115**: D24211, DOI: 10.1029/2010JD014532.

Sun Y, Solomon S, Dai A, Portmann RW. 2006. How often does it rain? *J. Climate* **19**: 916–934.

Wilcox EM, Donner LJ. 2007. The frequency of extreme rain events in satellite rain-rate estimates and an atmospheric General Circulation Model. *J. Climate* **20**: 53–69.

Xie S, Xu K-M, Cederwall RT, Bechtold P, Del Genio AD, Klein SA, Cripe DG, Ghan SJ, Gregory D, Iacobellis SF, Krueger SK, Lohmann U, Petch JC, Randall DA, Rotstayn LD, Somerville RCJ, Sud YC, Von Salzen K, Walker GK, Wolf A, Yio JJ, Zhang GJ, Zhang M. 2002. Intercomparison and evaluation of cumulus parametrizations under summertime midlatitude continental conditions. *Q. J. R. Meteorol. Soc.* **128**: 1095–1135.

Xie S, Hume T, Jakob C, Klein SA, McCoy RB, Zhang M. 2010. Observed large-scale structures and diabatic heating and drying profiles during TWP-ICE. *J. Climate* **23**: 57–79.

Xu K-M, Cederwall RT, Donner LJ, Grabowski WW, Guichard F, Johnson DE, Khairoutdinov M, Krueger SK, Petch JC, Randall DA, Seman CJ, Tao W-K, Wang D, Xie SC, Yio JJ, Zhang M-H. 2002. An intercomparison of cloud-resolving models with the Atmospheric Radiation Measurement summer 1997 Intensive Observation Period data. *Q. J. R. Meteorol. Soc.* **128**: 593–624.

Zhu P, Dudhia J, Field PR, Fridlind A, Varble A, Zipser E, Petch JC, Chen M, Zhu Z. 2012. A limited-area model (LAM) intercomparison study of a TWP-ICE active monsoon mesoscale convective event. *J. Geophys. Res.* **117**: D11208, DOI: 10.1029/2011JD016447.

Stochastic Behavior of Tropical Convection in Observations and a Multicloud Model

KARSTEN PETERS AND CHRISTIAN JAKOB

ARC Centre of Excellence for Climate System Science, School of Mathematical Sciences, Monash University, Clayton, Victoria, Australia

LAURA DAVIES

School of Mathematical Sciences, Monash University, Clayton, Victoria, Australia

BOUALEM KHOUIDER

Department of Mathematics and Statistics, University of Victoria, Victoria, British Columbia, Canada

ANDREW J. MAJDA

Centre for Atmosphere Ocean Science, Courant Institute of Mathematical Sciences, New York University, New York, New York

(Manuscript received 31 January 2013, in final form 4 June 2013)

ABSTRACT

The aim for a more accurate representation of tropical convection in global circulation models is a long-standing issue. Here, the relationships between large and convective scales in observations and a stochastic multicloud model (SMCM) to ultimately support the design of a novel convection parameterization with stochastic elements are investigated. Observations of tropical convection obtained at Darwin and Kwajalein are used here. It is found that the variability of observed tropical convection generally decreases with increasing large-scale forcing, implying a transition from stochastic to more deterministic behavior with increasing forcing. Convection shows a more systematic relationship with measures related to large-scale convergence compared to measures related to energetics (e.g., CAPE). Using the observations, the parameters in the SMCM are adjusted. Then, the SMCM is forced with the time series of the observed large-scale state and the simulated convective behavior is compared to that observed. It is found that the SMCM cloud fields compare better with observations when using predictors related to convergence rather than energetics. Furthermore, the underlying framework of the SMCM is able to reproduce the observed functional dependencies of convective variability on the imposed large-scale state—an encouraging result on the road toward a novel convection parameterization approach. However, establishing sound cause-and-effect relationships between tropical convection and the large-scale environment remains problematic and warrants further research.

1. Introduction

General circulation models (GCMs) employed in climate projections are the tool of choice when quantifying the anthropogenic influence on Earth's climate, ultimately answering the question as to the degree to which humanity has an influence on global-mean surface temperature. Over the past decades, GCMs have undergone considerable development, manifested in an ever larger increase in complexity and resolution. However, uncertainty in climate sensitivity has not been substantially reduced since its ad hoc introduction by Charney et al. (1979) and major atmospheric processes are still subject to considerable uncertainties. Of these, atmospheric convection and the clouds and feedbacks associated with it are most probably the most uncertain in the latest generation of GCMs (Randall et al. 2007). This is not only true for the multimodel ensemble of the phase 3 of the Coupled Model Intercomparison Project (CMIP3; Meehl et al. 2007), but

Corresponding author address: Karsten Peters, ARC Centre of Excellence for Climate System Science, School of Mathematical Sciences, Monash University, Clayton, VIC 3800, Australia.
E-mail: karsten.peters@monash.edu

DOI: 10.1175/JAS-D-13-031.1

model parameters associated with convection are often the most sensitive in perturbed parameter ensembles (Murphy et al. 2004; Klocke et al. 2011).

Uncertainties in the representation of convection in current-generation GCMs not only lead to uncertainties in estimates of climate sensitivity, but also manifest themselves in an erroneous simulation of precipitation. Generally, GCMs are capable of capturing the overall amount of precipitation well, but the spatial distribution and variance often compare poorly to observations (e.g., Dai 2006; Pincus et al. 2008). Because of the limited spatial resolution of a GCM, atmospheric convection is of subgrid-scale nature and can thus not be explicitly resolved and must be parameterized. Since the emergence of the first convection parameterization techniques some four decades ago, the response of convective elements to a given large-scale atmospheric state has mostly been formulated as purely deterministic [see Arakawa (2004) for a review], which implicitly prevents a particular model integration from developing convective variability beyond that given by the atmospheric state at the gridpoint level.

It is just in the last decade that a possible solution to this lack of variability in parameterized subgrid-scale processes has emerged. This solution is based on representing the variability in the response of unresolved processes to the large-scale environment in a dynamically stochastic rather than in a purely deterministic manner (Palmer 2001) and has been shown to increase predictive skill of numerical weather prediction (i.e., Buizza et al. 1999).

Specifically targeted toward improving the representation of convection, Lin and Neelin (2000, 2003) introduced random perturbations to convective available potential energy (CAPE) or the heating profile of the host convective scheme and found that even such a simple approach significantly enhanced precipitation variance toward that of observations. Randomly perturbing the trigger function of the Kain–Fritsch convection scheme also proved to yield an increase in predictive skill (Bright and Mullen 2002). Teixeira and Reynolds (2008) randomly sampled convective-parameterization-relevant variables from a subgrid-scale distribution and found an increase in the spread of an ensemble prediction system and in particular a better representation of tropical convection. A similarly simple approach was taken by Tompkins and Berner (2008), who randomly sampled a subgrid-scale relative humidity distribution to perturb a convective parcel's initial humidity and/or the humidity of the entrained air during ascent. Although promising results were obtained for midlatitudes, the methodology employed did not yield improvements in tropical convection. In all the studies mentioned above, the randomly sampled deviations were assumed proportional to the mean of the perturbed variable, an assumption shown to be valid when using cloud-resolving model data as a surrogate for observations (Shutts and Palmer 2007).

Taking a step further from just modifying the input parameters for existing convective parameterization closures and cloud models, several recent studies focused on formulating more advanced stochastic schemes. Majda and Khouider (2002) introduced a stochastic parameterization of convective inhibition (CIN) based on the Ising model of statistical mechanics. It is coarse grained to obtain a Markov birth–death process, which is two-way coupled to the large-scale dynamics and which can be integrated with very little computational overhead (Khouider et al. 2003). The stochastic CIN model is used in Khouider et al. (2003) and in Majda et al. (2008) to improve the wave variability and climate in an otherwise deficient mass flux–like parameterization in the context of a simple 1.5-layer toy GCM. Plant and Craig (2008) calculated a distribution of convective plumes and then randomly sampled this distribution to obtain a plume ensemble that matches a required gridbox-mean mass flux given by a CAPE closure. Testing in a single-column model environment yielded high variability for small grid boxes, approaching the deterministic limit with increasing gridbox size. Recently, this scheme was tested in a limited-area model ensemble over central Europe and results showed a promising increase in precipitation variance (Groenemeijer and Craig 2012). Although not concentrating on deep convection, the study of Dorrestijn et al. (2013) represents a notable approach to stochastic parameterization of shallow cumulus convection. They applied a Markov chain method to sample pairs of turbulent heat and moisture fluxes obtained from large-eddy simulations (LESs) and found a good agreement in the calculated ensemble spread compared to the LES data. Following the coarse-graining ideas used in Khouider et al. (2003), Khouider et al. (2010, hereafter KBM10) designed the stochastic multicloud model (SMCM) based on a birth–death process to represent tropical convection. The SMCM calculates the evolution of a cloud population consisting of three cloud types associated with tropical convection (congestus, deep convection, stratiform) constrained by the large-scale atmospheric state. The state of the cloud ensemble at any given time and large-scale forcing is represented by area fractions per cloud type on a subgrid-scale lattice. The SMCM was shown to reasonably simulate tropical convection and associated wave features when coupled to a simple two-layer atmospheric model [KBM10; Frenkel et al. 2012 (hereafter FMK12), 2013].

As the vast majority of today's GCM convection schemes are mass flux schemes, the cloud area fractions simulated by the SMCM could prove valuable for introducing a stochastic component to such schemes. Then

at least one part (area) of the cloud-base mass flux would yield a stochastic component, leaving the other part (updraft velocity) to be assigned in another suitable fashion.

It is the aim of this study to provide an assessment of whether the underlying framework of the SMCM is suitable to reproduce observed convective behavior. In doing so, we analyze observed convective behavior and subsequently adjust the model parameters, which have so far been based on sensible empirical assumptions (KBM10), to match the observed mean response of convection to the large-scale state. We then use the resulting adjusted model to test whether its underlying framework is suitable to reproduce the statistical mean behavior of observed convection, the positive outcome of which would render the SMCM a useful tool for convection parameterization.

The observational dataset that we use in this study is described in Davies et al. (2013) and represents a long-term, large-scale dataset for three consecutive wet seasons over Darwin, Australia, complemented by an identically derived but shorter dataset representative for Kwajalein. The Darwin dataset has been shown to contain valuable information for characterizing relationships between atmospheric convection and the large-scale state, with one of the most notable findings being that the relationships between convection and CAPE or vertical velocity are shown to be entirely stochastic or quasi deterministic, respectively (Davies et al. 2013).

We introduce the basics of the SMCM, the observational dataset, and the observation-derived forcing for the SMCM in section 2 and present the statistical relationships of observed convection to large-scale variables in section 3. We then adjust the parameters of the SMCM, force it with the observed large-scale state, and analyze the statistics of the modeled convection as well as the stochasticity of the model solution in section 4. Section 5 gives a summary, conclusions, and a short outlook.

2. Prerequisites: The model and the observations

In this study, we utilize the recently introduced SMCM (KBM10) in conjunction with a large-scale observational dataset representative of a tropical location. In a nutshell, we investigate the degree to which the mathematical framework of the SMCM is suitable to reproduce the behavior of observed tropical convection, a necessary step toward a possible future usage in GCMs. In the following, we briefly introduce the SMCM (section 2a) and the observational dataset (section 2b).

a. The SMCM: A short introduction

Given the temporal evolution of a large-scale atmospheric state representative of a tropical location, the SMCM simulates the evolution of an ensemble of three cloud types associated with tropical convection on a lattice containing $n \times n$ sites. The considered cloud types are congestus and deep convective as well as stratiform clouds (shallow convection is not considered) and the large-scale atmospheric state is given by two variables: one representing a proxy for convective propensity and the other representing a proxy for midtropospheric dryness (cf. section 2c). In the SMCM, the evolution of the cloud ensemble is represented by a coarse-grained birth–death process. This process is evolved in time by means of an acceptance–rejection Markov chain Monte Carlo method based on Gillespie's exact algorithm (Gillespie 1975; see KBM10 for details of the implementation). Each individual lattice site can take one of four states: clear sky, congestus cloud, deep convective cloud, or stratiform cloud. The total size of this lattice, say 20×20 sites, is assumed as being representative of a GCM grid box, but there is no explicit spatial scale associated with either the individual lattice sites or the total lattice. There is also no spatial coherence between individual lattice sites (i.e., the temporal evolution at one site is completely independent of that of its neighbors). However, local interactions between lattice sites can be easily incorporated, provided the strength and nature of these interactions are understood (Khouider 2013).

The evolution of this birth–death process is determined by a set of equations that define transition rates from one of the four states (see above) to another. Individual transition rates can, but need not, be dependent on the given large-scale state and their formulation is mainly inspired by physical intuition and based on specific rules; for example, a deep convective cloud is not allowed to form from a stratiform cloud (see KBM10 for details). The individual transition rates are associated with time scales assumed to be representative for a specific transition. These transition time scales have been chosen in an ad hoc but physically meaningful manner and represent the only parameters that can be used to tune the SMCM in its current formulation. KBM10 presented two sets of transition time scales, both of which are based on physical intuition gained from observations and modeling studies of tropical convection and should be considered as rough estimates. Recently, FMK12 found a third set of transition rates that improves the intermittency of simulated convection compared to the results of KBM10. In this study, we use observations to take a closer look at these previously made choices of transition time scales.

So far, the SMCM has not been used in combination with observations but was coupled to a simple two-layer atmospheric model capable of capturing the main

characteristics of tropical convection and associated wave features (Khouider and Majda 2006, 2008a,b; KBM10). There, simple formulations of precipitation formation and the associated heating profiles accounted for the feedback to the dynamics. Recently, FMK12 used the SMCM to explore its capabilities in the context of improving GCM convection parameterizations by using the abovementioned two-layer model to flows about an equatorial ring. They found that using the SMCM increases the variability of tropical convection compared to a deterministic convection parameterization and that the SMCM is able to produce a realistic Walker cell circulation when forced with a longitudinal SST gradient.

One may argue that the capability of the SMCM to produce sensible results is given by its design principles (e.g., prescribing certain transition time scales, assuming tropical convection to be dependent on two predictors only, or coupling it to a simple two-layer atmospheric model). In fact, a comparison of the SMCM-simulated cloud area fractions to observational data is still outstanding. It is the aim of this study to use the SMCM in a diagnostic fashion by forcing it with an observed large-scale state to investigate the feasibility of using its underlying stochastic concept for convective parameterizations in full GCMs.

b. *Two datasets of observed large-scale atmospheric state over tropical areas*

We utilize two datasets comprising various quantities describing the large-scale atmospheric state over a tropical location for the purpose of this study. One dataset covers an approximately $190 \times 190\,\mathrm{km}^2$ pentagon-shaped area centered over Darwin, Australia (Davies et al. 2013), investigated during the Tropical Warm Pool-International Cloud Experiment (TWP-ICE; May et al. 2008). The size of the area is chosen to approximately represent that of a typical GCM grid box and the gridbox-mean values of atmospheric variables are computed using a variational analysis after Zhang and Lin (1997). This variational analysis is applied to a large part of three consecutive wet seasons (2004/05, 2005/06, 2006/07). Over northern Australia, the wet season is defined as the time period between September of one year and April of the following year. The dataset and its documentation can be obtained via the Atmospheric Radiation Measurement (ARM) Climate Research Facility's website (http://www.arm.gov/data/pi/46) and we use all available data for the analysis presented here. Atmospheric variables are available every 6 h. Information on clouds and precipitation is retrieved from radar observations by the C-band polarimetric (CPOL) research radar (Keenan et al. 1998) located at Gunn Point and operated by the Australian Bureau of Meteorology. From those data, rain area fractions attributable to either stratiform or convective precipitation are determined after Steiner et al. (1995) and used as a proxy for stratiform and convective cloud fractions (Kumar et al. 2013b). Convective clouds are separated into congestus and deep convection according to cloud-top height (CTH): convective clouds having CTHs of less than 7 km are classified as congestus whereas clouds having higher CTHs are classified as deep convective clouds (Kumar et al. 2013a). The dataset encompasses the period of TWP-ICE (May et al. 2008), which took place in the same area during January and February 2006. The collected data of meteorological regimes encountered during TWP-ICE have already proven to be very valuable for the evaluation of GCM convective parameterizations (e.g., Lin et al. 2012).

The second dataset represents the large-scale atmospheric state over Kwajalein and is obtained by applying the same variational analysis as is used for the Darwin dataset. Convective- and stratiform-precipitation area fractions are also calculated according to Steiner et al. (1995); however, congestus area fractions are not available because the radar data available to us only consist of horizontal 2D scans. The Kwajalein dataset covers a shorter time period (May 2008–January 2009) and was produced to match the observation intensive period of the Year of Tropical Convection (YOTC; Waliser and Moncrieff 2007) project. For better comparability, the Kwajalein data are derived for an area identical to the pentagon-shaped one over Darwin.

We use both datasets in this study to show that the functional dependency of tropical convection on a given large-scale atmospheric state is similar for both locations although they are subject to distinctly different boundary conditions (e.g., land–sea distribution or monsoonal forcing).

To illustrate the multitude of meteorological regimes found in the datasets, we show the time series of selected atmospheric parameters for the time period of 10 November 2005–18 April 2006 over Darwin in Fig. 1. It is evident that apart from the variability during the TWP-ICE period (19 January–28 February 2006; May et al. 2008), the snapshot shown in Fig. 1 alone contains a number of evident meteorological regime changes that result in distinctly different cloud populations. Characterizing the middle-troposphere level, the time series of relative humidity qualitatively exemplifies "wet" periods around 20 January or 1 April 2006 (among others) and "dry" periods around 25 November 2005 or 1 March 2006 (among others) of the time series. As shown in the plot of derived convective and stratiform cloud fractions, the abovementioned wet and dry periods are each associated with specific cloud regimes: the wet

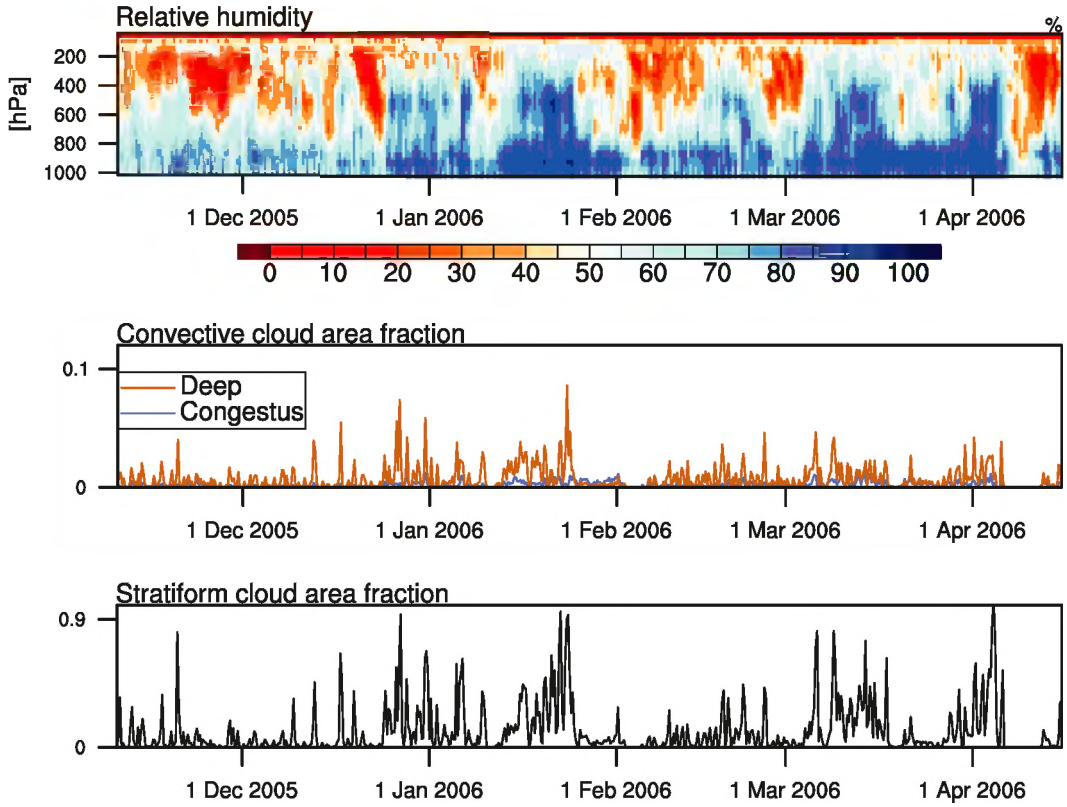

FIG. 1. Subset of the dataset comprising the atmospheric large-scale state over Darwin as used in this study. Time series covering the time period from 10 Nov 2005 to 15 Apr 2006 showing (top) vertically resolved relative humidity as well as (middle) convective and (bottom) stratiform cloud fractions obtained from a scanning rain radar situated at Darwin, Australia. See text for details.

periods are generally associated with higher cloud fractions compared to the dry periods. Stratiform clouds exhibit the highest cloud area fractions, with deep convective cloud fraction being about an order of magnitude less and congestus cloud fraction being again an order of magnitude less than that. It must be noted that the derived cloud area fractions are representative for precipitating clouds only. However, this does not present a serious issue; that is, fractions of tropical congestus, deep convective, or stratiform clouds derived from the scanning rain radar compare very well to those derived from a vertically pointing cloud radar (Kumar et al. 2013a).

It should be mentioned at this point that the observational data to which we are comparing the SMCM-simulated cloud fractions are also subject to uncertainties and give room for interpretation. The most prominent uncertainty, of course, is the estimation of rain rates from radar echoes, which is not too straightforward itself, and the subsequent assumption that the area of a particular type of rainfall [derived after Steiner et al. (1995)] is equal to the cloud fraction of that particular cloud type. Therefore, this analysis is limited to precipitating clouds only. Also, land surface characteristics of the geographical area covered by the large-scale observational dataset used in this study are far from homogeneous. The CPOL radar at Gunn Point covers both water and land surfaces, with some of the land surface areas being subject to a pronounced convective diurnal cycle that results in some of the deepest convection on the planet (Keenan et al. 1990; Crook 2001). As these events are locally driven, environmental conditions leading to their initiation cannot be represented in the observational dataset. This uncertainty in environmental conditions obviously does not apply to the Kwajalein data.

c. *Deriving model forcing parameters from the observations*

The evolution of the cloud ensemble as simulated by the SMCM with respect to the large-scale atmospheric state is designed to be dependent on two predictors. One parameter is used as a proxy for the environment's potential to develop and sustain convection C and the other is used as a proxy for midtropospheric dryness D. Here, the underlying assumption is that convection is

initiated (sustained) and hindered (depleted) by high values of C (D). Because we aim to use the SMCM in a diagnostic manner by forcing it with an observed large-scale atmospheric state, we have to derive C and D from the available observational data. This requires us to adapt the formulas for calculating C and D as given in KBM10 as these are defined to be used for a large-scale state given by the simple two-layer model (Majda and Shefter 2001; Khouider and Majda 2006).

As mentioned above, C and D are used as proxies for the convective potential of the tropospheric column and midtropospheric dryness, respectively. In the original SMCM these quantities are scaled to vary roughly between 0 and 2. For the evaluation of the SMCM, we derive a total of five (instead of just two) forcing predictors. We proceed in this way because there may exist a multitude of possible predictor constellations for adequately describing the dependency of tropical convection on the large-scale atmospheric state.

1) C—A PROXY VALUE FOR CONVECTIVE PROPENSITY

In the original formulation given in KBM10, C is given by the scaled CAPE (calculated for a parcel lifted from 990 hPa; C_C in the following). CAPE corresponding to the time series shown in Fig. 1 yields values in the range 0–1700 J kg^{-1}; we therefore scale the CAPE values by 1000 J kg^{-1} to achieve the desired range of $C_C \in [0; 2]$.

As it has been argued before that CAPE alone may not be a good proxy for characterizing the occurrence of tropical convection (e.g., Mapes and Houze 1992; Sherwood 1999; Sobel et al. 2004; Fletcher and Bretherton 2010), we also define additional versions of C, represented by scaled values of either the ratio of low-level CAPE (LCAPE; i.e., CAPE integrated only to the freezing level), to total CAPE (C_{rC}), or large-scale vertical velocity at 500 hPa ω_{500} (C_ω):

$$C_{\mathrm{rC}} = 2\left(\frac{\mathrm{LCAPE}}{\mathrm{CAPE}}\right),$$

$$C_\omega = -\left(\frac{1}{10}\,\mathrm{hPa}^{-1}\,\mathrm{h}\right)\omega_{500}, \quad \omega_{500} < 0. \qquad (1)$$

The choice to investigate the proxies C_C and C_ω is relatively intuitive and straightforward, whereas the choice of C_{rC} warrants explanation. KBM10 found that assuming that congestus activity is positively related to LCAPE (derived from a two-layer atmospheric model) rather than total CAPE improves the SMCM variability. However, our observations show that LCAPE alone is roughly constant throughout the whole observational period and it is only the ratio to total CAPE that resembles some relationship with observed convection. For illustrative purposes, we show the time series of C for the subset of the data shown in Fig. 1 in the top two panels in Fig. 2.

Recalling the preceding short analysis of wet and dry periods (section 2b), the pattern of C_C (Fig. 2, top) reveals no evident correlation to these periods. The relatively high values of C_C during the first 40 days of the time series should yield intense convective activity, but the observed cloud fractions do not support this. However, the observed low convective activity during those roughly 40 days could be explained by a relatively dry middle troposphere as indicated by the time series of D_{RH}, which may hinder the development of deep convection (e.g., Redelsperger et al. 2002). Furthermore, the wetter periods are characterized by low C_C values throughout. However, stratiform cloud fraction, most probably originating from deep convection, is notably high during these periods. This supports a separate analysis of the present dataset, which indeed suggests that, in the area of interest, convective precipitation shows no significant correlation with CAPE (Davies et al. 2013). In fact, CAPE has been shown to be approximately anticorrelated with or be entirely unrelated to precipitation for regions in relatively close proximity to the areas covered by our dataset (Mapes and Houze 1992; McBride and Frank 1999; Sobel et al. 2004).

When convective activity is high, C_{rC} exhibits large values (cf. Figs. 1 and 2), implying that in situations of intense convection the total CAPE is dominated by the contribution coming from below the freezing level. Because low-level CAPE itself does not vary too much, it is the lack of contributions to total CAPE coming from above the freezing level that makes up for high values of C_{rC}, consistent with the findings of McBride and Frank (1999), who concluded that high values of CAPE are dominated by contributions from above 600 hPa. High values of C_{rC} thus imply that during periods of intense convection, such as those shown in Fig. 1, the specific heating profile of stratiform precipitation (i.e., latent heating of the upper troposphere and evaporative cooling of the lower troposphere; e.g., Houze 1997) serves to adjust the lapse rate toward the moist adiabat. However, it is the occurrence of convection itself that may enforce high values of C_{rC}, resulting in possible ambiguities when attempting to use it as a predictor for convection.

From a dynamical perspective, it is well known that large-scale vertical ascent, and thus moisture convergence, is associated with and facilitates the development of deep convection [cf. the recent study of Hohenegger and Stevens (2013)]. Like the convective area fractions shown in Fig. 1, the time series of C_ω also appears highly intermittent and seems to very closely follow the former. This is especially true for the first roughly 40 days of the

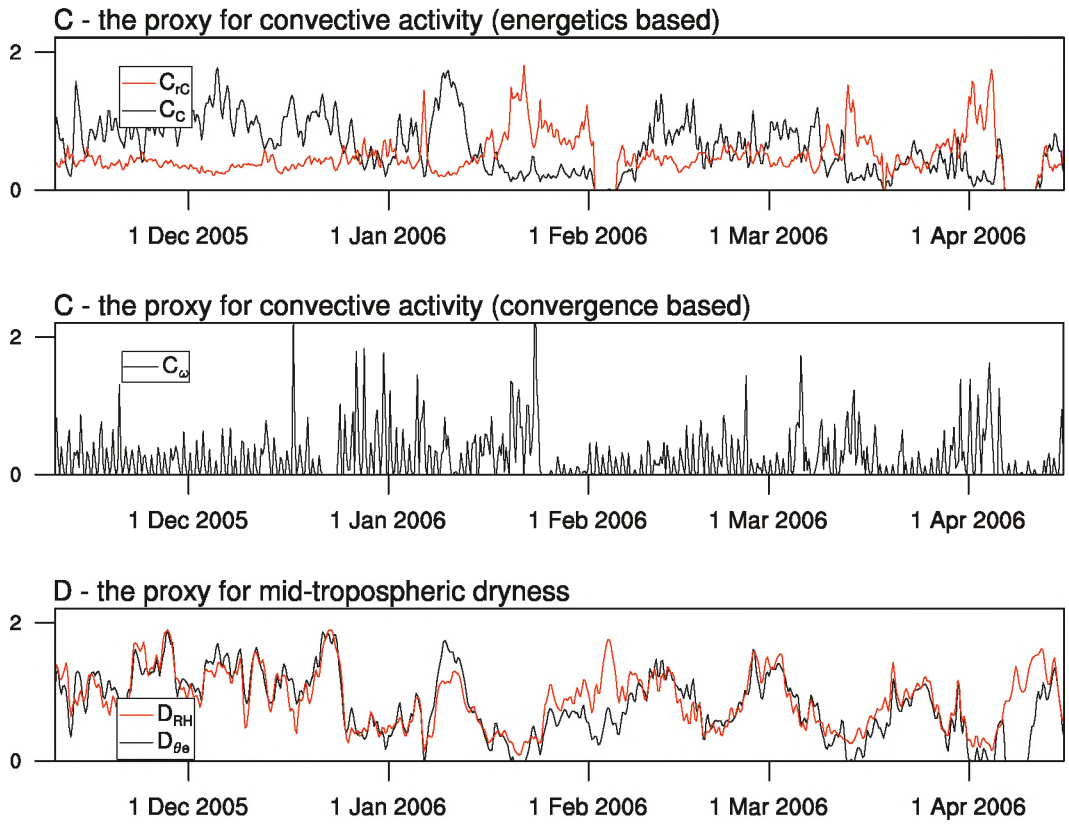

FIG. 2. Time series of model forcing predictors obtained from the large-scale state shown in Fig. 1. (top), (middle) Values for C (i.e., the proxy for convective propensity). (bottom) Values for D (i.e., the proxy for midtropospheric dryness). See text for calculation of the predictors.

time series in which the observed stratiform and convective cloud fractions are relatively low. During that particular period, C_ω shows relatively small values with higher ones occurring sparsely, indicating a weakly but somewhat constantly forced convective regime. However, ambiguities in establishing sound cause-and-effect relationships between C and convection are apparent for C_ω, which is directly related to large-scale convergence, which can in turn be considered as both a cause and consequence of convective heating. In fact, discussion of these ambiguities is one of the most persistent issues in the meteorological community. Ambiguities may also arise from the method to derive C_ω itself. Vertical pressure velocity ω is the key parameter obtained from the variational analysis used to derive the large-scale atmospheric state we use here. Since the variational analysis itself is constrained by total areal rainfall, ω is somewhat tuned to match observed rain rates. However, because we use area fractions, and not rain rates, of convective and stratiform rain in our analysis, the causal link to the data processing in the variational analysis is weak.

2) D—A PROXY FOR MIDTROPOSPHERIC DRYNESS

In the original formulation of the SMCM, the proxy for midtropospheric dryness D_{θ_e} is given by

$$D_{\theta_e} = \frac{\theta_{e,\mathrm{BL}} - \theta_{e,m}}{15\,\mathrm{K}}, \tag{2}$$

where $\theta_{e,\mathrm{BL}}$ is the equivalent potential temperature in the boundary layer, $\theta_{e,m}$ is the equivalent potential temperature in the midtroposphere, and 15 K is a climatological-mean scaling factor (Khouider and Majda 2006). Here, the underlying assumption is that the difference between the equivalent temperatures as given in Eq. (2) is large when the middle troposphere is dry compared to the boundary layer. For the calculation of D_{θ_e} from the observed large-scale state, we define $\theta_{e,\mathrm{BL}}$ and $\theta_{e,m}$ as the equivalent potential temperatures at 1000 and 500 hPa, respectively. To yield the desired range of $D_{\theta_e} \in [0; 2]$, we use a scaling factor of 10 K instead of 15 K.

Additional to the original formulation of D, we introduce a simpler proxy for representing the midtropospheric

dryness by use of the relative humidity at 500 hPa. Then, D_{RH} is given by

$$D_{\mathrm{RH}} = 2 \times (1 - \mathrm{RH}_{500}), \tag{3}$$

with $\mathrm{RH}_{500} \in [0; 1]$. The resulting time series of D calculated with both methods are shown in Fig. 2 (bottom).

Unlike the time series of C, the ones for D show a very high level of agreement. It is just for two short time periods when the values of D_{θ_e} and D_{RH} disagree significantly, namely around 5 February and 10 April 2006 of the time series displayed in Figs. 1 and 2. These periods are relatively dry compared to the rest of the time series, with low values of relative humidity reaching down into the boundary layer. For these two cases, relatively high values of D_{RH} indicate a dry case, whereas the low (or even negative) values of D_{θ_e} indicate a rather wet case. This is because low values of θ_e occur throughout the tropospheric column down to the surface, thereby not yielding the anticipated large difference between θ_e at 1000 and 500 hPa. Defining D_{θ_e} by Eq. (2) therefore poses a limitation for running the SMCM when using observational data. As D_{RH} agrees very well with D_{θ_e} throughout the rest of the time series, we will use D_{RH} for all further analyses presented in this study. Also, KBM10 used D_{θ_e} simply because it is more convenient in the context of the two-layer model.

3. The observed mean convective state at Darwin and Kwajalein

Before assessing whether the mathematical framework of the SMCM is suitable for reproducing observed convective behavior of tropical convection, we first analyze the observations laid out in section 2b in a manner suitable for direct comparison with SMCM output. Given the specific values of the forcing parameters C and D (cf. section 2c), the birth–death process used in the SMCM yields stationary cloud fraction distributions of every cloud type. Hence, it is possible to calculate a 2D histogram of the stationary cloud fraction as a function of C and D. Examples of such equilibrium cloud fraction distributions for a given set of transition time scales are given in KBM10. Here, we therefore calculate joint histograms of observed convective and stratiform cloud fractions in the parameter space of observed values of C and D to enable a straightforward comparison between observed and modeled convective behavior.

We show such joint histograms of mean observed cloud fractions for three sets of forcing parameters, as well as their relative standard deviations and number of measurements, in Figs. 3–5, for Darwin and Kwajalein. In the three sets of forcing parameters, the midtropospheric dryness parameter is represented by D_{RH} and the convection parameter C is represented by C_C, C_{rC}, or C_ω. Because of the observational limitations mentioned above, we only analyze deep convective and stratiform cloud fractions and neglect congestus clouds in the context of this study.

We only discuss the results for Darwin in detail. Generally, the data for Kwajalein show the same relationships as for Darwin, but with less frequent high values of the C parameter and generally smaller stratiform cloud fractions. The important finding to keep in mind is that convective and stratiform cloud area fractions show very similar behavior at both locations given a particular large-scale atmospheric state, justifying using the observations from both locations together to investigate cloud fractions simulated by the SMCM. These results are also not impaired by the inconsistent treatment of congestus cloud area fractions between the two regions (i.e., excluding such clouds for Darwin observations and necessarily including them for Kwajalein observations).

When we stratify the observational data using C_C as indicator for convective propensity (cf. Fig. 3), we obtain maximum area fractions for both cloud types for some of the smallest values of C_C and D_{RH}, indicating relatively high convective activity for small values of CAPE and a moist middle troposphere. Most observations fall into a range spanning the lower half of both parameter ranges, also resulting in the lowest cloud area fraction variability (i.e., relative standard deviation) in that range. Similar results are presented in McBride and Frank (1999), who found an inverse relationship between CAPE and precipitation when analyzing data obtained during active and break monsoon periods for a location in the Gulf of Carpentaria.

When stratifying the observations according to either one of the other two choices for C (cf. Figs. 4 and 5), we obtain a completely different functional dependency of convective and stratiform cloud fractions on C and D. Using C_{rC} and C_ω as choices for C leads to

1) maximum values for both cloud area fractions for highest values of C,
2) high and low cloud area fraction variability for low and high values of C respectively,
3) a sharp increase in cloud area fractions above a certain value of C and low values of D, and
4) most observations for low values of C spanning a wide range of D_{RH} values.

The results give valuable insight into tropical convective behavior. For weak forcing of convective activity (i.e., small values of C), average cloud area fractions are small but exhibit large variability, indicating a somewhat stochastic behavior. This is particularly interesting because a large part of the observations yields weak forcing,

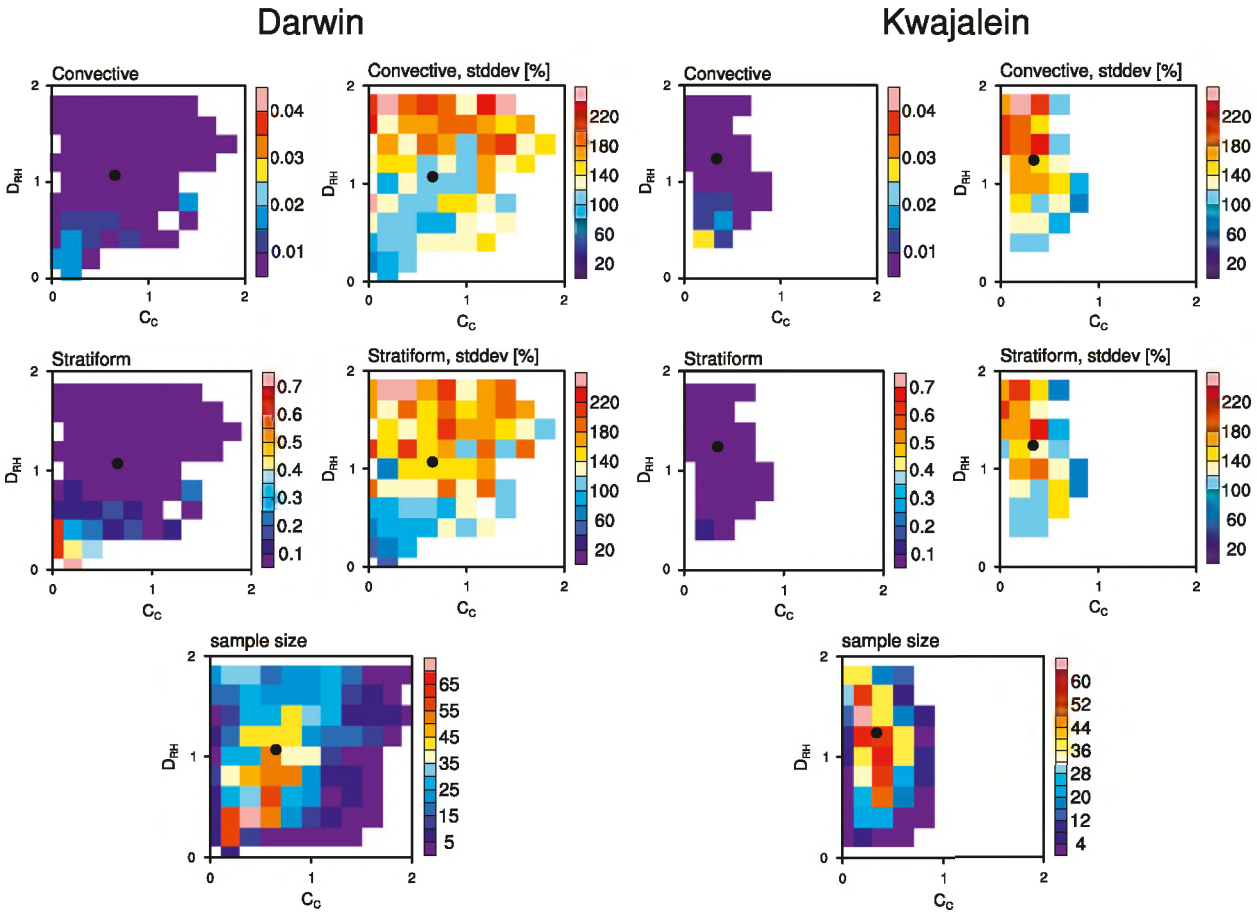

FIG. 3. Joint histogram of observed cloud area fractions and relative standard deviations as function of large-scale variables C_C and D_{RH} at the (left) Darwin and (right) Kwajalein sites: (top) deep convective clouds, (middle) stratiform clouds, and (bottom) sample size per bin. Only pixels having more than five observations are shown. The black markers denote the mean values of C_C and D_{RH}.

which would normally act to reduce sample variability. The stronger the forcing of convective activity gets, the fewer observations are registered per bin, suggestive of an expected increase in sample variability. However, cloud area fraction variability is lowest for strong forcing of convection, suggesting a more and more deterministic behavior of convection with increasing forcing, in line with other results derived from the same dataset (Davies et al. 2013). Physically, this implies that as forcing is weak, convection occurs more randomly in the domain, inducing large-scale convergence itself, which may lead to more large-scale organization and greater area fraction of convection. Examples for this behavior could be forcing of convection by local heterogeneities in land surface properties (and thus surface fluxes) or effects of land–sea breezes. This could in fact lead to a positive feedback loop on various scales. However, assessing the effect that this kind of feedback behavior would have on the vertical ascent on the scales considered here (i.e., $190 \times 190\,\mathrm{km}^2$) is beyond the scope of our study.

Our results, however, do not support the idea that the stochastic component of unresolved subgrid-scale processes scales linearly with their mean response as put forward in earlier studies (e.g., Buizza et al. 1999; Shutts and Palmer 2007). The sharp increase in cloud area fraction above a certain value of C, accompanied by low values of D, is consistent with the "threshold behavior" of convection as laid out in, for instance, Peters and Neelin (2006). Furthermore, the histograms we show in Figs. 4 and 5 indicate that at least for these two choices of C, deep convective as well as stratiform area fractions are anticorrelated with dryness at midlevels, broadly consistent with earlier findings from observational studies (Redelsperger et al. 2002; Derbyshire et al. 2004; Takemi et al. 2004; Takayabu et al. 2010).

We also note that regimes exhibiting both a strong forcing of convection and a dry middle troposphere basically do not exist at the locations considered in this study. This may be obvious, but such a result is not apparent from Fig. 3 where there still exist a quite large

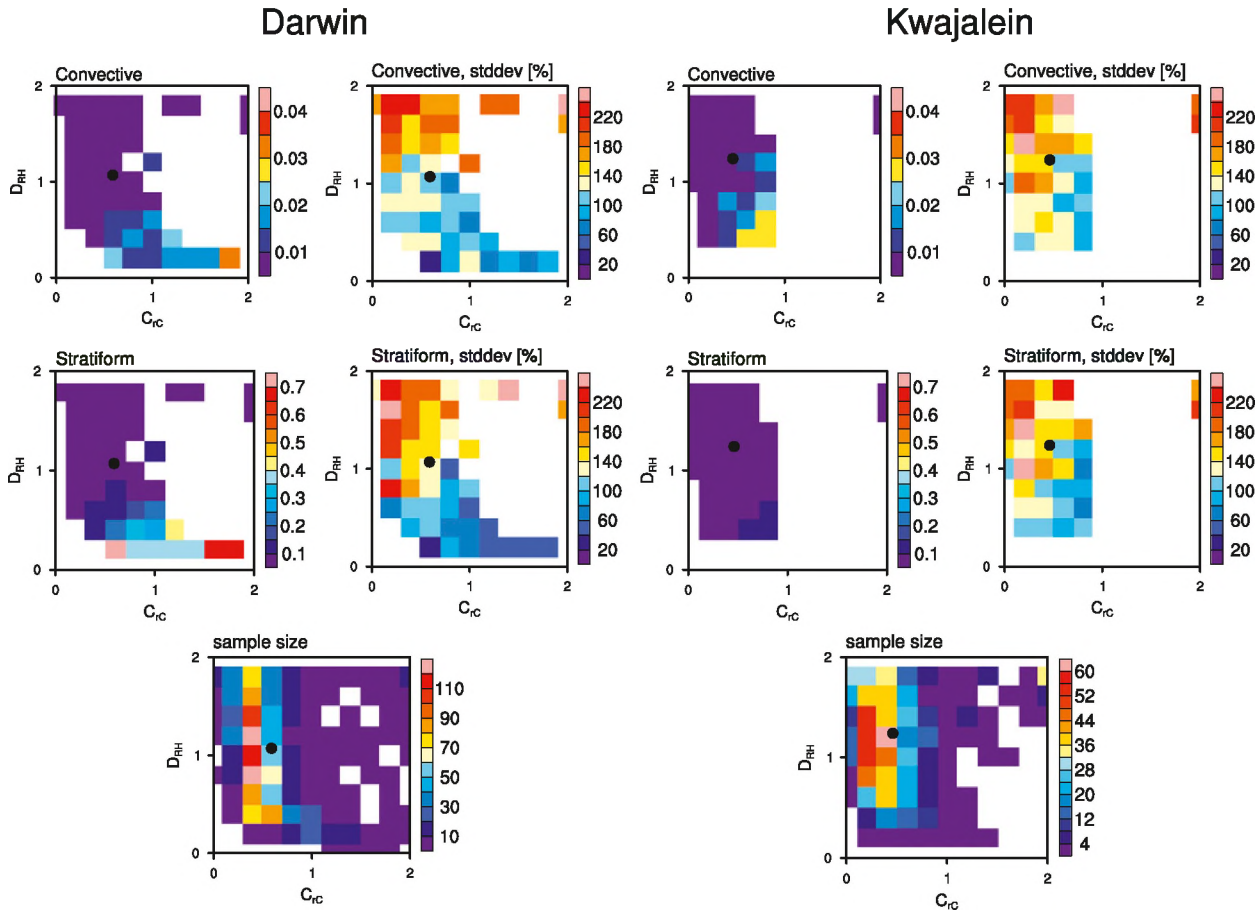

FIG. 4. As in Fig. 3, but for C_{rC} and D_{RH}. The black markers denote the mean values of C_{rC} and D_{RH}.

number of measurements yielding a combination of a dry middle troposphere and high values of C_C.

Histograms similar to those shown in Figs. 3–5 could in principle also be derived from GCM output. Because mass flux–based convective parameterization closures currently employed in state-of-the-art GCMs do not normally predict a parameter that directly corresponds to the deep convective area fraction that we use here, one could, for example, analyze the functional dependence of the total mass flux itself on large-scale parameters. Such an analysis, however, is beyond the scope of this study and will be left for future work.

4. Reproducing observed convective behavior using the SMCM

a. *Adjusting the model parameters*

The equilibrium cloud fractions of the multistate Markov chain used in the SMCM are calculated by analytically determining its stationary equilibrium distribution (cf. KBM10 for details). The purpose of this section is thus not to evolve the SMCM in time but to arrive at analytically exact equilibrium cloud fractions that allow for a tuning of the model to the observations presented in section 3. By the ergodic theorem of Markov chains, the equilibrium measure is unique and coincides with long-time-average area fractions of the three cloud types for each given set of model parameters (i.e., the transition time scales and the large-scale forcing). We show results from evolving tuned versions of the SMCM in time in section 4b. Here, the analytically derived equilibrium distribution is represented by area fractions for each of the four allowed states of the Markov chain (i.e., clear sky, congestus, deep convection, or stratiform clouds). The sum of all four area fractions for each pair of discrete C and D values is 1 and the distribution of area fractions among the four states can be adjusted by manipulating the transition time scales associated with the transition from one state to another.

In previous publications, the transition time scales used in the SMCM either were chosen in an ad hoc but physically meaningful manner (KBM10) or were picked to improve the intermittency of the simulated convection

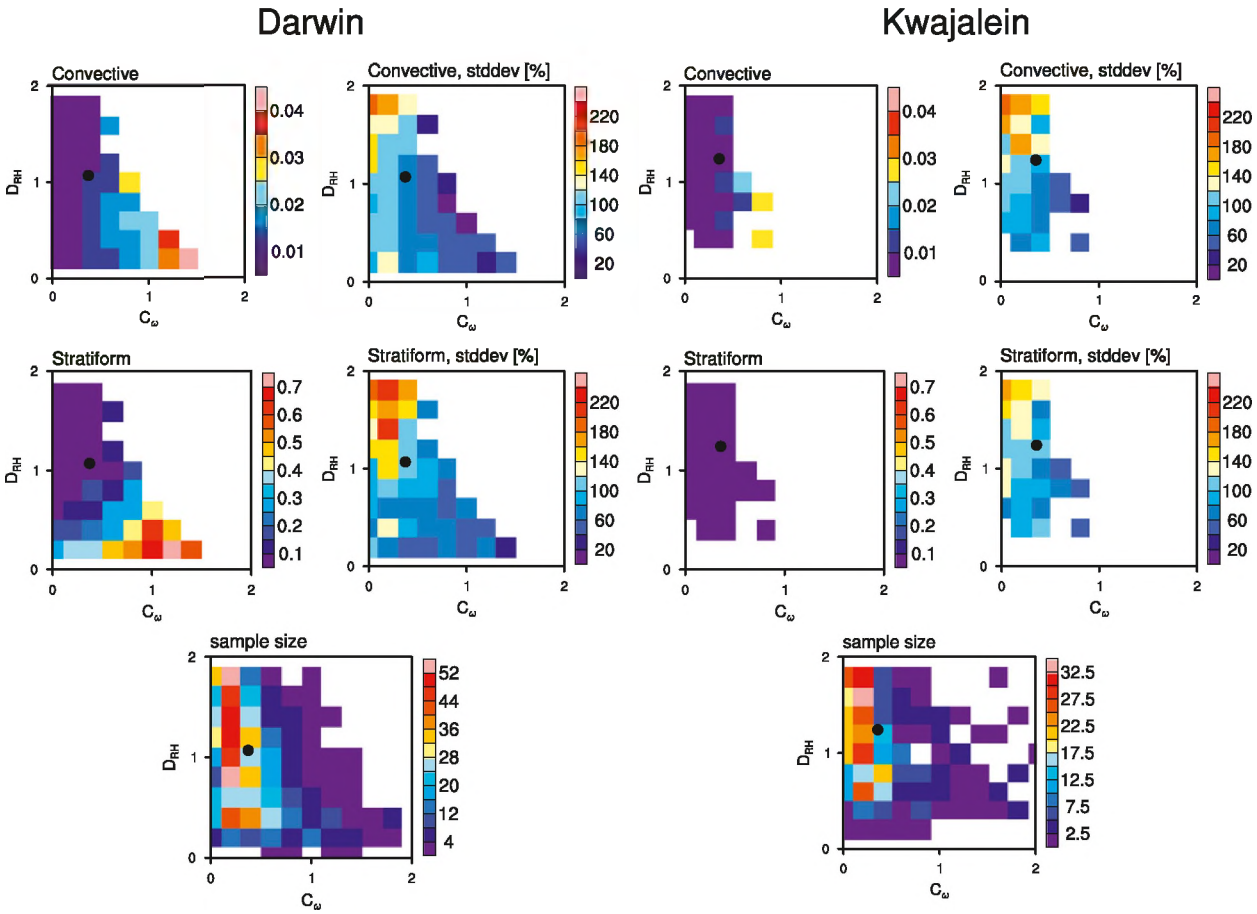

FIG. 5. As in Fig. 3, but for C_ω and D_{RH}. The black markers denote the mean values of C_ω and D_{RH}.

in idealized experiments (FMK12). Here we use observations to gauge the applicability of the chosen time scales to represent observed convective behavior. For reference purposes, we show the joint histograms of the analytically derived equilibrium deep convective area fractions for the transition time scales introduced in KBM10 and FMK12 (cf. Table 1) in Fig. 6. These joint histograms clearly indicate that the previously used transition time scales are not suited for reproducing the statistics of observed convection laid out in section 3 for several reasons. First, the transition time scales used in case 1 of KBM10 and in FMK12 yield equilibrium deep convective area fractions about an order of magnitude larger than those observed. Second, the transition time scales used in case 2 of KBM10 result in a deep convective area distribution unsuitable for reproducing observed behavior.

To obtain a model that is most suitable for reproducing the observed convective behavior, we systematically adjust the transition time scales until we arrive at a close visual match between the analytical equilibrium solution of the SMCM and the observed mean deep convective cloud fractions for each convective proxy (C_C, C_{rC}, C_ω) for Darwin shown in Figs. 3–5 (we only use data for Darwin here to test the robustness of the adjusted transition time scales by applying it to the Kwajalein data in the next section). This close match should ideally agree to the general cloud fraction distribution in C–D space in both magnitude and shape. Additionally, the equilibrium area fraction calculated for the mean observed C and D values (black dots in Figs. 3–5) should also match closely. The second requirement achieves a tuning of the model to the "mean observed climate," thus yielding an optimal representation of observed tropical convective cloud distribution, given that the cloud-type relationships imposed in the SMCM correspond to those in nature. We find that it proves difficult to adequately satisfy both conditions, leading to a trade-off of getting either the mean climate or the maxima right. In general, we focus on arriving at the correct mean climate cloud fractions as this is of higher relevance regarding a possible future implementation into GCMs. The final "best fit" transition time scales for

TABLE 1. Transition time scales (h) as used in the SMCM. The three leftmost columns contain the transition time scales introduced in previous studies (KBM10, FMK12), yielding the equilibrium deep convective area fraction distributions in Fig. 6. The three rightmost columns contain the visually derived "best fitting" transition time scales for each of the three convection proxies leading to the modeled equilibrium cloud fractions in Fig. 7 at Darwin.

	KBM10			This study		
Process	Case 1	Case 2	FMK12	C_C	C_{rC}	C_ω
Formation of congestus (τ_{01})	1	3	1	1	1	1
Decay of congestus (τ_{10})	5	2	1	1	1.2	1.2
Conversion of congestus to deep (τ_{12})	1	2	1	3	1.2	1.2
Formation of deep (τ_{02})	2	5	3	4	2.2	2.2
Conversion of deep to stratiform (τ_{23})	3	0.5	3	0.13	0.16	0.16
Decay of deep (τ_{20})	5	5	3	5	2.2	2.4
Decay of stratiform (τ_{30})	5	24	5	5	4	4

each convective proxy C are listed in Table 1 and a comparison of modeled equilibrium and observed mean deep convective area fractions as $f(C, D)$ is displayed in Fig. 7. Given the number of transition time scales (seven), we acknowledge that our approach toward tuning the SMCM appears simple and ad hoc and that there may be more sophisticated and quantitative methods. However, we are confident about the time scales we arrive at, as these do represent the visually closest match possible and any deviations from the chosen sets lead to substantial deterioration of the resulting equilibrium cloud fraction distributions shown in Figs. 3–5.

As expected from the observed mean cloud fractions as $f(C, D)$, we find that matching the SMCM equilibrium cloud fractions to the observed cloud fractions stratified by C_C results in starkly different time scales compared to the other two convection proxies (Table 1). However, all three sets of best-fit transition time scales preserve an important constraint laid out in KBM10, namely that cloud decay acts on identical or longer time scales than cloud formation. It must be kept in mind, however, that these best-fit time scales were found by visually matching the joint histograms of modeled and observed area fractions.

The joint histograms displayed in Fig. 7 indicate that each of the three analytical equilibrium deep convective area distributions corresponding to the best-fit transition time scales in Table 1 has some difficulty in reproducing certain aspects of the corresponding observations at Darwin. For every version of C, the model overestimates deep convective area fraction for almost the entire range of considered combinations of C and D.

This overestimation is highest when using C_{rC} to stratify the observations; however, the overall functional relationship is captured (cf. Fig. 4). Using observations stratified by C_C to adjust the transition time scales yields higher modeled area fractions at nearly every considered C–D pair, with the degree of overestimation

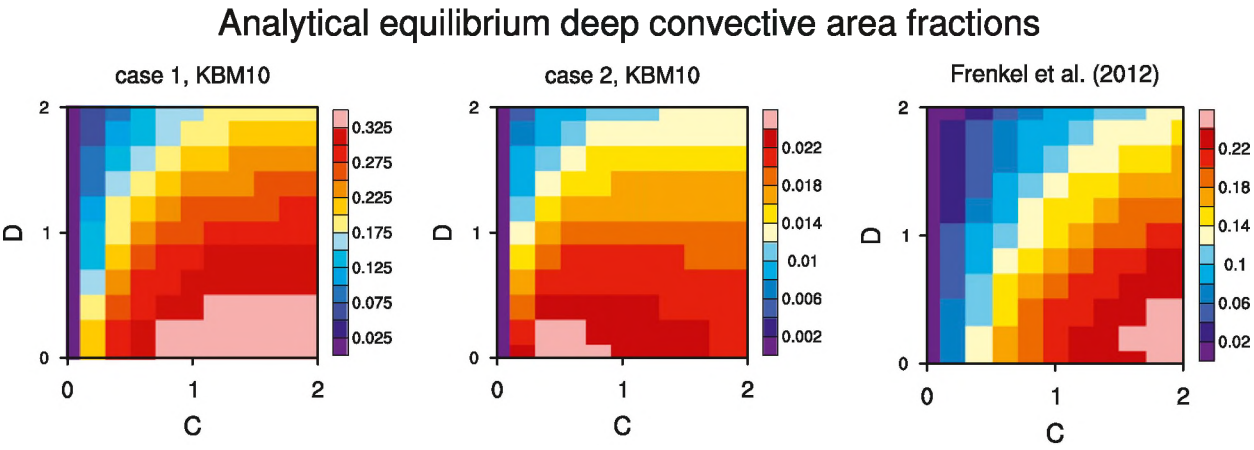

FIG. 6. Analytical equilibrium deep convective area fraction of the SMCM's birth–death process given the two sets of transition time scales introduced in KBM10 and FMK12 (Table 1): (left),(middle) case 1 and 2 time scales of KBM10, respectively, and (right) time scales used in FMK12. For the two cases of KBM10, the transition from deep convective to stratiform area depends on C. See text and KBM10 for details regarding the calculation of equilibrium area fractions.

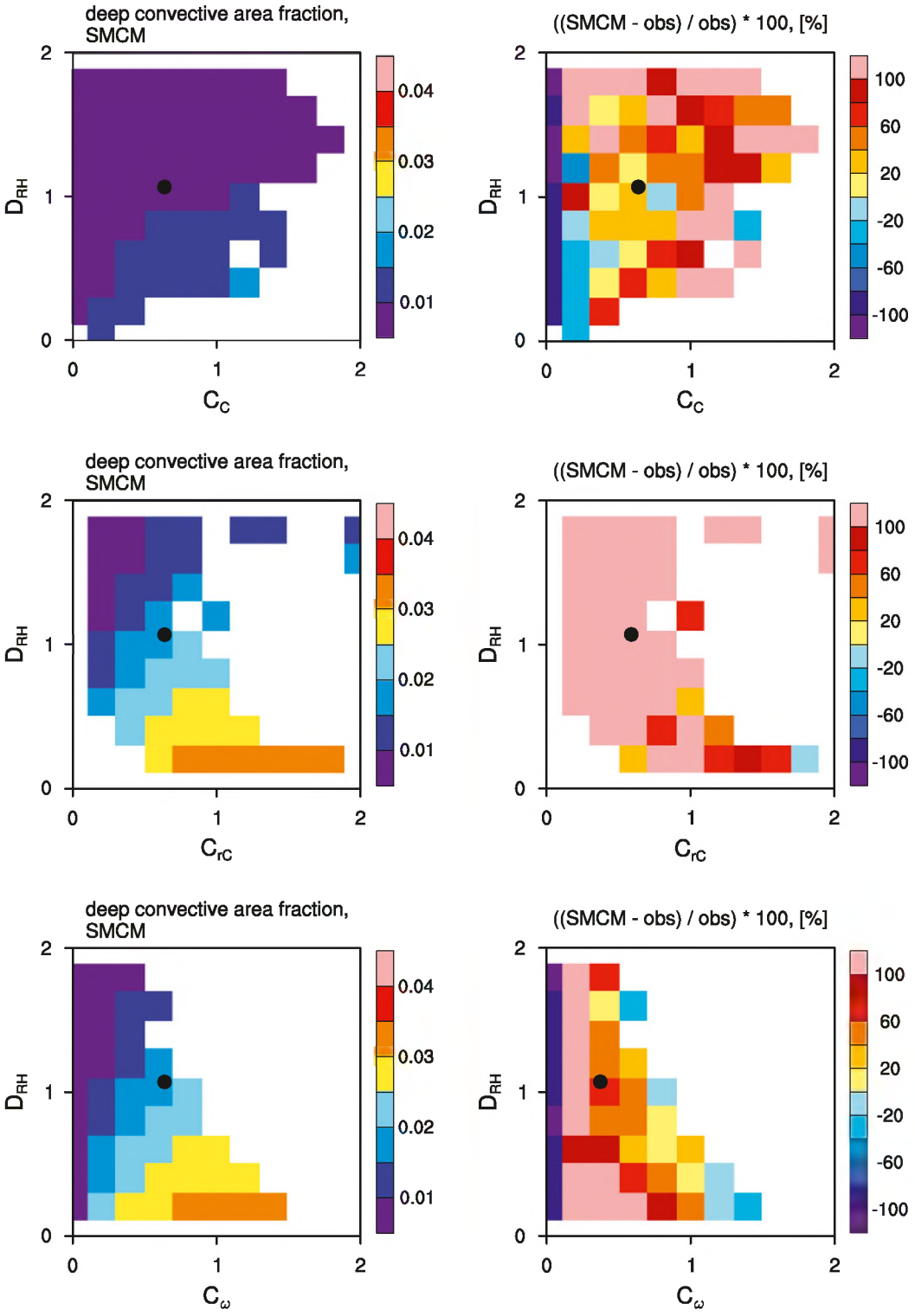

FIG. 7. (left) Joint histograms of analytically computed equilibrium deep convective area fractions of the SMCM and (right) the relative difference to observed mean deep convective area fractions at Darwin as a function of large-scale variables (top) C_C, (middle) C_{rC}, and (bottom) C_ω and D_{RH}. SMCM cloud fractions for each version of C correspond to the transition time scales shown in Table 1. Only histogram boxes having more than five observations are shown. The markers denote the mean observed values of C_C, C_{rC}, and C_ω and D_{RH} at Darwin, respectively.

showing no functional dependence on C and D. Using C_ω, the SMCM's equilibrium distribution resembles the functional dependency of the observations well. Furthermore, the relative difference of modeled versus observed area fractions shows an evident dependency on C and D. The model over- and underestimates deep convective area fractions for low and high values of C, respectively. This transition from over- to underestimating the area fractions appears systematic and gradual, a promising result in terms of possible future model adjustments (see below). The modeled joint histograms in Fig. 7, however, do not show the capability of the SMCM concept to reproduce observed temporally resolved tropical convection; they are merely analytical equilibrium solutions of the SMCM's internal birth–death process given a particular set of transition time scales (cf. KBM10 and references therein for details).

We conjecture that the main reason why the SMCM over- and underestimates deep convective area fraction for low and high values of C_ω (and C_{rC}), respectively, is not a matter of finding the correct transition time scales or of ill-formulated "transition rules" but is due to the functional dependency of transition rates on C and D. KBM10 formulate this dependency as

$$\Gamma(x) = 1 - e^{-x}, \quad x \in [0;2], \tag{4}$$

with x being either C or D and Eq. (4) being directly linked to transition rates R; for example,

$$R_{ab} \propto \Gamma(C)\Gamma(D) \tag{5}$$

indicates the transition rate R from cloud state a to b. This formulation leads pronounced changes in transition rates for small values of C or D with the response becoming less strong with increasing values of C and D. Therefore, the SMCM in its original formulation is not designed to reproduce the sharp increase in observed cloud fractions shown in Figs. 4 and 5 for higher values of C. Alternative formulations of $\Gamma(x)$ could be sought to improve the SMCM's capability to reproduce observed cloud area fraction distributions. This will be investigated in future research.

b. *Applying the SMCM to observations*

In this section, we use the three sets of observation-derived parameters discussed in sections 2c and 3 in combination with the best-fit transition time scales shown in Table 1 to perform simulations with the SMCM. We first quantitatively discuss the temporally resolved reproduction of cloud area fractions compared to observations in section 4b(1) and then carry out a more thorough statistical analysis in section 4b(2).

1) SMCM TEMPORALLY RESOLVED TROPICAL CONVECTION

We use the subsets of the data from the Darwin and Kwajalein locations introduced in section 4b to compare the time series of observed cloud area fractions to those modeled by the SMCM for illustrative purposes. As we obtained the best-fit transition time scales shown in Table 1 from analyzing just Darwin data, application of these time scales to Kwajalein provides a strong test for our method. We force the SMCM with each of the three combinations of C_C, C_{rC}, and C_ω with D_{RH}. The internal model time step is set to 5 min. The 6-hourly observations were linearly interpolated to match the model time step. The subgrid-scale lattice of the SMCM is set up to have 20×20 sites. As the whole domain covers an area of about $190 \times 190\ \mathrm{km}^2$, each lattice site thus has an edge length of about 10 km. There is currently no fixed spatial scale for an individual lattice point considered in the formulation of the SMCM. Preliminary analysis shows that an increase in lattice sites, and the reduction of lattice size going with it, reduces the simulated temporal variability compared to observations but has no effect on correlations. This is mainly an effect of the SMCM-modeled cloud fractions approaching the deterministic limit of the Markov process (cf. KBM10).

From a GCM convection parameterization perspective it thus seems attractive to use SMCM lattice sites with a globally uniform fixed spatial scale (e.g., $1 \times 1\ \mathrm{km}^2$), leading to increased convective variability with increasing GCM resolution (i.e., reduced GCM gridbox size). This would yield a more realistic representation of convection compared to current deterministic schemes.

The resulting modeled time series of deep convective cloud area fractions for Darwin and Kwajalein are shown in Figs. 8 and 9, with the observed time series included for reference purposes. We show neither observed and modeled congestus nor stratiform cloud fractions because our main interest lies in assessing the representation of deep convection as this is our current target for GCM convection parameterizations.

We first consider the observed and modeled deep convective area fractions over Darwin shown in Fig. 8 as we have adjusted the model parameters of the SMCM specifically for this location. Forcing the SMCM with C_C results in more or less constant convective cloud area fractions showing no resemblance of the different regimes found in the observations. Because of the nonnegative and mostly nonzero values of the C_C time series (cf. Fig. 2), the SMCM cannot reproduce the intermittency of cloud area fractions found in the observations. The same issue is apparent when forcing the SMCM with C_{rC}. However, periods of higher modeled deep

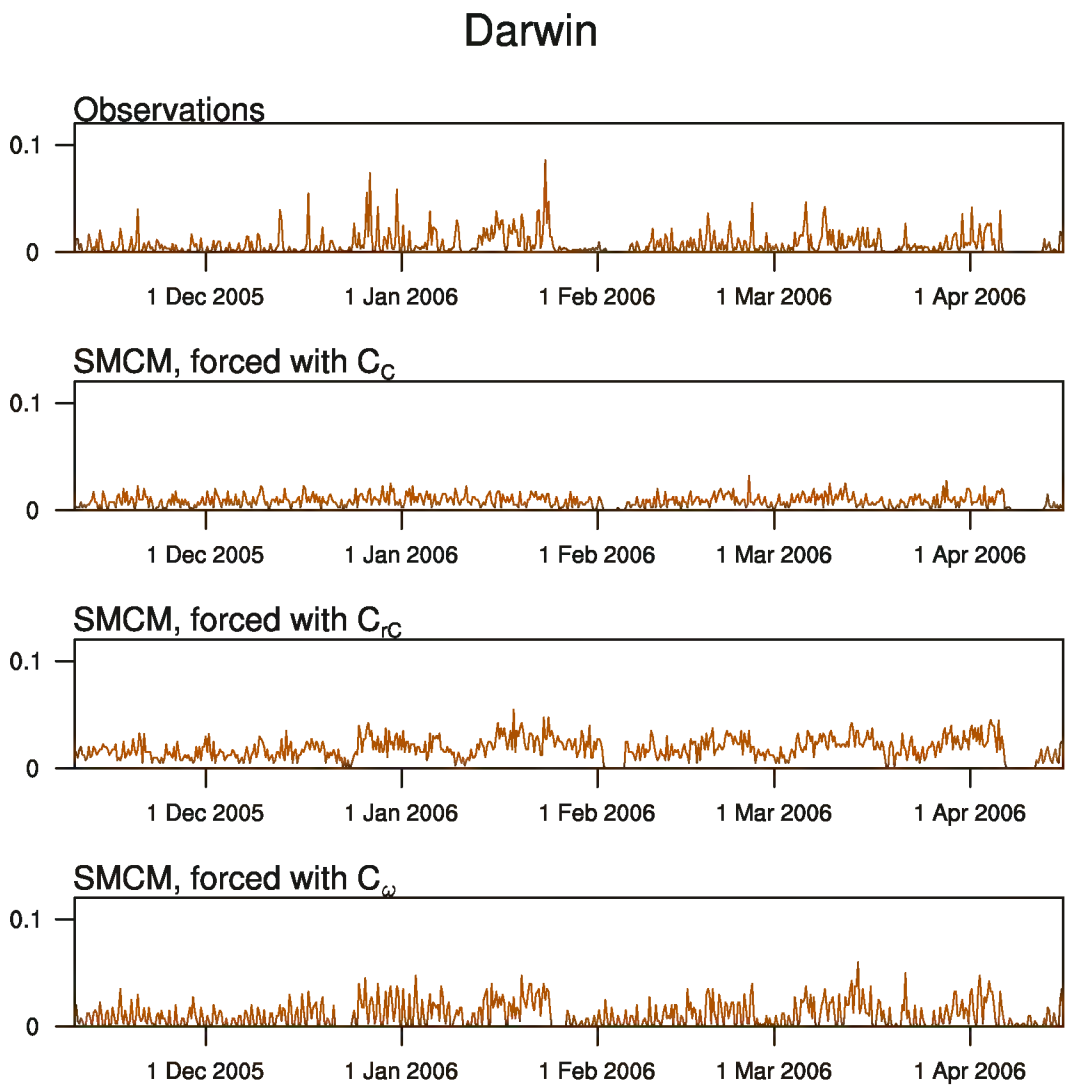

FIG. 8. Observed and SMCM-modeled time series of deep convective area fraction over Darwin during the time period 10 Nov 2005–18 Apr 2006. SMCM time series are obtained by forcing the SMCM with the observed C and D parameters introduced in section 2c and the transition time scales shown in Table 1. Results indicate one possible solution of the stochastic modeling approach.

convective cloud fraction seem to loosely correspond to periods of higher observed fractions, giving slightly more confidence in using C_{rC} over C_C.

The results from using C_ω to force the SMCM show substantially more agreement with the observations, with C_ω leading to more variability during periods of low convective activity, especially during the first month or so of the considered time period. Analysis of correlations between modeled and observed deep convective area fraction time series and probability distribution functions thereof confirms that using C_ω as proxy for convective propensity results in a better representation of convective behavior compared to the other two proxies (not shown). Despite these encouraging results, the issues raised toward the end of section 4 are apparent. For periods of weak forcing, the SMCM produces too high a deep convective cloud fraction whereas cloud fractions during strongly forced periods are substantially underestimated compared to observations. This is exactly what is to be expected from the modeled equilibrium cloud fractions shown in Fig. 7.

The observed and modeled time series of deep convective area fraction for the Kwajalein area (Fig. 9) generally show the same behavior as the ones for the Darwin area (Fig. 8). In particular, the over- and underestimation of deep convective area fractions for

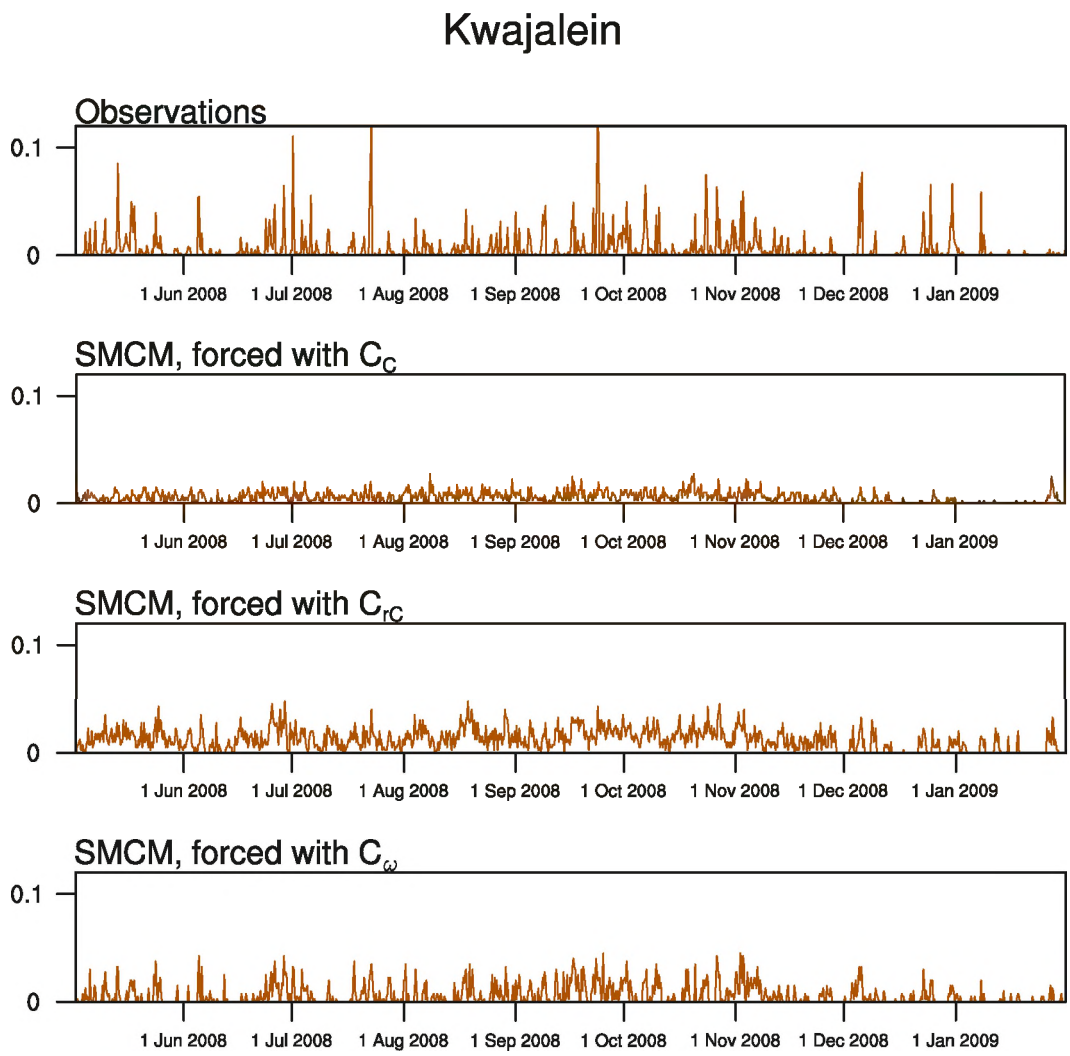

FIG. 9. As in Fig. 8, but over Kwajalein during the time period 2 May 2008–31 Jan 2009.

small and large values of C_ω, respectively, is evident. Nevertheless, C_ω proves to be the parameter of choice for reproducing deep convective features over Kwajalein with the SMCM. Considering that we did not use the Kwajalein data to adjust the transition time scales in the SMCM in the preceding part of this paper, this result confirms the findings presented in section 3, namely that convection over Kwajalein shows similar functional dependencies to the large-scale environment as does convection over Darwin. Furthermore, this result indicates that at least in the framework of the SMCM, tropical convection acts on similar time scales for both tropical locations considered here. It is, however, important to keep in mind the possible ambiguities when attempting to establish cause-and-effect relationships between the large-scale state and convection when using C_ω (cf. section 3).

2) STATISTICS OF SMCM-MODELED VERSUS OBSERVED TROPICAL CONVECTION

We now analyze the SMCM-modeled tropical convection to quantify the capability of the SMCM framework to reproduce the observed statistical properties of deep convective and stratiform area fractions laid out in section 3 as well as the actual stochasticity of the modeled convection. For the sake of brevity, we limit this analysis to experiments in which convection in the SMCM is determined by C_ω. We choose to do so because the SMCM versions using the two other parameters C_C and C_{rC} were shown unsuitable for reproducing the basic temporal behavior of convection [cf. section 4b(1)].

Similar to the analysis of observed convection presented in section 3, we stratify the modeled time series of deep convective and stratiform area fractions by the

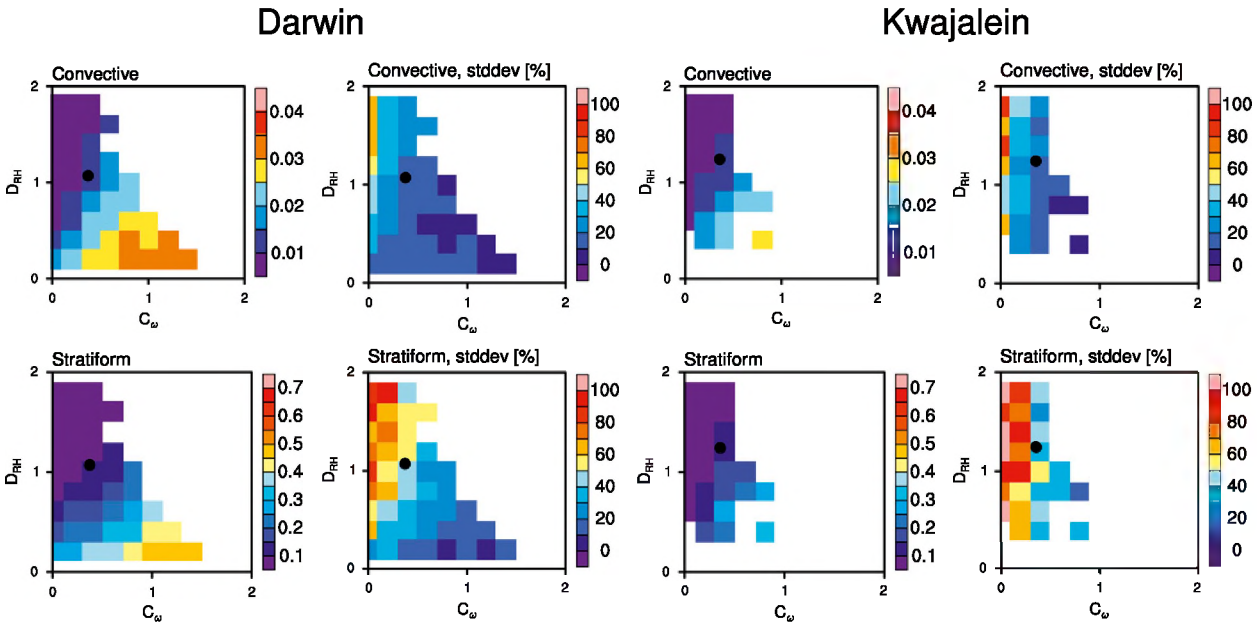

FIG. 10. Joint histogram of modeled cloud area fractions and relative standard deviations as function of large-scale variables C_ω and D_{RH} at the (left) Darwin and (right) Kwajalein sites derived from sampling the modeled cloud area fraction time series using all the available forcing data from observations (cf. section 4b) and the transition time scales from Table 1. Only pixels having more than five observations are shown. (top) Deep convective clouds and (bottom) stratiform clouds. Sample sizes per bin are as in Fig. 5. The black markers denote the mean values of C_ω and D_{RH}.

values of C_ω and D_{RH} used for forcing the model. To ensure comparability with the observations, we average the modeled area fractions over 6-h periods centered over each time step of the observed large-scale atmospheric state. Similar to the histograms shown in Figs. 3–5, we show the results obtained for Darwin and Kwajalein separately in Fig. 10, again providing a test for the validity of the chosen transition time scales for both locations.

As expected, the joint histogram of SMCM deep convective area fractions obtained from the modeled time series of the Darwin location very much resembles that of the analytically derived equilibrium area fraction for the same set of transition time scales (Fig. 7, bottom). These statistics of the modeled time series more clearly reveal the shortcomings of the SMCM framework in reproducing observed convection already mentioned in sections 4a and 4b(1). The order of magnitude of deep convective area fraction is generally well captured, with the SMCM over- and underestimating area fractions for weak and strong convective forcing, respectively. The same also holds for the simulated stratiform cloud fractions for the Darwin area, which we show here for illustrative purposes, mainly to highlight that the transition time scales that we determined in section 4a also yield sensible values for that cloud type. More importantly, the sample standard deviations of deep convective and stratiform area fractions of the modeled time series show similar behavior compared to those of the observations (i.e., area fractions show higher and lower variability for weaker and stronger convective forcing, respectively). Sensitivity tests in which we force "untuned" versions of the SMCM with the observed large-scale atmospheric state show that this behavior is in fact an intrinsic property of the SMCM framework and does not depend on the chosen set of transition time scales. The modeled time series underestimate the degree of variability throughout, however (note the different color scales in Fig. 10 compared to Fig. 5). So for the Darwin area, the SMCM framework is suitable for reproducing observed behavior of tropical convection, both in terms of deep convective and stratiform cloud area fractions and variability, as a function of the observed large-scale environment.

For the Kwajalein area, the joint histograms in Fig. 10 lead us to similar conclusions, thereby supporting the applicability of the SMCM framework to both tropical locations considered here. However, because of the sparse sampling of strong convective forcing over Kwajalein, the overestimation of cloud area fractions for weak convective forcing dominates the statistics. As mentioned in section 4a, the sometimes substantial overestimation of cloud area fractions could be mediated by using alternative formulations of Eq. (4), which will be a topic of future research.

5. Summary and conclusions

This study was driven by the need for alternatives to the mostly deterministic convection parameterizations used in general circulation models (GCMs). For this, we first determined statistics of observed tropical convection over Darwin and Kwajalein stratified by environmental conditions. Then, we used these observed statistics to investigate whether the underlying framework of the stochastic multicloud model (SMCM; KBM10) is suitable for reproducing observed tropical convection, a prerequisite to using the underlying stochastic framework of the SMCM in a GCM convection parameterization.

We investigated the dependency of tropical convection, given by the fractional area coverage with deep convective or stratiform clouds, on a set of two proxy values obtained from the observed large-scale atmospheric state (derived by means of variational analysis; Davies et al. 2013). One proxy (C) represents the ability of the atmospheric column to initiate/sustain convection whereas the second proxy (D) represents midtropospheric dryness. As there exists no generally accepted theory of which environmental conditions actually lead to tropical convection, we used three different formulations for C: CAPE, the ratio of low-level CAPE (LCAPE; i.e., CAPE integrated up to the freezing level) to CAPE, and vertical velocity at 500 hPa. The value of D is obtained from relative humidity at 500 hPa.

We found that the relationship of observed cloud area fractions with CAPE is very different compared to the other two C proxies. We find the highest deep convective and stratiform cloud area fractions for low values of CAPE, supporting earlier findings that CAPE is approximately anticorrelated or only weakly correlated with tropical precipitation (Mapes and Houze 1992; McBride and Frank 1999; Sobel et al. 2004; Fletcher and Bretherton 2010). Here, the studies of Mapes and Houze (1992) and Sobel et al. (2004) are of particular interest as they base their findings on observations gathered at Darwin and Kwajalein, respectively. On the other hand, deep convective and stratiform cloud area fractions are positively correlated with the other two C proxies. The cloud area fraction distributions as function of C and D also revealed that, for those two C proxies,

1) high and low cloud area fraction variability occurs for low and high values of C, respectively, implying that convection appears more random under weakly forced conditions and gets more and more deterministic with increasing forcing (cf. also Davies et al. 2013), thus contradicting the idea that the stochastic component of unresolved subgrid-scale processes scales linearly with their mean response (e.g., Buizza et al. 1999; Shutts and Palmer 2007);
2) cloud area fractions increase sharply above a certain value of C given low values of D, consistent with earlier reports on critical behavior of tropical convection (e.g., Peters and Neelin 2006);
3) cloud area fractions show identical relationships to environmental conditions for both locations (Darwin and Kwajalein), albeit with starkly different boundary conditions (e.g., land–sea distribution, monsoonal forcing); and
4) deep convective and stratiform cloud area fractions are anticorrelated with midtropospheric dryness [consistent with Redelsperger et al. (2002), Derbyshire et al. (2004), Takemi et al. (2004), and Takayabu et al. (2010)].

By design, the SMCM has a stationary equilibrium cloud area fraction distribution. By adjusting this distribution to the mean observed cloud area fractions, we tuned the SMCM for it to potentially reproduce the observed convection most closely. It proved difficult to exactly match the mean observed cloud area fraction distribution as $f(C, D)$, especially for the data stratified by CAPE. Generally, the SMCM yields too high and too low a cloud fraction for weak and strong large-scale forcing, respectively. We found that the values of the tuning parameters leading to a sensible match with the observed convection also respect the general rules for cloud transition probabilities laid out in KBM10, an overall very encouraging result.

Using the parameter-adjusted SMCM, we simulated convective area fractions using the time series of the observed large-scale state. We thus applied the SMCM in a diagnostic fashion and found that the modeled area fractions of deep convective and stratiform clouds compare better to observations when using the convection proxy related to convergence (i.e., vertical velocity at 500 hPa) rather than those related to stability (i.e., total CAPE and the ratio of low-level to total CAPE). This is most probably related to the nonintermittent and positive-definite nature of the latter proxies, which does not allow for simulation of the intermittent cloud features found in the observations.

When using the convergence-based convection proxy to force the SMCM to generate time series of tropical convection, we found that the framework of the SMCM is capable of reproducing the overall functional relationships as well as the statistics of observed tropical convection well. In particular, the SMCM tropical convection also shows higher variability in weakly forced conditions compared to stronger forced conditions. The degree of variability is underestimated compared to

observations though. We conjecture that the variability of the modeled convection would be higher if the SMCM were used in a prognostic framework rather than the diagnostic framework that we applied it to in this study. Furthermore, the 6-hourly time step of the observed large-scale state that we employ here may smear out part of the convective-scale variability, thus possibly constraining the stochastic process employed in the SMCM too strongly and also limiting the applicability to analysis of the diurnal cycle. Future work should thus also concentrate on deriving large-scale, long-term datasets of improved temporal resolution.

We acknowledge that there do exist ambiguities in establishing sound cause-and-effect relationships when attempting to relate tropical convection to large-scale convergence. Here, we argue for an integrated view of tropical convection over the entire range of atmospheric forcing strength of large-scale convergence. For weak (or even negative) convergence, convective area fractions are very small and show substantial variability about the mean (i.e., induced by very localized forcing such as land surface heterogeneities or land–sea breezes). However, these small-scale features induce some low-level convergence themselves, which may lead to more large-scale organization and greater area fraction of convection. This could in fact lead to a positive feedback loop on various scales. However, assessing the effect that this kind of feedback behavior would have on the vertical ascent on the scales considered here (i.e., $190 \times 190\,\mathrm{km}^2$) is beyond the scope of our study. In conclusion, we acknowledge the complex interactive relationship between convection and area-averaged vertical motion while noting that both directions in the interaction are likely at play and of importance with different weights based on the large-scale synoptic situation.

This study has shown that the stochastic concept behind the SMCM has the potential to underpin novel convection parameterizations in GCMs. As mass-flux convection parameterizations need to predict the vertical mass flux at cloud base, the concept of the SMCM would yield a stochastically based area and the updraft velocity could be given by another adequate formulation [e.g., such as that introduced in Jakob and Siebesma (2003)]. Furthermore, a reduction of GCM gridbox size (i.e., increasing resolution) would then lead to increased convective variability, making it superior to currently used deterministic convection schemes. Ultimately, future efforts will converge toward implementing a prototype version of a parameterization incorporating the SMCM framework into a full GCM.

Acknowledgments. The authors thank the constructive comments of three anonymous reviewers and the editor, which helped improve the paper. The research of L.D. is supported by the Office of Science (BER), U.S. Department of Energy under Grant DE-FG02-09ER64742. The research of B.K. is supported by the Natural Sciences and Engineering Council of Canada. The research of A.J.M. is partially supported by the grants from the National Science Foundation and the office of the Naval Research.

REFERENCES

Arakawa, A., 2004: The cumulus parameterization problem: Past, present, and future. *J. Climate,* **17,** 2493–2525.

Bright, D., and S. Mullen, 2002: Short-range ensemble forecasts of precipitation during the southwest monsoon. *Wea. Forecasting,* **17,** 1080–1100.

Buizza, R., M. Miller, and T. Palmer, 1999: Stochastic representation of model uncertainties in the ECMWF ensemble prediction system. *Quart. J. Roy. Meteor. Soc.,* **125,** 2887–2908.

Charney, J., and Coauthors, 1979: *Carbon Dioxide and Climate: A Scientific Assessment.* The National Academies Press, 22 pp.

Crook, N., 2001: Understanding Hector: The dynamics of island thunderstorms. *Mon. Wea. Rev.,* **129,** 1550–1563.

Dai, A., 2006: Precipitation characteristics in eighteen coupled climate models. *J. Climate,* **19,** 4605–4630.

Davies, L., C. Jakob, P. May, V. V. Kumar, and S. Xie, 2013: Relationships between the large-scale atmosphere and the small-scale convective state for Darwin, Australia. *J. Geophys. Res.,* doi:10.1002/jgrd.50645, in press.

Derbyshire, S., I. Beau, P. Bechtold, J. Grandpeix, J. Piriou, J. Redelsperger, and P. Soares, 2004: Sensitivity of moist convection to environmental humidity. *Quart. J. Roy. Meteor. Soc.,* **130,** 3055–3079.

Dorrestijn, J., D. Crommelin, A. Siebesma, and H. Jonker, 2013: Stochastic parameterization of shallow cumulus convection estimated from high-resolution model data. *Theor. Comp. Fluid Dyn.,* **27,** 133–148, doi:10.1007/s00162-012-0281-y.

Fletcher, J. K., and C. S. Bretherton, 2010: Evaluating boundary layer–based mass flux closures using cloud-resolving model simulations of deep convection. *J. Atmos. Sci.,* **67,** 2212–2225.

Frenkel, Y., A. Majda, and B. Khouider, 2012: Using the stochastic multicloud model to improve tropical convective parameterization: A paradigm example. *J. Atmos. Sci.,* **69,** 1080–1105.

——, ——, and ——, 2013: Stochastic and deterministic multicloud parameterizations for tropical convection. *Climate Dyn.,* in press.

Gillespie, D., 1975: An exact method for numerically simulating the stochastic coalescence process in a cloud. *J. Atmos. Sci.,* **32,** 1977–1989.

Groenemeijer, P., and G. C. Craig, 2012: Ensemble forecasting with a stochastic convective parametrization based on equilibrium statistics. *Atmos. Chem. Phys.,* **12,** 4555–4565, doi:10.5194/acp-12-4555-2012.

Hohenegger, C., and B. Stevens, 2013: Preconditioning deep convection with cumulus congestus. *J. Atmos. Sci.,* **70,** 448–464.

Houze, R., 1997: Stratiform precipitation in regions of convection: A meteorological paradox? *Bull. Amer. Meteor. Soc.,* **78,** 2179–2196.

Jakob, C., and A. Siebesma, 2003: A new subcloud model for mass-flux convection schemes: Influence on triggering, updraft properties, and model climate. *Mon. Wea. Rev.,* **131,** 2765–2778.

Keenan, T. D., B. R. Morton, X. S. Zhang, and K. Nyguen, 1990: Some characteristics of thunderstorms over Bathurst and Melville Islands near Darwin, Australia. *Quart. J. Roy. Meteor. Soc.,* **116,** 1153–1172, doi:10.1002/qj.49711649508.

——, K. Glasson, F. Cummings, T. Bird, J. Keeler, and J. Lutz, 1998: The BMRC/NCAR C-band polarimetric (C-Pol) radar system. *J. Atmos. Oceanic Technol.,* **15,** 871–886.

Khouider, B., 2013: A coarse grained stochastic multi-type particle interacting model for tropical convection: Nearest neighbour interactions. *Commun. Math. Sci.,* in press.

——, and A. Majda, 2006: A simple multicloud parameterization for convectively coupled tropical waves. Part I: Linear analysis. *J. Atmos. Sci.,* **63,** 1308–1323.

——, and ——, 2008a: Equatorial convectively coupled waves in a simple multicloud model. *J. Atmos. Sci.,* **65,** 3376–3397.

——, and ——, 2008b: Multicloud models for organized tropical convection: Enhanced congestus heating. *J. Atmos. Sci.,* **65,** 895–914.

——, ——, and M. Katsoulakis, 2003: Coarse-grained stochastic models for tropical convection and climate. *Proc. Natl. Acad. Sci. USA,* **100,** 11 941–11 946.

——, J. Biello, and A. Majda, 2010: A stochastic multicloud model for tropical convection. *Commun. Math. Sci.,* **8,** 187–216.

Klocke, D., R. Pincus, and J. Quaas, 2011: On constraining estimates of climate sensitivity with present-day observations through model weighting. *J. Climate,* **24,** 6092–6099.

Kumar, V. V., C. Jakob, A. Protat, P. T. May, and L. Davies, 2013a: The four cumulus cloud modes and their progression during rainfall events: A C-band polarimetric radar perspective. *J. Geophys. Res.,* **118,** 8375–8389, doi:10.1002/jgrd.50640.

——, A. Protat, P. May, C. Jakob, G. Penide, S. Kumar, and L. Davies, 2013b: On the effects of large-scale environment and surface types on convective cloud characteristics over Darwin, Australia. *Mon. Wea. Rev.,* **141,** 1358–1374.

Lin, J., and J. Neelin, 2000: Influence of a stochastic moist convective parameterization on tropical climate variability. *Geophys. Res. Lett.,* **27,** 3691–3694.

——, and ——, 2003: Toward stochastic deep convective parameterization in general circulation models. *Geophys. Res. Lett.,* **30,** 1162, doi:10.1029/2002GL016203.

Lin, Y., and Coauthors, 2012: TWP-ICE global atmospheric model intercomparison: Convection responsiveness and resolution impact. *J. Geophys. Res.,* **117,** D09111, doi:10.1029/2011JD017018.

Majda, A., and M. Shefter, 2001: Models for stratiform instability and convectively coupled waves. *J. Atmos. Sci.,* **58,** 1567–1584.

——, and B. Khouider, 2002: Stochastic and mesoscopic models for tropical convection. *Proc. Natl. Acad. Sci. USA,* **99,** 1123–1128.

——, C. Franzke, and B. Khouider, 2008: An applied mathematics perspective on stochastic modelling for climate. *Philos. Trans. Roy. Soc.,* **366A,** 2427–2453.

Mapes, B., and R. A. Houze, 1992: An integrated view of the 1987 Australian monsoon and its mesoscale convective systems. I: Horizontal structure. *Quart. J. Roy. Meteor. Soc.,* **118,** 927–963.

May, P., J. Mather, G. Vaughan, C. Jakob, G. McFarquhar, K. Bower, and G. Mace, 2008: The Tropical Warm Pool International Cloud Experiment. *Bull. Amer. Meteor. Soc.,* **89,** 629–646.

McBride, J., and W. Frank, 1999: Relationships between stability and monsoon convection. *J. Atmos. Sci.,* **56,** 24–36.

Meehl, G., C. Covey, T. Delworth, M. Latif, B. McAvaney, J. Mitchell, R. Stouffer, and K. Taylor, 2007: The WCRP CMIP3 multimodel dataset: A new era in climate change research. *Bull. Amer. Meteor. Soc.,* **88,** 1383–1394.

Murphy, J., D. Sexton, D. Barnett, G. Jones, M. Webb, M. Collins, and D. Stainforth, 2004: Quantification of modelling uncertainties in a large ensemble of climate change simulations. *Nature,* **430,** 768–772, doi:10.1038/nature02771.

Palmer, T., 2001: A nonlinear dynamical perspective on model error: A proposal for non-local stochastic-dynamic parametrization in weather and climate prediction models. *Quart. J. Roy. Meteor. Soc.,* **127,** 279–304.

Peters, O., and J. Neelin, 2006: Critical phenomena in atmospheric precipitation. *Nat. Phys.,* **2,** 393–396, doi:10.1038/nphys314.

Pincus, R., C. Batstone, R. Hofmann, K. Taylor, and P. Glecker, 2008: Evaluating the present-day simulation of clouds, precipitation, and radiation in climate models. *J. Geophys. Res.,* **113,** D14209, doi:10.1029/2007JD009334.

Plant, R., and G. Craig, 2008: A stochastic parameterization for deep convection based on equilibrium statistics. *J. Atmos. Sci.,* **65,** 87–105.

Randall, D. A., and Coauthors, 2007: Climate models and their evaluation. *Climate Change 2007: The Physical Science Basis,* S. Solomon et al., Eds., Cambridge University Press, 589–662.

Redelsperger, J., D. Parsons, and F. Guichard, 2002: Recovery processes and factors limiting cloud-top height following the arrival of a dry intrusion observed during TOGA COARE. *J. Atmos. Sci.,* **59,** 2438–2457.

Sherwood, S., 1999: Convective precursors and predictability in the tropical western Pacific. *Mon. Wea. Rev.,* **127,** 2977–2991.

Shutts, G., and T. Palmer, 2007: Convective forcing fluctuations in a cloud-resolving model: Relevance to the stochastic parameterization problem. *J. Climate,* **20,** 187–202.

Sobel, A. H., S. E. Yuter, C. S. Bretherton, and G. N. Kiladis, 2004: Large-scale meteorology and deep convection during TRMM KWAJEX. *Mon. Wea. Rev.,* **132,** 422–444.

Steiner, M., R. Houze, and S. Yuter, 1995: Climatological characterization of three-dimensional storm structure from operational radar and rain gauge data. *J. Appl. Meteor.,* **34,** 1978–2007.

Takayabu, Y., S. Shige, W. Tao, and N. Hirota, 2010: Shallow and deep latent heating modes over tropical oceans observed with TRMM PR spectral latent heating data. *J. Climate,* **23,** 2030–2046.

Takemi, T., O. Hirayama, and C. Liu, 2004: Factors responsible for the vertical development of tropical oceanic cumulus convection. *Geophys. Res. Lett.,* **31,** L11109, doi:10.1029/2004GL020225.

Teixeira, J., and C. Reynolds, 2008: Stochastic nature of physical parameterizations in ensemble prediction: A stochastic convection approach. *Mon. Wea. Rev.,* **136,** 483–496.

Tompkins, A., and J. Berner, 2008: A stochastic convective approach to account for model uncertainty due to unresolved humidity variability. *J. Geophys. Res.,* **113,** D18101, doi:10.1029/2007JD009284.

Waliser, D., and M. Moncrieff, 2007: Year of Tropical Convection—A joint WCRP–THORPEX activity to address the challenge of tropical convection. *GEWEX News,* No. 17(2), International GEWEX Project Office, Silver Spring, MD, 8–9.

Zhang, M., and J. Lin, 1997: Constrained variational analysis of sounding data based on column-integrated budgets of mass, heat, moisture, and momentum: Approach and application to ARM measurements. *J. Atmos. Sci.,* **54,** 1503–1524.

JOURNAL OF GEOPHYSICAL RESEARCH: ATMOSPHERES, VOL. 118, 11,534–11,545, doi:10.1002/jgrd.50645, 2013

Relationships between the large-scale atmosphere and the small-scale convective state for Darwin, Australia

L. Davies,[1] C. Jakob,[2] P. May,[3] V. V. Kumar,[3] and S. Xie[4]

Received 6 March 2013; revised 10 July 2013; accepted 10 July 2013; published 25 October 2013.

[1] A persistent problem for numerical weather and climate models is the representation of tropical convective precipitation which for the most part occurs on spatial and temporal scales too small and too short to be explicitly resolved. Given that model parameterizations represent this subgrid convection as a function of the large-scale atmospheric state, an understanding of the strongest relationships between the two scales is needed. This study introduces a method to create two concurrent long-term data sets that describe both the large-scale atmosphere and the characteristics of the small-scale convection. Important relationships between these two scales are then investigated. It is found that convective precipitation, through convective precipitation area, has the strongest relationship with dynamical variables such as moisture convergence and vertical velocity at midlevels. The magnitude of the fluctuations of convective strength about the mean is found to be anticorrelated with the strength of the large-scale variables, indicating a more stochastic behavior of tropical convection in weakly than strongly forced regimes, respectively. Atmospheric stability related variables are not found to be positively related to either convective precipitation area or convective precipitation intensity, which is often an assumption made in convective parameterization. On the contrary, in a more unstable atmosphere, there is lower convective precipitation.

Citation: Davies, L., C. Jakob, P. May, V. V. Kumar, and S. Xie (2013), Relationships between the large-scale atmosphere and the small-scale convective state for Darwin, Australia, *J. Geophys. Res. Atmos.*, *118*, 11,534–11,545, doi:10.1002/jgrd.50645.

1. Introduction

[2] Atmospheric convection is an important phenomenon which drives weather and climate in the tropics as well as the global general circulation. Convection is relevant on a range of spatial and temporal scales from large-scale phenomena, such as the Inter-Tropical Convergence Zone, El Nino-Southern Oscillation, and the Madden-Julian Oscillation, to short weather time scales, such as an individual squall line and mesoscale convective systems. Numerical models exhibit limitations in their ability to capture convective phenomena. Particular examples include biases in the tropical mean precipitation distribution [*Sun et al.*, 2006; *Zhang et al.*, 2007] and significant timing errors in the diurnal cycle of convection over land [*Yang and Slingo*, 2001]. Shortcomings in model simulations have been related to the model representation of convection [e.g., *Neale et al.*, 2008; *Bechtold et al.*, 2008; *Zhang et al.*, 2006; *Neale and Slingo*, 2003; *Wang and Schlesinger*, 1999]. This is largely due to the limitations of the convective parameterizations used in models to represent the subgrid scale behavior of convection in relation to the resolved large-scale processes. Accurate representation of convection is particularly important for the tropics where precipitation is generally associated with convective cloud systems.

[3] Convective parameterizations (see *Arakawa* [2004] for a full review of convective parameterization approaches) generally exploit some relationship between the large-scale, given by the atmospheric state at the model grid box scale, and the convective scale. The schemes mostly invoke an assumption that the two scales are in quasi-equilibrium [*Arakawa and Schubert*, 1974; *Emanuel*, 1991; *Brown and Bretherton*, 1997] and use these assumptions to provide closure to the model equations. A variable which characterizes the thermodynamic state of the atmosphere, such as Convectively Available Potential Energy (CAPE), is often used to determine convective strength. CAPE is the vertical integral of the temperature perturbation of a buoyant air parcel ascending from near the surface to its level of neutral buoyancy. A comprehensive investigation of other possible relationships, between a large range of large-scale and small-scale variables, which may be used in the closure of convective parameterizations is somewhat lacking.

[1]School of Mathematics, Monash University, Melbourne, Victoria, Australia.
[2]ARC Centre of Excellence for Climate System Science, Monash University, Melbourne, Victoria, Australia.
[3]Centre for Australian Weather and Climate Research, Bureau of Meteorology, Melbourne, Victoria, Australia.
[4]Atmospheric Sciences Division, Lawrence Livermore National Laboratory, Livermore, California, USA.

Corresponding author: L. Davies, School of Earth Sciences, The University of Melbourne, Melbourne 3010, Victoria, Australia. (laura.davies@unimelb.edu.au)

2169-897X/13/10.1002/jgrd.50645

[4] Another possible limitation of convective parameterizations (and other parameterizations in general) is that they determine the subgrid scale convective behavior deterministically, meaning that for a given large-scale state, only one possible convective state can be attained. This is unlikely to be true in the real atmosphere, but traditional parameterizations cannot produce variability about their mean relationship between the two scales. Several cloud-resolving models (CRM) studies have identified variability in the large to small-scale relationships, however, to our knowledge there are no observational studies investigating the stochastic nature of these relationships [e.g., *Cohen and Craig*, 2006; *Shutts and Palmer*, 2007; *Plant and Craig*, 2008]. There have been several attempts to include stochastic elements in the description of convection in models. *Buizza et al.* [1999] showed that applying multiplicative noise to the physics tendencies improved modeled skill. *Lin and Neelin* [2007] used empirical relationships to adjust the convective parameterization. *Khouider and Majda* [2006] used a Markov chain lattice to stochastically describe the evolution of convective cloud types in a model grid-cell. *Plant and Craig* [2008] developed a fully stochastic convective parameterization. These studies have used either assumptions of empirical relationships or higher resolution models, such as CRM, to study the stochastic nature of the relationships. This study aims to supplement this earlier work by providing observations of the key relationships and also quantifying their stochastic components.

[5] In this study, we first develop two concurrent data sets, one representing the large-scale atmosphere and another the small-scale convective state, over a sufficiently long time period to sample a large range of different states. These data sets are then used to investigate important relationships between the two scales and furthermore to determine the stochastic nature of the relationships. Section 2 describes the methodology used to derive data sets for the large-scale atmospheric state and the concurrent small-scale convective state. Section 3 then discusses some key relationships between the two scales that are relevant for convective parameterizations. The stochastic nature of these relationships is probed in section 4. The following sections then discuss the results (section 5) and summarize the main conclusions (section 6).

2. Deriving Concurrent Long-Term Large-Scale Atmospheric and Convective States

[6] To investigate relationships between the large-scale atmospheric state and associated convection, two concurrent data sets are required, one that describes the average state of the atmosphere over an area similar to that of a Global Climate Model (GCM) grid-box and another that describes the subgrid-scale behavior of convection. In order to investigate a wide range of meteorological conditions and to increase sampling, these data sets should be as long as possible. This section describes the derivation of two such data sets for a tropical location, i.e., Darwin, Australia.

2.1. The Large-Scale State for a Tropical Location

[7] In order to study convection, the large-scale state data set should, ideally, include both thermodynamic and dynamic variables with a high degree of accuracy. An important source of such large-scale state data sets are the observations made during the intensive observation periods of field experiments such as TOGA-COARE: (Tropical Ocean-Global Atmosphere-The Coupled Ocean-Atmosphere Response Experiment) and Global Atmospheric Research Program's Atlantic Tropical Experiment (GATE) [*Webster and Lukas*, 1992; *Houze Jr and Betts*, 1981]. Such studies often deploy arrays of radiosonde observations and collect surface and top of the atmosphere data including energy and water fluxes. A useful method to analyze this data is the variational budget analysis developed by *Zhang and Lin* [1997] where radiosonde, top of the atmosphere (TOA), and surface data are combined and constrained by the vertically integrated heat and moisture budgets. *Zhang et al.* [2001] showed that surface precipitation data significantly improved the quality of the analysis. While field experiments produce the most comprehensive data sets to study tropical convection, they are usually of short duration, which prevents a large-sample statistical analysis of the relationship between convection and the large-scale state of the atmosphere. The top panel of Figure 1 shows an example of the results from such a field experiment. It shows the time-height evolution of vertical motion during the recent Tropical Warm Pool-International Cloud Experiment (TWP-ICE) at Darwin, Australia [*May et al.*, 2008] as derived by the variational analysis technique described above [*Xie et al.*, 2010]. It can be seen that there is strong upward motion during the active monsoon period (before day 25 which is 25 January 2006). A subsequent suppressed monsoon period is associated with downward motion between 700 and 200 hPa and toward the end of the TWP-ICE period (after day 33 which is 3 February 2006), the diurnal cycle becomes dominant with frequently alternating upward and downward motion.

[8] A source of long-term large-scale data sets is operational or reanalyses of the atmosphere as provided by several numerical weather prediction (NWP) centers. Such data sets cover many years and in principle provide a good source of large-scale information. However, analysis techniques in the tropics are not as far advanced as those in the extratropics and the lack of dynamical constraints, as well as the increased role of diabatic processes, limits the accuracy of the resulting analysis products. This is exemplified by the middle panel of Figure 1 which shows vertical motion for TWP-ICE from the European Centre for Medium-Range Weather Forecasts (ECMWF) operational analysis. It shows upward motion during the active monsoon consistent with the observations, although the vertical structure differs somewhat. It appears the timing of peak precipitation lags the observations, and this behavior is discussed in *Petch et al.* [2013]. During the suppressed period, the analysis fails to show the midlevel downward motion (compare to the observations, top panel) and the diurnally driven period is not well captured.

[9] To exploit both the strengths of the variational analysis technique and to overcome some of the weaknesses of NWP analysis results, a hybrid approach was developed by *Xie et al.* [2004]. NWP analysis is used as a replacement for radiosonde observations which provides higher temporal resolution sounding data than the twice daily long-term observations available. The analysis data are combined with surface and TOA observations at the Atmospheric Radiation

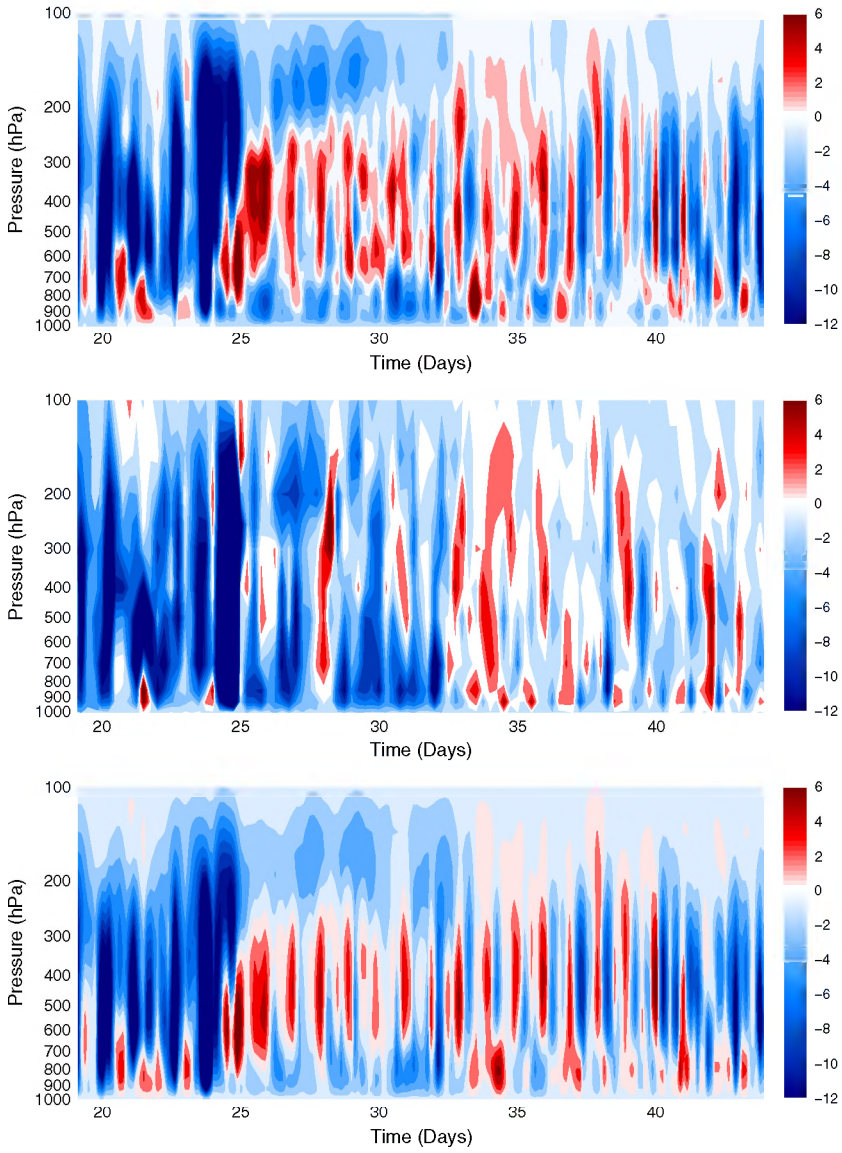

Figure 1. Timeseries of vertical profiles of vertical velocity in pressure coordinates (omega) using all observations, i.e., (top panel) the best-estimate values as described in *Xie et al.* [2010], (middle panel) the direct ECMWF analysis, and (bottom panel) using the hybrid approach described here. Data are shown for the TWP-ICE period (19 January–14 February 2006) at Darwin, Australia.

Measurement site at the U.S. Southern Great Plains using the variational analysis technique of *Zhang and Lin* [1997]. The surface data are radar-derived precipitation rates, and TOA microwave radiometer total column water vapor is used to constrain the moisture budget. *Xie et al.* [2004] demonstrated that for this extratropical location, the hybrid approach can successfully provide large-scale state data for long, continuous periods of time. The key observations for using this technique are long-term observations for surface precipitation and TOA radiation.

[10] We apply the hybrid approach to the TWP-ICE period so that its results can (i) be compared with the full field-experiment data and (ii) be evaluated against the ECWMF analysis to gauge any improvement over a pure NWP system. To do so, ECMWF analysis grid-points around Darwin are used to replace the TWP-ICE radiosonde observations. Specifically, the vertical profiles of zonal and meridional winds, temperature, and specific humidity are interpolated to the locations of the radiosonde launch sites. The method used was Barnes interpolation, however, experimentation with bilinear interpolation suggests that the resulting profiles are not sensitive to the method used.

[11] The bottom panel of Figure 1 shows vertical velocity derived using the hybrid technique. During the active period, vertical motion is similar to when using all observations, in particular the timing of the peak vertical motion is improved compared to the ECMWF analysis (middle panel). During the suppressed period, the hybrid approach shows downward motion in midlevels. Although the structure is somewhat different to using all observations, it resembles the observations (top panel). At the end of the TWP-ICE period, there is correctly intermittent upward and downward motion.

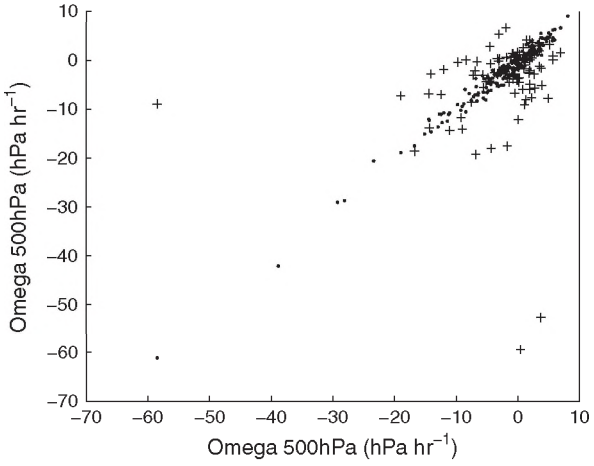

Figure 2. Relationship of 500 hPa vertical velocity in pressure coordinates (omega) derived using the variational approach from all observations on the *x* axis against both omega at 500 hPa from ECMWF analysis shown as crosses and 500 hPa omega derived using the variational method but using the hybrid approach (as discussed in the text) shown as points. Data are shown for the TWP-ICE period (19 January–14 February 2006) at Darwin, Australia.

[12] Figure 2 compares vertical velocity at 500 hPa derived with variational analysis using the hybrid approach and the ECMWF analysis to vertical velocity at 500 hPa derived with variational analysis from all observations. It is clear that when using the hybrid approach, the representation of vertical velocity substantially improves compared to the ECMWF analysis. Correlating all observed values of vertical velocity at 500 hPa with those derived from the hybrid approach and the ECMWF analysis yields correlation coefficients of 0.98 and 0.25, respectively.

[13] Having demonstrated the utility of the hybrid approach in providing reliable estimates of large-scale information, we apply the technique to derive three wet seasons (2004/2005, 2005/2006, and 2006/2007) of the large-scale state information for the TWP-ICE region around Darwin. The analysis technique is limited to periods, such as the wet season, when there are sufficient observations of precipitation. This data set is derived using the ECMWF operational analysis as radiosonde surrogate and constraining the variational analysis with area-mean surface precipitation derived from the polarimetric C-band radar (CPOL) [*Keenan et al.*, 1998] using the algorithm of *Bringi et al.* [2004]. It is worth noting that the use of the area-mean total precipitation as a constraint in the variational analysis limits its use as a surrogate for convective activity below. The radar data are processed in the same way as during the TWP-ICE experiment [see *Xie et al.*, 2010 for more detail]. The resulting data set has approximately 1900 samples at 6-hourly intervals.

2.2. Defining the Concurrent Convective State

[14] To correctly associate a particular large-scale atmospheric condition with a convective state, a description of the latter is also required concurrent in space and time with the large-scale state. To achieve this, a detailed analysis of the CPOL observations at 2.5 km above the surface is performed. Firstly, the data are classified into its convective and stratiform components using the algorithm of *Steiner et al.* [1995]. This method classifies pixels with large values of radar reflectivity as convective and then associates sufficiently intense, nearby precipitation values as also convective. Other precipitating radar pixels are classified as stratiform. The classified data are then area-averaged over the 6 h periods which are ±3 h the time of the large-scale state to produce convective and stratiform precipitation rates. Precipitation rates are further decomposed into area and intensity as given by $P = \sigma I$, where P is precipitation, σ is precipitation area, and I is precipitation intensity (defined as precipitation per unit precipitation area), for the same 6 h periods. Additional information on the small-scale state is found by analyzing the statistics of convective cells using the Thunderstorm Identification, Tracking, Analysis, and Nowcasting (TITAN) radar data analysis tool [*Dixon and Wiener*, 1993] which identifies characteristics of individual convective storms. Further detail on this analysis can be found in *Kumar et al.* [2012].

[15] While the focus of this study is on how the convective scale variables relate to the large scale, it is worthwhile determining how the small-scale variables relate to each other. Table 1 shows correlations coefficients between the small-scale variables related to both the convective and stratiform parts of the precipitation processes. Domain-averaged total precipitation is strongly correlated with both convective precipitation (through convective precipitation area) and stratiform precipitation. This result may be related to the finding of *Mapes et al.* [2006] who suggested that convective and stratiform precipitation exhibit similar relationships over different spatial and temporal scales. Total precipitation area is very strongly correlated with stratiform precipitation area as stratiform precipitation dominates the areal coverage. While both convective and stratiform

Table 1. Summary of Correlations Between Small-Scale Precipitation Variables

	Precipitation Area	Convective Precipitation	Convective Precipitation Area	Precipitation Stratiform	Stratiform Precipitation Area	Convective Precipitation Intensity	Stratiform Precipitation Intensity
Precipitation	0.85	0.94	0.93	0.94	0.81	0.50	0.44
Precipitation area	1.00	0.65	0.71	0.93	0.99	0.34	0.23
Convective precipitation		1.00	0.96	0.75	0.61	0.57	0.49
Convective precipitation area			1.00	0.79	0.66	0.52	0.49
Stratiform precipitation				1.00	0.92	0.37	0.33
Stratiform precipitation area					1.00	0.31	0.20
Convective precipitation intensity						1.00	0.88

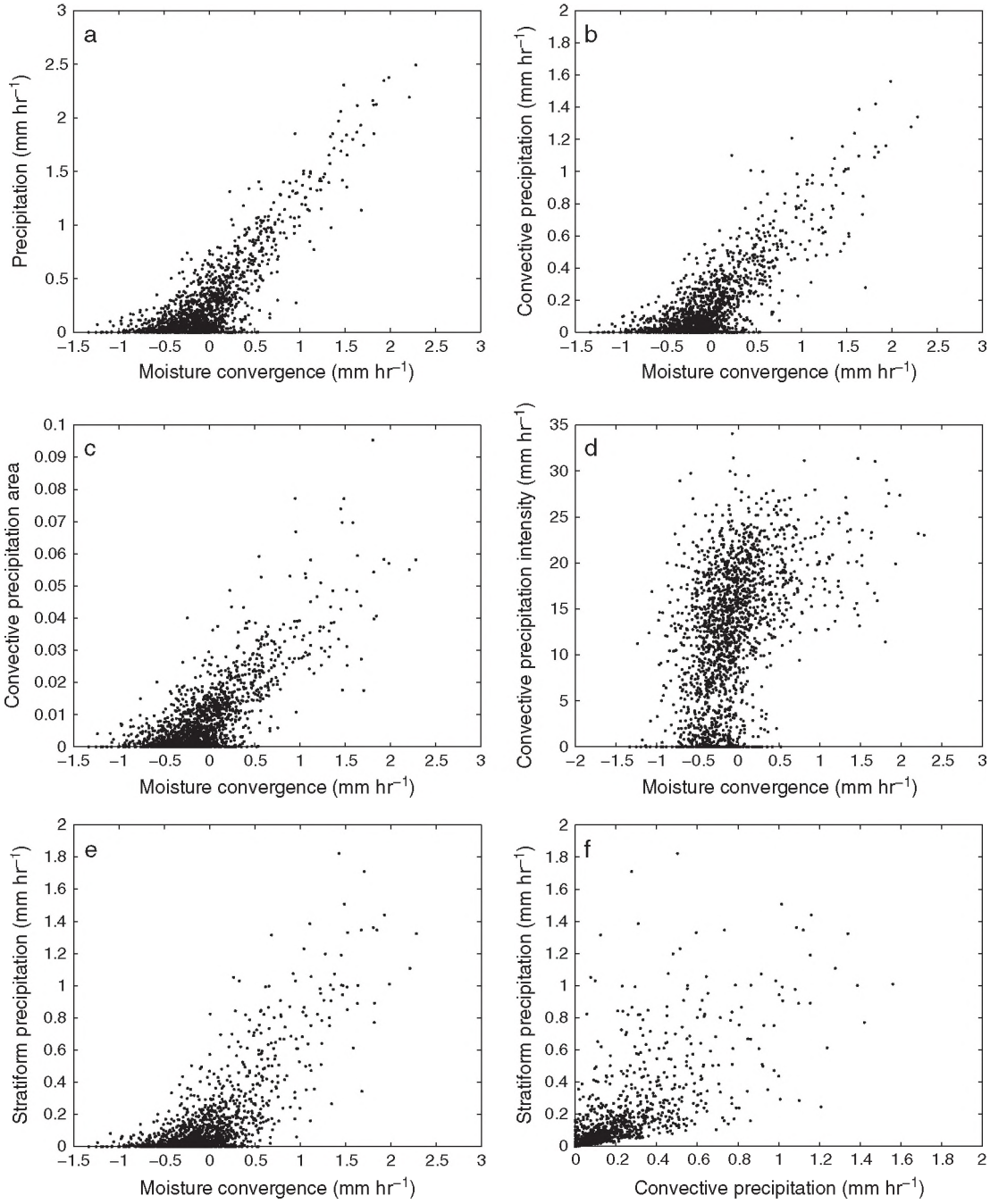

Figure 3. Relationship of moisture convergence with (a) precipitation, (b) convective precipitation, (c) convective precipitation area fraction, (d) convective precipitation intensity, and (e) stratiform precipitation. (f) Relationship of convective precipitation and stratiform precipitation.

precipitation are strongly correlated with their precipitation areas (0.96 and 0.92, respectively), there is weaker correlation (0.75) between convective and stratiform precipitation components. Convective and stratiform precipitation are also less related to the other's area (0.61 and 0.79, respectively). While there is some relationship between convective intensity and stratiform intensity (0.88 correlation), there are weak correlations with all other precipitation and area variables. Further investigation attributes this to complex nonlinearities in the relationships (cf. section 3). Convective precipitation, which is dominated by convective precipitation area, and convective precipitation intensity are key variables for convective parameterizations. These small-scale variables form the main basis for further analysis in the subsequent sections.

3. Relationships Between the Large-Scale Atmospheric State and Convection

[16] We now use the two concurrent data sets described in section 2 to investigate relationships between the large- and the small-scale states, i.e., between atmospheric

Table 2. Summary of Correlations Between Moisture Convergence and Omega at 700 hPa and Various Small-Scale Convective Precipitation Terms

	Moisture Convergence	Omega (700 hPa)
Precipitation	0.81	–0.79
Precipitation area	0.65	–0.61
Convective precipitation	0.78	–0.76
Convective precipitation area	0.75	–0.76
Convective precipitation intensity	0.45	–0.39

dynamics/thermodynamics and convection. Given the possible large number of large-scale variables, the investigation is divided to three overall categories, dynamics, thermodynamics, and atmospheric stability.

3.1. Relationships Involving Dynamical Processes

[17] This section investigates the relationships of the convective state to a few dynamical characteristics of the large-scale state. Specifically, the dynamical variables considered are vertically integrated moisture convergence and vertical velocity in pressure coordinates (ω). Figure 3 shows the relationships between some key small-scale variables and moisture convergence, and Table 2 shows the associated correlations. While moisture convergence is a vertically integrated variable, it is found to be strongly correlated with vertical motion at 700 hPa (–0.69). Precipitation is highly correlated with both dynamical variables, with this correlation being slightly higher for moisture convergence (0.81) compared to ω at 700 hPa (–0.79). Figure 3a shows that indeed the largest precipitation occurs with the strongest moisture convergence. While there is generally lower precipitation associated with negative moisture convergence, precipitation can occur when there is net divergence and hence likely subsiding condition due to shallow but precipitating convective clouds. There is scatter about this relationship particularly for low values of moisture convergence.

[18] This data set does not allow for the interpretation of causality as convective heating and precipitation are known to induce moisture convergence, and equally under conditions of high moisture convergence, convection is more likely. This issue of cause and effect has been discussed in the context of the assumptions made in convective parameterizations e.g., *Arakawa* [2004], and it has been argued [*Emanuel*, 1994] that convergence is a consequence, rather than a cause, of convection. Investigation shows that the relationship between convective precipitation and the dynamical variable at the previous 6 h interval is somewhat weaker (0.30 for moisture convergence and –0.27 for ω at 700 hPa). This issue will be discussed further in section 5.

[19] It is worth noting again that a strong relationship between total precipitation and large-scale vertical motion is expected as a result of the use of total precipitation in the construction of the large-scale data set. Hence, further analysis will focus on variables that are not a direct input to the variational analysis scheme used here.

[20] In section 2.2, we showed that there are strong relationships between total precipitation and both convective precipitation and convective precipitation area. It is therefore not surprising that the relationship existing between moisture convergence and total precipitation is also apparent with convective precipitation and convective precipitation area (Figures 3b and 3c; Table 2). The correlations are slightly weaker, however, 0.78 and 0.75, respectively. This suggests that larger moisture convergence is associated with increased convective precipitation through predominantly increasing the convective precipitation area. The same applies to ω at 700 hPa although correlations are lower. This result provides observational support for a finding from cloud-resolving modeling studies, e.g., *Cohen and Craig* [2006], that convection responds to an increase in prescribed model "forcing" predominantly through an increase in convective area. Figure 3d and Table 2 show that the relationship is different when considering convective precipitation intensity. There is little discernible relationship between moisture convergence and precipitation intensity, although large values of moisture convergence tend to produce intensities above 10 mm h^{-1}, and negative moisture convergence results in a wide range of lower precipitation intensities. This complex interaction results in low correlations between the large-scale atmospheric state and precipitation intensity and may be related the dependence of precipitation intensity on raindrop terminal velocity [*Parodi and Emanuel*, 2009].

[21] As shown in Table 1, there is a strong correlation between total precipitation and stratiform precipitation. Therefore, stratiform precipitation is also strongly correlated with moisture convergence (Figure 3e) and ω at 700 hPa (0.75 and –0.71, respectively), although the correlation is weaker than with convective precipitation. Such a relationship exists as there is a strong relationship between convective and stratiform precipitation (Figure 3f and Table 2) which may be expected as convection is the source of stratiform cloud in many cases. For this reason, we focus on convective characteristics hereon.

3.2. Relationships Involving Moisture

[22] This section investigates the relationship of convective-scale behavior in relation to large-scale moisture. Specifically, the large-scale moisture variable considered is midlevel moisture which is defined as the specific humidity at 600 hPa. Similar relationships are observed with other moisture variables, for example, midlevel moisture is correlated 0.96 with column-integrated relative humidity and 0.95 with precipitable water. Also, as there are strong relationships between precipitation, convective precipitation, and convective precipitation area, which are also apparent in the relationships with large-scale variables (cf. sections 2.2 and 3.1), this section will focus on convective precipitation area and convective precipitation intensity only.

[23] Figure 4 shows the relationship between midlevel moisture and small-scale convective variables. While there is a general tendency for larger convective precipitation area in moister atmospheres, there is much scatter in that relationship. Essentially, atmospheres which are more moist support large convective areas with a small increase in the likelihood of large area with increased moisture. There are two possible reasons for this (i) because the atmosphere is moist, the effects of entrainment on convective strength are reduced leading to more convective precipitation or (ii) in a strongly convecting atmosphere, evaporation of both precipitation and detrained condensate will moisten

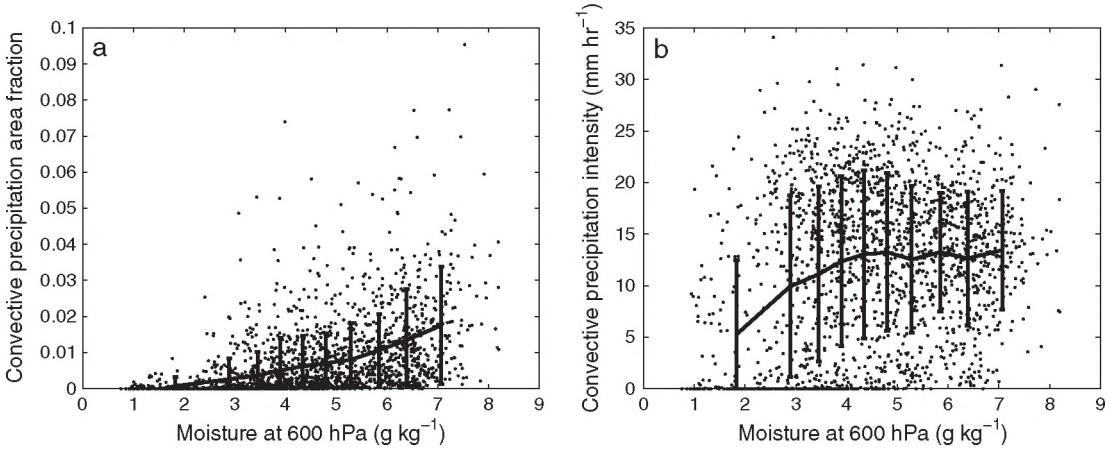

Figure 4. Relationship of 600 hPa moisture with (a) convective precipitation area fraction and (b) convective precipitation intensity. Also shown are mean and ±1 standard deviation values for deciles of the data set.

the atmosphere. This result does not suggest causality but shows that a weak relationship exists. Figure 4a, using convective precipitation area rather than total precipitation, somewhat resembles distributions in *Bretherton et al.* [2004] and *Holloway and Neelin* [2009] with increasing precipitation area for larger values of moisture. However, the relationship does not have the strong pickup in precipitation shown in *Holloway and Neelin* [2009] who used 1 h radiosonde data nor the more gradual increase *Bretherton et al.* [2004] found using daily data. Figure 4a shows that there is much scatter in the relationship between midlevel moisture and convective area consistent with the findings of *Peters and Neelin* [2006] who found an increase in precipitation variance for high values of precipitable water. The differences between the findings in this study and the results in previous studies may be somewhat explained by *Masunaga* [2012] who found that the timescales investigated were important when determining the nature of the relationship between precipitable water and precipitation. Figure 4b shows the perhaps surprising result that convective precipitation intensity does not show much discernible relationship with midlevel moisture, with the exception that in a very dry atmosphere domain-mean convective intensity is slightly lower. This implies that at least small but strong convective clouds can exist in any atmosphere and that once again, it is the area of convection that increases in atmospheres that are more moist.

[24] Figure 5 shows a different perspective on how convective precipitation relates to moisture. Here probability distributions of precipitation in convective cells from the TITAN analysis [*Kumar et al.*, 2012], averaged over 6 h, are shown as a function of midlevel (600 hPa) moisture. The precipitation distributions are sorted into deciles based on midlevel moisture and then averaged over each decile. Red colors represent averages with the largest moisture and blue colors averages with the low moisture. In general, many more convective cells are observed when the atmosphere is moist, thus reflecting the increased convective area shown in Figure 3. Therefore, for each decile, the distribution is normalized by the number of convective cells observed in that decile. When the atmosphere is moist, the numerous convective cells tend to have lower precipitation intensity. As the atmosphere dries, there is a shift in the distribution toward fewer convective cells but with larger values of precipitation intensity. This shows that in a moist atmosphere, convective cells are less intense, but more numerous; however, in a drier atmosphere, while there are fewer convective cells over all, the individual cells are more likely to be more intense.

3.3. Relationships Involving Atmospheric Stability

[25] This section will investigate the relationship of convective scale activity with two measures of atmospheric stability: Convective Available Potential Energy (CAPE), which is a vertically integrated measure of the buoyancy of a parcel lifted from 990 hPa, and a measure more frequently used by weather forecasters to predict convective showers and thunderstorms called the *K*-index [*Charba*, 1977].

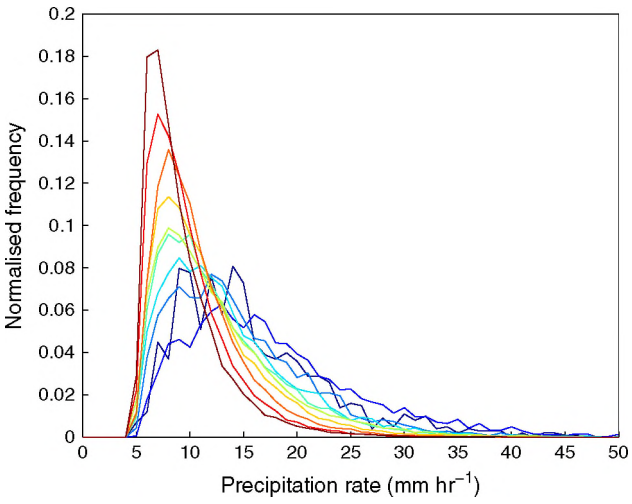

Figure 5. Distribution of precipitation rate per convective cell averaged over deciles of 600 hPa moisture. The distribution is normalized by the total number of convective cells in each decile. Deciles with large moisture are in red and deciles with low moisture are in blue.

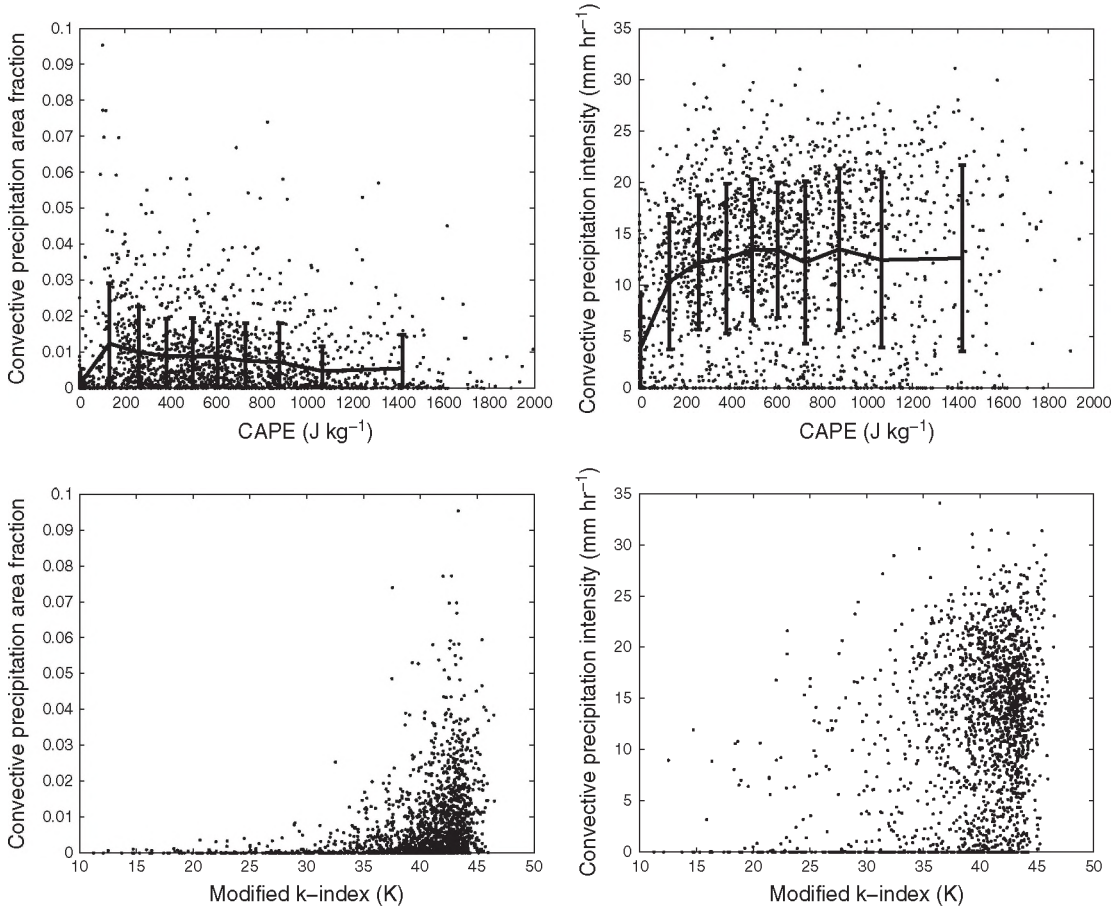

Figure 6. Relationship of (top) CAPE and (bottom) *K*-index with (left) convective precipitation area fraction and (right) convective precipitation intensity. In the top panels, also shown are mean and ±1 standard deviation values for deciles of the data set.

The *K*-index is calculated based on temperature (T) and dew point temperature (T_d) at key pressure levels as shown in equation (1).

$$K = \underbrace{\frac{T_{1000\ \mathrm{hPa}} + T_{850\ \mathrm{hPa}}}{2} - T_{500\ \mathrm{hPa}}}_{\text{(a)}} + \underbrace{\frac{T_{d,1000\ \mathrm{hPa}} + T_{d,850\ \mathrm{hPa}}}{2}}_{\text{(b)}} - \underbrace{(T_{700\ \mathrm{hPa}} - T_{d,700\ \mathrm{hPa}})}_{\text{(c)}} \quad (1)$$

[26] Figure 6 shows the relationships between CAPE, *K*-index, and selected small-scale variables. Convective precipitation and CAPE effectively have zero correlation (–0.003) showing that, at least for this data set, CAPE is not likely to be a good predictor of convective precipitation consistent with *McBride and Frank* [1999]. The relationship between CAPE and precipitation has been also discussed in *Xie and Zhang* [2000] and *Zhang* [2002]. CAPE at the previous 6 h interval has slight positive correlation with convective precipitation (0.06) which is discussed further in section 5. Detailed investigation shows that CAPE increases through a combination of an increased height of the level of neutral buoyancy and larger perturbations in the parcel temperature throughout the atmosphere compared to the environment. Convective precipitation intensity also does not have a strong relationship with CAPE.

[27] The *K*-index on the other hand has a very different relationship with convective precipitation. Figure 6 (bottom left) shows that convective precipitation values greater than 0.5 mm h^{-1} only occur for values of *K*-index greater than 35 K. Generally, in the forecasting context, *K*-index values greater than 30 K indicate potential of Mesoscale Convective Cloud (MCC) and greater than 40 K almost 100% chance of thunderstorms.

[28] Equation (1) indicates that the *K*-index has three distinct components. Term (a) relates to lower tropospheric stability, term (b), a measure of mean low-level (boundary layer) moisture, and finally, term (c) relates to midlevel humidity. Given that the *K*-index includes term (a), which is also relevant for CAPE, it is instructive to investigate which of these terms, if any, has the dominant role in determining the relationship to convective precipitation. Investigation shows that the stability component of the *K*-index (term a) has very similar relationship with convective precipitation to that of CAPE (Figure 6, top left). CAPE and the stability component of the *K*-index are correlated 0.7. The low-level moisture and midlevel humidity components of the *K*-index (terms b and c) are correlated 0.77 and 0.94, respectively, with the full *K*-index, rendering these terms important for determining the *K*-index values. The relationship between the humidity component of the *K*-index and convective precipitation, in particular, resembles Figure 4a.

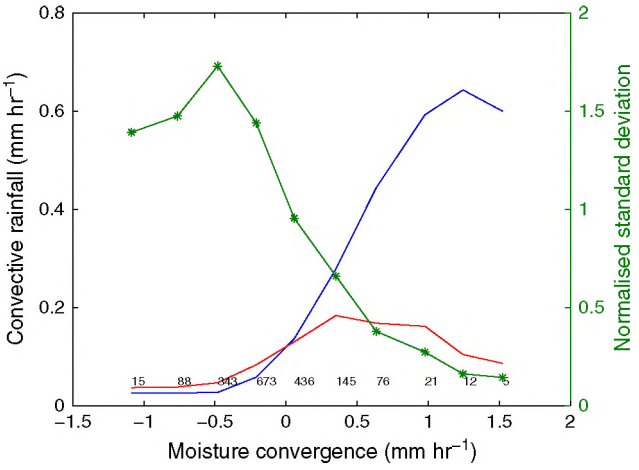

Figure 7. Mean and standard deviation 6 h mean convective precipitation (blue and red lines, respectively, and shown on left y axis) as a function of moisture convergence. The data are computed over 10 bins, and the number of points in each bin is shown above the x axis. Also shown is the ratio of the standard deviation to the mean (green line shown on the right y axis).

Hence, these terms of the K-index are the main contributors to the full K-index and when combined are correlated 0.96 with the full K-index. For this data set at least, the K-index is a predictor for precipitation based on low-level moisture and/or midlevel humidity rather than on estimate of atmospheric stability.

[29] Figure 6 (bottom right) shows that there is very little relationship between K-index and convective precipitation intensity. Large values of K-index tend to be associated with a range of convective precipitation intensities.

4. The Stochastic Nature of the Large-Scale to Small-Scale Relationships

[30] Section 3 has shown that there exist a number of relationships between the large-scale state of the tropical atmosphere and the state of convection. However, it was also shown that even the strongest of those relationships, such as that between moisture convergence and convective rainfall area, show a considerable amount of scatter, confirming the at least partially stochastic nature of small- to large-scale relationships. As the degree of stochastic behavior has significant consequences for the representation of small-scale processes such as convection in coarse-resolution (>10 km) models, it is worthwhile to try and further quantify some simple statistical properties of the relationships, which is the goal of this section.

[31] We choose the apparently strongest relationship, namely that between convective precipitation and moisture convergence (Figure 3b) for this investigation. First, the moisture convergence values are grouped into 10 equally-sized bins. Then, for each bin, we calculate the mean and standard deviation of its respective convective precipitation values. Figure 7 shows these quantities and also their ratio. The mean convective precipitation is low for small values of moisture convergence and increases with increasing values of moisture convergence. The standard deviation of convective precipitation also increases with increasing values of moisture convergence. It is clear that for negative values of moisture convergence, the standard deviation of convective precipitation is larger than the mean value suggesting that convective precipitation appears rather stochastic in weak dynamical conditions. For positive and increasing moisture convergence, the mean convective precipitation increases more rapidly than the standard deviation showing that larger values of convective precipitation are likely more deterministically related to the large scale. This is confirmed by the ratio of standard deviation to mean which is around 1.5 for negative values of moisture convergence and above 0.5 for large positive values of moisture convergence. This finding confirms the empirical fact that convective storms in the tropics are easier to predict when embedded into large-scale dynamical features, such as a monsoon trough or the active phase of the Madden-Julian Oscillation, than in weakly forced conditions.

[32] It is interesting to note that the nature of this relationship is not consistent with some existing implementations aimed at characterizing small-scale stochastic behavior in large-scale models, such as multiplicative noise [*Buizza et al.*, 1999; *Teixeira and Reynolds*, 2008] but rather that noise (or the stochastic behavior) decreases as a function of increasing forcing.

5. Discussion

[33] Results in the previous sections have shown that convective precipitation and in particular the area covered by convection are related to a number of characteristics of the large-scale state, in particular moisture convergence and midlevel vertical velocity. One caveat of this study is the location for which the data were available. Given the region around Darwin consists of both areas of land and areas of ocean, it is possible that there may be a strong diurnal component to the found relationships. In particular, the Tiwi Island have strong convective storms each afternoon which may contribute considerably to the total convective precipitation [*Keenan et al.*, 1990; *Crook*, 2001].

[34] The role of the diurnal cycle is further investigated by first calculating the mean diurnal cycle of vertical profiles of vertical velocity (ω). Then the mean diurnal cycle is removed from the timeseries of the vertical profiles of ω. Figure 8 shows the mean ω for deciles of convective precipitation. Red colors represent averages with the largest convective precipitation and blue colors averages with the low convective precipitation. The solid lines are without the diurnal cycle removed and the dotted lines after the diurnal component is removed. It can clearly be seen that the role of the diurnal cycle is to modify the structure of the vertical profiles rather than to significantly alter the magnitude or the relationship of vertical motion with convective precipitation. In fact, the correlations of convective precipitation and moisture convergence or ω at 700 hPa (with the diurnal cycle removed) are 0.77, and all correlations are similar to those in Table 2. Similar results are found when considering moisture and stability variables with the conclusion that the diurnal cycle does not substantially effect the relationships discussed in section 3. Another test for the robustness of the relationships is to divide the data set by wind direction, which in the Darwin region is well known to affect

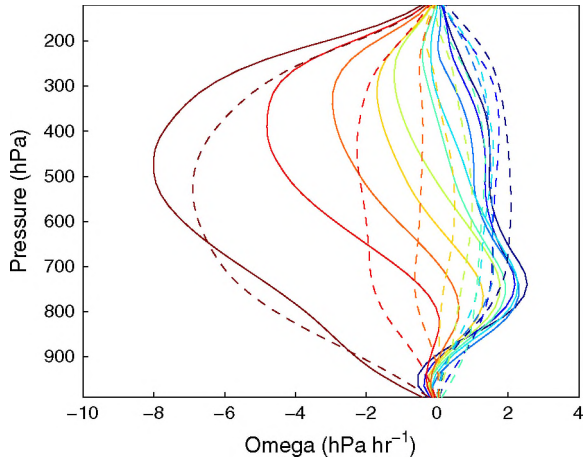

Figure 8. Profiles of vertical motion (omega) over the TWP-ICE domain averaged over deciles of 6 h mean convective precipitation. Deciles with strong precipitation are red and low convective precipitation are blue. The dashed lines show omega with the diurnal cycle removed.

the nature of the convection from more continental in easterly conditions to more oceanic in westerly conditions [*May et al.*, 2008]. There are no discernible differences in the large-to-small-scale relationships when doing so (not shown). Finally, preliminary investigations using similar data sets for another location, namely the largely land-free Kwajalein atoll, also confirm this result (not shown).

[35] As discussed in section 3.1, it is difficult to establish cause and effect relationships between convection and the atmospheric large-scale state from this data, it can only be shown that such relationships exist. For example, convection and moisture convergence are shown to be strongly related in this study and, although the relationship is weaker when considering the moisture convergence 6 h previous, there is still positive correlation. It is likely that, while convection can enhance convergence in a general sense, the relationship is more subtle than simply attributing either cause or effect to either moisture convergence or convection.

[36] An important factor to consider when interpreting the above results is the effect of the temporal resolution and the spatial averaging of the data set on the relationships identified. For example, the relationship between moisture convergence and convective precipitation (Figure 3b) shows that convective precipitation does occur under subsidence conditions. Given that the data are averaged over 6 h periods over a large area, it may be that subsidence does not occur for the whole period or at all locations. There may be localized convergence associated with the precipitation. Another interesting result is that this data set does not show strong relationship between convection and CAPE. The amount of convective precipitation at a grid box in a numerical model is often related to the strength of CAPE through the closure of the convective parameterization. These results, however, suggest the reverse is true, i.e., that convective precipitation is small when CAPE is large. This is understandable as CAPE suggests the presence of instability in the atmosphere; and should convection, and associated convective heating and precipitation develop, the instability would be reduced or removed. In fact, it may be more reasonable to consider that CAPE at some previous point in time might be a predictor for subsequent convective precipitation. This data set suggests a weak positive relationship between convection and CAPE, however, the 6 h temporal resolution of the data limits further detailed investigation of the relationship. Finally, over short-time periods and small spatial areas, convection dries the atmosphere by removing moisture through precipitation. The results here (section 3.2 and Figure 4a) that show that large convective precipitation is associated with large precipitable water may, again, be due to the low temporal resolution data, which is averaged over large areas.

6. Summary

[37] This study uses concurrent observations of the large-scale and convective scale state of the tropical atmosphere at Darwin, Australia to investigate the nature of the relationship between the two scales. It first presents an application of a hybrid approach for deriving the large-scale state of the atmosphere for a tropical location. Testing of the methodology for the period of the TWP-ICE experiment shows that constraining ECMWF analyses with observed precipitation improve the estimates of large-scale variables, such as vertical velocity, compared to the ECMWF analyses alone. It is shown that the hybrid data set is a close approximation of that derived using all observations from the field experiment. The concurrent data set describing the small-scale atmospheric state is derived through the analysis of CPOL radar observations. The radar-derived precipitation data is classified into convective and stratiform components. Complex relationships are found between the small-scale precipitation variables themselves. This study focuses on convective precipitation, convective precipitation area, and convective precipitation intensity as these are the first-order characteristics that need to be represented in convective parameterizations used in GCM. Their faithful representation is a prerequisite for describing the more complex interaction of convection with its associated stratiform cloud systems. It is found, averaged over a domain similar in size to a GCM grid box, that convective precipitation mainly increases through increasing the area that precipitates, which supports the findings of earlier CRM studies.

[38] Investigation into the relationships between the large- and the small-scale states shows that the strongest relationships of the convective scale are with dynamical variables such as moisture convergence or vertical velocity. While the issue of cause and effect cannot easily be separated, the data show clearly that strong convective precipitation is associated with positive moisture convergence while lower convective precipitation occurs under weak or divergence conditions. It is also shown that the stochastic nature of this relationship is dependent on the strength of the large-scale forcing, which is inconsistent with multiplicative noise used in some convective parameterizations. When convection is embedded in a strong dynamically active state, the relationship between the two is highly deterministic. In weak dynamical conditions, although convection is less active, there is much scatter in the relationship. In a relative sense, convection is therefore more stochastic when "weakly forced." This fact is well known to

forecasters in tropical regions when forecasting weather on a daily basis.

[39] Strong relationships with stability related variables, such as CAPE, are neither found with convective precipitation area nor convective precipitation intensity. The relationship identified suggests that when convective precipitation is large, CAPE is most likely to be small, although there is much scatter in the relationship. In fact, a model of convection based on CAPE would suggest a highly stochastic relationship which highlights a possible limitation of current deterministic convective parameterization that are based on CAPE closures.

[40] This study shows that the construction of a high quality long-term data set describing the large-scale atmosphere at a tropical location is possible. In addition to NWP analysis data, the method requires frequent radar observations to calculate precipitation and related small-scale variables. Such data sets can be used to investigate the fundamental relationships between convection and the large-scale atmosphere. Furthermore, where relationships are identified, their deterministic or stochastic nature can be determined. Such data sets provide valuable observational evidence to develop convective parameterizations.

[41] **Acknowledgments.** Davies and Jakob are supported by the Office of Science (BER), U.S. Department of Energy under grant DE-SC0002731.

[42] The contributions of S. Xie to this work were performed under the auspices of the U. S. Department of Energy (DOE), Office of Science, Office of Biological and Environmental Research by Lawrence Livermore National Laboratory under contract DE-AC52-07NA27344 and supported by the Atmospheric Radiation Measurement Program of the Office of Science at the DOE.

References

Arakawa, A. (2004), The cumulus parameterisation problem: Past, present and future, *J. Atmos. Sci.*, *17*(13), 2493–2525.

Arakawa, A., and W. Schubert (1974), Interaction of a cumulus cloud ensemble with the large-scale environment, Part1, *J. Atmos. Sci.*, *31*, 674–701, doi:10.1175/1520-0469(1974)031<0674:IOACCE>2.0.CO;2.

Bechtold, P., M. Köhler, T. Jung, F. Doblas-Reyes, M. Leutbecher, M. J. Rodwell, F. Vitart, and G. Balsamo (2008), Advances in simulating atmospheric variability with the ECMWF model: From synoptic to decadal time-scales, *Q. J. R. Meteorol. Soc.*, *134*(634), 1337–1351.

Bretherton, C. S., M. Peters, and L. Black (2004), Relationships between water vapor path and precipitation over the tropical oceans, *J. Clim.*, *17*, 1517–1528.

Bringi, V., T. Tang, and V. Chandrasekar (2004), Evaluation of a new polarmetrically based Z-R relation, *J. Atmos. Oceanic Technol.*, *21*, 612–623.

Brown, R. G., and C. Bretherton (1997), A test of the strict quasi-equilibrium theory on long time and space scales, *J. Atmos. Sci.*, *54*, 624–638.

Buizza, R., M. Miller, and T. N. Palmer (1999), Stochastic representation of model uncertainties in the ECMWF ensemble prediction system, *Q. J. R. Meteorol. Soc.*, *125*, 2887–2908.

Charba, J. P. (1977), *Operational System for Predicting Thunderstorms Two to Six Hours in Advance*, National Weather Service, NOAA.

Cohen, B., and G. Craig (2006), Fluctuations in an equilibrium convective ensemble. Part II: Numerical experiments, *J. Atmos. Sci.*, *63*, 2005–2015.

Crook, N. A. (2001), Understanding Hector: The dynamics of island thunderstorms, *Mon. Weather Rev.*, *129*(6), 1550–1563.

Dixon, M., and G. Wiener (1993), TITAN: Thunderstorm identification, tracking, analysis, and nowcasting-A radar-based methodology, *J. Atmos. Oceanic Technol.*, *10*(6), 785–797.

Emanuel, K. (1991), A scheme for representing cumulus convection in large-scale models, *J. Atmos. Sci.*, *48*(21), 2313–2329.

Emanuel, K. A. (1994), *Atmospheric Convection*, 1st ed., Oxford University Press.

Holloway, C. E., and J. D. Neelin (2009), Moisture vertical structure, column water vapor, and tropical deep convection, *J. Atmos. Sci.*, *66*(6), 1665–1683.

Houze Jr, R. A., and A. K. Betts (1981), Convection in gate, *Rev. Geophys.*, *19*(4), 541–576.

Keenan, T., B. Morton, X. S. Zhang, and K. Nyguen (1990), Some characteristics of thunderstorms over Bathurst and Melville Islands near Darwin, Australia, *Q. J. R. Meteorol. Soc.*, *116*(495), 1153–1172.

Keenan, T. D., K. Glasson, F. Cummings, T. S. Bird, J. Keller, and J. Lutz (1998), The BMRC/NCAR C-band polarimetric (CPOL) radar system, *J. Atmos. Oceanic Technol.*, *15*, 871–886.

Khouider, B., and A. Majda (2006), Multicloud convective parametrizations with crude vertical structure, *Theor. Comput. Fluid Dyn.*, *20*, 351–375.

Kumar, V. V., A. Protat, P. T. May, C. Jakob, G. Penide, S. Kumar, and L. Davies (2012), On the effects of large-scale environment and surface types on convective cloud characteristics over Darwin, Australia, *Mon. Weather Rev.*, *141*, 1358–1374.

Lin, J., and J. Neelin (2007), Toward stochastic deep convective parameterization in general circulation models, *Geophys. Res. Lett.*, *30*(4), 1162, doi:10.1029/2002GL016203.

Mapes, B., S. Tulich, J. Lin, and P. Zuidema (2006), The mesoscale convection life cycle: Building block or prototype for large-scale tropical waves? *Dyn. Atmos. Oceans*, *42*, 3–29.

Masunaga, H. (2012), Short-term versus climatological relationship between precipitation and tropospheric humidity, *J. Clim.*, *25*, 7983–7990.

May, P. T., J. H. Mather, G. Vaughan, C. Jakob, G. M. McFarquhar, K. N. Bower, and G. G. Mace (2008), The tropical warm pool international cloud experiment, *Bull. Am. Meteorol. Soc.*, *89*, 629–645.

McBride, J. L., and W. M. Frank (1999), Relationships between stability and monsoon convection, *J. Atmos. Sci.*, *56*, 2436.

Neale, R., and J. Slingo (2003), The maritime continent and its role in the global climate: A GCM study, *J. Clim.*, *16*(5), 834–848.

Neale, R. B., J. H. Richter, and M. Jochum (2008), The impact of convection on ENSO: From a delayed oscillator to a series of events, *J. Clim.*, *21*(22), 5904–5924.

Parodi, A., and K. Emanuel (2009), A theory for buoyancy and velocity scales in deep moist convection, *J. Atmos. Sci.*, *66*(11), 3449–3463.

Petch, J., A. Hill, L. Davies, A. Fridlind, C. Jakob, Y. Lin, S. Xie, and P. Zhu (2013), Evaluation of intercomparisons of four different types of model simulating TWP-ICE, *Q. J. R. Meteorol. Soc.*, doi:10.1002/qj.2192.

Peters, O., and J. D. Neelin (2006), Critical phenomena in atmospheric precipitation, *Nat. Phys.*, *2*, 393–396.

Plant, R. S., and G. C. Craig (2008), A stochastic parameterization for deep convection based on equilibrium statistics, *J. Atmos. Sci.*, *65*, 87–105.

Shutts, G., and T. Palmer (2007), Convective forcing fluctuations in a cloud-resolving model: Relevance to the stochastic parameterization problem, *J. Clim.*, *20*, 187–202.

Steiner, M., R. Houze, and S. Yuter (1995), Climatological characterisation of three-dimensional storm structure from operational radar and rain gauge data, *J. Appl. Meteorol.*, *34*, 1978–2007.

Sun, Y., S. Solomon, A. Dai, and R. W. Portmann (2006), How often does it rain?, *J. Clim.*, *19*(6), 916–934.

Teixeira, J., and C. A. Reynolds (2008), Stochastic nature of physical parameterizations in ensemble prediction: A stochastic convection approach, *Mon. Weather Rev.*, *136*(2), 483–496.

Wang, W., and M. E. Schlesinger (1999), The dependence on convection parameterization of the tropical intraseasonal oscillation simulated by the UIUC 11-layer atmospheric GCM, *J. Clim.*, *12*(5), 1423–1457.

Webster, P., and R. Lukas (1992), TOGA-COARE: The coupled ocean-atmosphere response experiment, *Bull. Am. Meteorol. Soc.*, *73*(9), 1377–1416.

Xie, S., R. T. Cederwall, and M. Zhang (2004), Developing long-term single-column model/cloud system - resolving model forcing data using numerical weather prediction products constrained by surface and top of the atmosphere observations, *J. Geophys. Res.*, *109*, D01104, doi:10.1029/2003JD004045.

Xie, S., T. Hume, C. Jakob, S. A. Klein, R. B. McCoy, and M. Zhang (2010), Observed large-scale structures and diabatic heating and drying profiles during TWP-ICE, *J. Clim.*, *23*, 57–79.

Xie, S., and M. Zhang (2000), Impact of the convection triggering function on single-column model simulations, *J. Geophys. Res.*, *105*(D11), 14–983.

Yang, G. Y., and J. Slingo (2001), The diurnal cycle in the tropics, *Mon. Weather Rev.*, *129*, 784–801.

Zhang, C., M. Dong, S. Gualdi, H. H. Hendon, E. D. Maloney, A. Marshall, K. R. Sperber, and W. Wang (2006), Simulations of the Madden–Julian oscillation in four pairs of coupled and uncoupled global models, *Clim. Dyn.*, *27*(6), 573–592.

Zhang, G. J. (2002), Convective quasi-equilibrium in midlatitude continental environment and its effect on convective parameterization, *J. Geophys. Res.*, *107*(D14), doi:10.1029/2001JD001005.

Zhang, M. H., and J. L. Lin (1997), Constrained variational analysis of sounding data based on column integrated budgets of mass, heat, moisture, and momentum: Approach and application to ARM measurements, *J. Atmos. Sci.*, *54*, 1503–1524.

Zhang, M. H., J. L. Lin, R. T. Cederwall, J. J. Yio, and S. C. Xie (2001), Objective analysis of ARM IOP data: Method and sensitivity, *Mon. Weather Rev.*, *129*, 295–311.

Zhang, X., W. Lin, and M. Zhang (2007), Toward understanding the double intertropical convergence zone pathology in coupled ocean-atmosphere general circulation models, *J. Geophys. Res.*, *112*, D12102, doi:10.1029/2006JD007878.

On the Effects of Large-Scale Environment and Surface Types on Convective Cloud Characteristics over Darwin, Australia

VICKAL V. KUMAR,* ALAIN PROTAT,+ PETER T. MAY,+ CHRISTIAN JAKOB,# GUILLAUME PENIDE,@ SUSHIL KUMAR,& AND LAURA DAVIES#

* *School of Mathematical Sciences, Monash University, and Centre for Australian Weather and Climate Research,** Melbourne, Victoria, Australia*
+ *Centre for Australian Weather and Climate Research, Melbourne, Victoria, Australia*
# *School of Mathematical Sciences, Monash University, Melbourne, Victoria, Australia*
@ *Université Sciences et Technologie de Lille, UFR de Physique Bâtiment P5 Laboratoire d'optique Atmosphérique, Lille, France*
& *School of Engineering and Physics, The University of the South Pacific, Fiji Islands*

(Manuscript received 24 May 2012, in final form 4 October 2012)

ABSTRACT

Two seasons of Darwin, Australia, C-band polarimetric (CPOL) research radar, radiosoundings, and lightning data are examined to study the relative influence of the large-scale atmospheric regimes and the underlying surface types on tropical convective cloud properties and their diurnal evolution. The authors find that in the "deep westerly" regime, which corresponds to the monsoon period, the convective cloud occurrence rate is highest, consistent with its highest relative humidity. However, these convective clouds have relatively low cloud-top heights, smaller-than-average cell volumes, and are electrically least active. In this regime, the cloud cell volume does not vary significantly across different underlying surfaces and afternoon convective activity is suppressed. Thus, the picture emerging is that the convective cloud activity in the deep westerly regime is primarily regulated by the large-scale conditions. The remaining regimes ("easterly," "shallow westerly," and "moist easterly") also demonstrate strong dependence on the large-scale forcing and a secondary dependence on the underlying surface type. The easterly regime has a small convective cloud occurrence rate and low cloud heights but higher lightning counts per convective cloud. The other two regimes have moderate convective cloud occurrence rates and larger cloud sizes. The easterly, shallow westerly, and moist easterly regimes exhibit a strong, clearly defined semidiurnal convective cloud occurrence pattern, with peaks in the early morning and afternoon periods. The cell onset times in these three regimes depend on the combination of local time and the underlying surface.

1. Introduction

Convection patterns in the vicinity of Darwin, Australia, a site typical of the monsoon climate of northern Australia, have been investigated using ground remote sensing observations (e.g., Keenan and Carbone 1992; Rutledge et al. 1992; Williams et al. 1992; May et al. 2008; Protat et al. 2011). The main reasons for focusing on Darwin are that 1) the site has one of the most comprehensive long-term meteorological observational networks anywhere in the tropics; and 2) it experiences a wide variety of convective systems, and therefore should have important implications for the wider tropical Asia–Pacific region. Furthermore, the Darwin site combines seasonally varying meteorological conditions with distinct dry, wet, and transition seasons, with a complex topography of coastlines, islands, and oceanic areas. This makes Darwin an ideal location to investigate the relative roles of large-scale meteorology and surface types.

Past studies using data around Darwin explored the statistical characteristics of convection, where meteorological regimes were broadly separated into two categories; the buildup–break periods with low-level easterly winds and monsoon periods with low-level westerly winds (e.g., Keenan and Carbone 1992; Rutledge et al.

** The Centre for Australian Weather and Climate Research is a partnership between the Bureau of Meteorology and the Commonwealth Scientific and Industrial Research Organisation.

Corresponding author address: Vickal V. Kumar, Centre for Australian Weather and Climate Research, Australian Bureau of Meteorology and CSIRO, GPO Box 1289, Melbourne 3001, Australia.
E-mail: v.kumar@bom.gov.au

DOI: 10.1175/MWR-D-12-00160.1

1992; Williams et al. 1992; May and Ballinger 2007). In break periods, cloud cells were reported to be more intense, taller, and electrically more active compared to monsoon periods. However, the daily total rain accumulation is higher during monsoon periods, with a ~50% contribution from stratiform rain (May et al. 2012).

Recent cluster analysis of thermodynamic sounding data using 49 wet seasons (defined as October–April) of radiosonde measurements showed that the Darwin wet season can be subdivided into five objective regimes, which have significantly different synoptic environments (Pope et al. 2009a). These regimes have been shown to be associated with significantly different properties of ice clouds for the Darwin region (Protat et al. 2011). Consequently it is worthwhile to investigate how convective cloud properties may change when data are separated into the five regimes instead of using the simple monsoon–break separation. Such a separation can aid the evaluation and development of convective parameterizations in models (e.g., Jakob 2003, 2010) as it can help better identify the relationship between the large-scale state (as defined by the cluster regimes) and small-scale cloud properties.

Several convective cloud properties will be considered in this study, including convective cloud occurrence and convective cloud-top heights, volume, kinematics, cell onset times, and electrical properties. Another important element affecting the growth of convective cloud systems is the merging of individual clouds since this leads to formation of larger cloud systems (Westcott 1994; Simpson et al. 1993). Previous research efforts in this area generally focused on a single convective cloud property. For example, Westcott (1994) considered case studies of convective cell merging and proposed that merging occurs because of horizontal expansion. Carbone et al. (2000) studied the Hector storms over Tiwi Islands and found that they formed mostly due to sea-breeze convergence. Pope et al. (2009b), using six wet seasons of satellite observations, found that in the north Australian region, mesoscale convective systems (MCSs) during the westerly (easterly) flow generally first formed over the western (eastern) side of Australia and then move across the continent. Building on these previous studies, a unified study of several convective cloud properties as to be carried out here will provide a more complete understanding of convective cloud properties and competing factors that regulate cloud growth.

May and Ballinger (2007) considered a small subset of aforementioned convective cloud properties for the Darwin region, which were identified using the automated Thunderstorm Identification, Tracking, Analysis and Nowcasting (TITAN) radar analysis tool (Dixon and Wiener 1993). Their convective radar echo-top height (ETH) statistics showed little evidence for a multimodal distribution as hypothesized by early observations (Johnson et al. 1999) and models (Liu and Moncrieff, 1998). Instead they found a continuous distribution of ETH with the peak of the distribution shifting toward the tropical tropopause layer (~15 km) as the distributions are conditioned on higher reflectivity (May and Ballinger 2007). But they did not provide any information on the variations with respect to underlying surface and local time or the variability with respect to recently identified large-scale atmospheric regimes.

The present paper aims to extend the May and Ballinger (2007) study. The specific objectives of this study are 1) to assess how the large-scale atmospheric regime affects the distribution of the convective clouds, ETH, and associated electrical activity by analyzing the diurnal and spatial variability; 2) to examine the variability of convective cell volume, kinematics, and cell onset times during the respective large-scale atmospheric regimes; and 3) attempt to ascertain the significance of the large-scale regime against other competing factors such as underlying surface and diurnal cycle, in the production of tropical convective clouds. This paper is organized as follows: the datasets, together with the techniques employed to extract convective cloud properties from radar reflectivities are described in section 2. The basic characteristics and spatial variability of convective clouds properties as a function of the large-scale atmospheric regimes is described in section 3a, followed by an analysis of the diurnal variability in section 3b. Finally, the results are summarized and discussed in section 4.

2. Datasets and method

The study makes use of two wet seasons (October 2005–April 2006 and October 2006–April 2007) of data from the Darwin C-band polarimetric research radar (CPOL; Keenan et al. 1998), the Australian GPATS (http://www.gpats.com.au/) lightning products and radiosoundings at Darwin airport. The sounding data are from the daily 2300 UTC (0830 LT) operational observations. The 2300 UTC data are selected to avoid modification of the environment by strong diurnal convection.

The CPOL radar (12.25°S, 131.04°E) as shown in Fig. 1, collects a three-dimensional volume of data out to a range of 150 km once every 10 min. Each volume consists of a series of 16 conical sweeps at elevations ranging from 0.5° to 42°. The radar transmits alternate linear horizontal and vertical polarization pulses of wavelength 5.3 cm. The main data source used in the present paper is the three-dimensional radar reflectivity after attenuation by rain is corrected for using the method developed by Bringi and Chandrasekar (2001). Other important

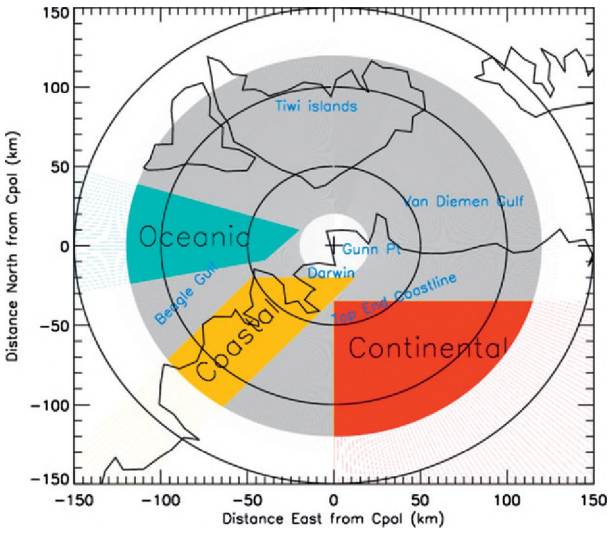

FIG. 1. Sampling domain of the Darwin C-band polarimetric radar (CPOL). The concentric rings in this figure and all subsequent figures are 50 km apart. Only data from the shaded gray region (i.e., ranges 20–120 km) are analyzed in this paper. To better quantify the effects of the underlying surface type, the data for Fig. 12 are separated into oceanic (blue, ~2380 km^2), coastal (yellow, ~4160 km^2), and continental sectors (red, ~7280 km^2).

polarimetric radar retrievals, such as drop size distribution and precipitating water contents are analyzed separately in a paper in preparation.

Figure 1 shows the extent of the domain sampled by the CPOL radar. Only data from the highlighted gray region (radar ranges of 20–120 km) are analyzed in this paper. This is done to reduce errors resulting from limited sample size at close ranges caused by the "cone of silence" occurring at elevation angles greater than 42° and at large ranges due to beam spreading. We also found that the mean radar ETH near maximum range of 150 km is ~1 km higher than the mean ETH within 120 km of radar center. The radar ETH statistics has a small range bias due to the radar scanning geometry; however, this effect is quite small within our radar sampling domain.

Reflectivity data are gridded by constructing a series of the constant altitude plan position indicator (CAPPI) at every 0.5 km in height (with a horizontal bin size of 2.5 km × 2.5 km) extending up to 20 km, using the Sorted Position Radar Interpolation (SPRINT) software. The gridded reflectivity data at a CAPPI level of altitude 2.5 km are processed using the "Steiner" convective–stratiform classification algorithm (Steiner et al. 1995) to determine the occurrence of the convective and stratiform precipitation at individual radar pixels. The Steiner algorithm classifies the gridded reflectivity as convective if the reflectivity value is at least 40 dBZ or greater than a fluctuating threshold depending on the area-averaged background reflectivity (within a radius of 11 km around the grid point). Each convective center has a radius of influence (ranging from 1 to 5 km) also depending on the surrounding background reflectivity (Steiner et al. 1995).

For each identified convective pixel at 2.5-km CAPPI level, the maximum height of the 5-dBZ echoes is computed to provide an estimate of the ETH. Specifically, the ETH corresponded to radar echo height whose reflectivity is the closest to 5 dBZ, but with a reflectivity value within the range of 0–10 dBZ, and provided there are continuous (in the vertical) reflectivity fields between the 2.5-km CAPPI level and this ETH. This procedure filtered out any possible effects of detached cloud layers situated above the convective towers. The 5-dBZ radar ETH definition has been previously used by May and Ballinger (2007).

In most cases, the true cloud-top height will extend higher than the 5-dBZ ETH; however, using *CloudSat* data the difference between cloud-top heights and radar 0- or 10-dBZ ETH has been found to often be within 2 km (Casey et al. 2012). Selecting the lowest available reflectivity per convective column might appear to be a better proxy of cloud-top height. However, this will introduce artifacts because the radar sensitivity drops with range, leading to fewer signals detected at longer ranges. The radar detection sensitivity is 0 dBZ near its maximum range of 150 km, so the choice of 5-dBZ threshold is sufficiently high to allow for detection of echoes at any radar range considered in this study.

This study also makes use of cell-based analysis, such as cell lifetime, speed, direction of movement, and volume. These parameters are derived using the TITAN radar analysis tool (Dixon and Wiener 1993). TITAN identifies convective cloud volumes based on radar reflectivity and volume thresholds. It then tracks these cloud volumes (hereafter referred as simply as "cells") in space at discrete times (every 10 min in this case). Here a minimum volume requirement of 30 km^3 and a reflectivity threshold of 35 dBZ are used to identify convective cells (e.g., May and Ballinger 2007). To reduce noise, filters are applied to the data. We only use information from cells that could be tracked over at least two consecutive radar scans. Thus, the analyzed cells had a minimum lifetime of 10 min. Moreover, only cells that formed and decayed within the radar sampling domain are used in the analysis. This is achieved by rejecting any track that passed beyond a 140-km radius (the maximum radar coverage radius is 150 km). Similar TITAN cell selection criteria have been used elsewhere (Goudenhoofdt et al. 2010). Overall, from a total of 50 485 cells that were detected by TITAN during the two seasons, these filters rejected ~56% of the cells, leaving just over 22 000 cells in our analysis. However, if one chooses to restrict the maximum radius to 120 km, as has been done for the Steiner method, 4500

TABLE 1. Distribution of the large-scale atmospheric regimes, convective cloud activity, and associated lightning strokes in our two-season sample. The data ranges represent the 95% confidence intervals.

		Steiner pixels		TITAN cells with lifetime >10 min				
Regime	Tot days [Oct, Nov, Dec, Jan Feb, Mar, Apr]	Counts per day	Lightning flashes per minute per pixel	Counts per day	Lightning flashes per minute per cell	Lifetime (min)	Speed ($m\ s^{-1}$)	Volume (km^3)
Dry east (DE)	38 [18, 11, 4, 0, 2, 0, 3]	156–407	0.11–0.19	2–6	20.2–28.7	40.2–52.4	6.6–8.7	76–129
East (E)	25 [0, 7, 8, 0, 0, 0, 10]	1210–1861	0.12–0.17	20–35	15.2–18. 2	41.3–47.23	3.6–4.4	84–120
Deep west (DW)	64 [1, 2, 3, 27, 1, 28, 2]	11 076–11 827	0.008–0.010	91–100	0.9–1.3	38.8–40.4	5.89–7.5	61–75
Shallow west (SW)	59 [0, 12, 4, 16, 18, 5, 4]	7957–8390	0.07–0.09	54–67	10.4–11.1	42.1–44.8	5.0–6.0	87–107
Moist east (ME)	175 [0, 19, 43, 19, 35, 29, 30]	7261–7896	0.06–0.07	60–70	8.2–9.1	43.5–45.1	4.5–5.0	93–105

more TITAN cells are discarded. Importantly, the TITAN analysis tool does not require gridded radar data, so the interpolation of the observed conical scans into CAPPIs is not a concern, which allows for an investigation of up to the 140-km range.

A crucial difference between the Steiner and TITAN methods of convective cell identification is that the former is likely to capture small cells such as those in the early growth or decay phase as well as mature cells, while TITAN has been designed to find mostly mature, intense cells. This is because the Steiner method does not have a minimum volume or lifetime requirement and permits lower reflectivities in the analysis (Steiner et al. 1995).

Finally, the electrical properties of the convective clouds are estimated using GPATS lightning data. Similar to other lightning detection networks, the GPATS network uses GPS-synchronized time stamps of the observed lightning sferics signals from each station and locates the strokes using the time of arrival method. To study the response of lightning associated with convective clouds, a lightning stroke was only used for the subsequent analysis provided there was at least one convective pixel occurring within a radius 10 km in distance and 10 min in time of this lightning stroke. These criteria rejected ~6% of strokes, from a total of 153 125 strokes detected within the radar domain over the two seasons.

In the subsequent analysis, the lightning occurrences are expressed in units of flashes per minute per pixel–cell. Several thousands of convective pixels had no lightning stroke associated with them and these "0" flash rates are retained during the calculation.

3. Results

a. Basic convective cloud characteristics during the different large-scale atmospheric regimes

1) MEAN REGIME CHARACTERISTICS

This section provides an account of the average cloud characteristics and associated electrical properties (Table 1), together with horizontal wind vectors, vertical shear of horizontal winds (hereafter, vertical wind shear), and vertical profile of humidity profiles (Fig. 2) for the five large-scale atmospheric regimes identified by Pope et al. (2009a). The long-term thermodynamic profiles and the large-scale environment are described in Pope et al. (2009a). Note that their details, but not their broadscale characteristics, will differ somewhat from our results because of interannual variability. The vertical wind shear profile complement results from Pope et al. (2009a), as wind shear has long been known to have an impact on convective organization, strength, and propagation properties (e.g., Rotunno et al. 1988).

Table 1 shows the 95% confidence interval range of the number of Steiner-identified convective pixels and TITAN cells, together with the lightning flash rate per pixel/cell as a function of the large-scale atmospheric regime. As TITAN keeps track of cell splits and mergers during successive radar volume scans, cell identification can be complex. Here, all cells that had the same "complex track identification number" are treated as one cell. The complex track number remains the same even if the cell splits or merges during its lifetime. For the study period, 78% of the detected TITAN tracks have a simple structure free of any splitting or merging events. The remaining 22% of cells have a complex structure, with a majority of them undergoing cell mergers. Merged cells are typically taller and larger than simple cells (Westcott 1994). The Steiner method treats each individual radar pixel independently.

Note that the 95% confidence interval of the convective occurrence frequency for the respective regimes does not overlap when using the Steiner method (Table 1). This is an initial indication that significantly different convective occurrence patterns do occur during the five large-scale regimes. Differences in convective cloud properties such as cell volume, propagation speed, and lifetime are significant when one compares the results of the deep westerly (DW) regime (corresponds to the active monsoon period) against that of the other regimes.

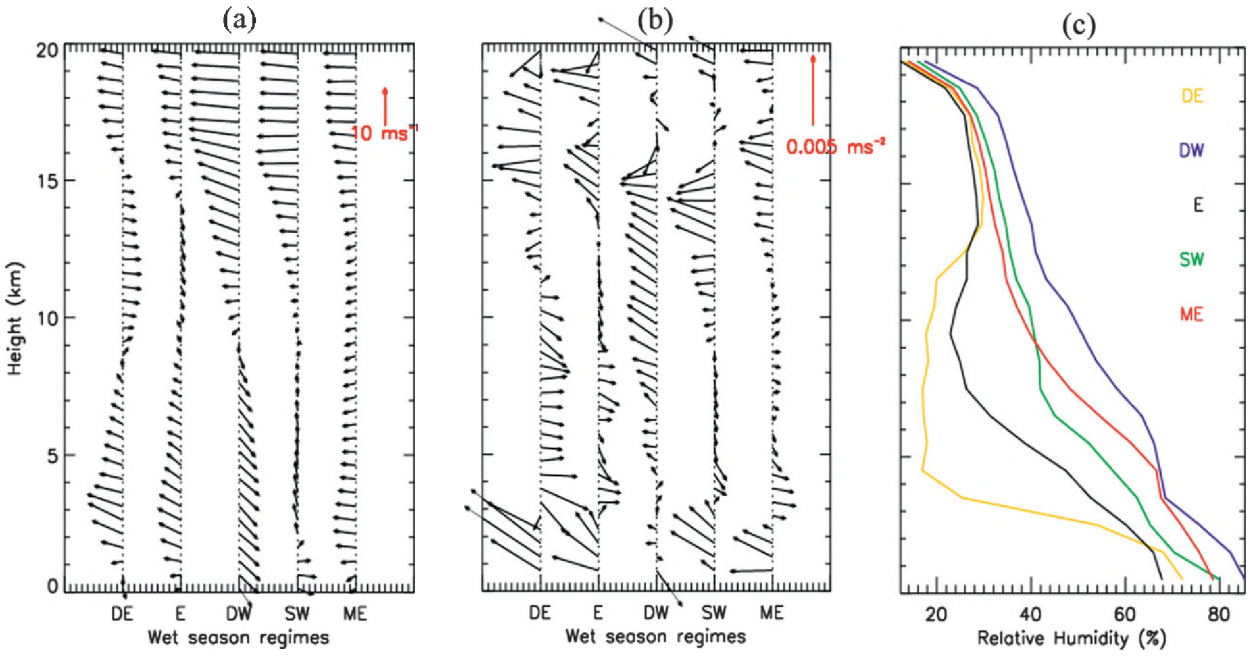

FIG. 2. The 2-yr mean profile of radiosonde measurements of (a) horizontal winds at 0.5-km vertical resolution, (b) corresponding vertical wind shear, and (c) relative humidity for the five large-scale atmospheric regimes [yellow: dry east (DE); black: east (E); blue: deep west (DW); green: shallow west (SW); red: moist east (ME)]. The length of vectors in (a),(b) corresponds to the magnitude of the vectors; the scale is given on the top right-hand corners. The north direction points upward in these figures.

The dry easterly (DE) regime may be viewed as the trade wind regime. It mainly occurs in October and November (Table 1). The winds are southeasterly in this regime at low altitudes (Fig. 2a), reversing to westerly at ~8 km and back to easterly above a 16-km height. The upper-level (>15 km) easterly winds occur persistently in all regimes and are due to the presence of an upper-level jet. The DE regime has cells that typically lasted longer than other regimes. This could be due to the strongest low-level (0–3 km) and midlevel vertical wind shear (Fig. 2b). Robe and Emanuel (2001) and several earlier studies indeed suggested that strong shear in the lower levels produced more organized and longer lived convection. Both the Steiner and TITAN methods show that this regime has the lowest rate of convective activity; however, the lightning flash rate per convective pixel or cell is the highest. Low convective cloud activity is consistent with the lowest relative humidity (Fig. 2c), which is due to a dry continental air mass being advected over Darwin (Pope et al. 2009a). The existence of higher lightning flash rates during premonsoon (and monsoon break) conditions, than during the active monsoon period, has been previously documented over Darwin using lightning data from a separate lightning network (Höller et al. 2009; Labrador et al. 2009). Overall, the DE regime occurs ~11% of the time in our two-season sample and contains only very few detectable radar convective pixels (on average 312 pixels per day). We, therefore, choose not to show any further results from this regime from hereon.

The easterly (E) regime is typically seen as the transition between the trade wind regime and monsoon onset. It occurs mainly in the early and late part of the wet season. For the study period, this regime is the least frequent and accounts for only 7% of our total sample. The E regime has a higher average number of both convective pixels and cells than the DE regime, but is still smaller compared to the other regimes. The large-scale synoptic environment advects an air mass from the Coral Sea over Darwin (Pope et al. 2009a), which creates a moister environment than that of the DE regime (Fig. 2c). The horizontal wind vectors and vertical shear wind profile are similar to the DE regime except in the midtroposphere (8–15 km) where they are much weaker in the E regime (Figs. 2a,b). The lightning flash rate per pixel is moderately high in this regime and is consistent with premonsoonal lightning features (Höller et al. 2009; Labrador et al. 2009).

The DW regime is associated with typical monsoon conditions, and its occurrence peaks between January and March (Table 1). It accounts for 18% of the total sample. The large-scale synoptic environment indicates the presence of northwesterly winds at low levels (Fig. 2a) transporting an air mass of equatorial origin into the

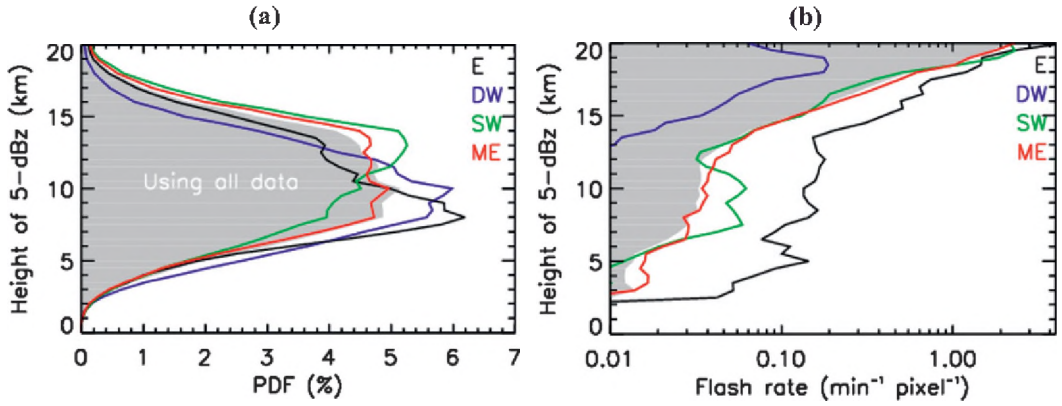

FIG. 3. (a) PDF of the maximum height of 5-dBZ echoes (ETH) for the respective large-scale atmospheric regimes using bin sizes of 1.0 km in height. (b) The lightning occurrence rate (strokes per number of convective pixels in each height bin) as a function of large-scale atmospheric regimes. The lightning flash occurrence varies significantly with increasing ETH, so a log scale has been used in (b). The gray shaded region in both figures represents the PDF obtained using data from all regimes, including the dry east regime.

region (Pope et al. 2009a). They also found that this regime produced the highest amount of rainfall consistent with the highest relative humidity of all regimes (Fig. 2c). Both the Steiner and TITAN methods reveal that the DW regime generates the highest convective area and cell counts per day, respectively. However, the mean volume of the convective cells in the DW regime is relatively small, ~68 km^3, compared to the other regimes with a mean cell volume of close to ~100 km^3. This may be partly because ~90% of cells in this regime have a simple track structure, whereas the other two convective activity regimes [i.e., the shallow westerly (SW) and the moist easterly (ME) regimes described below] have only 67%–70% cells as simple. Also, the low and midlevel vertical wind shear is weakest in this regime, so the convection is predicted to be relatively short lived (e.g., Table 1) and less organized (e.g., Rotunno et al. 1988; Robe and Emanuel 2001). Consistent with previous studies, the DW regime is found to have the least amount of lightning discharges (Höller et al. 2009; Labrador et al. 2009).

The SW regime has previously been found to occur when the active monsoon region moves to the east of Darwin (Pope et al. 2009a). They found this regime to be associated with the largest mean convective available potential energy (CAPE) values of about 1100 J kg^{-1} and potentially stronger updrafts. The SW regime occurs 16% of the sample time. Table 1 shows that the SW regime has the second highest convective area per day and similar number of convective cells as the ME regime (described next). The SW regime is found to have the highest percentage of cells undergoing merger. Also, the electrical activity is consistently higher than in the other two frequently occurring regimes (DW and ME) regardless of the data processing procedure. The wind vectors in the SW regime change fairly rapidly in the first 2 km, veering from westerly near the surface to southerly at ~2 km (Fig. 2a). Between 2–8 km, the winds in the SW regime continued to be southerly and then strongly easterly above 15-km height. The rapid changes in the near-surface winds caused the low-level shear in the SW regime to be approximately 7 times more than in the DW regime (Fig. 2b). The relative humidity level is slightly less than that observed during the DW regime (Fig. 2c).

The ME regime can be viewed as the typical break monsoon period. This regime is the most frequent, occurring 48% of the sample time, and could be interpreted as the "default" state of the Darwin wet season. The convective area and cells numbers are similar to the SW regime but electrical activity seems to be slightly lower. The large-scale synoptic environment indicates the presence of easterly wind anomalies transporting an air mass of equatorial origin, together with large region of convergence over Darwin (Pope et al. 2009a). The sounding data (Fig. 2a) highlight the presence of easterly winds extending throughout the troposphere with the lowest wind magnitude near the ground level and at ~10 km. The low and midlevel vertical wind shear is moderately high in this regime, and therefore favors more organized convection compared to the DW regime.

2) CONVECTIVE 5-DBZ ECHO-TOP HEIGHTS AND ASSOCIATED LIGHTNING

This section shows the overall variation of the 5-dBZ ETH extracted using Steiner convective pixels and associated lightning as a function of the large-scale atmospheric regime. The diurnal features of these two cloud properties are in section 3b(2). Figure 3a shows

the probability distribution function (PDFs) for ETH using 1-km bins in height for the four regimes with sufficient samples: E, DW, SW, and ME. The shaded gray region in this figure and all subsequent figures is the average distribution obtained using data from all days, regardless of regime classification. Figure 3b shows the vertical profile of the lightning flash rate per pixel.

The ETH distribution for all convective pixels (gray shaded region) shows a broad peak between 8 and 14 km (Fig. 3a). Each large-scale atmospheric regime shows a single peak occurrence in the ETH. There is no clear evidence of a multimodal distribution of convective ETH as reported by previous studies (e.g., Liu and Moncrieff 1998; Johnson et al. 1999) even though a significant amount of cumulus congestus cloud is present in our analysis. Our analysis is unable to reproduce the trimodal distribution of Johnson et al. (1999) because 1) each individual convective cloud could have several ETH, which will smear out the less-dominant peak occurring near the tropopause layer [~15 km; our main goal here is to study the convective fractions, so ETH data are considered more suitable than cloud-top height (CTH)]; and 2) the shallow cumulus clouds with peak heights within 1–2 km are usually missed because they are typically nonprecipitating and so cannot be captured with our C-band radar due to minimum detectable signal and sampling issues. However, there seems to be some evidence of a multimodal peak in convective ETH when it is presented as a function of diurnal cycle (see Fig. 11).

Figure 3a shows that the E regime (black) has the peak occurrence at the lowest height of all regimes (~8 km), followed by the DW regime (~11 km). The deepest convective clouds form in the SW regime with a peak occurrence at ~14 km and could be associated with stronger updrafts (e.g., Pope et al. 2009a). The mean distribution (gray shaded region) and the ME regime are mostly similar, since the ME regime is by far the most frequent (see Table 1). The TITAN method also produces the same dependence of ETH on large-scale regime except that the occurrence peak height is higher by 1–2 km (not shown).

The lightning occurrence profiles (Fig. 3b) show that the lightning rates increase strongly with convective ETH, with all but the DW regime showing the most lightning for the deepest clouds. The convective clouds in the E regime produce about 2–3 times more lightning than other regimes for all ETH up to a height of ~15 km. Notably, the SW regime has a secondary peak in lightning production rate associated with ETH around 10 km (Fig. 3b). In general, lightning is believed to be triggered when there is interaction between the upward flux of supercooled liquid water and the downward flux of graupel in the mixed phase (−10° and −40°C) of thunderstorms (Deierling et al. 2008). To maintain this process, sufficient CAPE to support vertical motions in excess of 6–7 m s^{-1} is required to supply supercooled liquid water in the mixed phase (van den Broeke et al. 2005). Large CAPE values potentially lead to stronger updrafts and higher ETH, so it is logical to expect the lightning flash rates to increase with ETH.

Figure 4 provides the spatial distribution of the average ETH, convective cloud occurrence frequency, and associated lightning flash rates. All data in this figure are interpolated to a 5 km × 5 km grid. We notice that the average ETH (top panels) is slightly higher beyond the ranges of 120 km (not shown) due to the beam spreading effect. Small size convective cells (which are typically shallow in height) with a narrow horizontal cross-sectional area become less frequent as the horizontal distance between adjacent beams widen at farther ranges because they are likely to be missed during the SPRINT interpolation. As a result mostly wider, taller cells contribute to the mean ETH near the maximum sampling range.

During the E regime (left column) a maximum in convective clouds is found over the ocean. The oceanic clouds in this regime generally have a higher mean ETH of ~10.5 km, compared to those occurring over land, whose average height is ~8 km. The lightning occurrence peaks tend to be collocated with regions of higher average ETH, with a significant proportion occurring along the coastline. Data from lightning networks have also shown significant lightning along the top end coastline of Darwin (e.g., Labrador et al. 2009).

During the DW regime the convective cloud occurrences are found to be larger over the western half of the domain, with the majority of them occurring in the Beagle Gulf (see Fig. 1 for location) and its coastal boundary regions. This region has been shown to have maximum precipitation during Darwin monsoon periods (May et al. 2012). The mean ETH is ~10 km, which is low compared to the other convectively active regimes (SW and ME), but convective cloud occurrence rate, especially over the ocean, is highest in this regime. This may be because during the DW regime, convection is embedded in a large-scale ascending region associated with the monsoon trough (May et al. 2012). The lightning locations are generally widespread and low in occurrence, with a maximum lightning occurrence being collocated with the maximum occurrence of convective cells.

A comparison of the spatial maps of the SW regime against the DW regime suggests that the peak convective occurrence locations show some tendency to shift eastward, from the western half in the DW regime to the region within 50 km surrounding the radar center. This

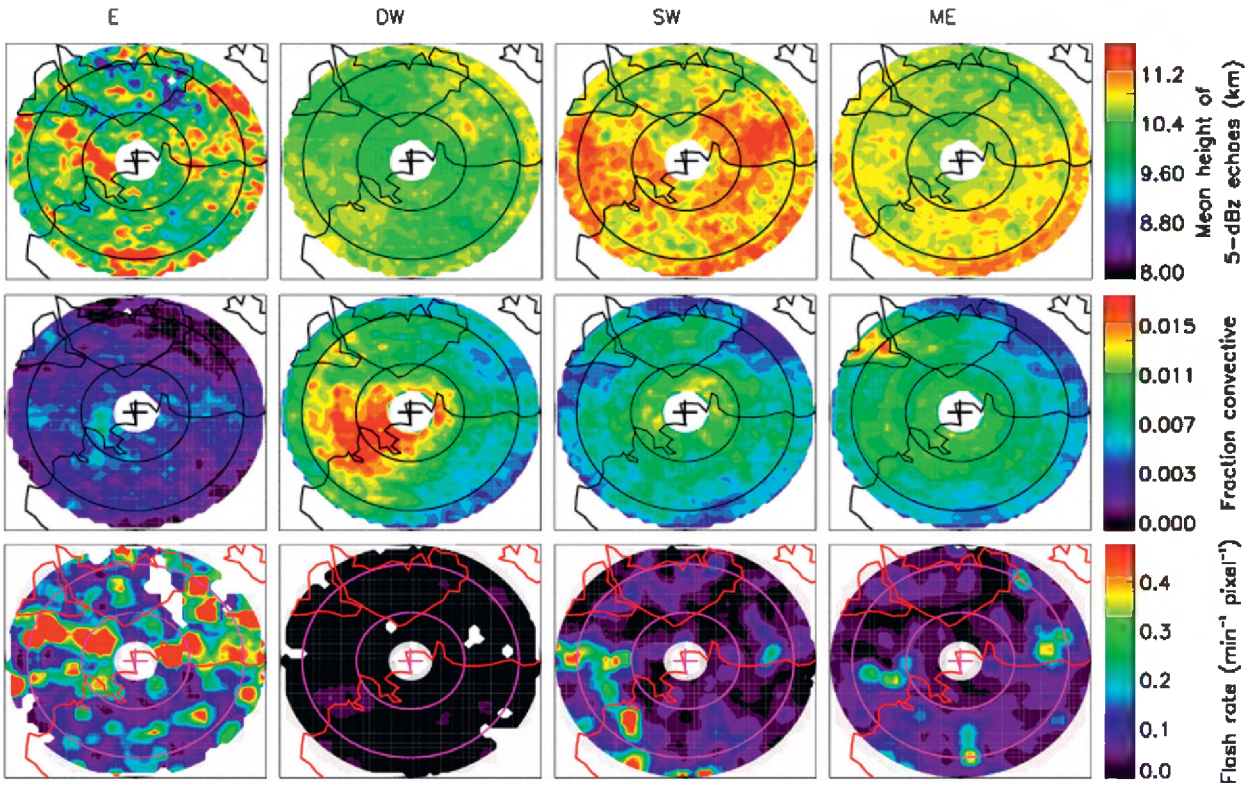

FIG. 4. Spatial maps showing (top) the mean height of the 5-dBZ echoes, (middle) the occurrence counts of convective pixels, and (bottom) the occurrence count of lightning strokes associated with these convective pixels for (from left to right) the respective large-scale atmospheric regimes. A bin size of 5 km × 5 km is used here with maximum coverage of 120 km from the radar center. The occurrence counts in second panels are expressed as a fraction of maximum possible number of measurements per bin.

is consistent with the conjecture that during the SW regime, the active monsoon region has moved to the east of Darwin (Pope et al. 2009a). The mean ETH is clearly the highest of all the regimes. The lightning occurrence rate is also the higher in this regime compared to the DW regime, with the maximum lightning occurrence located mainly over the ocean. Possible reasons for the higher lightning occurrence over the ocean than the land are discussed in section 3b. A closer examination of radar reflectivity loops and lightning occurrence reveals that the observed lightning occurrence peak is due to a significant number of events, not just a few extreme events.

During the most common regime (ME), maximum convective cloud occurrences are on the western part of the Tiwi Islands, consistent with the frequent occurrence of Hector storms (e.g., Carbone et al. 2000). Early storms typically occur over the eastern part of the Tiwi Islands and propagate westward during the break monsoon conditions. Carbone et al. (2000) explains that these storms intensify as they approach the west coast due to cell merger, and so more convective pixels are detected by the radar on the western part of Tiwi Islands. However, these Hector storms do not seem to be as electrically active as storms forming along the top end coastline. Focusing only over the Tiwi Islands, the lightning flash rate per convective pixel seems to the highest along the west coast region where the cell merger is most likely to occur. This is consistent with the electrical activity associated with typical Hector storms (Carey and Rutledge 2000). They found no significant lightning during the developing stage of the Hector storms and the maximum flash intensity was associated with the cell merger during the mature phase. The mean ETH shows moderate dependence on the underlying surface, with ETH slightly higher over the mainland than over ocean and Tiwi Islands. The convective activity is minimum northeast of Darwin in this ME regime.

Overall, the results shown in Figs. 3 and 4 indicate that convective cloud occurrence, ETH, and associated lightning depend both on the large-scale atmospheric conditions (as exemplified by the Pope et al. 2009a regimes) and the underlying surface. In the next sections, we investigate the effects of these two factors on other properties of convective cells such as cell lifetime, propagation parameters, volume, and cell genesis time.

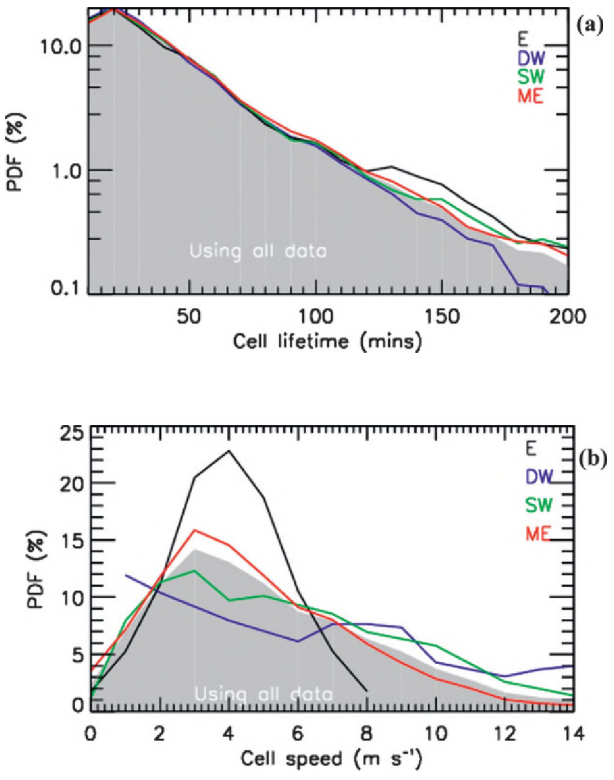

FIG. 5. As in Fig. 3a, but showing the PDFs of TITAN (a) cell lifetime using a bin size of 10 min in time and (b) cell speed using a bin size of 1 m s^{-1} for the respective large-scale atmospheric regimes. As discussed in the text, only TITAN cells with lifetimes > 10 min (and cells that formed and decayed within 140 km of the radar center) are used in this figure and all subsequent figures.

These cell properties are derived using the TITAN analysis tool.

3) CONVECTIVE CELL KINEMATICS

The aim of this section is to examine the variation of convective cell kinematics (i.e., cell lifetime, speed, direction, and displacement) obtained using the TITAN tool and their spatial distribution in the four large-scale atmospheric regimes. Results for the DE regime are again not presented because on average this regime had two TITAN cell tracks per day. In all four regimes, the cells are mostly short lived with a mode occurrence lifetime of 20 min and a strongly positively skewed duration frequency (Fig. 5a). Longer-lived cells, such as those with lifetime exceeding 100 min (~5% of all TITAN cells), are found to be least frequent in the DW regime.

In contrast, the cell speed varied significantly during the respective regimes (Fig. 5b). The easterly regimes (E and ME) exhibit a much narrower distribution of cell speed with a peak occurrence near 3 m s^{-1}. However, the westerly regimes (SW and DW) are characterized by a broader distribution, with 30% (15%) of the cells in the DW (SW) regime having cell speeds exceeding 10 m s^{-1}. This greater cell speed in the westerly regime, particularly the DW regime, is because the steering flow speeds (wind speed at 700 hPa or ~3 km, see Fig. 2a) are larger in those regimes.

Figure 6 shows spatial maps of the cell track distribution and their average displacement, lifetime, and speed, as a function of regime. The cell displacement is calculated as follows. First, the coordinates of the cell center at first detection ($t = 0$ h) are grouped into 20 km × 20 km bins with respect to radar center. A 20 km × 20 km bin size is chosen to give at least 5 TITAN tracks per bin. Then for all cells in a bin the average location of the cell center at decay (t = termination of cell) is calculated. The average displacement vector is then defined as the position of cell decay relative to its onset and is shown as an arrow for each bin in the third panels of Fig. 6.

The spatial distribution of the TITAN tracks (top panels in Fig. 6) is similar to the distribution of convective pixels (second panels in Fig. 4). The most noticeable difference occurs in the ME regime, with the western part of Tiwi Islands showing comparatively less TITAN tracks than convective pixels. This can be explained since the TITAN occurrence maps show a given track only once at cell onset. As indicated above, the western island maximum found by the Steiner method represents Hector storms, which are usually born on the eastern part of the Tiwi Islands and then they propagate westward where the sea-breeze interaction makes them more intense (Carbone et al. 2000).

According to the bottom three panels in Fig. 6, cells tend to propagate for larger distances in regions located on the windward side of the incoming large-scale atmospheric circulation. For example, cells located in the northwest half of the domain in the DW regime and those in the southeast half in ME regime propagated for longer distances since they last longer and/or propagate faster. The steering flow mainly controls the direction of propagation of the TITAN cell, but it cannot explain the gradual drop in the cell propagation distance as they move from the windward side to the leeward side. The hypothesis that this gradual drop in cell propagation is an artifact because fast-moving and long-lived cells are more likely to be filtered out from the leeward side by our cell selection criteria (since they are more likely to propagate beyond 140 km from the radar center) was investigated and rejected. A similar result is obtained when we used all cells, even those that extended beyond 140 km from the radar center.

To further investigate this, we calculated spatial variation of the percentage of cells rejected compared to all

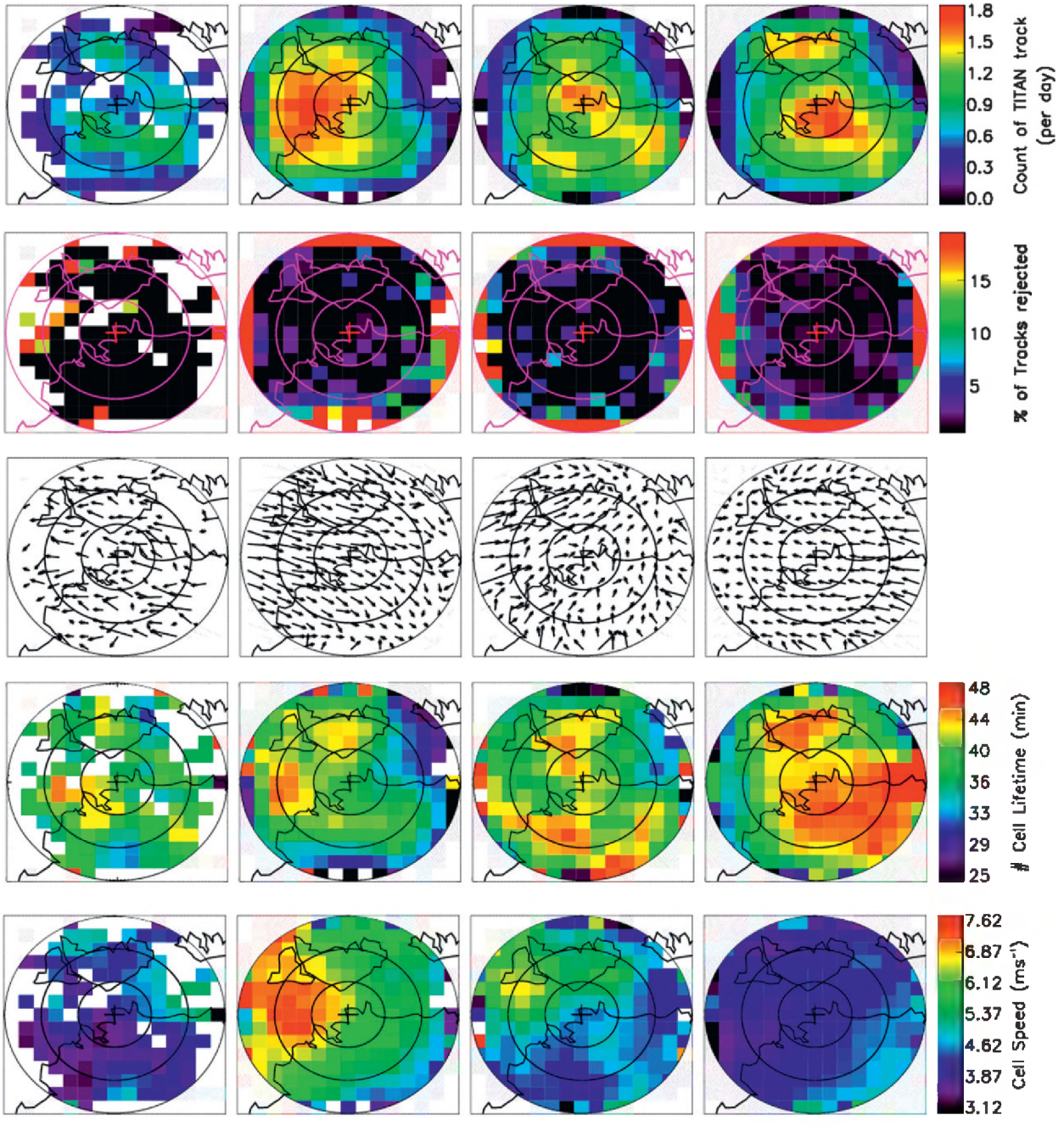

FIG. 6. Spatial maps of (from top to bottom) total number of TITAN tracks per day in 20 km × 20 km bins, percentage of TITAN cells rejected by our filters (cells within 140 km vs all cells with lifetimes >10 min), their average displacement using a feather plot, average lifetime, and average speed for the respective large-scale atmospheric regimes. Spatial bins with missing vectors or white colors indicate that the bins contained <5 TITAN tracks. The length of vectors in the third row represents the mean ground displacement of the cells.

cells when using a 140-km maximum radius requirement (provided the cell lifetime was at least 10 min). The results of this analysis are shown in the second panels of Fig. 6. It shows that our filters rejected less than 2% of cells in the circular region of radius 100 km bounded by the second concentric ring. Importantly this region does not show any spatial gradient in the cell-rejection frequency, but we still observed longer-propagating cells on the windward side compared to the leeward side in this inner region. Analysis of the spatial variation of the ratio of merged cells to all cells (results not shown) indicated that cell mergers on the windward side tend to

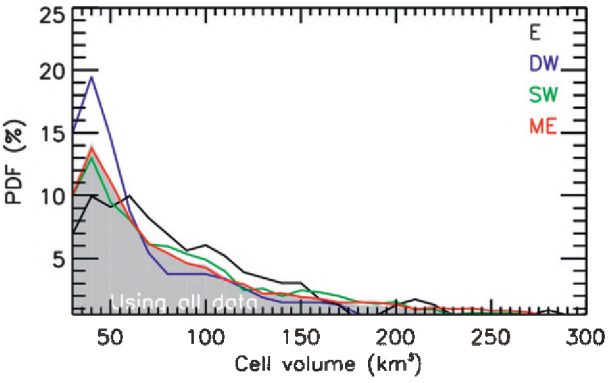

FIG. 7. As in Fig. 3a, but for the PDFs of TITAN cell volume using a bin size of 20 km^3.

be higher than on the leeward side. This result supports the observations of longer-lived cells (e.g., Westcott 1994). High-resolution 3D winds and gridded thermodynamic profiles for the region around Darwin would be needed to further understand the salient cloud physics causing this effect, which will be the subject of further investigations.

4) CONVECTIVE CELL VOLUME

The aim of this section is to examine the variation of convective cell volume and its spatial distribution with a large-scale atmospheric regime.

The SW and ME regime show a similar distribution of TITAN cell volumes (Fig. 7), with both the DW and E regimes deviating from the mean distribution more significantly. The proportion of cells with a small volume of 30 km^3 is ~15% for the SW and ME regimes, while it is much larger (~22%) for the DW regime and smaller (~11%) for the E regime. Bigger volume cells are most frequent in the E regime, though results are drawn from a smaller number of events. Within the convectively active regimes (DW, SW, and ME), cells with a large volume are more frequent in the SW regime (55% of the cells had volume >60 km^3) and ME (51%) regimes compared to the DW regime (37%). An interesting feature of the SW and ME regimes is that the cells over land have a larger volume compared to those occurring over ocean (Fig. 8). In contrast, in the DW regime the cell volume shows little dependency on the underlying surface. The drop in cell volume at the far southeast of Darwin could be an artifact associated with increase in the rejection of TITAN cells by our filters (second panels Fig. 6). Overall, this points out that the convective clouds in the DW regime are embedded within the large-scale monsoon trough.

Overall, the variability in cell volume is linked to both the large-scale atmospheric circulations and the nature of the underlying surface. For example, cell volume is largest in the E regime, smallest in the DW regime, and intermediate in the SW and ME regimes. Comparing the three most frequent regimes, they all, except for the DW regime, have larger cells over the continent than over the ocean. Since cell volume (Fig. 8) reveals a similar response as the cell area (results not shown here) and to some extend as the ETH (top panels Fig. 4), it is fair to assume that cells with larger volume will have a greater mean ETH and a wider horizontal extent.

b. *Effects of the large-scale regime on the diurnal cycle of convection*

Having identified significant differences in basic cloud cell characteristics for the four large-scale regimes used in this study, this section focuses on the diurnal cycle of cell characteristics, in particular convective ETH occurrence and associated lightning, as they are indicative of the intensity and microphysical characteristics of the convective systems.

1) CONVECTIVE CELL ONSET TIME

In this section we examine variation in cell onset time by binning the onset times with respect to the Darwin local time (LT = UTC + 9 h, 30 min). The distribution of cell onset times (Fig. 9) shows that most of the cells are triggered during the day with a secondary peak occurring in the early morning period. For the DW regime, the daytime peak of the cell onset occurs the earliest,

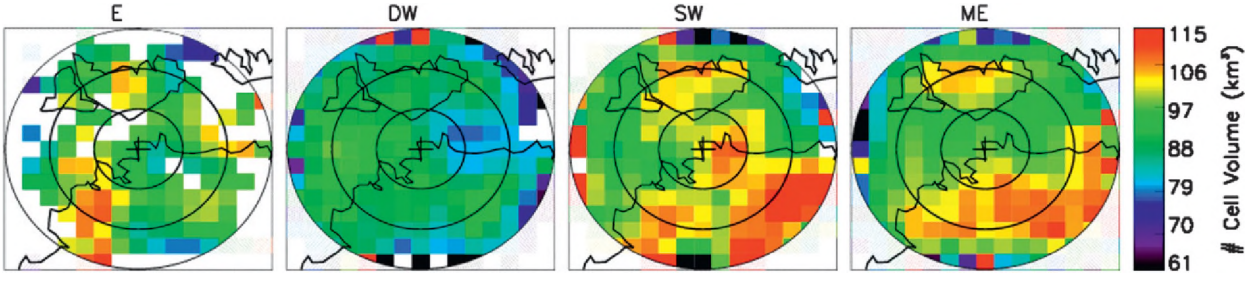

FIG. 8. As in Fig. 6, but for the spatial maps of average cell volume per 20 km × 20 km bins.

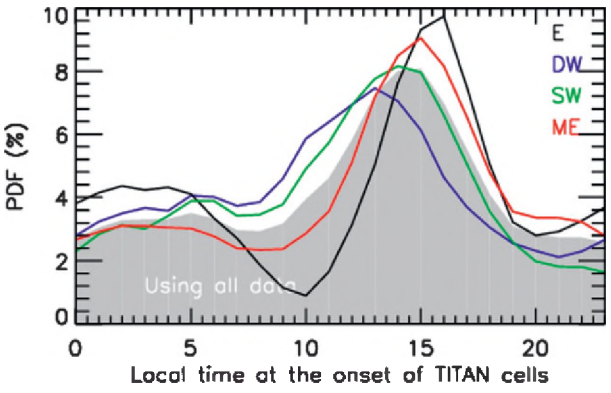

FIG. 9. As in Fig. 3a, but for the PDFs of the TITAN cell onset times using bin size of 1 h in LT.

around midday, followed by the SW regime at 1400 LT and around 1500 LT for the easterly regimes.

The spatial maps of the cell onset times (Fig. 10) show well-defined differences in the dominant local time of the onset of convective cells with respect to the underlying surface. Some caution must be exercised when interpreting the results shown in Fig. 10, as the colors only represent the modal local time of the onset of convective cell development. Obviously some cells will be born outside the modal local time period for a given underlying surface. Over the ocean, the cells are triggered mainly in the early morning and in some cases around midnight, regardless of the regime type. Over land, the cells are predominantly triggered in the afternoon except for the DW regime. In the DW regime, the triggering of the cells within ~60 km from the coastline happens around midday, while for the remaining land region it still occurs in the afternoon. These features in the diurnal cycle of cell onset time with respect to different underlying surface types are consistent with earlier research (Liu and Zipser 2008 and references therein).

In all regimes except the DW regime, convective cells over land are likely initiated by sea breezes whereas ocean cells are predominantly triggered by the land breeze. Thus, the cell onset times are strongly dependent on diurnal cycle and on the underlying surface, in at least three out of four regimes. In contrast, in the DW regime (or monsoon period) with extensive cloud cover, radiative heating of the land is less effective resulting in changes to the mechanisms that trigger convection (May et al. 2012).

2) THE DIURNAL CYCLE OF CONVECTIVE ETH

Figure 11 shows the evolution of ETH occurrence frequency as a function of time of day and height for each of the large-scale regimes. The ETH occurrences are calculated separately for each bin of 1 h in local time and 1 km in height, and then normalized by the number of days in each regime. For clarity, the counts are then further divided by the peak occurrence value in each panel (peak values given on the bottom right-hand corner). The density of points as a percentage of the maximum occurrence is presented using a color scale with white indicating that no data is recorded in this bin.

In the E regime, the convective echo occurrence is highest in the afternoon and in the early morning period (Fig. 11). It appears that, especially in the afternoon period, the clouds are generally shallow during the early growth phase and progressively develop into deeper clouds in the mature stage. This diurnal cycle is consistent with that of the nonprecipitating ice clouds over Darwin during that same regime, as characterized in Protat et al. (2011). This consistency suggests that in the E regime, nonprecipitating ice clouds are predominantly convectively generated. At all times, except for the afternoon period, mean ETH (black curve) during the E regime is lower than the mean values for all regimes (black–white dashed curve). The electrical activity in the E regime is semidiurnal and follows the convective echo occurrence frequency, with the lightning flash rate peaks occurring fewer hours prior to peaks in convective ETH occurrence (white curve).

The DW regime shows a prolonged period of occurrence of convective clouds from midnight through the morning with a peak around midday, and a clear

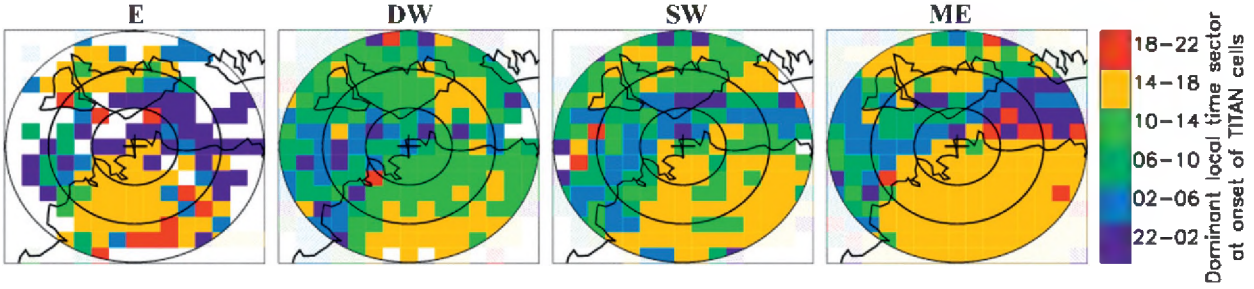

FIG. 10. As in Fig. 6, but for the spatial maps of the dominant local time period at the onset of TITAN cells per 20 km × 20 km bins.

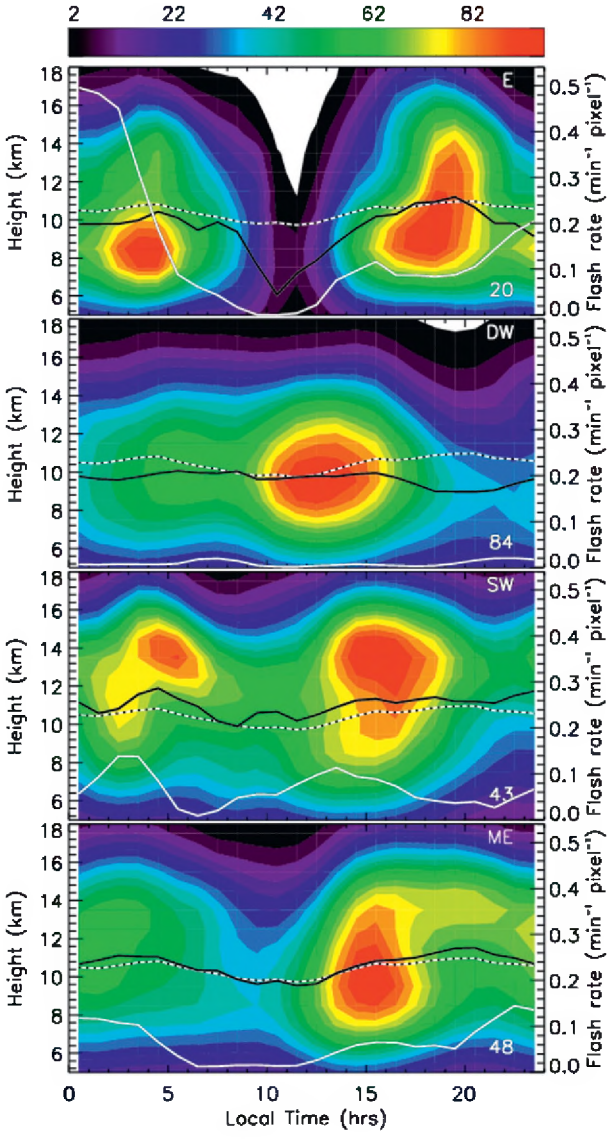

FIG. 11. The time–height distribution of the frequency of occurrence of 5-dBZ echoes at the top of convective clouds identified using the Steiner classification (from top to bottom) for the E, DW, SW, and ME. A bin size of 1 h in LT and 1 km in height is used in these plots. The echo counts per bin are first divided by total number of days of respective regime, and then expressed as a percentage of the highest bin echo count per panel. The highest count is stated on the bottom right-hand corner in each panel. The black curves are the mean diurnal variation of 5-dBZ cloud height with the solid curve for each regime and the black–white dashed curve calculated using data from all regimes, including the dry east regime. The solid white curve is total lightning counts.

occurrence minimum in the evening (Fig. 11). Typically during monsoon conditions, which the DW regime represents, there is a large proportion of stratiform clouds (May and Ballinger 2007). Hence, the convective ETH diurnal cycle is expected to deviate from that of rainfall, which often shows a maximum in the afternoon and evening. Overall, the average ETH of ~10 km is generally lower than in the all-regime average. The DW regime is the least active in terms of lightning and this could be due to insufficient updraft speeds within the convective core to produce lightning (e.g., van den Broeke et al. 2005). Unlike the E regime, the frequency of occurrence of nonprecipitating ice clouds in the DW regime in Protat et al. (2011) is very different from the convective ETH statistics obtained here. The maximum in nonprecipitating ice cloud occurrence occurs later than the convective ETH occurrence maximum, between 1500–2000 LT (Fig. 2d in Protat et al. 2011). This comparison suggests that during the DW regime, thick nonprecipitating anvils and cirrus decks produced by deep convection are much longer lived than during other regimes. During the DW regime, the diurnal variation in atmospheric temperature is weak due to widespread cloud cover reducing the daytime heating of the land (May et al. 2012). This largely explains the lack of a strong evening peak in the occurrence of convection during this regime.

During the SW regime the average ETH is higher than the mean values for all regimes at all times of the diurnal cycle, with two peaks: one in the morning and one in the afternoon. We previously have shown that the SW regime also contains the tallest convective ETH (Fig. 3a) and with moderate cell volume (Fig. 7) possibly due to stronger updrafts and increased occurrence of cell merging. The peak in nonprecipitating ice cloud occurrence (Protat et al. 2011) is shifted to a later time (2000–2400 LT), suggesting again the production of extended anvils by deep convection associated with the SW regime, as is the case for the DW regime as well. The SW regime is found to have the second highest lightning activity, with the majority of lightning strokes generated by the early morning storms. Again the peak in lightning flash rates tends to occur few hours ahead of the peak in convective ETH occurrence.

During the most frequent ME regime, the results reveal that the early phase of storm development occurs at ~1500 LT with a peak height of 9 km (Fig. 11). These cells mature within a few hours, becoming towering cumulonimbus clouds with a peak occurrence height of 14 km. This diurnal cycle is consistent with that of the nonprecipitating ice clouds (Protat et al. 2011) in this regime. This suggests that thick anvils and cirrus decks produced by deep convection are shorter lived than during the DW and SW regimes. From the evening through the night the convective systems gradually decay causing a gradual drop in ETH. This drop is also found in the nonprecipitating ice cloud statistics (Protat et al. 2011). The infrared satellite observations analyzed

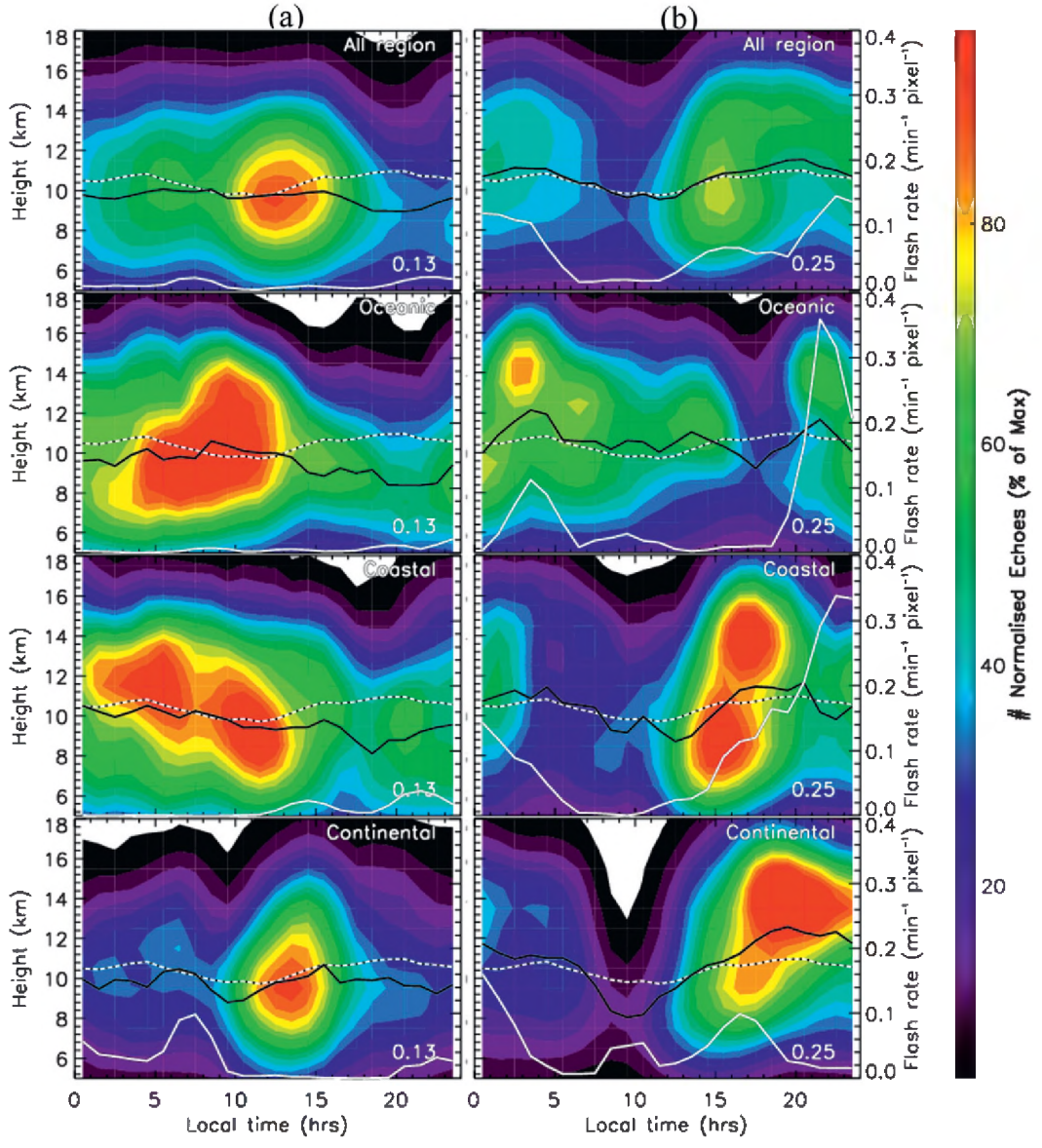

FIG. 12. The time–height distribution of the frequency of occurrence of 5-dBZ echoes above convective clouds identified using Steiner classification for the (a) DW and (b) ME regimes. (from top to bottom) All echoes, echoes located above the oceanic region, coastal region, and continental regions. All panels are as in Fig. 11, but the count has been normalized by respective area of each underlying surface type. The three underlying surface types are highlighted in Fig. 1

by Pope et al. (2009b) confirm a mesoscale convective system genesis time near 1500 LT during monsoon break periods, and these usually decay within approximately 3 h. The lightning flash rates are highest when the ETH reached the peak heights in the evening period.

A shortfall in Fig. 11 is that the responses in ETH may be affected by the complex topographic environment around Darwin. We attempt to rectify this by further splitting the time–height pdfs of ETH into three groups of different underlying surface types, namely, oceanic, coastal, and continental. The results are shown in Fig. 12 and the area covered by the three surface types is shown in Fig. 1. In the DW regime (Fig. 12a), the peak occurrence in convective clouds occurs earliest over the oceanic surface in the early morning period and progressively shifts inland, peaking over the continental surface near midday. This progression of convective cloud activity from the oceanic region through coastal and then over land is consistent with the picture that convection in the DW regime is embedded in the large-scale forcing by

the monsoon trough. In contrast, convection in the ME regimes seems to be primarily dependent on conditioning of the atmosphere by land and sea-breeze processes. For example, the majority of convective cloud activity occurs above the oceanic region in the early morning period, with peak heights at 14 km. In contrast, during the afternoon and evening periods, the convective cloud occurrence is highest above the coastal (bimodal peak height of 9 and 14 km) and continent (peak height of 14 km) regions, respectively. There is little evidence to suggest that the early born coastal convection is progressing over the continent since storms in the ME regime mainly propagate toward the ocean (see Fig. 6). Results for the E and SW regimes are not shown because they exhibited less noticeable differences in the convective cloud occurrence over the three underlying surfaces.

Overall, the results shown in Figs. 11 and 12 indicate that the diurnal cycle of convective cloud occurrence and their top heights, and spatial location of the convective clouds, contrast considerably among the four large-scale atmospheric regimes. First, all the regimes, except the DW regime, show intense convective activity in the late afternoon, presumably initiated by the sea-breeze circulation that forms on the top end coastline. The results also indicate that sea-breeze effects are less important during the DW regime. Second, the DW regime clearly shows oceanic characteristics, while the ME regime demonstrates much more continental characteristics. Third, the SW regime (and the E regime, though results are drawn from a smaller number of events) show high convective activity after midnight and in the early morning, thus showing that convection in this regime exhibits somewhat oceanic characteristics. Finally, the comparison of the diurnal cycle nonprecipitating ice clouds and convective cloud towers indicate that the thick anvils and cirrus decks produced by deep convection are shorter lived during easterly regimes (E, ME) and longer lived during the westerly regimes (DW, SW).

Higher lightning flash rates after midnight (vs afternoon or evening), particularly in the E and SW regime, and over the coastal boundary region (vs continent) do not seem to be consistent with the traditional picture of having more lightning over land and in the afternoon period. The complex topography of coastlines, islands, and oceanic areas within our sample area combined with the distinct wet regimes may be contributing toward this discrepancy. On the other hand, since the Darwin site with its Doppler radar pair can provide higher-resolution 3D wind data, it will offer an opportunity in the future to derive upward mass fluxes and to check consistency with lightning activity (e.g., Deierling et al. 2008). The question is as follows: for a given mass flux rate, do convective cells produce more lightning when located over land (vs sea) or in the afternoon period (vs the early morning period)? This is the subject of ongoing investigations.

4. Conclusions and summary

Polarimetric weather radar data collected over two wet seasons (October 2005–April 2006; October 2006–April 2007) at the tropical low-latitude station of Darwin, northern Australia, are used to study the variability of convective cloud properties with both the large-scale state of the atmosphere, the diurnal cycle, and the underlying surface type. The properties of convection studied here include the frequency of convective cloud occurrence, 5-dBZ echo-top heights (ETH), kinematics (lifetime, speed, and direction of propagation), cell structures, and volumes. Both the spatial and diurnal variability of these tropical convective cloud properties are studied as a function of the identified main large-scale atmospheric states in this area.

A summary of the key findings is as follows:

1) The most frequent ME (break) regime shows the highest convective activity from afternoon to midnight and a secondary occurrence peak in the early morning. These convective clouds occur most frequently on the western part of Tiwi Islands, which is consistent with the signature of the well-known Hector storms. In the afternoon the convective clouds are initially shallow with a modal height of ~9 km, and within a few hours grow into deeper convective towers with a modal height of ~14 km. The ETHs are higher and the cloud cell volumes are larger over land than sea. It is also very clear from the results that the land cells in this regime are predominantly initiated in the afternoon by sea-breeze processes whereas ocean cells pop up in the early morning due to land breeze effects. Overall, the convection in the ME regimes seems to be well organized and shows characteristics similar to continental convection. Since this regime occurred for nearly 48% of the wet season, its convection patterns could be a fair representation of the default climatology of Darwin.
2) In contrast, the DW regime, which corresponds to the active monsoon period, exhibits the highest overall probability of generating convective cells. It has a peak convective cloud occurrence over the coastal boundary region from midnight to early afternoon. The evening convective activity is least frequent in this regime and is thought to be due to the presence of continuous cloud cover reducing daytime heating that prevents the establishment of sea-breeze

convergence. The vertical wind shear in the low levels, convective ETH, cloud cell volumes, and lightning activity are all smaller in this regime compared to the other convectively activity regimes (SW and ME regimes). Also, the effect of the underlying surface types on most convective cloud properties is the weakest in the DW regime. Overall, clouds in this regime exhibit oceanic characteristics, with convection being embedded in the large-scale forcing of the monsoon trough.

3) In the SW regime, the peak convective occurrence location shifts eastward compared to the DW regime. This observation supports the hypothesis that these two regimes are connected to the eastward propagation of the monsoon trough. Another feature in the SW regime that matches with the DW regime is the increase in occurrence of convective clouds in the early morning period. However, unlike the DW regime, the effect of the underlying surface on the convective cloud properties is somewhat strong in the SW regime. For example, the land cells predominantly initiate in the afternoon and have a larger volume compared to those that form in the early morning over the ocean. Another contrasting feature is that the convective cloud activity in the SW regime is moderately high in the afternoon. Overall, this indicates that the SW regime are regulated by a mixture of large-scale forcing that are important for the DW regime and the sea-breeze effects that dominate the ME regime.
4) The E regime behaves in a similar manner to the SW regime. Like the DW regime, the E regime has the highest convective cloud activity in the early morning period. While the observed secondary peak in convective cloud activity in the evening period can be attributed to the sea-breeze effects, the effect of the underlying surface on the convective cloud properties is moderate. Contrary to the SW and ME regimes, the E regime has somewhat higher ETHs and larger cloud volumes over ocean than land. The convective clouds in this regime have one of the highest tendencies of producing lightning flashes, and most of these electrically active clouds are located at the top end of the Darwin coastline.

The main purpose of the study was to use the complex meteorological and topographic environment around Darwin to study the relative influence of the large-scale atmospheric conditions, as represented by a set of synoptic regimes, and the underlying surface types on the basic characteristics of convective systems and their diurnal evolution. The picture emerging from this study shows an intricate interplay between the large-scale regime and surface-type influences on the properties of convection. To first order, the large-scale regime determines much of the convective evolution, as exemplified by the rare occurrence of convection in the E and DE regimes, and the widespread occurrence of relatively weak convection in the DW regime. However, complex topography, such as the presence of coastlines, is a major secondary factor in determining the structural characteristics of convection. For example, during the ME regime, much of the convection is triggered along sea-breeze fronts either over the Tiwi Islands or the mainland. This indicates that the large-scale state does not allow convection to occur spontaneously over the ocean, but does allow for more organized forms of convection. This picture is likely typical not only for the north of Australia, but the entire Maritime Continent, where the existence of numerous islands of varying size can trigger sea-breeze convection even in large-scale conditions unfavorable for widespread convection over oceanic areas. In contrast, during the DW regime, the surface influence becomes negligible, as the large-scale upward motion associated with the monsoon trough provides sufficient forcing to allow widespread convection with large areas of long-lived stratiform cloud, which in turn suppresses the daytime heating of the land.

Acknowledgments. This work has been supported by the U.S. Department of Energy ARM. We would like to acknowledge the contributions of Brad Atkinson and Michael Whimpey in supporting the Darwin observatory and data management. Rodney Potts and Kevin Cheong are thanked for providing the TITAN data and for their discussion about it. James Sofra is thanked for GPATs lightning data. Special thanks to Susan Rennie and Surendra Rauniyar for their discussion and comments.

REFERENCES

Bringi, V. N., and V. Chandrasekar, 2001: *Polarimetric Doppler Weather Radar: Principles and Applications.* Cambridge University Press, 636 pp.

Carbone, R. E., J. W. Wilson, T. D. Keenan, and J. M. Hacker, 2000: Tropical island convection in the absence of significant topography. Part I: Life cycle of diurnally forced convection. *Mon. Wea. Rev.,* **128,** 3459–3480.

Carey, L. D., and S. A. Rutledge, 2000: The relationship between precipitation and lightning in tropical island convection: A C-band polarimetric radar study. *Mon. Wea. Rev.,* **128,** 2687–2710.

Casey, S. P. F., E. J. Fetzer, and B. H. Kahn, 2012: Revised identification of tropical oceanic cumulus congestus as viewed by CloudSat. *Atmos. Chem. Phys.,* **12,** 1587–1595.

Deierling, W., W. A. Petersen, J. Latham, S. Ellis, and H. J. Christian, 2008: The relationship between lightning activity and ice fluxes in thunderstorms. *J. Geophys. Res.,* **113,** D15210, doi:10.1029/2007JD009700.

Dixon, M., and G. Wiener, 1993: TITAN: Thunderstorm Identification, Tracking, Analysis, and Nowcasting—A radar-based methodology. *J. Atmos. Oceanic Technol.,* **10,** 785–797.

Goudenhoofdt, E., M. Reyniers, and L. Delobbe, 2010: Long term analysis of convective storm tracks based on C-band radar reflectivity measurements. *Proc. Sixth European Conf. on Radar in Meteorology and Hydrology,* Sibiu, Romania, National Meteorological Administration, 1–7.

Höller, H., H.-D. Betz, K. Schmidt, R. V. Calheiros, P. T. May, E. Houngninou, and G. Scialom, 2009: Lightning characteristics observed by a VLF/LF lightning detection network (LINET) in Brazil, Australia, Africa and Germany. *Atmos. Chem. Phys.,* **9,** 7795–7824, doi:10.5194/acp-9-7795-2009.

Jakob, C., 2003: An improved strategy for the evaluation of cloud parameterizations in GCMs. *Bull. Amer. Meteor. Soc.,* **84,** 1387–1401.

——, 2010: Accelerating progress in global atmospheric model development through improved parameterizations—Challenges, opportunities, and strategies. *Bull. Amer. Meteor. Soc.,* **91,** 869–875.

Johnson, R. H., T. M. Rickenbach, S. A. Rutledge, P. E. Ciesielski, and W. H. Schubert, 1999: Trimodal characteristics of tropical convection. *J. Climate,* **12,** 2397–2418.

Keenan, T. D., and R. E. Carbone, 1992: A preliminary morphology of precipitation systems in tropical northern Australia. *Quart. J. Roy. Meteor. Soc.,* **118,** 283–326.

——, K. Glasson, F. Cummings, T. S. Bird, J. Keeler, and J. Lutz, 1998: The BMRC/NCAR C-band polarimetric (CPOL) radar system. *J. Atmos. Oceanic Technol.,* **15,** 871–886.

Labrador, L., G. Vaughan, W. Heyes, D. Waddicor, A. Volz-Thomas, H.-W. Pätz, and H. Höller, 2009: Lightning-produced NO_x during the Northern Australian monsoon; results from the ACTIVE campaign. *Atmos. Chem. Phys.,* **9,** 7419–7429, doi:10.5194/acp-9-7419-2009.

Liu, C., and M. W. Moncrieff, 1998: A numerical study of diurnal cycle of tropical oceanic convection. *J. Atmos. Sci.,* **55,** 2339–2344.

——, and E. J. Zipser, 2008: Diurnal cycles of precipitation, clouds, and lightning in the tropics from 9 years of TRMM observations. *Geophys. Res. Lett.,* **35,** L04819, doi:10.1029/2007GL032437.

May, P. T., and A. Ballinger, 2007: The statistical characteristics of convective cells in a monsoon regime (Darwin, Northern Australia). *Mon. Wea. Rev.,* **135,** 82–92.

——, J. H. Mather, G. Vaughan, C. Jakob, G. M. McFarquhar, K. N. Bower, and G. G. Mace, 2008: The Tropical Warm Pool International Cloud Experiment. *Bull. Amer. Meteor. Soc.,* **89,** 629–645.

——, C. N. Long, and A. Protat, 2012: The diurnal cycle of the boundary layer, convection, clouds, and surface radiation in a coastal monsoon environment (Darwin, Australia). *J. Climate,* **25,** 5309–5326.

Pope, M., C. Jakob, and M. Reeder, 2009a: Regimes of the north Australian wet season. *J. Climate,* **22,** 6699–6715.

——, ——, and ——, 2009b: Objective classification of tropical mesoscale convective systems. *J. Climate,* **22,** 5797–5808.

Protat, A., J. Delanoë, P. T. May, J. Haynes, C. Jakob, E. O'Connor, M. Pope, and M. C. Wheeler, 2011: The variability of tropical ice cloud properties as a function of the large-scale context from ground-based radar-lidar observations over Darwin, Australia. *Atmos. Chem. Phys.,* **11,** 8363–8384.

Robe, F. R., and K. A. Emanuel, 2001: The effect of vertical wind shear on radiative convective equilibrium states. *J. Atmos. Sci.,* **58,** 1427–1445.

Rotunno, R., J. B. Klemp, and M. L. Weisman, 1988: A theory for strong, long-lived squall lines. *J. Atmos. Sci.,* **45,** 463–485.

Rutledge, S. A., E. R. Williams, and T. D. Keenan, 1992: The Down Upper Doppler and Electricity Experiment (DUNDEE): Overview and preliminary results. *Bull. Amer. Meteor. Soc.,* **73,** 3–16.

Simpson, J., T. D. Keenan, B. Ferrier, R. H. Simpson, and G. J. Holland, 1993: Cumulus mergers in the maritime continent. *Meteor. Atmos. Phys.,* **51,** 73–99.

Steiner, M., R. A. Houze Jr., and S. E. Yuter, 1995: Climatological characterization of three-dimensional storm structure from operational radar and rain gauge data. *J. Appl. Meteor.,* **34,** 1978–2007.

van den Broeke, M. S., D. M. Schultz, R. H. Johns, J. S. Evans, and J. E. Hales, 2005: Cloud-to-ground lightning production in strongly forced, low-instability convective lines associated with damaging wind. *Wea. Forecasting,* **20,** 517–530.

Westcott, N. E., 1994: Merging of convective clouds: Cloud initiation, bridging, and subsequent growth. *Mon. Wea. Rev.,* **122,** 780–790.

Williams, E. R., S. A. Rutledge, S. G. Geotis, N. Renno, E. Rasmussen, and T. Rickenbach, 1992: A radar and electrical study of tropical hot towers. *J. Atmos. Sci.,* **49,** 1386–1395.

JOURNAL OF GEOPHYSICAL RESEARCH: ATMOSPHERES, VOL. 118, 8375–8389, doi:10.1002/jgrd.50640, 2013

The four cumulus cloud modes and their progression during rainfall events: A C-band polarimetric radar perspective

Vickal V. Kumar,[1,2] Christian Jakob,[1,3] Alain Protat,[2] Peter T. May,[2] and Laura Davies[1]

Received 14 April 2013; revised 20 June 2013; accepted 9 July 2013; published 13 August 2013.

[1] There is no objective definition to separate cumulus congestus clouds from the shallow cumulus and deep clouds. This has generated misinterpretation about the role of congestus clouds to promote deep convection through the potential of moistening the middle troposphere. In this study, an objective identification for the different tropical cumulus modes is found by examining the occurrence frequency of the cloud cell top heights (CTHs) and near-ground (at 2.5 km height) rainfall properties of these cells using a three-season database of the Darwin C-band polarimetric radar. Four cumulus modes were identified, namely a shallow cumulus mode with CTH in the trade inversion layer (1–3 km), a congestus mode with tops in the highly stable middle troposphere (3–6.5 km), a deep convective mode with tops in the region of free convection (6.5–15 km), and an overshooting convection mode with tops in the tropical tropopause layer (CTH >15 km). The study also investigates the connections between these cumulus modes during heavy rainfall events. The congestus mode occurs predominantly from ~10 h prior to the peak rainfall event to ~2 h past the event. The deep cloud populations (Modes 3 and 4) have their maxima at and shortly after the time of the rainfall peak, with maximum occurrence just below the tropical tropopause layer. A comparison of the heavy rainfall events occurring in morning (oceanic) conditions against the afternoon (continental) conditions revealed a higher ratio of the shallow to the deep cloud population and a shorter transition time from the shallow to the onset of deep population in the morning-oceanic conditions than the afternoon-land conditions. It is also found through the analysis of the large-scale moisture budget data set that for both the morning and afternoon events, the moistening peaked before the peak in the congestus populations.

Citation: Kumar, V. V., C. Jakob, A. Protat, P. T. May, and L. Davies (2013), The four cumulus cloud modes and their progression during rainfall events: A C-band polarimetric radar perspective, *J. Geophys. Res. Atmos.*, *118*, 8375–8389, doi:10.1002/jgrd.50640.

1. Introduction

[2] Progress in simulating clouds in general circulation models depends substantially on improvements in the cumulus cloud parameterizations and their coupling to boundary layer and cloud processes [*Jakob*, 2010]. Cumulus clouds have historically been thought of as primarily consisting of two modes: shallow cumulus, with cloud top heights near the trade inversion layer, 1–2 km above the surface, and deep cumulonimbus clouds, with cloud tops near the tropopause [*Malkus and Riehl*, 1964]. *Johnson et al.* [1999] provided observational evidence of a distinct third cumulus cloud mode, the midlevel cumulus congestus clouds, with cloud tops near the 0°C melting level. Because of their small cell size and their transitional nature from nonprecipitating to precipitating convection, it is relatively difficult to observe congestus clouds with remote sensors [e.g., *Miller et al.*, 1998; *Melnikov et al.*, 2011]. Yet, they have been implicated in playing an important role in the transition from shallow to deep convection through the potential of moistening the middle troposphere [e.g., *Kuang and Bretherton*, 2006; *Waite and Khouider*, 2010], although there is still some ambiguity if the moistening itself is vital to trigger deep convection [e.g., *Hohenegger and Stevens*, 2012]. It is the goal of this study to further investigate the role of congestus clouds in the transition from shallow to deep convection by providing an improved analysis of radar observations of this transition at Darwin, Australia, and by directly linking the radar observations to the large-scale dynamical state of the tropical atmosphere.

[1]School of Mathematical Sciences, Monash University, Melbourne, Victoria, Australia.
[2]Centre for Australian Weather and Climate Research, Australian Bureau of Meteorology and CSIRO, Melbourne, Victoria, Australia.
[3]ARC Centre of Excellence for Climate System Science, Monash University, Melbourne, Victoria, Australia.

Corresponding author: V. V. Kumar, Centre for Australian Weather and Climate Research, Australian Bureau of Meteorology and CSIRO, GPO Box 1289, Melbourne, Vic 3001, Australia. (v.kumar@bom.gov.au)

2169-897X/13/10.1002/jgrd.50640

[3] There has been ongoing improvement in observing congestus clouds from radar observations with a focus on refining the criteria for their identification. Early studies identified congestus clouds as any precipitating convective cloud with cloud top heights (CTHs) between 5 and 9 km [*Johnson et al.*, 1999], while later studies included the criterion of the existence of a continuous radar echo from the near surface to the CTH [*Jensen and Del Genio*, 2006]. However, none of these studies provide a clear justification of choosing a 9 km CTH threshold. Early field campaigns, such as Global Atmospheric Research Program Atlantic Tropical Experiment [e.g., *Houze and Cheng*, 1977] and Tropical Ocean-Global Atmosphere Coupled Ocean-Atmosphere Response Experiment [e.g., *Rickenbach and Rutledge*, 1998], contained evidence of weak bimodality in cumulus occurrence. However, in these studies, cloud top peaks occurred near 2–3 and 6 km, with no evidence of a maximum at 9 km. Recent radar echo top analyses at Darwin using long-term data sets spanning several wet seasons showed limited support of multimodal distribution [e.g., *May and Ballinger*, 2007; *Kumar et al.*, 2013]. As there is still no agreed "definition" of congestus occurrence derived from radar observations, a first aim of this study is to develop a more objective identification of congestus and deep clouds. This will be achieved by a careful analysis not only of CTH occurrence frequency but also of the radar retrieved rainfall properties taking advantage of the polarimetric capabilities of the research radar deployed at Darwin (C-band polarimetric (CPOL) radar) [*Keenan et al.*, 1998].

[4] Once a method of identifying congestus and deep clouds has been established, a major motivation of this paper is to study the progression of different cumulus modes through the storm life cycle. Specifically, the goal here is to better comprehend the role of cumulus congestus clouds in preconditioning the atmosphere for deep convection. Several studies have found that the occurrence frequency of congestus clouds increases prior to peak rainfall events associated with deep convection [*Mapes et al.*, 2006; *Chen and Del Genio*, 2009; *Tromeur and Rossow*, 2010; *Del Genio et al.*, 2012]. *Kikuchi and Takayabu* [2004] performed a composite analysis of CTHs and thermodynamic profile as a function of the life cycle of the Madden-Julian oscillation, which revealed that the three cumulus cloud modes developed in stages. Initially, the weakening of the trade inversion layer corresponds to the shift from shallow cumulus to congestus cumulus. In the next stage, the cumulus congestus clouds moisten the atmosphere below the 0°C level, preconditioning the atmosphere for deep convection [*Kemball-Cook and Weare*, 2001; *Lin and Johnson*, 1996]. However, recently *Hohenegger and Stevens* [2012], using 1 month of satellite observations, found the transition time from congestus to deep convection to be much shorter (2 h over land and 4 h over the ocean) than the time needed (10 h and longer) for congestus clouds to sufficiently moisten the atmosphere. Their results do not support the idea that congestus moistening itself enhances the formation of deep convection. Rather, they suggested that dynamical processes, potentially related to the heating from congestus clouds, are likely an important ingredient in promoting the transition to deep convection. This study will further investigate this link by relating the observed cloud behavior to the large-scale state of the atmosphere around Darwin.

[5] In this paper, we use three wet seasons (573 days) of Darwin CPOL radar observations to investigate the statistical properties of cumulus congestus clouds, deep convective clouds, and overshooting convection, and their progression during rainfall events. In section 2 of this paper, the CPOL database is described. In this section, we also compare the CTH frequency derived from CPOL with concurrent CTH retrievals from a Darwin MilliMetre Cloud Radar (MMCR) [*Moran et al.*, 1998] to estimate the percentage of congestus clouds which could not be detected by the CPOL radar. Section 3 describes the statistical properties of the identified convective clouds as a function of CTH. This section will provide an objective method to identify cumulus modes, including congestus. Section 4 then focuses on the temporal evolution of the convective cell characteristics around heavy rain rate events to investigate the evolution of the cumulus modes throughout the storm life cycle. Section 5 investigates the potential connection of cloud growth to dynamical processes by analyzing moisture and heating tendencies around the rain events identified in section 4. We summarize our findings in section 6.

2. Data Sets and Method

2.1. The Darwin C-Band Polarimetric (CPOL) Radar

[6] The study primarily uses three wet seasons of data (October 2004–April 2005, October 2005–April 2006, and October 2006–April 2007) from the Darwin CPOL radar. The CPOL radar (12.25°S, 131.04°E) collects a three-dimensional volume of data out to a range of 150 km once every 10 min. Each volume consists of a series of 16 conical sweeps at elevations ranging from 0.5° to 42°. The radar transmits alternate linear horizontal and vertical polarization pulses, which give access to key polarimetric variables such as the horizontal reflectivity (Z_h), the differential reflectivity (Z_{dr}), and the specific differential phase (K_{dp}) [e.g., *Zrnić and Ryzhkov*, 1998].

[7] Next, the data are gridded by constructing a series of the constant altitude plan position indicator (CAPPI) at every 0.5 km in height (with a horizontal bin size of 2.5 km × 2.5 km) extending up to 20 km, using the Sorted Position Radar INTerpolation software. To minimize any issues that might occur during the interpolation from PPIs to CAPPIs, only data in the range 20–100 km and at heights greater than 2.5 km are analyzed. Furthermore, as the focus of this study is on the development of convective clouds in the transition from shallow to deep modes, the stratiform pixels are also excluded from the analysis.

[8] The individual radar pixels at a CAPPI level of 2.5 km are characterized as convective or stratiform using an algorithm by *Steiner et al.* [1995]. The Steiner algorithm classifies the gridded reflectivity as convective if the reflectivity value is at least 40 dBZ or greater than a fluctuating threshold depending on the area-averaged background reflectivity (within a radius of 11 km around the grid point). Each convective center has a radius of influence (ranging from 1 to 5 km) also depending on the surrounding background reflectivity [*Steiner et al.*, 1995]. This method of identifying the convective and stratiform radar pixels has been used in previous studies over the Darwin region [e.g., *May and Ballinger*, 2007; *Kumar et al.*, 2013; *Penide et al.*, 2013].

[9] All radar pixels in the vertical column above the altitude of 2.5 km are assigned the same Steiner classification as that at the 2.5 km CAPPI level. This assumption is reasonable since the vertical shear of horizontal wind between the heights of 2.5 and 12 km in convectively active Darwin wet season regimes is small, typically on the order of $10^{-4}\,s^{-1}$ [e.g., *Kumar et al.*, 2013]. Furthermore, as explained later, CTH values are calculated per cloud cell (i.e., several adjoining convective radar pixels) not per single vertical radar column. So the tilt of the convective core due to wind shear is expected to have a minimal effect on the cell-based CTH retrievals.

[10] From this gridded reflectivity data, CTH is calculated using the following two methods. First, the algorithm identifies convective cells occurring at the 2.5 km CAPPI level. Specifically, once a convective radar pixel is detected at 2.5 km height, the algorithm then searches in all directions in the horizontal plane from this convective pixel for any connected convective pixels and stops when no convective pixel is found (radar pixel classified as stratiform or clear air). The procedure is repeated in all directions, defining the contours of each convective cell. Some cells, typically those with low CTH, could have a sectional area of a size equal to one radar pixel with an area of 6.25 km^2 (2.5 km × 2.5 km). The next area size for two pixels is 12.5 km^2 and so on. Second, for each identified convective cell, the maximum height of the 0 dB echo at any of the pixels in the cell is computed to provide an estimate of a single CTH for that convective cell. Specifically, the CTH corresponds to the radar echo height whose reflectivity is the closest to 0 dB, but with a reflectivity value within the range of −5 to +5 dB, and provided there is a vertically continuous reflectivity greater than 0 dB between the 2.5 km CAPPI level and this CTH. This procedure filtered out any possible effects of detached cloud layers situated above the convective towers.

[11] This definition of CTH is similar to the definition of an echo top height (ETH) used in previous studies [e.g., *Kumar et al.*, 2013], except that in those studies ETH was calculated for individual convective column instead of the whole convective cells used here. Using the common single-column ETH, a convective cell will have a distribution of ETHs and pixels from the same cell will potentially be classified in different cumulus cell categories, which complicates the use of this definition in studying the transition to deep convection. Using the same reasoning, the 0 dB height per cell is taken as the maximum height reached by any near-0 dB pixel in the cell, and not an average of all near-0 dB ETHs in that cell. In summary, throughout the paper, with the exception of Figure 1, one CTH per convective cell is used in the analysis. The reasons for the exception will be explained when introducing the figure.

[12] The choice of the 0 dB level as cell threshold is a compromise. The minimum detectable reflectivity (R_{min}) above the noise level as a function of CPOL range (R in km) is R_{min} (dB) = −41.25 + 20 log(R). *May and Ballinger* [2007] and *Kumar et al.* [2013] used 5 dB echo top height criteria mainly because they choose to use a large domain around the radar. Here, we use CPOL data only up to a range of 100 km (R_{min} = −1.25 dB), so the 0 dB threshold is sufficiently high to allow for detection of echoes at radar ranges considered in this study. The 0 dB top height criteria also ensure that the radar-determined CTH is even closer to the true CTH.

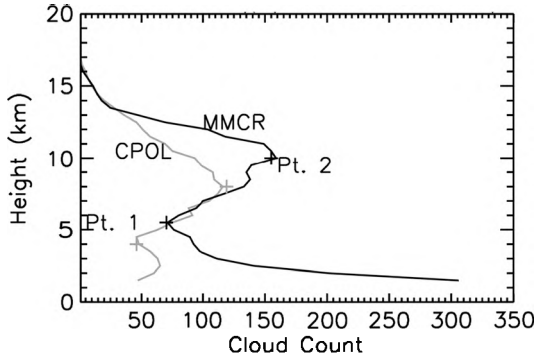

Figure 1. Distribution of cloud top height (CTH) occurrence frequency over the Darwin Atmospheric Radiation Measurement (ARM) site, 25 km from the Darwin C-band polarimetric (CPOL) radar center. The black and grey curves are the CTH frequency computed using the MilliMetre Cloud Radar (MMCR) and the range-height indicator (RHI) scan of CPOL, respectively. A bin size of 0.5 km in height is used in this figure and all subsequent figures.

[13] Apart from the CTH information per cell, we also make use of radar reflectivities, drop size distributions (DSD) parameters, and rain rate retrievals from the 2.5 km CAPPI level bounded by the respective convective cell area. As for CTH, we define only one value per cell rather than using individual pixel values. This is done by calculating the cell mean reflectivity, rain rate, drop size diameter (D_0), and number concentration of small hydrometers (N_w) at each vertical level. Descriptions of the algorithm used to retrieve drop size distributions (DSD) parameters and rain rates from the polarimetric radar variables are given in *Bringi et al.* [2009]. It assumes a normalized gamma DSD form [*Testud et al.*, 2001] described by the median volume diameter (D_0) and the "generalized" intercept parameter (N_w). For simplicity, N_w can be thought as the number concentration of small hydrometers. N_w is the same as the intercept parameter of an exponential DSD with the same D_0 and liquid water content as the gamma DSD. This algorithm uses a multiparameter approach to take advantage of the complementary information contained in the polarized backscattered signals. First, D_0 is retrieved from the differential reflectivity using polynomial fits (e.g., $D_0 = f(Z_{dr})$), then N_w is estimated using a power law of the form $Z_h/N_w = c.(D_0)^d$, and finally, the rain rate is estimated using either a function of the form $R = f(K_{dp})$, $R = f(Z_h, Z_{dr})$, or $R = f(Z_h)$ depending on various thresholds and a decision tree [*Bringi et al.*, 2009].

2.2. Cloud Radar Data and its Comparison to CPOL

[14] A major objective of this paper is to study the features of cumulus congestus clouds. These clouds have been typically studied using data from a millimeter-wavelength MMCR, except in *Johnson et al.* [1999], where C-band radar measurements were used. Millimeter-wavelength radar has been preferred to study congestus clouds because some of the clouds in this mode could be nonprecipitating and thus will be missed by a centimeter-wavelength radar. Darwin hosts both a vertically pointing MMCR with a wavelength of 8.6 mm [*Moran et al.*, 1998] at the U.S. Department of Energy's Atmospheric Radiation Measurement (ARM)

[*Stokes and Schwartz*, 1994; *Ackerman and Stokes*, 2003] site and the scanning CPOL (5.3 cm) operating over the wet season, thus offering the potential of estimating the congestus cloud fraction which will be missed by the C-band radar.

[15] The best way to achieve a reasonable space-time overlap between the vertically pointing MMCR and scanning CPOL radars is to use the data from the range-height indicator (RHI) scanning mode of the CPOL radar. CPOL performs RHI scans over the MMCR site lasting for approximately 10 s using 70 different elevations ranging from 0.02° to 45.8°, once every 10 min. Thus, RHI scans have a much finer vertical resolution (10 m near the surface and ~15 m at maximum elevation) than the PPI mode, which uses 16 elevations and has a vertical resolution on the order of few hundreds of meters. The RHI scanning routine on CPOL commenced only in October 2005; only 2 years of statistics is used in the comparison of the two radar results.

[16] The reflectivity data from the RHI scans are averaged over three adjacent range gates centered on the MMCR site (25 km) [e.g., *Bringi et al.*, 2009]. Then, height profiles are constructed using the radar beams at the 70 different elevation angles. In comparison, the MMCR radar does a continuous vertical sounding with a temporal resolution of 35 s and a fixed height resolution of 90 m. We time-match the two radars by selecting only the MMCR scans closest to the RHI scan times. RHI scans which had no echo detection at the MMCR location, and vice versa, were still kept to build the time-matched array. Apart from inevitable instruments problems, it is fair to assume that both radars over the time-matched interval observe the same type of clouds. Next, the column ETH is computed using the reflectivity profiles from both radars, using the same criteria defined in *Jensen and Del Genio* [2006]. Specifically, ETH is computed as the maximum height reached by the radar echo, provided there is a continuous echo from cloud base to the ETH. Note that the starting cloud base height for both radars is required to be less than 2 km. Because of this requirement, the cloud data used in this analysis are likely mainly convective in nature [e.g., *Jensen and Del Genio*, 2006]. At the ETH, the CPOL reflectivity is required to reach 0 dB, but for the MMCR, the reflectivity at the ETH is set to the lowest available reflectivity per column, which was typically ~ −20 dB. Even though the minimum reflectivity that could be measured by CPOL at the range of 25 km is $R_{\min} = -13$ dB, well below the 0 dB ETH requirement, 0 dB ETHs are preferred so that the radar comparison remains relevant for all CPOL ranges (20–100 km) used in the rest of this study.

[17] Figure 1 shows the cloud count from MMCR (black) and CPOL RHI (grey) radars in CTH bins of 0.5 km. There are several interesting similarities and differences in the two CTH profiles. As one would expect, the MMCR detects significantly more clouds below 4 km, owing to its ability to see nonprecipitating cloud particles. Above 8 km the top heights from the CPOL radar are approximately 2 km lower than those obtained from the MMCR. Again, this is likely because the MMCR can detect much lower reflectivities (the modal reflectivity value is near −20 dB), whereas the CPOL reflectivities at the ETH are set to be 0 dB. So the true cloud top height for deep clouds is likely within 2 km of the 0 dB CTH of CPOL, consistent with those estimated by previous studies [e.g., *Kingsmill and Wakimoto*, 1991; *Casey et al.*, 2012]. Interestingly, in the range of congestus cloud top heights between 4 and 8 km, the radars agree well.

[18] Overall, CPOL detects 67% of the clouds detected by MMCR; most of the missing clouds are in the shallow cumulus mode below 4 km. At the heights of 4 and 8 km, the ratio of CPOL detection to MMCR detection is 50% and 82%, respectively. However, such direct comparison for a given height is thought to be less useful due to the difference in the sensitivity of the two radars. Instead, we estimate the CPOL efficiency using the following procedure. The first local minimum (Pt. 1, 4.0 km in CPOL and 5.5 km MMCR) in both curves is assumed to be the breakpoint height of the shallow clouds, and comparing the total cloud counts below this level from both radars gives a detection efficiency of 30% on CPOL compared to MMCR. Similarly between Pt. 1 and Pt. 2 (possibly the congestus fractions), the CPOL efficiency is 64%, and above Pt. 2 it is 127%. The CPOL radar detects more of the deeper clouds compared to MMCR since the millimeter-wavelength signals are often attenuated during periods of moderate and heavy rain rates associated with deep clouds [e.g., *Kumar and Ramachandran*, 2004].

2.3. The Large-Scale Atmospheric State

[19] It is a goal of this study to connect the cloud evolution in the transition from shallow to deep convection to the dynamical evolution of the large-scale atmospheric state. To do so, we require reliable estimates of the large-scale state concurrent with the radar observations. *Jakob et al.* [2011] have derived such a data set for the Darwin region for the same wet seasons for which radar observations are available in this study.

[20] The data set is constructed by applying the variational budget analysis algorithm of *Zhang and Lin* [1997]. This algorithm usually requires an array of atmospheric sounding data, as well as observations of surface precipitation and top of the atmosphere radiation, to optimally estimate all terms of the vertically resolved heat, moisture, and momentum budgets. In the absence of a radiosonde array, *Xie et al.* [2004] proposed to use results of numerical weather prediction analyses as a surrogate. To test this approach in the Darwin region, *Jakob et al.* [2011] applied this approach to the Tropical Warm Pool International Cloud Experiment [*May et al.*, 2008] data set and showed that the use of soundings extracted from the operational analyses of the European Centre for Medium-Range Weather Forecasts provided a very close approximation to budget estimates using a full sounding array. They then applied the method to three full seasons of data using surface precipitation rainfall, calculated from the CPOL radar as a key constraint to the moisture budget. The resulting large-scale data set used here includes vertical profiles of heat and moisture budgets as well as thermodynamic and dynamic variables at 40 hPa vertical and 6 h temporal resolution. The spatial domain of the large-scale data set is shown in *Xie et al.* [2010] and is comparable to the CPOL domain with a radius of 100 km.

3. The Statistical Rain Properties of Individual Convective Cells

[21] In this section, the CPOL observations are used to study in detail the near-surface (at a fixed height of 2.5 km) characteristics of two of the three cumulus cloud modes

identified in *Johnson et al.* [1999]: congestus and deep clouds. As will be shown, the deep cloud mode is found to comprise two distinct types of cloud with very different properties. The shallow cumulus mode cannot be included here because many shallow cumulus clouds do not produce sufficiently large droplets to be detected by the C-band radar (cf. Figure 1). Another limitation is that at the maximum range of the radar used here (100 km), the first conical scan of elevation 0.5° has a minimum detection height of 1 km, hence missing the very shallow cumulus clouds forming at further ranges.

[22] A total of 640,419 convective cells were identified over the three seasons, and their frequency of occurrence in 0.5 km bins of CTH is shown Figure 2a. An overall occurrence peak is evident at 7 km, with no clear evidence of a distinct third peak associated with the deep clouds. Instead, there is a near-constant reduction in the number of clouds with CTH. Thus, at face value, there is limited evidence supporting the cumulus trimodality theory [e.g., *May and Ballinger*, 2007; *Kumar et al.*, 2013]. Note that in our data set, a third occurrence peak associated with deep clouds becomes noticeable on many afternoons associated with sea breeze convergence [*Kumar et al.*, 2013] and during heavy rainfall events (see below).

[23] Instead of focusing purely on numbers, we investigate the convective rainfall properties as a function of CTH. The solid lines in Figures 2b and 2c, respectively, show the mean cell area and convective area fractions at 2.5 km height as a function of CTH. Convective area fraction is the ratio of the total area covered by all convective cells belonging to a certain CTH bin divided by overall total convective area. Hence, the area fraction response is proportional to the product of mean cell area (solid line in Figure 2b) and total number of cells (Figure 2a). Thus, it follows from here that the increase in convective area fraction below 7 km is mainly due to the rapid increase in the number of cells (Figure 2a), since the mean cell area is constant for these cumulus congestus clouds. In contrast, the convective area fraction with cells with CTH between 7 and 13 km is remarkably constant. This is because even though the cell numbers reduce with increasing CTH in this region (Figure 2a), their cross-sectional area at 2.5 km height grows wider as they become taller (solid line in Figure 2b). The deepest convective cells (CTH > 13 km) have the largest convective area fraction, though only 1% higher than that from clouds with a CTH between 7 and 13 km. This largest contribution of deeper convective clouds is linked to a rapid increase in the mean horizontal area of cells (solid line in Figure 2b) with CTH > 13 km (Figure 2a).

[24] The convective rain accumulation fractions (dotted line in Figure 2c) increase almost linearly with increasing CTH up to a CTH of 17 km. This parameter is the ratio of the total rain accumulation associated with a given CTH bin divided by overall total convective rainfall. The rain accumulation fraction response is related to the product of the number of convective cells (Figure 2a), mean cell area (solid line in Figure 2b), and the mean cell rain intensity (dotted line in Figure 2b). Thus, the almost linear behavior in convective rain accumulation fraction is caused by two of the three controlling variables, the cell raining area and cell rain intensity, both of which increase somewhat exponentially with CTH.

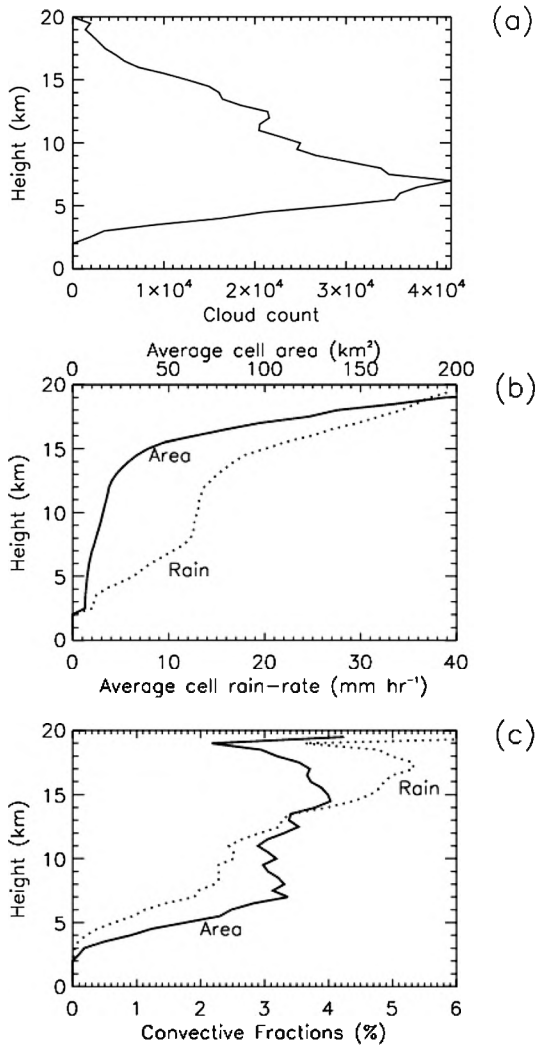

Figure 2. (a) The same format as Figure 1 except the CTH is computed using gridded (CAPPI) CPOL data. (b) Average cell area (solid) and cell rain rate (dotted) using data from 2.5 km CAPPI levels bounded by the convective cell area, as a function of CTH. (c) The same format as Figure 2b and shows the fraction (total at a given CTH divided by overall convective total) contributed by each CTH bin.

[25] The behavior of mean cell rain intensity as a function of CTH (dotted line in Figure 2b) perhaps reveals the most convincing evidence of the different cumulus categories. Specifically, the rain intensity at 2.5 km increases at a rate of 1.9 mm h^{-1} km^{-1} with increasing CTH when CTH is below 7 km. It increases at the much lower rate of 0.4 mm h^{-1} km^{-1} when CTH is between the 7 and 15 km, and then again displays a very large increase at a rate of 4.3 mm h^{-1} km^{-1} when CTH is above 15 km. This behavior is intriguing, suggesting the possibility of three (instead of the usual two) modes of precipitating convection in addition to the shallow mode (undetectable in this study). This hypothesis is further explored below using the radar reflectivity and all DSD parameters.

[26] Figure 3 shows the probability distribution function (PDF) of radar reflectivity at 2.5 km in 0.5 km bins of CTH.

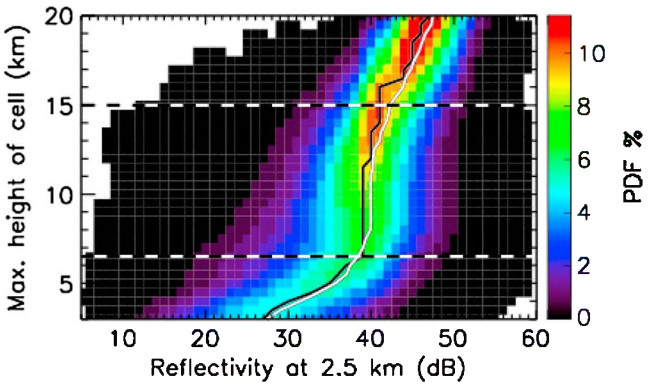

Figure 3. PDF of reflectivity using a bin size of 1 dB and as a function of CTH. One mean reflectivity was obtained per convective cell using reflectivity pixels that are bounded by the respective convective cells at the 2.5 km CAPPI level. The white curve is the overall mean reflectivity at each CTH level, and the black curve is the modal reflectivity. The dashed horizontal lines correspond to the breakpoints in the reflectivity trend indicating the lower (6.5 km) and the upper (15 km) CTH boundary for the "normal deep convection."

Recall from section 2 that each cell is assigned one reflectivity value, which is the mean of the radar reflectivity pixels from the 2.5 km CAPPI level belonging to that cell. The evolution of the 2.5 km reflectivity distributions with CTH clearly indicates the presence of two separate inflection levels: one at 6.5 km and another at 15 km (marked by horizontal lines). Cells with CTH below 6.5 km have a broad distribution in reflectivity at 2.5 km height with the smallest modal (black curve) and mean (white curve) reflectivities of all CTH classes. With increasing CTH, the reflectivity distribution at 2.5 km height becomes narrower with the mode-mean reflectivity values strongly increasing. The broad distribution in reflectivity PDFs in cells with lower CTH is thought to be because it is made of a mixture of nongrowing terminal congestus clouds with mainly lower reflectivities and growing transient congestus cloud with predominantly higher reflectivities. This hypothesis is being further explored in a separate study. When cell CTH is between 6.5 and 15 km, the 2.5 km reflectivity distribution is nearly constant with some narrowing with CTH evident. The modal and mean reflectivities are both around 38 dBZ, though the lower reflectivity cells do become also frequent with increasing CTH. In contrast, above 15 km the response in reflectivity with increasing CTH is similar to cells with CTH below 6.5 km, except that the distributions are much narrower and have much higher modal and mean reflectivities.

[27] Figures 1–3 together with the three-season average temperature lapse rates (Figure 4) support the existence of four different cumulus cloud modes:

[28] 1. Mode 1 (not studied here) consists of shallow cumulus clouds and is the most dominant cloud type. The CTHs of these clouds are in the trade inversion layer (1–3 km), which had a high static stability of the lapse rate ranging from -6 to -5 K km^{-1}.

[29] 2. Mode 2 represents the congestus cloud category, and the CTH of these clouds is between 3 and 6.5 km. Its minimum boundary height of 3 km is marked by an increase in midlevel stability, which reached the maximum stability at the melting level (ML) of 5 km. The relative humidity also increases from 3 km to the ML and from thereon decreased steadily with height (not shown).

[30] 3. Mode 3 is denoted as the "normal" deep convective cloud mode with top heights between 6.5 km and the level of zero clear-sky radiative heating (~15 km).

[31] 4. Mode 4 represents overshooting deep convection and with tops in the tropical tropopause layer (TTL; CTH >15 km). As these clouds penetrate through the strongly stable tropopause, they represent the most vigorous convection, as indicated by their high reflectivity at 2.5 km.

[32] We continue the investigation of the hypothesized modes of convection by exploring the distributions of rain rate and key DSD parameter retrievals at 2.5 km in the same manner as the reflectivity. Figure 5 shows the distributions of cell rain rate, D_0, and N_w at 2.5 km confirming the existence

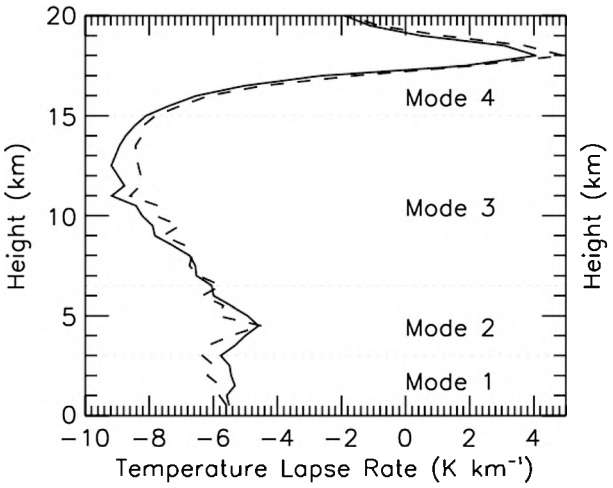

Figure 4. Average (solid) and median (dashed) temperature lapse rates associated with the convective cells. Prior to data processing, each convective cell is tagged with the nearest radiosonde profile, provided the sounding is within ±3 h of the convective cell identification time. Thus, an individual sounding profile may be used several times and some convective cells had no sounding data. The significances of Modes 1–4 have been explained in the text.

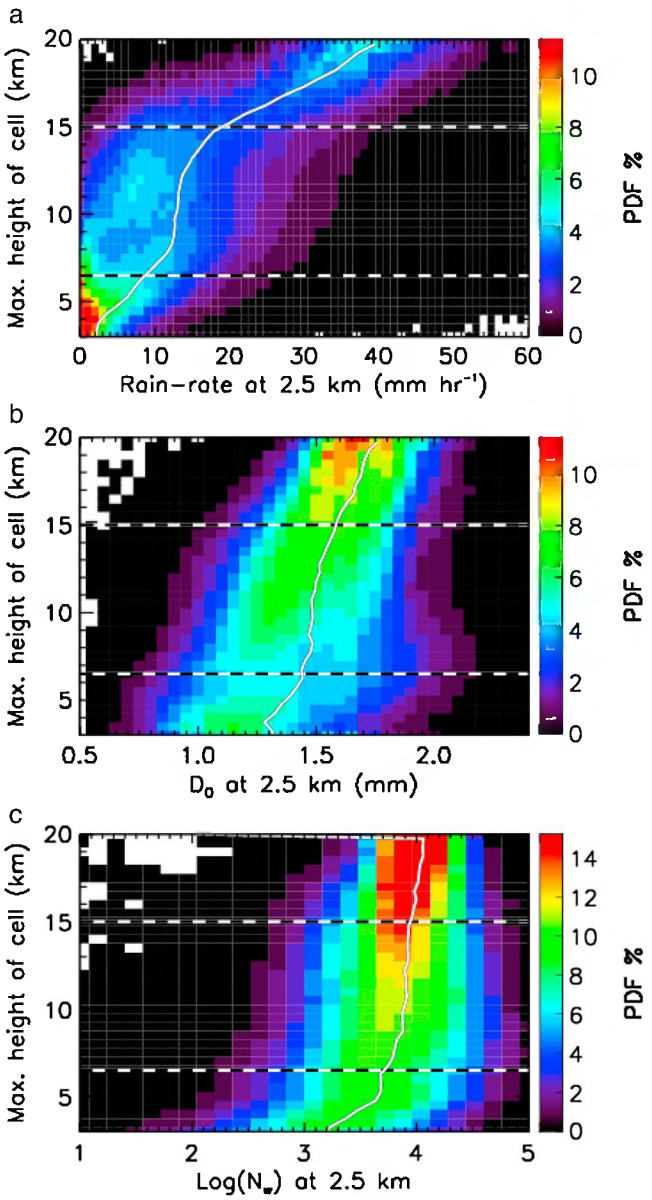

Figure 5. The same format as Figure 3 and shows PDF of (a) rain rate using a bin size of 1 mm h^{-1}, (b) D_0 using a bin size of 0.05 mm, and (c) $\log_{10}(N_w)$ using a bin size of 0.15. The white curve is the overall mean of the rainfall properties in each CTH bin.

of the three precipitating cumulus modes proposed earlier. The congestus mode displays strongly positively skewed rain rates at 2.5 km height, with the mean rain rate increasing as the cells grow higher (Figure 5a). They also typically have a small median volume diameter (D_0) and small concentrations of small hydrometeors (N_w) at 2.5 km height compared to the other two deeper cloud modes. The deep convective mode had the largest range in rain rate distribution at 2.5 km height. However, as is the case with reflectivity, the rate of increase in rain rate with increasing CTH is small. For the overshooting mode, the rain rate and DSD parameter distributions at 2.5 km height are narrow. The mean rain rate increased steeply as the cells grow taller into the TTL layer. Another notable observation is that rain rates of intensity greater than 30 mm h^{-1} occurred almost exclusively with Mode 4, highlighting the potential importance of this mode for extreme convective rainfall.

[33] Having focused on the 2.5 km only so far, next we investigate vertical profiles of reflectivity for different CTH classes by calculating the reflectivity lapse rate for some selected CTH levels (Figure 6a). The reflectivity lapse rate is defined as the vertical gradient of reflectivity [e.g., *Zipser and Lutz*, 1994]. Recall from our method of calculating CTH, the maximum reflectivity value at the top of the cell will be near 0 dB. Also, to aid the discussion, the relative humidity profiles associated with the different CTH classes are shown in Figure 6b. Again, even the vertical profile of reflectivity (Figure 6a) clearly shows the presence of the three separate precipitating cumulus cloud modes. The congestus mode (black and grey in Figure 6a) has the largest reflectivity lapse rate of approximately 7 dB km^{-1}. A broad

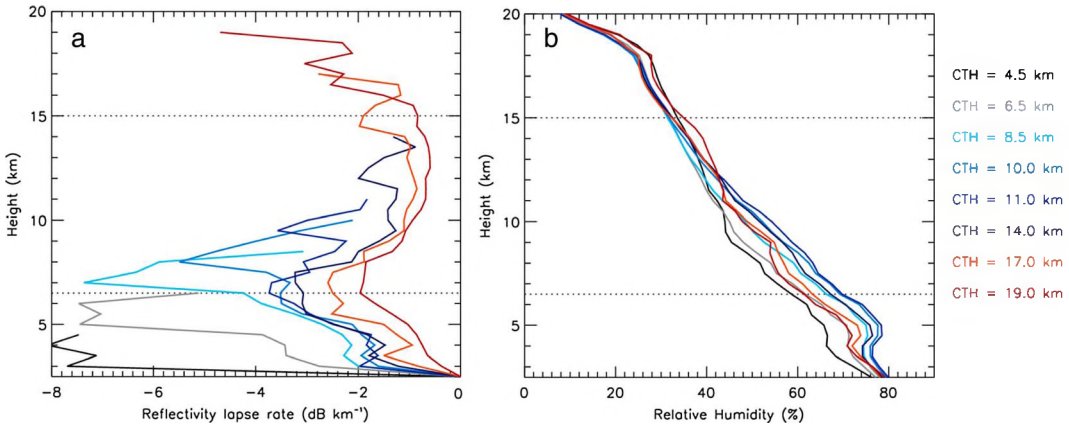

Figure 6. (a) Vertical profile of reflectivity lapse rate (defined as vertical gradient of reflectivity) within the convective cloud from the altitude of 2.5 km to CTH. The lines represent the lapse rates for selected CTH types. (b) Vertical profile of relative humidity associated with clouds in each CTH bin. The sounding profiles are selected in the same manner as temperature lapse rates in Figure 4. Note that an individual sounding profile is attributed to several different CTH types occurring within the 6 h window. However, by calculating a mean profile of several thousand cases of a particular CTH type, the underlying signature will likely be revealed.

peak in lapse rate occurs in the region from roughly 1.5 km below the CTH to CTH. In contrast, cells in the deep convective mode (light blue-dark blue) have a much narrower peak in lapse rate at ~1.5 km below the CTH and a second peak of approximately 3.5 dB km^{-1} occurs near the ML. The overshooting deep convective mode (light red-dark red) also had a maximum at the ML and then lapse rate increased steadily in the TTL. Overall, all CTH classes seem to suffer a large loss in vertical momentum as they penetrate past the highly stable "ML lid." The consistent peak in lapse rate at ~1.5 km below the CTH, which for Mode 2 clouds and shallow clouds in Mode 3 is mixed with the ML peak, is an indication that the vertical momentum of cumulus cells is reducing rather abruptly as the convective mass flux detrains into stratiform anvils as they approach their equilibrium heights.

[34] It is clear that the maximum reflectivity lapse rate is the largest in cells with lower CTH and this amplitude decreased gradually with increasing CTHs. This result is likely a direct consequence of weaker vertical velocities in shallow cells compared to deep convective cells [e.g., *Zipser and Lutz*, 1994]. However, the atmosphere is found to be drier when there are shallow cells (Figure 6b), and dry air entrainment into clouds will also limit the vertical extent of convection [e.g., *Redelsperger et al.*, 2002]. Similar arguments can be made about deep and overshooting convection; they are growing higher because they either have strong updraft speed and/or the middle atmosphere is moist. Interestingly, it is the Mode 3 "weaker" deep convection that occurs in the highest relative humidity, while the stronger Mode 4 convection occurs at intermediate relative humidity, indicating that the relationship between the depth of convection and middle tropospheric humidity is far from simple. Of course, this relationship is potentially affected by the coarse temporal and spatial resolution of radiosounding data. It is well known that strong convection in the Darwin area occurs near coastlines and over islands [e.g., *Schafer et al.*, 2001] and processes associated with the development of convection in complex terrain are likely factors in determining the CTH. We will investigate this further in the following section.

4. The Life Cycle of Convective Rainfall Events

[35] The characteristics of convective clouds during heavy rainfall events (hereafter referred as storms) are known to depend on a number of variables, such as the large-scale atmospheric state, local time, the underlying surface type, and internal storm dynamics [e.g., *Simpson et al.*, 1993; *Pope et al.*, 2009b; *May et al.*, 2012; *Kumar et al.*, 2013]. In this section, a composite method is used to identify peak convective rainfall events and to examine variations in convective cell characteristics several hours prior and after the peak rainfall time. This will provide some insights into the evolution of the convective modes identified in section 3 around main rainfall events including insights into the transition from shallow to deep convection.

4.1. Heavy Rainfall Events and Their Temporal Evolution

[36] To identify isolated heavy rainfall events in the CPOL data, two selection filters operating in sequence were used here. The first pass includes the computation of the 10 min domain-mean convective rain rate (DMCR) using data at the 2.5 km CAPPI level over the three seasons. Specifically, the DMCR is the sum of rainfall at all convective rain pixels (2.5 km × 2.5 km) divided by the constant radar coverage area of 43,982 km^2. The hourly running average DMCR values are calculated using the 10 min radar measurements, and this is done to remove short-timescale variations in DMCR. Rainfall events are then found by requiring the hourly running average DMCR peak to be larger than the three-season median DMCR of value 0.05 mm h^{-1}, and DMCR values to decrease on either side of this peak. Once each peak is identified, the hourly running average DMCR values on either side of the peak are scanned to determine the local minima. The local minima must be below the three-season

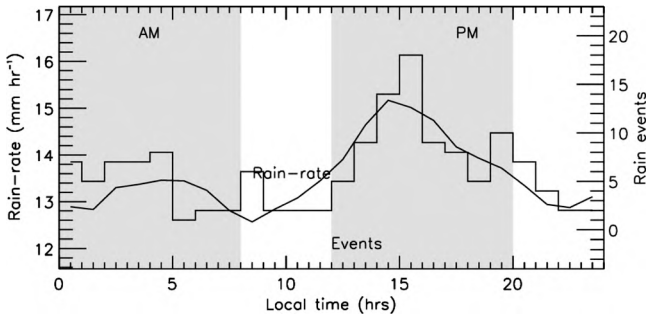

Figure 7. Diurnal variation of radar rain rate (curve) and count of identified rain events (line). The shaded grey region highlights our AM (00:00 A.M.–08:00 A.M.) and PM (12:00 P.M.–08:00 P.M.). These local time intervals are analyzed separately in the subsequent figures.

median DMCR and must be at least 1 h in time away from the peak DMCR. This way all events will have a lifetime of at least 2 h. As our focus is on the transition from shallow to deep convection, it was also ensured that only the first peak from multipeak rain events was selected for the analysis. A total of 371 events were selected using this first pass.

[37] The second pass keeps only those events that fall in the heavy rainfall category determined using the 6-hourly CPOL domain mean rain rate. Note that the 6-hourly domain mean rain rates were calculated using both stratiform and convective 10 min radar rain rate data. The lower limit of the heavy rainfall category is found to be ~0.4 mm h^{-1}, which corresponds to the upper tercile of the 6-hourly domain mean rain rates after periods without rain are excluded.

[38] This second pass just keeps 144 events from the initial total of 371 events, and the histogram of the diurnal variation of this final set of events is shown in Figure 7 (line). Also shown in this figure is the three-season average convective rain intensity (curve). The rain intensity response is reminiscent of the typical tropical maritime continent climate, with a strong afternoon and weak morning peak associated with land and oceanic underlying surface types, respectively [e.g., *Liu and Zipser*, 2008]. The histogram of the storm events also follows the rain intensity variation, with a dominant occurrence peak in the afternoon.

[39] Figure 7 confirms that rainfall in Darwin, when averaged over long times, shows a semidiurnal variations often associated with the underlying surface [e.g., *Kumar et al.*, 2013; *May et al.*, 2012]. For this reason, the convective cell characteristics during the rainfall events will be studied separately for the two broad local time categories: 00:00 A.M.–08:00 A.M. (hereafter AM class with 39 events) and 12:00 P.M.–08:00 P.M. (hereafter PM class with 78 events). The spatial distribution of convective rain intensity for these events is calculated using radar data from within 1 h on either side of the peak rainfall events and is shown in Figure 8. It is evident that the AM and the PM class strongly separate by the location of the highest rain intensity over ocean and land, respectively. We also find that nearly 60% of rainfall events in the PM class and 40% of events in the AM class occur in the most commonly observed moist easterly regime associated with the buildup and retreat of the Australian monsoon as well as monsoon breaks [*Pope et al.*, 2009a; *Kumar et al.*, 2013]. The second highest occurrence (nearly 30%) of rainfall events in the AM class is during the deep westerly "monsoon" regime and that in the PM class is in the shallow westerly regime, both of which are typical for monsoon conditions.

4.2. The Composite Life Cycle of Convective Cell Properties

[40] Figure 9 shows the results of a composite analysis of the radar data 12 h on either side of each peak DMCR event. The DMCR amounts are shown in Figure 9a. Figure 9b shows some of the components that constitute the DMCR including the total number of convective cells (black), the

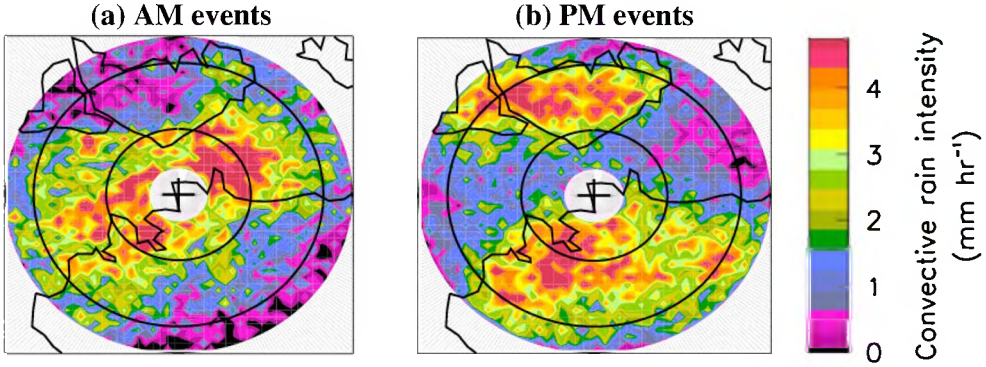

Figure 8. Spatial map of mean convective rain intensity within 1 h on either side of convective rain events that were identified to occur within (a) 00:00 A.M.–08:00 A.M. and (b) 12:00 P.M.–08:00 P.M. The concentric rings are 50 km apart.

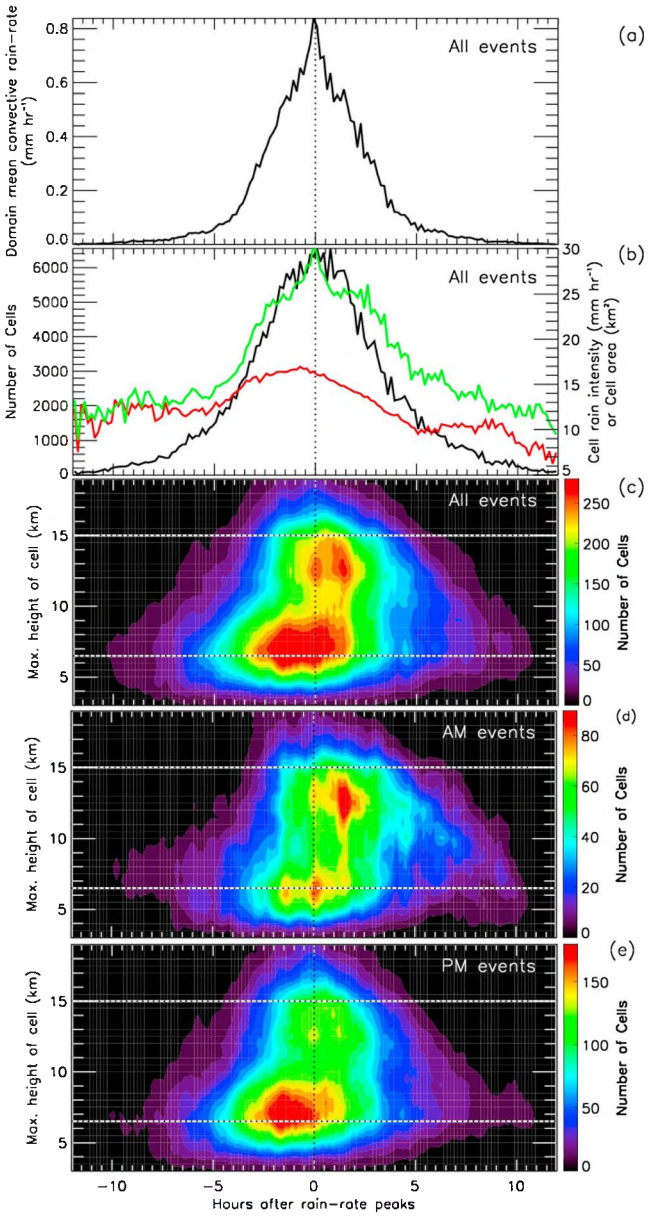

Figure 9. Composite responses of CTH for up to 12 h on either side of convective rain accumulation peaks to define controls ($t = 0$). A bin size of 10 min in time was used in this figure. (a) Composite of the 10 min domain average convective rain rate. (b) Composite of the total number of cells (black), average rain intensity (red), and average convective cloud area (green). (c) Composite of cloud top counts using a bin size of 0.5 km in height. (d and e) The same as Figure 9c except only using control times which are within AM and PM periods, respectively.

average cell area at 2.5 km (green), and the average cell rain rate (red). Figures 9a–9c show the results using all rainfall events (144 in total), while Figures 9d and 9e show the AM (39 events) and PM (78 events) classes separately.

[41] As is evident from Figure 9b, rainfall events start with a small number of small cells of medium intensity approximately 10 h before the peak in DMCR. From thereon, the cell number steadily increases up to its peak coincident with the DMCR peak. In contrast, cell size and intensity remain constant until a distinct increase roughly 5 h before the peak. Rain intensity peaks about 1 h before the DMCR peak, while cell size continues to grow peaking at the same time as DMCR. In other words, it is the rain area (determined by both the number and size of the cells) that determines the timing of the rainfall peak, not the rain intensity. This feature is most clearly defined in the PM class (not shown) with a lag time of 40 min between the intensity and DMCR peaks.

[42] Figure 9c shows the distribution of CTH in bins of 0.5 km and as a function of storm time. Figure 9c reveals two dominant cell populations. The first of these has CTH from 5 to 8 km (Mode 2), while the second shows CTH between 10 and 15 km (Mode 3) and, while less frequent, evidence of overshooting convection (Mode 4). Cell counts for Mode 1 (not shown because CPOL does not detect most of the shallow cumulus clouds) actually peaked shortly before the peak in Mode 2 and remained higher throughout

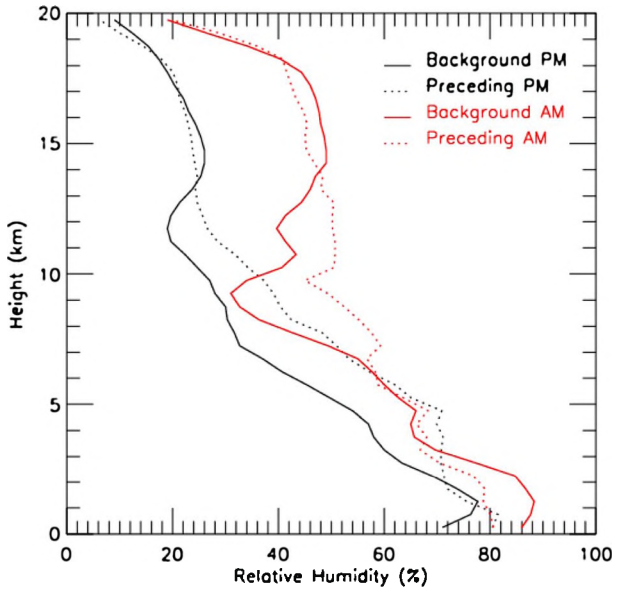

Figure 10. Mean vertical profile of relative humidity using radiosounding data during the interval 0–6 h preceding the onset of the 39 AM events (dashed red curve) and 78 PM events (dashed black curve). The solid red and black curves are background mean profiles obtained using all the 3 year radiosounding profiles between 00:00 A.M.–08:00 A.M. and 12:00 P.M.–08:00 P.M., respectively.

the heavy raining time. The shallower cloud population (Mode 2) occurs predominantly (more than 100 cells per bin) from ~8–10 h prior to the peak rainfall event to ~2 h after the event, with its peak frequency leading the peak rainfall by about 2 h. One notable feature in Figure 9c is that the increase in cell size and intensity noticed above coincides with a rapid growth in cloud depth about 5 h before the DMCR peak. The deep cloud population (Modes 3 and 4) has a maximum occurrence just below the TTL and maxima at and shortly after the time of the rainfall peak. The onset time of the deep cloud population lags that of the shallower one by 4 h, with a more uniform decay of both deep and shallow clouds 2–3 h after the peak rainfall. From the above results, we can identify roughly three stages of the storm development—a buildup phase (~5–10 h before the peak rainfall), a mature phase (5 h before to 1 h after the peak), and a decay phase (from 1 h after the rainfall peak).

[43] The distribution of CTH in the PM class (Figure 9e) is mostly similar to that observed in Figure 9c (all 144 events), since the PM class had 54% of rainfall events (see Figure 7). Notable features in the AM class (Figure 9d) which are somewhat different when compared to all events (Figure 9c) and PM statistics (Figure 9e) included the following: the ratio of the deep to the shallow population is higher (80% versus 30% in the PM class) and the lag time between the onset of the shallow to the onset of the deep population appears to be shorter. Also, the mode heights of the two dominant cell populations are lower in the AM class than in the PM class, and there are relatively less overshooting deep convective cells in the AM class.

[44] It seems intuitively consistent that in the AM class (oceanic) there is a faster transition time and higher deep to shallow cloud cell population ratios than for the PM class (continental) since the atmospheric moisture content is expected to be higher over ocean than land. Figure 10 shows that in the hours preceding the onset of heavy rainfall events in both classes, the relative humidity is higher in the middle troposphere (6–14 km; dotted lines in Figure 10) than in the background averages (solid lines). The feature of higher midlevel tropospheric moisture preceding deep convection has been documented in several studies [e.g., *Sherwood and Wahrlich*, 1999; *Mapes et al.*, 2006]. It is also evident from Figure 10 that the relative humidity associated with the AM events is higher in the middle troposphere, ranging between 50% and 60%, compared to that with the PM events with means between 25% and 50%. The presence of more moisture in the middle troposphere preceding the AM events compared to PM events will allow deep convection to form rather easily and quickly after shallow convection. An important question is what the source of this moistening preceding the onset of deep convection in both classes is. This will be further explored in section 5.

[45] Next, we explore the associated composite life cycle of convective cell microphysics around the rainfall peak using rain rate, mean drop diameter D_0, and drop concentration N_w retrieved at the 2.5 km CAPPI level from the dual-polarization radar observations (Figure 11). The objective here is to investigate the role played by convective-scale microphysics in the temporal evolution of rainfall over the composite life cycle shown in Figure 9, as well as in differences between AM and PM events. The "all events" plot is not shown, as it exhibits features very similar to the PM class (Figure 11, right). To help with the interpretation, we also show selected contours of normalized CTH occurrence frequency (black curves) from Figures 9d (AM class) and 9e (PM class). Note that the total CTH count is divided by the number of events in each class.

[46] Looking at Figure 11 (right), it appears clearly that the three main steps identified for the life cycle of convective cloud tops are all associated with major changes in convective-scale microphysics. In the buildup phase (~5–10 h before the peak rainfall), the D_0 and N_w at 2.5 km progressively increase as cloud top height increases over time, from about $D_0 = 1.2$ mm (and $\log10(N_w) = 3.8$) at $t = -10$ h for shallow congestus cloud top heights (below 7 km) to $D_0 = 1.6$ mm (and $\log10(N_w) = 4.3$) at $t = -5$ h for deep convective cloud tops reaching 10 km. The AM events (Figure 11, left) results are very different in that buildup phase, which are characterized by a large decrease in D_0 associated with deep convective cloud tops reaching 7 to 12 km (unlike the PM events) and an increase in mean N_w (like the PM events). Interestingly, this decrease in mean drop diameters in deep convective storms is also associated with a large reduction of rainfall rate at 2.5 km associated with the AM event when compared with the PM events (not shown). This indicates that breakup and evaporation processes play a more important role in rainfall production within the AM events, while coalescence is probably more efficient within the PM events.

[47] In the mature phase (5 h before to 1 h after the peak) where increasingly higher convective cloud tops associated with deep convection are found (Figure 9c), there is a large increase in D_0 and a decrease in N_w when compared with the buildup phase. This clearly indicates that coalescence processes are more efficient in that phase than during the

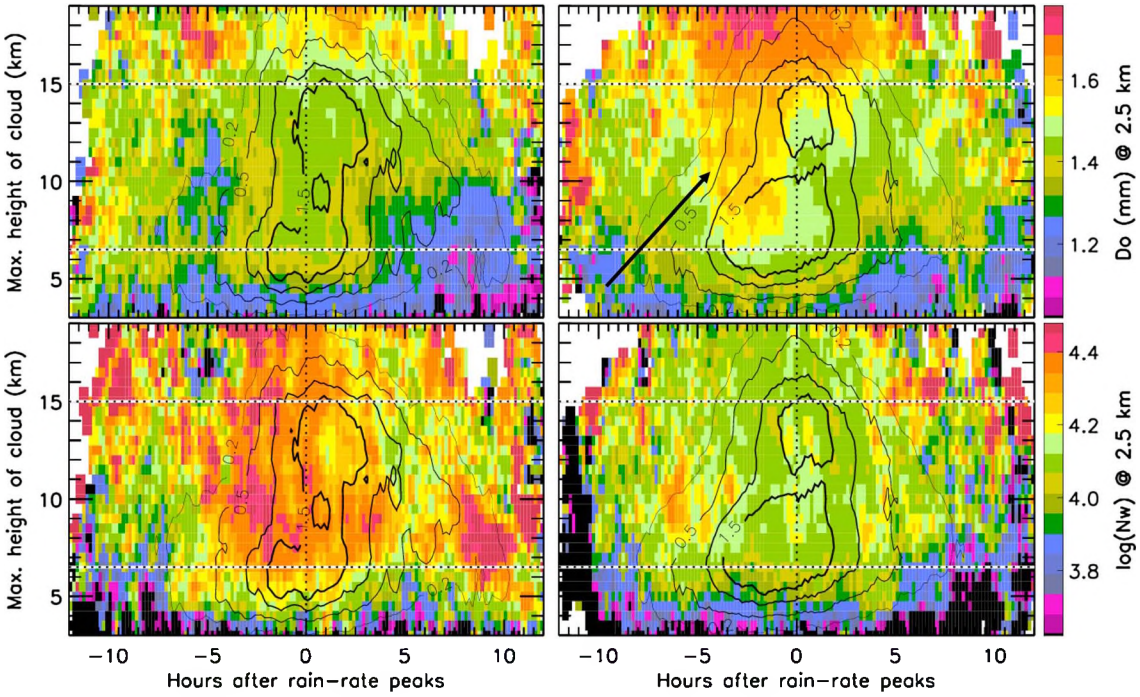

Figure 11. The same format as Figures 9d and 9e, except shows (top) D_0 and (bottom) N_w at 2.5 km associated with events in the (left) AM class and (right) PM class. The overplotted contour curves in black represent the CTH frequency as shown in Figures 9d and 9e, normalized by the number of events in each class.

buildup phase. It is striking to see how the microphysics of deep convective storms is very different in that mature phase between the AM and PM events. In the AM events, the N_w is actually increasing a lot, ~400% higher, when entering the mature phase (while it was slightly decreasing in the PM events), while the D_0 is increasing, but with a time lag with respect to the PM events similar to that observed for the increase in convective cloud top heights. Overall it is found that drops in the AM deep convective clouds are on average larger but in much smaller concentration than those in the PM deep convective clouds. In other words, deep convective rainfall characteristics in the mature stage of the life cycle of the AM and PM events are completely different.

[48] Finally, in the decay phase (from 1 h after the rainfall peak), the atmosphere returns to the same conditions as during the buildup phase for the PM events (Figure 11, right) and "all events" (not shown). It is not the case at all for the AM events, in which the rainfall parameters are very different from the buildup phase, especially for convective tops lower than 10 km, where mean drop diameters are much smaller and N_w are larger than during the buildup. This higher N_w is indicative of new convective developments. This seems to be in good agreement with larger frequencies of occurrence of cloud top heights in the 7–12 km height layer in Figure 9d as compared to Figure 9e.

5. The Temporal Evolution of the Large-Scale Moisture Budget During Rain Events

[49] In this section, we explore the evolution of large-scale moisture budget around the rainfall events identified above with the goal to better understand the relative role of dynamical and physical processes in the transition from shallow to deep convection. Due to their structural differences, the analysis is performed separately for the morning and afternoon rainfall events defined above. Figures 12a and 12b show the time evolution of the vertically resolved budget of specific humidity for ±12 h on either side of the AM and PM events, respectively. The large-scale moisture budget is divided into four terms, namely the moisture tendency (q tend) which arises from contributions from horizontal advection (q adv h), vertical advection (q adv v), and the residual term ($Q2$). In summary, q tend = q adv h + q adv v + $Q2$. The $Q2$ term represents the collective effects of all subdomain-scale processes [see *Yanai et al.*, 1973]. All terms are scaled to the same units of humidity change with time, i.e., g kg^{-1} h^{-1}.

[50] The large-scale data set has a 6-hourly resolution, and so within the 24 h window around each rainfall event, there will be between four and five profiles. The time stamps of the large-scale data with respect to the onset time of the rain events in both the AM and PM classes are represented by the short vertical lines above the humidity tendency panels. It is clear from this illustration that due to the high time resolution (10 min) of the radar data used to define the rain events, the timing of the large-scale data entering the composite is nearly continuous around $t = 0$ h. Thus, the observed temporal evolution of the moisture budget terms in Figure 11 is robust even on an hourly scale, despite using the 6-hourly forcing data set.

[51] Considering the humidity tendency itself, it is evident that both classes of events are characterized by moistening during the storm buildup phase that gradually increases in depth from the boundary layer to the middle troposphere. For the AM events, the moistening starts earlier than for the

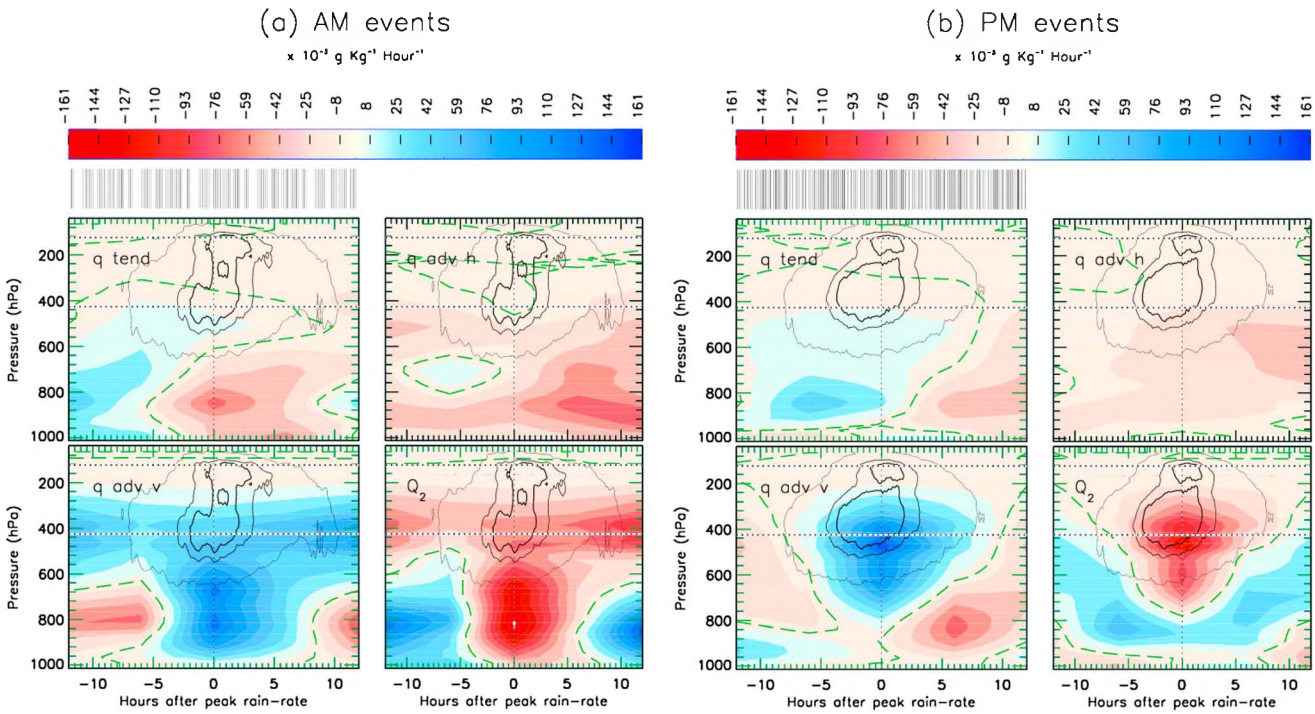

Figure 12. Superposed epoch analyses (composite) responses of Q terms for up to 12 h on either side of rain events identified to occur within (a) 00:00 A.M.–08:00 A.M. and (b) 12:00 P.M.–08:00 P.M. A bin size of 6 h in time and 50 hPa in pressure was used in this figure. The overplotted green curve shows the location of "0 amounts" in each panel, and the series of black curve is the CTH frequency as shown in Figures 9d and 9e. The vertical black lines above the humidity tendency panels indicate the large-scale profile times relative to the rainfall events used in the composite analysis.

PM events. It is often speculated that the main source of the midlevel moistening are cumulus congestus clouds. While not entirely conclusive, the breakdown of the humidity tendency into three components allows for an investigation of this hypothesis.

[52] It is evident that for both types of events, the horizontal advection terms are negative. This is understandable as areas of heavy rain are moist, making it likely that the surrounding area is drier leading to negative humidity gradients away from the rainy area. For both sets of events, it is the vertical advection term as well as the subdomain-scale terms that contribute to the midlevel moistening, albeit in quite different ways between the event types.

[53] For the AM events, which have been shown to be mostly oceanic in nature, the period from −12 to −5 h is characterized by drying of the middle troposphere (implying downward large-scale motion), compensated by moistening by subdomain processes. While it is tempting to ascribe this moistening to congestus clouds, it is evident from the evolution of the cloud characteristics (Figure 9 and replotted as grey contours in Figure 12) that no such clouds exist at this time. The fact that the atmosphere is ascending above the midlevels while the subgrid processes dry the upper troposphere makes it more likely that the middle tropospheric moistening by small-scale processes is a result of the evaporation of precipitation from stratiform clouds that are likely remnants of previous convective events. This is also consistent with a very similar evolution of the moisture budget after the main rain events (+9 h and onward). Approximately 8 h before the rainfall event, the vertical advection term turns positive near the surface increasing in depth as time progresses, reaching its peak during the event at midlevels. This implies a profile of increasing vertical motion with height, and hence low-level convergence, and indicates that it is large-scale dynamical, not small-scale, processes that dominate the evolution from shallow to deep convection. This is consistent with the findings of *Hohenegger and Stevens* [2012].

[54] The moisture evolution for the (land-based) PM events is somewhat different. The vertical advection term is positive at low levels for the entire prerainfall period. This is likely a result of net convergence into the domain in support of the widespread sea breeze circulations developing during the day. The moistening from this term is weak and increases in height a few hours before the main rainfall event. There is a distinct peak in moistening from small-scale processes approximately 5 h before the main rainfall event at 800 hPa, accompanied by the drying of the levels below, indicative of the presence of nonprecipitating shallow cumulus clouds. As is evident from the overlaid radar CTH evolution, the bulk of the congestus clouds appears after this peak and is not directly associated with it. In fact, the moistening by small-scale processes weakens when the congestus clouds appear, making it unlikely that they play a major role in setting the conditions for deep convection. More likely, they constitute a transitional stage of convection as the large-scale atmosphere transits from suppressed (−12 to −5 h) to convectively active (−5 to +5 h) conditions. The latter are characterized by a very strong compensation in the humidity tendency between large-scale dynamical

processes (moistening) and small-scale convective processes (drying), indicating the very strongly dynamically coupled nature of precipitating deep convection.

6. Conclusion and Summary

[55] Wet season (October–April) C-band polarimetric (CPOL) radar observations of cumulus cloud top heights (CTHs) and their rainfall properties over a 3 year period (2004–2007) at the Darwin site have been used to objectively identify different tropical cumulus modes. Once these cumulus modes were established, the study then focused on studying the progression of the different modes around several carefully selected heavy rainfall events by using a composite analysis applied separately to events experienced in morning (oceanic) and afternoon (continental) conditions. The large-scale moisture budget was analyzed to reveal the relative role of dynamical and physical processes in the transition from shallow to deep convection during the rainfall events.

[56] The study first showed that the CPOL radar is capable of observing cumulus congestus mode (aka, Mode 2) but misses most of the shallow cumulus mode (aka, Mode 1). This was verified by comparing the CTH statistics from CPOL with concurrent observations from a millimeter-wavelength cloud radar (MMCR). In deeper convection (aka, Modes 3 and 4), the CPOL performance was shown to be better than that of the MMCR, as expected.

[57] The identification and further study of individual cumulus cloud cells revealed that the cell rainfall properties at 2.5 km height change remarkably with CTH. This allowed an objective way of identifying four different cloud types: a shallow cumulus mode with CTH in the trade inversion layer (1–3 km), a congestus mode with tops in the highly stable middle troposphere (3–6.5 km), a deep convective mode with tops in the region of free convection (6.5–15 km), and an overshooting convection mode with tops in the tropical tropopause layer (CTH > 15 km). The four CTH layers of the cumulus modes are also visible in temperature lapse rates. Furthermore, the vertical profile of the reflectivity lapse rates is also found to contrast strongly between the different cumulus cloud modes.

[58] The study then examined the temporal evolution of the identified cumulus modes during heavy rainfall events. Overall, the daily rainfall pattern in the Darwin region is semidiurnal in nature, with the larger afternoon peak clearly associated with continental-based convection and the secondary peak associated with oceanic convection. The two types of events were studied separately by considering events between 00:00 A.M. and 08:00 A.M. local time (AM class with 39 events) and 12:00 P.M.–08:00 P.M. local time (PM class with 78 events). In both sets of events, there is a distinct evolution of cloud top height involving a "congestus" phase that starts 5–8 h before the rainfall peak. The deeper modes begin to form shortly before the onset time of rainfall events. All cumulus modes decay nearly at the same time, approximately 3 h after the rainfall peak. For the oceanic AM events, the ratio of the shallow to the deep population is higher and the transition time from the shallow to the onset of deep population is shorter than for the continental PM events. The convective-scale microphysical properties, represented by retrieved mean drop diameter D_0 and drop concentration N_w, were found to be very different between the two rain event classes. This indicates that different microphysical processes dominate over different underlying surfaces during convective storms.

[59] A composite analysis of the large-scale moisture budget during the rainfall events implies that for both the AM and PM events, the moistening peaks before the peak in the congestus population. In both sets of events, large-scale dynamical processes play a significant role in the transition from shallow to deep clouds. This leads to the conclusion that the transition to deep convection is characterized by a close interplay between a moistening of the middle troposphere by congestus clouds and the heating-induced convergence on larger scales.

[60] Many more studies of this kind using a combination of instruments such as merged cloud radar, CPOL, and in situ observations, and over different underlying surface conditions such as oceanic and continental are needed to further understand the rainfall properties of the four cumulus cloud modes identified here and their evolution during rainfall events. In particular, the shallow cumulus mode (Mode 1), its rainfall properties and role, if any, in increasing the congestus formation (Mode 2) and subsequent deep clouds (Modes 3 and 4) needs to be investigated with more suitable scanning radars and higher resolution space-time observation of the atmospheric moisture and thermal gradients. Also, it would be worthwhile to analyze the tropical data with strategies developed in studies already undertaken at midlatitudes [e.g., *Zhang and Klein*, 2010].

[61] **Acknowledgments.** This work has been supported by the U.S. Department of Energy ARM Program (DE-FG02-09ER64742). We would like to acknowledge the contributions of Brad Atkinson and Michael Whimpey in supporting the Darwin observatory and data management.

References

Ackerman, T. A., and G. M. Stokes (2003), The atmospheric radiation measurement program, *Phys. Today*, *56*, 38–45.

Bringi, V. N., C. R. Williams, M. Thurai, and P. T. May (2009), Using dual-polarized radar and dual-frequency profiler for DSD characterization: A case study from Darwin, Australia, *J. Atmos. Oceanic Tech.*, *26*, 2107–2122.

Casey, S. P. F., E. J. Fetzer, and B. H. Kahn (2012), Revised identification of tropical oceanic cumulus congestus as viewed by CloudSat, *Atmos. Chem. Phys.*, *12*, 1587–1595.

Chen, Y., and A. D. Del Genio (2009), Evaluation of tropical cloud regimes in observations and a general circulation model, *Climate Dynam.*, *32*, 355–369.

Del Genio, A. D., Y.-H. Chen, D. Kim, and M.-S. Yao (2012), The MJO transition from shallow to deep convection in CloudSat/CALIPSO data and GISS GCM simulations, *J. Climate*, *25*, 3755–3770, doi:10.1175/JCLI-D-11-00384.1.

Hohenegger, C., and B. Stevens (2012), Preconditioning deep convection with cumulus congestus, *J. Atmos. Sci.*, *70*, 448–464, doi:10.1175/JAS-D-12-089.1.

Houze, R. A., and C.-P. Cheng (1977), Radar characteristics of tropical convection observed during GATE: Mean properties and trends over the summer season, *Mon. Weather Rev.*, *105*, 964–980.

Jakob, C. (2010), Accelerating progress in global atmospheric model development through improved parameterizations: Challenges, opportunities and strategies, *Bull. Am. Meteorol. Soc.*, *91*, 869–875.

Jakob, C., L. Davies, V. V. Kumar, and P. T. May (2011), Representing convection in models — How stochastic does it need to be?, *Proceedings of the ECMWF Workshop on "Representing Model Uncertainty and Error in Weather and Climate Prediction"*, ECMWF.

Jensen, M. P., and A. D. Del Genio (2006), Factors limiting convective cloud-top height at the ARM Nauru Island climate research facility, *J. Climate*, *19*, 2105–2117.

Johnson, R. H., T. M. Rickenbach, S. A. Rutledge, P. E. Ciesielski, and W. H. Schubert (1999), Trimodal characteristics of tropical convection, *J. Climate*, *12*, 2397–2418.

Keenan, T. D., K. Glasson, F. Cummings, T. S. Bird, J. Keeler, and J. Lutz (1998), The BMRC/NCAR C-band polarimetric (CPOL) radar system, *J. Atmos. Oceanic Tech.*, *15*, 871–886.

Kemball-Cook, S. R., and B. C. Weare (2001), The onset of convection in the Madden-Julian oscillation, *J. Climate*, *14*, 780–793.

Kikuchi, K., and Y. N. Takayabu (2004), The development of organized convection associated with the MJO during TOGA COARE IOP: Trimodal characteristics, *Geophys. Res. Lett.*, *31*, L10101, doi:10.1029/2004GL019601.

Kingsmill, D. E., and R. M. Wakimoto (1991), Kinematic, dynamic, and thermodynamic analysis of a weakly sheared severe thunderstorm over northern Alabama, *Mon. Weather Rev.*, *119*, 262–297.

Kuang, Z., and C. S. Bretherton (2006), A mass-flux scheme view of a high-resolution simulation of a transition from shallow to deep cumulus convection, *J. Atmos. Sci.*, *63*, 1895–1909.

Kumar, V. V., A. Protat, P. T. May, C. Jacob, G. Penide, S. Kumar, and L. Davies (2013), On the effects of large-scale environment and surface conditions on convective cloud characteristics over Darwin, Australia, *Mon. Weather Rev.*, doi:10.1175/MWR-D-12-00160.1.

Kumar V. V., and V. Ramachandran (2004), Rain-attenuation measurement at 11.6 GHz in Suva, Fiji, *Electron. Lett*, Institution of Electrical Engineers, United Kingdom, *40*(22), 1429–1431.

Lin, X., and R. H. Johnson (1996), Heating, moistening, and rainfall over the western Pacific warm pool during TOGA COARE, *J. Atmos. Sci.*, *53*, 3367–3383.

Liu, C., and E. J. Zipser (2008), Diurnal cycles of precipitation, clouds, and lightning in the tropics from 9 years of TRMM observations, *Geophys. Res. Lett.*, *35*, L04819, doi:10.1029/2007GL032437.

Malkus, J. S., and H. Riehl (1964), *Cloud Structure and Distributions Over the Tropical Pacific Ocean*, pp. 229, University of California Press, London, England.

Mapes, B. E., S. Tulich, J. Lin, and P. Zuidema (2006), The mesoscale convection life cycle: Building block or prototype for large-scale tropical waves?, *Dyn. Atmos. Oceans*, *42*, 3–29.

May, P. T., C. Long, and A. Protat (2012), The diurnal cycle of the boundary layer, convection, clouds, and surface radiation in a coastal monsoon environment (Darwin Australia), *J. Climate*, *25*, 5309–5326, doi:10.1175/JCLI-D-11-00538.1.

May, P. T., and A. Ballinger (2007), The statistical characteristics of convective cells in a monsoon regime (Darwin, Northern Australia), *Mon. Weather Rev.*, *138*, 55–73.

May, P. T., J. H. Mather, G. Vaughan, C. Jakob, G. M. McFarquhXar, K. N. Bower, and G. G. Mace (2008), The Tropical Warm Pool International Cloud Experiment, *Bull. Am. Meteorol. Soc.*, *89*, 629–645.

Melnikov, V. M., D. S. Zrnić, R. J. Doviak, P. B. Chilson, D. B. Mechem, and Y. Kogan (2011), Prospects of the WSR-88D radar for cloud studies, *J. Appl. Meteorol. Climatol.*, *50*, 859–872.

Miller, M. A., J. Verlinde, C. V. Gilbert, G. J. Lehenbauer, J. S. Tongue, and E. E. Clothiaux (1998), Detection of nonprecipitating clouds with the WSR-88D: A theoretical and experimental survey of capabilities and limitations, *Wea. Forecasting*, *13*, 1046–1062.

Moran, K. P., B. E. Martner, M. J. Post, R. A. Kropfli, D. C. Welsh, and K. P. Widener (1998), An unattended cloud-profiling radar for use in climate research, *Bull. Am. Meteorol. Soc.*, *79*, 443–455.

Penide, G., V. V. Kumar, A. Protat, and P. T. May (2013), Statistics of drop size distribution parameters and rain rates for stratiform and convective precipitation during the North Australian wet season, *Mon. Weather Rev.*, doi:10.1175/MWR-D-12-00262.1.

Pope, M., C. Jakob, and M. Reeder (2009a), Regimes of the North Australian wet season, *J. Climate*, *22*, 6699–6715.

Pope, M., C. Jakob, and M. Reeder (2009b), Objective classification of tropical mesoscale convective systems, *J. Climate*, *22*, 5797–5808.

Redelsperger, J. -L., D. B. Parsons, and F. Guichard (2002), Recovery processes and factors limiting cloud-top height following the arrival of a dry intrusion observed during TOGA COARE, *J. Atmos. Sci.*, *59*, 2438–2457.

Rickenbach, T. M., and S. A. Rutledge (1998), Convection in TOGA COARE: Horizontal scale, morphology, and rainfall production, *J. Atmos. Sci.*, *55*, 2715–2729.

Schafer, R., P. T. May, T. D. Keenan, K. McGuffie, W. L. Ecklund, P. E. Johnston, and K. S. Gage (2001), Boundary layer development over a tropical island during the Maritime Continent Thunderstorm Experiment, *J. Atmos. Sci.*, *58*, 2163–2179.

Sherwood, S. C., and R. Wahrlich (1999), Observed evolution of tropical deep convective events and their environment, *Mon. Weather Rev.*, *127*, 1777–1795.

Simpson, J., T. D. Keenan, B. Ferrier, R. H. Simpson, and G. J. Holland (1993), Cumulus mergers in the maritime continent region, *Meteorol. Atmos. Phys.*, *51*, 73–99.

Steiner, M., R. A. Houze Jr., and S. E. Yuter (1995), Climatological characterization of three-dimensional storm structure from operational radar and rain gauge data, *J. Appl. Meteorol.*, *34*, 1978–2007.

Stokes, G. M., and S. E. Schwartz (1994), The Atmospheric Radiation Measurement (ARM) Program: Programmatic background and design of the cloud and radiation testbed, *Bull. Am. Meteorol. Soc.*, *75*, 1201–1221.

Testud, J., S. Oury, P. Amayenc, and R. A. Black (2001), The concept of "normalized" distributions to describe raindrop spectra: A tool for cloud physics and cloud remote sensing, *J. Appl. Meteorol.*, *40*, 1118–1140.

Tromeur, E., and W. B. Rossow (2010), Interaction of tropical deep convection with the large-scale circulation in the MJO, *J. Climate*, *23*, 1837–1853.

Waite, M. L., and B. Khouider (2010), The deepening of tropical convection by congestus preconditioning, *J. Atmos. Sci.*, *67*, 2601–2615.

Xie, S., R. T. Cederwall, and M. Zhang (2004), Developing long-term single-column model/cloud system—Resolving model forcing data using numerical weather prediction products constrained by surface and top of the atmosphere observations, *J. Geophys. Res.*, *109*, D01104, doi:10.1029/2003JD004045.

Xie, S., T. Hume, C. Jakob, S. A. Klein, R. McCoy, and M. Zhang (2010), Observed large-scale structures and diabatic heating and drying profiles during TWP-ICE, *J. Climate*, *23*, 57–79.

Yanai, M., S. Esbensen, and J. Chu (1973), Determination of bulk properties of tropical cloud clusters from large-scale heat and moisture budgets, *J. Atmos. Sci.*, *30*, 611–627.

Zhang, M., and J. Lin (1997), Constrained variational analysis of sounding data based on column-integrated budgets of mass, heat, moisture, and momentum: Approach and application to ARM measurements, *J. Atmos. Sci.*, *54*(11), 1503–1524.

Zhang, Y., and S. A. Klein (2010), Mechanisms affecting the transition from shallow to deep convection over land: Inferences from observations of the diurnal cycle collected at the ARM Southern Great Plains site, *J. Atmos. Sci.*, *67*, doi:10.1175/2010JAS3366.1.

Zipser, E. J., and K. R. Lutz (1994), The vertical profile of radar reflectivity of convective cells: A strong indicator of storm intensity and lightning probability?, *Mon. Weather Rev.*, *122*, 1751–1759.

Zrnić, D. S., and A. V. Ryzhkov (1998), Polarimetry for weather surveillance radars, *Bull. Am. Meteorol. Soc.*, *80*(3), 389–406.

JOURNAL OF GEOPHYSICAL RESEARCH: ATMOSPHERES, VOL. 118, 6544–6563, doi:10.1002/jgrd.50450, 2013

A single-column model ensemble approach applied to the TWP-ICE experiment

L. Davies,[1] C. Jakob,[2] K. Cheung,[3] A. Del Genio,[4] A. Hill,[5] T. Hume,[6] R. J. Keane,[7] T. Komori,[8] V. E. Larson,[9] Y. Lin,[10,11] X. Liu,[12] B. J. Nielsen,[9] J. Petch,[5] R. S. Plant,[13] M. S. Singh,[14] X. Shi,[12] X. Song,[15] W. Wang,[16] M. A. Whitall,[13] A. Wolf,[17] S. Xie,[18] and G. Zhang[15]

Received 25 October 2012; revised 23 April 2013; accepted 24 April 2013; published 24 June 2013.

[1] Single-column models (SCM) are useful test beds for investigating the parameterization schemes of numerical weather prediction and climate models. The usefulness of SCM simulations are limited, however, by the accuracy of the best estimate large-scale observations prescribed. Errors estimating the observations will result in uncertainty in modeled simulations. One method to address the modeled uncertainty is to simulate an ensemble where the ensemble members span observational uncertainty. This study first derives an ensemble of large-scale data for the Tropical Warm Pool International Cloud Experiment (TWP-ICE) based on an estimate of a possible source of error in the best estimate product. These data are then used to carry out simulations with 11 SCM and two cloud-resolving models (CRM). Best estimate simulations are also performed. All models show that moisture-related variables are close to observations and there are limited differences between the best estimate and ensemble mean values. The models, however, show different sensitivities to changes in the forcing particularly when weakly forced. The ensemble simulations highlight important differences in the surface evaporation term of the moisture budget between the SCM and CRM. Differences are also apparent between the models in the ensemble mean vertical structure of cloud variables, while for each model, cloud properties are relatively insensitive to forcing. The ensemble is further used to investigate cloud variables and precipitation and identifies differences between CRM and SCM particularly for relationships involving ice. This study highlights the additional analysis that can be performed using ensemble simulations and hence enables a more complete model investigation compared to using the more traditional single best estimate simulation only.

Citation: Davies, L., et al. (2013), A single-column model ensemble approach applied to the TWP-ICE experiment, *J. Geophys. Res. Atmos.*, *118*, 6544–6563, doi:10.1002/jgrd.50450.

1. Introduction

[2] The Tropical Warm Pool International Cloud Experiment (TWP-ICE) took place around Darwin from 20 January to 13 February 2006 [*May et al.*, 2008]. The data collected during the experiment provides an opportunity to investigate several different states of tropical convection. The

[1]School of Mathematics, Monash University, Melbourne, Victoria, Australia.
[2]ARC Centre of Excellence for Climate System Science, Monash University, Melbourne, Victoria, Australia.
[3]Bureau of Meteorology, Melbourne, Victoria, Australia.
[4]NASA Goddard Institute for Space Studies, New York, New York, USA.
[5]Met Office, Exeter, UK.
[6]Centre for Australian Weather and Climate Research, Bureau of Meteorology, Melbourne, Victoria, Australia.
[7]Meteorologisches Institut, Ludwig-Maximilians-Universitat Munchen, Munich, Germany.
[8]Japan Meteorological Agency, Tokyo, Japan.
[9]University of Wisconsin-Milwaukee, Milwaukee, Wisconsin, USA.
[10]University Corporation for Atmospheric Research, Boulder, Colorado, USA.
[11]NOAA Geophysical Fluid Dynamics Laboratory, Princeton, New Jersey, USA.
[12]Pacific Northwestern National Laboratory, Richland, Washington, USA.
[13]Department of Meteorology, University of Reading, Reading, UK.
[14]Massachusetts Institute of Technology, Cambridge, Massachusetts, USA.
[15]University of California, San Diego, California, USA.
[16]IMSG@NOAA National Centers for Environmental Prediction, College Park, Maryland, USA.
[17]Department of Applied Physics and Applied Mathematics, Columbia University, New York, New York, USA.
[18]Lawrence Livermore National Laboratory, Livermore, California, USA.

Corresponding author: L. Davies, School of Earth Sciences, The University of Melbourne, Melbourne 3010, Victoria, Australia. (laura.davies@unimelb.edu.au)

2169-897X/13/10.1002/jgrd.50450

experiment collected sufficient information to derive both the large-scale heat and momentum and moisture budgets [*Xie et al.*, 2004] as well as detailed information on the state of the smaller scale convection and associated clouds. Such data sets are commonly used in the modeling community to carry out process-oriented studies in particular applying cloud-resolving models (CRM) and single-column models (SCM). One of the primary motivations for TWP-ICE was to enable the improvement of global climate models (GCM), which are known to be deficient in the representation of cloud and rainfall particularly associated with tropical convection. The international research community has conducted a suite of multimodel studies for TWP-ICE. A hierarchy of experiments enables the investigation of model errors as discussed in J. Petch et al. (Evaluation of intercomparisons of four different types of model simulating TWP-ICE, submitted to *Quarterly Journal of the Royal Meteorological Society*, 2012) and includes GCM [*Lin et al.*, 2012] and Limited Area Models [*Zhu et al.*, 2012] forced with European Centre for Medium-Range Weather Forecasts (ECMWF) reanalysis as well as a CRM study [*Fridlind et al.*, 2012] performing simulations driven by a single "best estimate" large-scale budget data set [*Xie et al.*, 2010]. This paper reports on the SCM component of the overall modeling strategy. One innovation applied here will be the use of an ensemble of SCM simulations to elucidate uncertainties in the estimation of model errors and to explore model sensitivities to changes in the data set driving the model simulations.

[3] The investigation of model shortcomings through SCMs is a well-used method in the model development research community. Model development studies, which include a SCM component, have been instigated by the Global Energy and Water-Cycle Experiment (GEWEX) Cloud System Study (GCSS) [*Randall et al.*, 2003] in conjunction with the U.S. Department of Energy Atmospheric System Research (ASR) to investigate a wide range of test cases including deep convection over the tropical ocean using data from the Tropical Ocean Global Atmosphere (TOGA) Coupled Ocean-Atmosphere Response Experiment (COARE) [*Webster and Lukas*, 1992] intensive observation period [e.g., *Woolnough et al.*, 2010; *Bechtold et al.*, 2000] and convection over land exploiting extensive observations [e.g., *Grabowski et al.*, 2006; *Xie et al.*, 2005, 2002; *Ghan et al.*, 2000]. Investigation of the specific problem of the diurnal cycle was conducted by the European Cloud Systems (EUROCS) project and discussed in *Guichard et al.* [2004]. These studies focussed on a limited number of model simulations forced by a single data set, from hereon referred to as the "best estimate" forcing. While best estimates of the large-scale atmosphere are usually derived to depict the most probable state of the large-scale atmosphere, they do contain errors of usually unknown magnitude. These errors complicate the interpretation of the results of SCM simulations, as the discrepancies between the model-simulated fields and observations may be attributed to two sources, from prescribing an incorrect large-scale state or due to errors in model processes. By using a single-model realization of the large-scale state, it is impossible to separate these two error sources.

[4] Ensemble techniques are commonly used in numerical weather prediction (NWP) and climate models to investigate model sensitivities and to determine uncertainty. These ensembles may include perturbed initial conditions or varying model parameters within a limited range. Multimodel ensembles have also been used to provide an estimate of the range of simulations. A limited number of studies also derived ensemble techniques for use in SCM studies. *Hack and Pedretti* [2000] added random perturbations to the initial conditions of their ensemble simulations and found considerable variations in simulated fields. Similar results were found when modifying the prescribed vertical motion field in a similar manner. Given the bifurcations discussed in *Hack and Pedretti* [2000], *Hume and Jakob* [2005, 2007] and *Ball and Plant* [2008] determined that an ensemble technique was appropriate for SCM. *Hume and Jakob* [2005] found that after about 18 h of simulation, results were increasingly sensitive to the prescribed forcing rather than differences in the initial conditions. For this reason, this TWP-ICE study uses an ensemble of large-scale forcing.

[5] The goal of this study is to apply an ensemble SCM technique to the TWP-ICE experiment and to highlight additional opportunities for model evaluation that such a technique may provide. The technique is applied to a wide range of SCMs as well as a small number of CRMs, enabling the investigation of a range of model behaviors. The results from the ensemble simulation will be compared to those of single "best estimate" simulations. It will be shown that a particularly interesting aspect of the use of the ensemble technique in this context is the possibility to study model sensitivities with changing forcing data set. It is shown that the different models exhibit distinctly different ensemble behavior that is not apparent when comparing simulations with a single forcing data set. Section 2 summarizes the experimental design including the methodology used in the derivation of the ensemble large-scale forcing, the case specification, and a description of the models. The main results of the study are discussed in section 3 followed by a summary and the main conclusions in section 4.

2. Experimental Design

[6] The experiments conducted here use both a best estimate forcing and an ensemble of forcing data sets. The best estimate data set used is that derived by *Xie et al.* [2010] and is identical to that used in *Fridlind et al.* [2012]. Using an ensemble approach enables a better understanding of model accuracy and model sensitivity to be calculated. As this study includes a number of different models, these characteristics are determined dependent on model. This section will detail the design of the study including the ensemble forcing design, the case specification, and the participating models.

2.1. Ensemble Design

[7] A number of techniques exist to derive budgets from observational data collected in field campaigns. Here, the variational analysis technique of *Zhang and Lin* [1997] is used in the analysis of TWP-ICE observations. This technique provides an estimate of area-averaged atmospheric and surface conditions using a combination of surface observations, vertical profiles of the atmosphere, satellite observations, and numerical model data. The variational analysis process minimizes a cost function for the heat, moisture, and

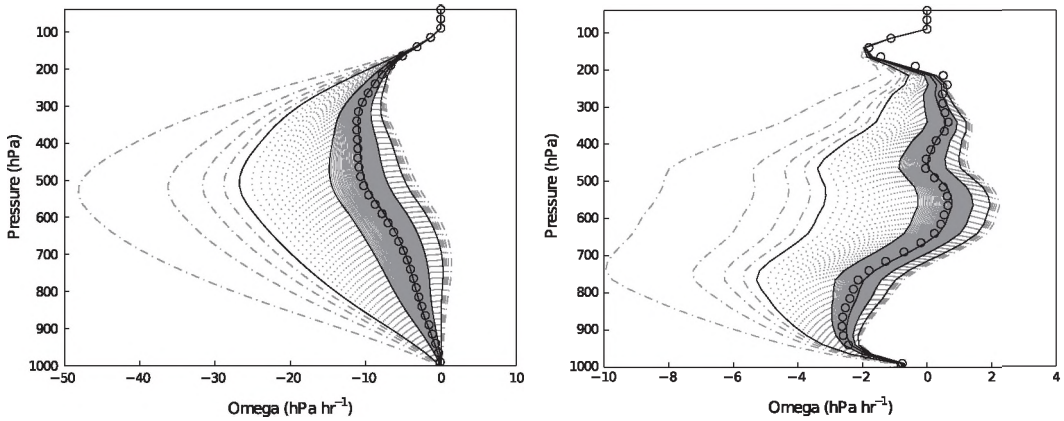

Figure 1. Time-averaged vertical profiles of omega over active (left) and suppressed (right) monsoon for all ensemble members. Broken and light-colored lines show all ensemble members with key ensemble members (5th, 25th, 50th, 75th, and 95th percentiles) as black continuous lines. The best estimate forcing, used here and in the CRM intercomparison, is shown by small circles. Note the different x axis.

momentum budgets using constraints of top of atmosphere and surface energy and moisture.

[8] One of the constraints used in the variational analysis method is the domain-average surface rainfall. In the case of the TWP-ICE experiment, this domain-mean surface rainfall is derived from radar data. Compared to the use of rain gauge observations, this improves the spatial representativeness of the estimate, but this comes at the expense of accuracy of the local rainfall estimates as radar measurements need to be converted to rainfall. It has been shown [*Zhang et al.*, 2001] that the surface rainfall has a large effect on the derived forcing data set; for example, the analyzed vertical velocity is very sensitive to rainfall. Furthermore, the derivation of surface rainfall from radar data is also highly complex and liable to large errors [*Joss and Waldvogel*, 1990]. These errors will have a large effect on the derived forcing data set.

[9] One method to address uncertainty in large-scale forcing data is to derive an ensemble of forcing data. Only a short summary of the method to derive such an ensemble is given here, with more details provided in the Appendix. The method is principally based on estimates of errors in the rainfall estimates that are a key input to the variational budget analysis. A comparison of radar-derived and rain gauge data is carried out to provide an estimate of the error in the radar estimates of domain-average rainfall. From these error estimates, 100 equally likely alternative domain-mean rainfall time series are calculated. The 100 rainfall time series are then used as inputs to the variational analysis to derive 100 alternative versions of the large-scale state using the same variational technique as is used to derive the best estimate large-scale state. These 100 large-scale states constitute the forcing ensemble used in this study.

[10] When deriving the large-scale state using these alternate rainfall time series, all other observations have the same values as the best estimate, for example, temperature, moisture, and horizontal wind fields. Given that the boundary values of temperature and moisture are identical between all realizations, the horizontal advection terms of temperature and moisture differ very little. The variational analysis process generally equates larger values of rainfall with increased low-level convergence and upper level divergence and therefore generally larger values of vertical velocity. The structure of the derived vertical velocity, however, is also dependent on other budget terms so that vertical velocity does not monotonically increase with rainfall.

[11] Figure 1 shows the vertical velocity profile averaged over both the active and suppressed monsoon for each ensemble member as well as key percentiles of the ensemble. Stronger vertical motion is derived from time series with larger rainfall. In the active monsoon, there is always strong upward vertical motion, although the ensemble members with weaker rainfall have weaker vertical motion. During the suppressed monsoon, the ensemble members with strong rainfall have upward vertical motion at all levels. The ensemble members with weaker rainfall have upward motion at lower levels (below 650 hPa) but downward motion above. In addition to the ensemble members, Figure 1 shows the standard best estimate for vertical velocity. As is evident, the best estimate results are close, but not identical, to the 50th percentile of the ensemble forcing. While there is a large spread in omega, it is worth noting that 50% of the ensemble members lie in the limited range between the 25th and 75th percentile lines. While each ensemble member is equally likely, most cluster around the 50th ensemble member and the best estimate, and the most extreme omega values are rare. These differences in omega imply changes in low-level convergence and upper level divergence through the continuity equation and will have an effect on convection. These 100 large-scale "forcing" data sets are then used as input to the model simulations discussed below.

2.2. Case Description

[12] The TWP-ICE experiment experienced a range of atmospheric conditions. At the start of the experiment, the region experienced monsoon conditions. Between 23 and 24 January, a strong mesoscale convective system (MCS) passed through the domain followed by relatively suppressed conditions. There were then clear conditions from 3 to 5 February with little rain followed by monsoon break conditions to the end of the field campaign. Full details of the meteorological conditions can be found in *May et al.* [2008]. In this study, the focus is on the active period defined as 20 00Z–25 12Z Jan and the suppressed period defined as

Table 1. Models Contributing to SCM Study[a]

Model	Full Name	Modeler	Reference
UM-GR	Unified Model-Gregory and Rowntree	M. Whitall/R. Plant	*Davies et al.* [2005]
UM-PC	Unified Model-Plant/Craig	R. Keane/R. Plant	*Davies et al.* [2005]
SCAMS	Single-Column Community Atmospheric Model	X. Liu/X. Shi	*Collins et al.* [2006]
SCAML	Single-Column Community Atmospheric Model	X. Liu/X. Shi	*Wang et al.* [2009]
SCAMR	Single-Column Community Atmospheric Model	X. Song/G. Zhang	*Collins et al.* [2006]
NCEPG	NCEP GFS Model	W. Wang	*EMC* [2003]
GFDL2	GFDL-AM2 Model	Y. Lin	*GAMDT* [2004]
GISS	GISS Model	A. Wolf/A. DelGenio	*Schmidt et al.* [2006]
CLUBB	Cloud Layers Unified by Binormals model	B. Nielsen/V. Larson	*Golaz et al.* [2002]
JMA1	Japan Meteorological Agency	T. Komori	*JMA* [2007]; *Nakagawa* [2009]
JMA2	Japan Meteorological Agency	T. Komori	*JMA* [2007]; *Nakagawa* [2009]
2-D LEM	UK Met Office Large Eddy Model	A. Hill	*Gray et al.* [2001]
3-D SAM	System for Atmospheric Modeling	L. Davies	*Khairoutdinov and Randall* [2003]

[a]Includes the acronym used in this paper, the full model name, contributing author(s), and the main reference for the model. Further model details are given in the text and the references therein. Note that there are two cloud-resolving models as part of this study.

28 00Z Jan–2 12Z Feb. The conditions during the clear and break periods are dominated by a strong diurnal cycle, which is driven by the land-sea contrast in the experiment domain. As SCMs cannot usually represent such contrasts in a single grid box, the later part of the experiment is excluded from the simulations presented here.

[13] In order to investigate the performance of the ensemble technique proposed here in different meteorological conditions, the study applies two sets of large-scale forcing data. The first is a best estimate simulation forced using the standard data set [*Xie et al.*, 2010]. These simulations can be directly compared to the CRM results [*Fridlind et al.*, 2012], and the best estimate simulations also form the basis of discussion in J. Petch et al. (submitted manuscript, 2012). In this study, the best estimate simulations will be used to form a SCM multimodel ensemble. In addition to the best estimate simulations, all models were run using the 100-member ensemble of forcing data derived above. It was found that some models showed numerical instabilities for the strongest forcing data sets (i.e., those derived from the largest rainfall) when using their standard time-stepping. As a consequence, the 10 strongest forcing data sets and, for reasons of symmetry, the 10 weakest ones are excluded from further analysis, reducing the ensemble size to 80.

[14] The aim when defining the model specification is to impinge as little as possible on the inherent characteristics of the individual models, and modelers are encouraged to use their preferred configurations; however, the following requirements are made for all simulations:

[15] 1. The TWP-ICE domain has mixed surface types making the choice of surface type unclear. All simulations assume an ocean surface consistent with *Fridlind et al.* [2012]. Fixed time-invariant SST = 29°C is used. Interactive surface fluxes are required to be calculated in the boundary layer scheme.

[16] 2. Simulations are initialized with observed temperature and moisture profiles at 0300Z 19 January 2006.

[17] 3. An observed ozone profile is used where possible, but the McClatchey ozone profile [*McClatchey et al.*, 1972] is used above the maximum height of observations (40 mbar).

[18] 4. Full interactive radiation is used with a diurnal cycle for a domain centered on the Atmospheric Radiation Measurement (ARM) site (12.425°S, 130.891°E).

[19] 5. Mean horizontal winds are relaxed to observed profiles with a 2 h time scale. There is no nudging of the temperature and moisture fields which are left free to respond to the forcing.

[20] 6. Horizontal advective tendencies for temperature and moisture are prescribed, but the vertical terms are calculated by the models. Sensitivity studies showed a warm temperature bias above the tropopause when prescribing a total forcing as the model cannot freely evolve vertical advection associated with this warming and reduce the temperature bias. This method differs from *Fridlind et al.* [2012] where temperature and moisture were nudged towards observed profiles to avoid such temperature biases.

2.3. Models

[21] In this section, a brief description of all models used in this study will be given. Table 1 gives a summary of the models with further details given below. The study also includes two CRM which also simulate the ensemble. The CRM provide an important reference for the SCM and link to the CRM study [*Fridlind et al.*, 2012].

[22] The UK Met Office SCM [*Davies et al.*, 2005] contains parameterizations for radiation [*Edwards and Slingo*, 1996], layer-cloud microphysics [*Wilson and Forbes*, 2004; *Wilson and Ballard*, 1999], boundary layer processes [*Lock et al.*, 2000], and convection; see also *Martin et al.* [2006]. Results were submitted for both the default UM convection scheme [*Gregory and Rowntree*, 1990; *Martin et al.*, 2006; *Derbyshire et al.*, 2011] (UM-GR) and the *Plant and Craig* [2008] stochastic spectral mass-flux scheme (UM-PC). In the default scheme, convection is triggered by instability of surface parcels at the lifting condensation level (LCL); a CAPE closure is used for deep convection, and the closure for shallow convection is based on *Grant* [2001]. In the Plant-Craig scheme, convection is triggered by constructing potential updraft source layers and evaluating their buoyancy at the LCL; a CAPE closure is used. The stochastic variability of the Plant-Craig scheme depends upon the column size—an area of $(50\ \mathrm{km})^2$ was used here.

[23] The single-column model of the NCAR CAM3 (SCAM) contains the radiation scheme as described in *Collins et al.* [2006]. The treatment of cloud condensation and microphysics in CAM3 [*Boville et al.*, 2006] is based on *Rasch and Kristjánsson* [1998] as updated by

Zhang et al. [2003] with separate prognostic equations for the liquid and ice-phase condensate. The boundary layer scheme is based on *Holtslag and Boville* [1993] and *Boville et al.* [2006]. CAM3 includes the convection scheme of *Zhang and McFarlane* [1995] with CAPE closure. CAM3-Liu (SCAML) [*Wang et al.*, 2009] differs from SCAM with modification for cloud microphysics by introducing a double-moment cloud microphysics [*Liu et al.*, 2007], explicit treatment of ice nucleation [*Liu and Penner*, 2005], and water vapor deposition on ice crystals and Bergeron-Findeisen process in pure ice and mixed-phase clouds. SCAMR differs most fundamentally from SCAMS as the deep convection parameterization is replaced by the revised *Zhang and McFarlane* [1995] scheme proposed by *Zhang* [2002]. The new convection scheme uses CAPE changes due to large-scale forcing (e.g., large-scale advection, radiative cooling) in the free troposphere, instead of CAPE itself, for closure.

[24] In the NCEP GFS model, the longwave radiation scheme follows *Fels and Schwarzkopf* [1975] and *Schwarzkopf and Fels* [1991]. The shortwave radiation formulation uses multiband techniques [*Slingo*, 1989; *Chou et al.*, 1998; *Kiehl et al.*, 1998]. The cloud condensate is prognosed from a single-moment microphysics scheme [*Zhao and Carr*, 1997]. The boundary layer parameterization uses a nonlocal scheme [*Hong and Pan*, 1996]. Penetrative convection scheme [*Pan and Wu*, 1995] is simplified from *Arakawa and Schubert* [1974], with a quasi-equilibrium assumption as a closure. Convection is trigged when a cloud work function exceeds a threshold. Shallow convection is parameterized as an extension of the vertical diffusion scheme [*Tiedtke*, 1983].

[25] The GFDL AM2 uses the shortwave radiation algorithm of *Freidenreich and Ramaswamy* [1999], and the longwave radiation follows *Schwarzkopf and Ramaswamy* [1999]. It uses *Slingo* [1989] and *Held et al.* [1993] for liquid cloud radiative properties and *Fu and Liou* [1993] for ice clouds. The microphysics scheme uses *Rotstayn* [1979] with cloud fraction prognosed following *Tiedtke* [1993]. The microphysics used for convective clouds is rather crude with prescribed precipitation efficiencies for shallow and deep convections. Boundary layer scheme follows *Lock et al.* [2000]. GFDL uses the relaxed Arakawa-Schubert scheme [*Moorthi and Suarez*, 1992] with a CAPE closure for shallow and deep convection.

[26] The GISS SCM used here is a developmental update of the *Schmidt et al.* [2006] model. Radiation uses explicit multiple scattering calculations and the k-distribution approach to absorption. Large-scale clouds are based on the prognostic cloud water parameterization of *Del Genio et al.* [1996], including all relevant microphysical processes, detrainment, and cloud top entrainment. Convective microphysics follows *Del Genio et al.* [2005], which interactively partitions condensate into precipitating, detrained, and vertically advected components. The boundary layer uses dry conserved variables and includes local (diffusive) and counter-gradient flux terms. Moist convection is parameterized using a mass-flux scheme with convection triggered when a lifted parcel becomes buoyant. The mass flux is that required to produce neutral buoyancy at cloud base, with updraft speeds and entrainment rates based on *Gregory* [2001].

[27] The CLUBB model, in these TWP-ICE simulations, is used in conjunction with the BUGSrad radiative transfer scheme [*Stephens et al.*, 2001] and a single microphysics scheme [*Morrison et al.*, 2009] for all clouds. Although in the prior literature CLUBB was tested only for boundary layer cloud cases [*Golaz et al.*, 2002; *Larson and Golaz*, 2005; *Larson et al.*, 2012], here CLUBB is used to simulate both deep and shallow clouds with a single, unified equation set. Unlike *Larson et al.* [2012], here CLUBB is run as a single-column model and handles all cloud types without the use of a cloud-resolving model or any other host model. CLUBB prognoses various higher-order moments and achieves closure by use of a single multivariate subgrid PDF of velocity, moisture, and temperature. CLUBB has no explicit convective trigger; rather, the turbulence and thermodynamic variability generated in shallow convection are intended to evolve into deep convection when and where the large-scale forcings are appropriate.

[28] The single-column model JMA1 contains the parameterizations of the default Global Spectral Model [*JMA*, 2007; *Nakagawa*, 2009]. The radiation scheme has two-stream with delta-Eddington approximation for shortwave and table look-up and k-distribution methods for longwave. Cloud condensation and microphysics are based on *Smith* [1990] and *Sundqvist et al.* [1989]. The boundary layer scheme is the level 2 closure scheme of *Mellor and Yamada* [1974]. The convection scheme is a multiplume type with cloud work function closure based on *Arakawa and Schubert* [1974], two types (for shallow and deep convection) of prognostic equations of the upward mass-flux [*Randall and Pan*, 1993] and triggering functions [*Xie and Zhang*, 2000]. JMA2 is the same as JMA1, except for using modified convection and cloud schemes (T. Komori and K. Yoshimoto, Evaluation from a perspective of spin-down problem: Moistening effect of convective parameterization, submitted to *CAS/JSC WGNE Research Activities in Atmospheric and Oceanic Modeling*, 2012).

[29] There are two CRM in the study which are briefly described here. The UKMO Large Eddy simulation model (LEM) uses the shortwave and longwave radiation scheme of *Edwards and Slingo* [1996]. The LEM employs a three-phase microphysics scheme, which is described in *Gray et al.* [2001], and the microphysical configuration is the same as the UKMO-2A setup described in *Fridlind et al.* [2012]. The subgrid mixing scheme is a modified first-order Smagorinksky-Lilly scheme, which is described in *MacVean and Mason* [1990].

[30] The model used in the System for Atmospheric Modeling (SAM) is described by *Khairoutdinov and Randall* [2003] and uses the BUGSrad radiation scheme described in *Stephens et al.* [2001]. Single-moment microphysics were used as outlined in *Khairoutdinov and Randall* [2003]. The subgrid mixing scheme is a 1.5-order closure model [*Khairoutdinov and Kogan*, 1999]. The SAM model simulates nine ensemble members equally spaced in the range 10–90.

3. Results

3.1. Simulations of Humidity and Precipitation

[31] This section gives an overview of both the temporal evolution and the vertical structure of the simulation

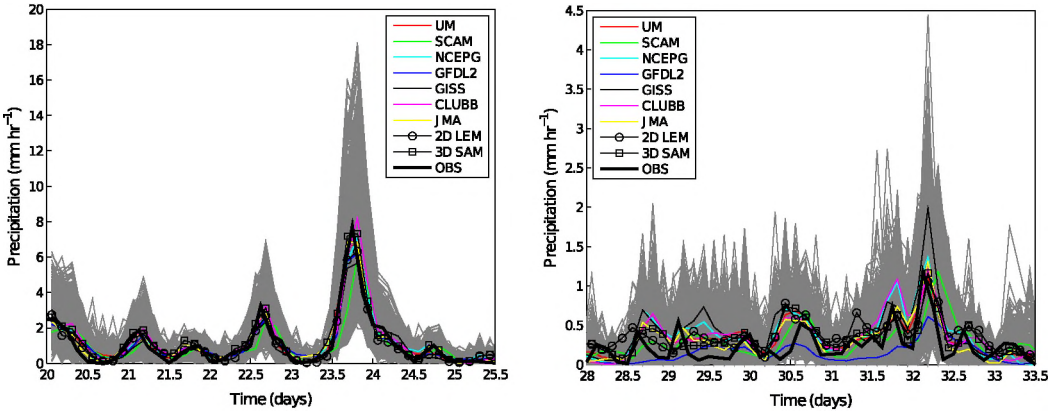

Figure 2. Time series of precipitation for the active period (left) and suppressed period (right) for each model type. Colored lines show the average for each model type (e.g., all UM SCM, all SCAM, and all JMA models are averaged together) and gray lines the 80-member ensemble for all models. The best estimate observed precipitation is given in the heavy black line. Note the different y axis.

of several moisture-related variables in the various models. Particular focus is given to comparing moisture-related variables as large errors can arise in models potentially due to the dependence of moisture on error-prone parameterizations. The convective component of total surface precipitation is discussed to highlight the different roles of model parameterization between the active and suppressed periods. Model accuracy will be discussed by comparison to observations for each model. The ensemble is then used to investigate model sensitivity in terms in the sources and sinks in the moisture budget. The best estimate is contrasted with the ensemble mean to directly determine how using an average of many simulations might affect results compared to a single simulation.

3.1.1. Overall Simulation Behavior

[32] Figure 2 shows time series of surface precipitation for the active and suppressed periods. Model ensemble means are shown as colored lines with individual ensemble members from all model simulations overlaid in gray. In this figure, all UM-type, SCAM-type, and JMA-type models are averaged together as they are very similar. Observations are shown as a heavy black line. This plot allows broad interpretation of the characteristics of each model while capturing the spread of the ensemble. Figure 2 shows that all models have a similar precipitation during the active period with moderate precipitation before the passage of the MCS on 23–24 January. All models have similar heavy rain associated with the MCS. The ensemble is spread around this mean

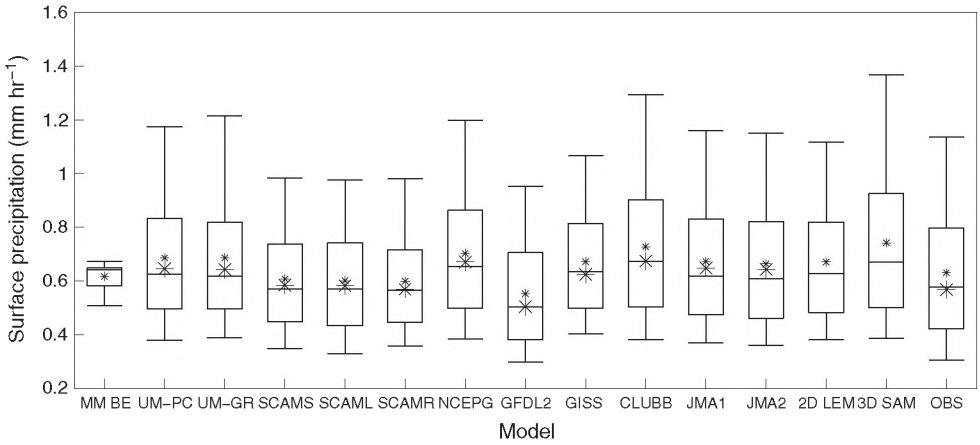

Figure 3. Mean precipitation averaged over the active and suppressed periods. The left box is the multimodel ensemble constructed from the best estimate simulations (MM BE) averaged over the period for each model. There are nine individual ensemble SCM with 80 members and two ensemble CRMs, a 2-D Met Office LEM simulation with 80 members, and a 3-D SAM model with 9 members. The far right has the ensemble of observations. The box represents the 25th, 50th, and 75th percentiles with the 5th and 95th percentiles being shown by the horizontal bars. The ensemble mean data are shown by the small asterisk. The best estimate is shown for the SCM data and observations as large asterisks. The ensemble is averaged for each ensemble member over all times.

with the largest spread occurring during the MCS. Modeled precipitation is close to observations which may be anticipated, as in strongly forced conditions precipitation will be predominantly driven by forcing in all ensemble members [*Xie et al.*, 2005; *Xu et al.*, 2002; *Woolnough et al.*, 2010].

[33] Period-mean precipitation during the suppressed period is lower than during the active period. It is evident that the relative differences in the ensemble mean time evolution between models as well as the differences from observations are larger than those in the active period. This might be expected as the forcing is weaker and as a consequence has less of an influence on the model solutions. In weakly forced conditions, it is expected that the details of the parameterizations in the various models exert a stronger influence, which explains the larger differences in the suppressed period. The ensemble spread is rather uniform and does not increase substantially with rainfall, which remains light throughout the period. The CRM behave similarly to the SCM. In the active period, solutions from the two model types track each other closely, again highlighting that precipitation is constrained by the forcing in that period. Just as for the SCM, the differences between CRMs as well as to observations increase (in a relative sense) in the suppressed period. The CRM results in the active period strongly resemble the results of the larger CRM comparison [*Fridlind et al.*, 2012], indicating that the CRMs shown here provide a representative sample for this family of models.

[34] Figure 3 provides a comparison of the multimodel best estimate ensemble and individual model ensembles for the time-mean surface precipitation averaged over the active and suppressed periods for all simulations used in this study. Each model is included as a box-whisker plot constructed from the time-averaged precipitation for each ensemble member. Observations are also included. It can clearly be seen that the ensemble SCM and CRM encompass a wide range of surface precipitation values. The models capture the spread seen in the observations. This is due to strong coupling between the forcing, which is primarily through vertical velocity, and rainfall.

[35] The multimodel ensemble has a limited spread of surface precipitation as all models are simulating the same forcing. Figure 3 provides a useful check that the multimodel ensemble has limited spread compared to the SCM and CRM simulations. This result supports findings of *Hume and Jakob* [2005] that largest spread in an SCM ensemble will be found by varying the forcing (the boundary conditions). Figure 3 also shows the ensemble mean (small asterisk) and best estimate mean (large asterisk) precipitation for the observations and models. For most models, the magnitude of the best estimate observed precipitation is very close to the 50th percentile (median) precipitation with the ensemble mean larger. This is due to the ensemble having a distribution which is skewed towards high values of precipitation leading to larger means than medians.

[36] Figure 4 shows time-height cross sections of the observed, SCM-mean and CRM-mean modeled relative humidity. Relative humidity provides a useful perspective on the model simulations, since unlike precipitation, which is primarily driven by forcing, relative humidity is less constrained by the forcing and more affected by model physics [*Emanuel and Zivkovic-Rothman*, 1999]. Given the model setup (section 2.2), the models have freedom to develop

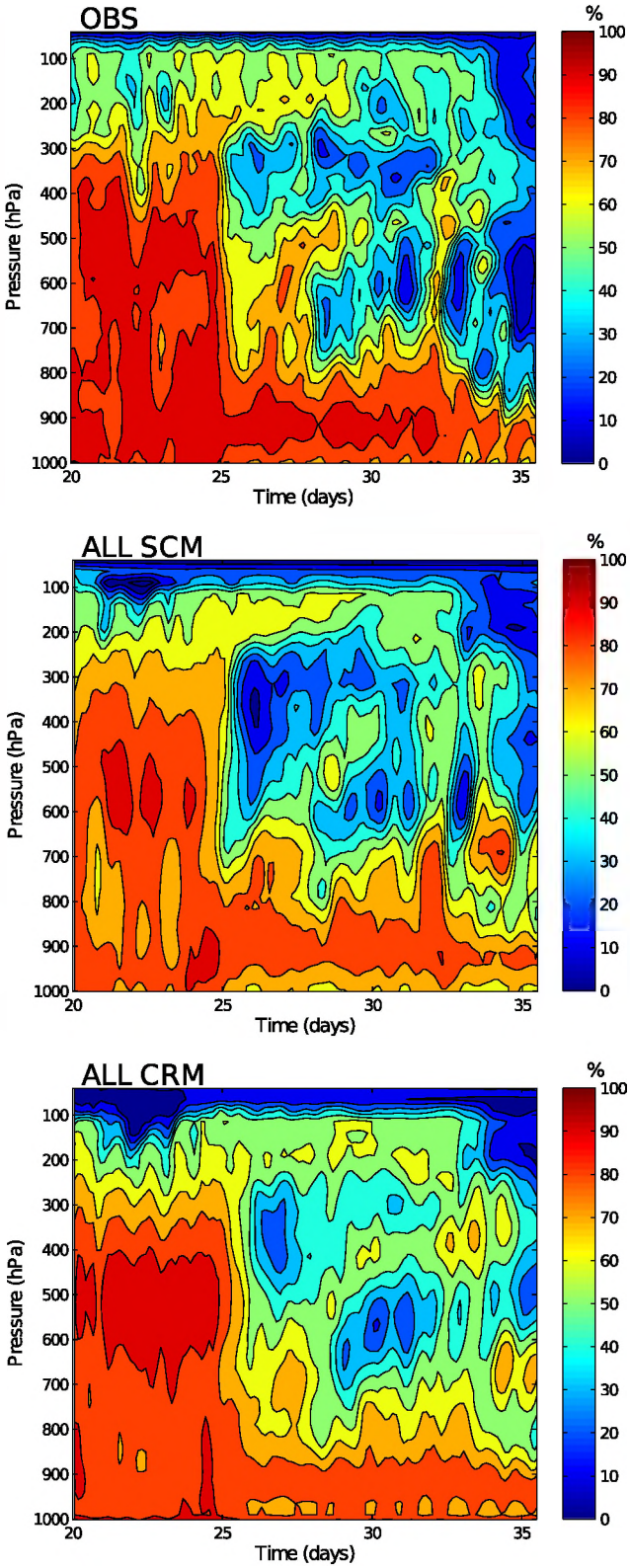

Figure 4. Time-pressure relative humidity (with respect to water) for the active and suppressed periods for observations and SCM and CRM simulations. The SCM and CRM data are averaged over all models and all available ensemble members in the range 10–90.

certain moisture source/sink terms such as moisture convergence and surface evaporation. The ensemble sensitivity to these terms will be addressed in section 3.1.3. Relative humidity with respect to water has been calculated using Teten's formula [*Lowe*, 1977, equation 6] for each individual simulation from values of temperature, water vapor, and pressure to ensure consistency across models. The modeled data shown in Figure 4 is an average over all models and all ensemble members used. Detailed investigation shows that relative humidity differences are primarily caused by differences in moisture as temperature varies little across the simulations and is close to observations.

[37] Observations show that the atmosphere has high relative humidity through a deep layer during the active period, but the models generally underestimate humidity particularly at low levels. During the suppressed period, observations show lower humidity above 800 hPa but large values in the boundary layer. All models capture the reduction in relative humidity caused by drying on the transition to the suppressed period above 700 hPa, although the SCM overestimate the reduction in humidity. Both SCM and CRM persist with low values of humidity in the boundary layer compared to observations.

[38] While Figure 4 shows the evolution of the mean state, the ensemble simulations also allow investigation of model sensitivity. Figure 5 shows time series of 500 mbar relative humidity for all ensemble members for each model compared to their best estimate simulations, ensemble mean, and observations. Relative humidity at 500 mbar is chosen, as accurate representation of moisture in midlevels is important if models are to correctly represent cloud. All models have high 500 mbar relative humidity during the active period consistent with the observations, but most SCM tend to have lower relative humidity than the CRM. The JMA and GISS models have particularly low relative humidity which is about 10% and 15% lower than the observations, respectively. The CLUBB and NCEP models have slightly larger relative humidity compared to the observations. All models have very limited spread during the active period.

[39] Observations show that during the transition to the suppressed period, humidity reduces to around 60% after the passage of the MCS. Relative humidity increases slightly before it reduces again from 70% to 30% between days 27 and 31 (27–31 January). There is a big difference between the responses of the SCM and CRM during this period. The CRM capture the transition to the suppressed period reasonably well with relative humidity 10% too low but its temporal evolution well captured. SCM generally reduce relative humidity too much in the transition period with mean values after the transition ranging from 40% (UM) to 10% (JMA). An exception to this is the CLUBB model which does not excessively reduce relative humidity during the transition and is then too moist during the suppressed period.

[40] The CRM show limited spread during the active period and the passage of the MCS. The spread in both model types is largest during the suppressed period. The SCM show larger but limited spread in the active period and in the transition associated with the MCS. Just like the CRM, they show increased spread during the suppressed period. This suggests a hypothesis that the simulation of midlevel relative humidity may be more sensitive to changes in the forcing when the forcing is weak. Furthermore, this sensitivity results in nonlinearity between the ensemble members which is particularly apparent during the suppressed period. For example, around 30 January, the SCAMS model shows that ensemble members with weaker (stronger) forcing have the lowest (highest) relative humidity despite the forcing not being the weakest (strongest) forcing.

[41] Figure 5 shows that in general the ensemble mean and best estimate simulation results follow each other quite closely so that their differences from observations are similar. On some limited occasions, the ensemble mean is closer to the observations than the best estimate, for example, UM-PC during both the active and suppressed periods and CLUBB and SCAMS during the suppressed period. To further investigate the ensemble mean to best estimate behavior, Figure 6 shows profiles of the difference between the best estimate and the ensemble mean relative humidity for all SCM for the active period. Figure 6 shows that when averaged over this period most models have similar best estimate and ensemble mean relative humidity. However, there are some important exceptions. For example, the UM-PC has larger ensemble mean relative humidity than its best estimate throughout the depth of the troposphere. This larger relative humidity in the ensemble mean represents an improvement in the model simulations by bringing the values closer to observations. As UM-PC is the only SCM to include a stochastic parameterization, this result highlights that ensemble simulations are necessary when using models with stochastic components. The usefulness of the ensemble approach will be investigated further below.

[42] When comparing the ensemble simulations with observations (Figure 5), it is possible, for some models and periods, to determine whether the errors are due to the prescribed forcing or are models errors. Given that the observed forcing spans the range of possible observations, none of the JMA ensemble members closely approximate the observed relative humidity during the active period. Therefore, this model clearly has limitations correctly simulating relative humidity during this period. For many models (including SCAM, NCEP, GISS, and JMA), the ensemble shows that the transition to the suppressed period is likely to be attributable to model error rather than errors in the forcing. The GISS model also consistently underestimates relative humidity during the suppressed period.

3.1.2. Precipitation Partitioning

[43] An interesting question in the simulation of tropical convection is how the various SCMs partition the precipitation between convection and the resolved scale motion. Furthermore, given the construction of the ensemble used here, it is possible to study how this partitioning changes with forcing strength and meteorological situation. Figure 7 shows the time average convective precipitation fraction (CPF), defined as the ratio of convective precipitation to total precipitation at the surface, against total precipitation for both the active and suppressed periods. Each SCM is shown by a color with different symbols used for the different models. Each point represents a single ensemble member averaged over the period of interest. An increase in total precipitation (x axis) indicates an increase in forcing strength. The multimodel best estimate ensemble is shown as large asterisks.

[44] Generally, there is a wide spread in the magnitude of CPF between the models ranging from 0.2 to 0.9 in the

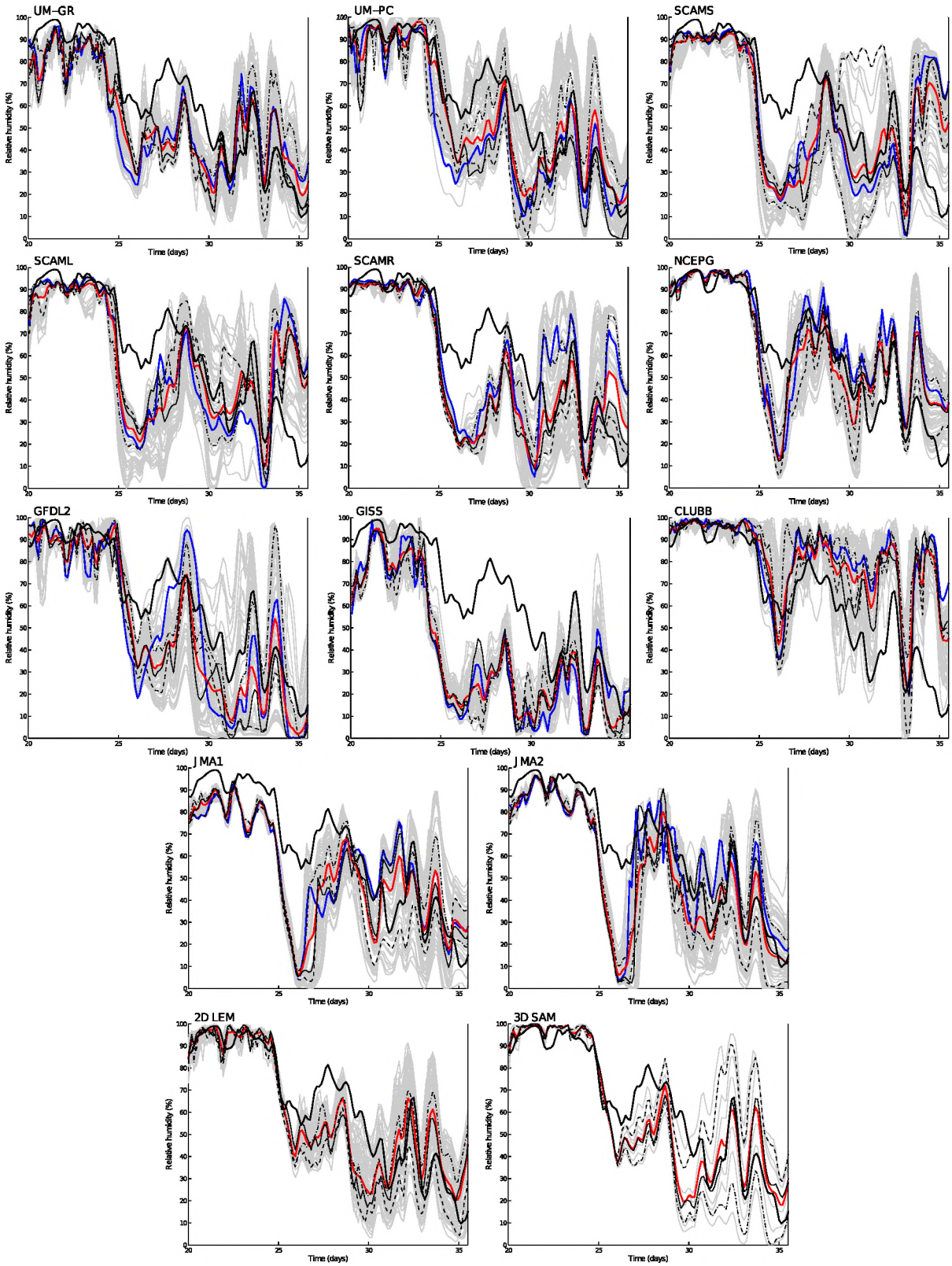

Figure 5. Time series of RH at 500 mbar for all SCM and CRM. Blue lines show best estimate simulations, red lines ensemble mean simulations, and the black line is observations. Gray lines show all ensemble members in the range 10–90. Key ensemble members, the 25th, 50th, and 75th percentiles of the 80-member large-scale "forcing," are highlighted as thin black lines which are dash-dotted, solid, and dashed, respectively. Note that the CRM do not report best estimate data.

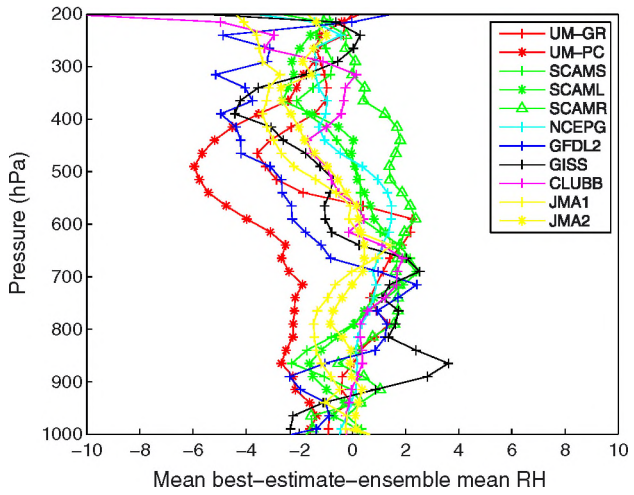

Figure 6. Mean period-averaged difference between the best estimate and ensemble mean relative humidity for the active period for each SCM.

active period and 0.5 to 1 in the suppressed period. In the active period, the models also show a very diverse behavior with forcing strength, with some showing an increase in CPF (e.g., GISS, UM-GR), some showing a near-constant CPF (e.g., NCEP, SCAM), and some showing a decrease (e.g., UM-PC). The GFDL2 model shows a somewhat erratic behavior. Models of the same type show different behavior depending on the parameterization scheme used (e.g., UM-PC versus UM-GR).

[45] In the suppressed period, all SCMs have a CPF of greater than 50%. There is a tendency in almost all models for the CPF to increase with increasing forcing although there is much scatter in the relationship. There are two groups of models, with either very high or relatively low CPF. There is some consistency between the periods, with the GISS and UM-PC models showing the lowest CPF in both.

[46] The rather wide spread in model behavior is likely indicative of large differences in the assumptions made in the different convection treatments on how to partition rainfall between convection and the larger scales. As this will likely have an impact on the vertical distribution of heating and moistening, an important issue for future work is to provide observational constraints for the relationships shown here.

3.1.3. Ensemble Moisture Budget Characteristics

[47] The ensemble provides an opportunity to investigate the interplay between modeled moisture and the moisture budget terms. In particular, this study permits a comparison between how the models control their moisture budgets. Given that the models are forced by prescribing horizontal advection terms and vertical velocity, they independently develop moisture budget terms such as vertical advection terms and moisture convergence in addition to the moisture contributions from parametrized processes such as convection and surface evaporation. This is an important difference between this study and previous intercomparisons [e.g., *Woolnough et al.*, 2010; *Guichard et al.*, 2004] where the total moisture forcing was prescribed. Furthermore, given that this study also includes both best estimate and ensemble simulations, comparison can be made about the additional model characteristics exposed using an ensemble compared to a single best estimate simulation.

[48] Figure 8 shows time average precipitable water against various terms in the moisture budget for the active period for all models and ensembles in this study. Very similar results are obtained for the suppressed period (not shown). Figure 8a shows that during the active period, the SCMs tend to divide into models in which lower precipitable water is associated with larger precipitation (GISS and SCAM), models where precipitable water is higher for larger values of precipitation (UM and CLUBB), and those models, including CRM, where precipitation is independent of precipitable water. The GFDL model is somewhat an exception as its relationship shows significant scatter.

[49] The largest term in the moisture budget is the moisture convergence term which is shown in Figure 8b. In all models, the moisture convergence term shows a similar magnitude and characteristics to precipitation which is not surprising as it is the largest source of moisture for the grid box exceeding surface evaporation by an order of magnitude (see below). Furthermore, Figure 8b shows that the moisture

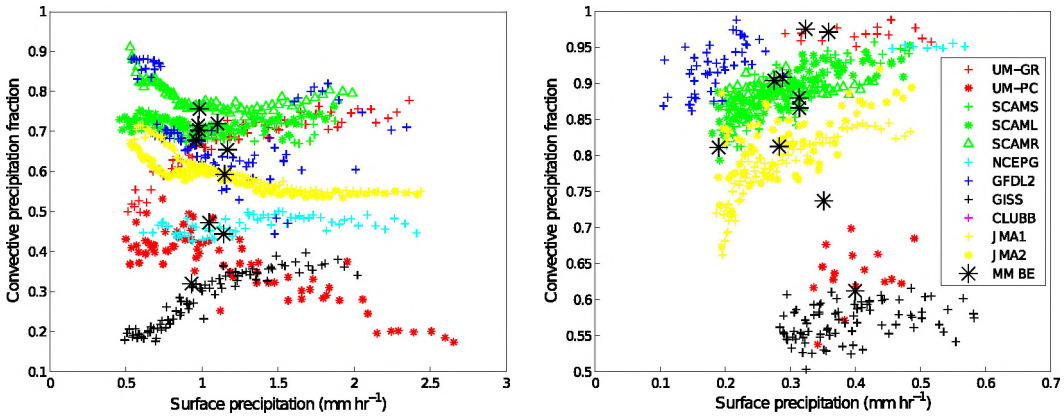

Figure 7. Time-averaged scatter plots of surface precipitation against convective precipitation (shown as a fraction of the total surface precipitation) over the active (left) and suppressed (right) periods for ensemble members 10–90. Each model type is represented by a color and each model of a given type by a symbol. The multimodel best estimate ensemble is represented by a large asterisk. The CLUBB model and CRM do not submit partitioned precipitation data.

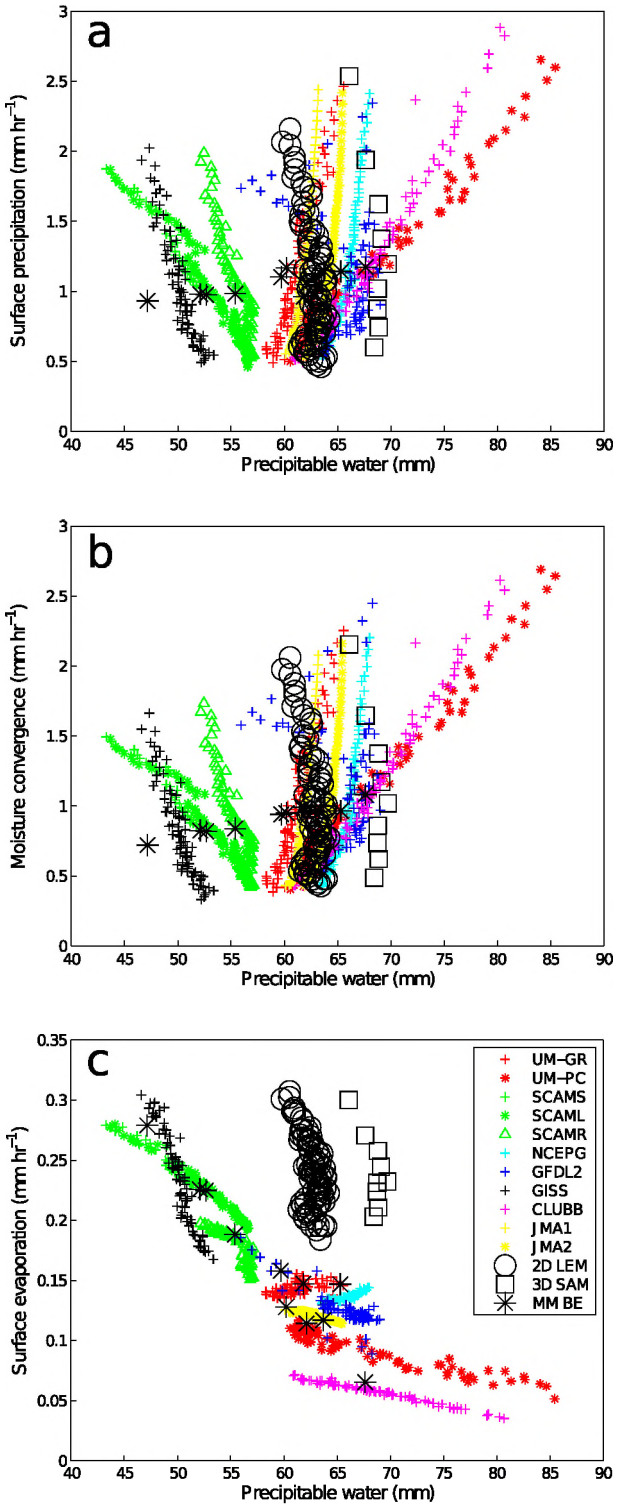

Figure 8. Time-averaged scatter plots of PW against (a) precipitation, (b) moisture convergence, and (c) surface evaporation over the active period for ensemble members 10–90. Each model type is represented by a color and each model of a given type by a symbol. The CRM are represented by large open symbols and the multimodel best estimate ensemble by a large asterisk.

convergence acts as feedback mechanism where SCM with larger values of precipitable water enhance moisture supply and produce more precipitation. Other models, despite the strong forcing, have lower precipitable water and lower moisture convergence. Petch et al. (submitted manuscript, 2012) discusses a likely reason by investigating the method used to force the SCM compared to the method used to force the CRM as used in *Fridlind et al.* [2012]. It was found that given a positive moisture bias, convergence (which occurs during the active period) increases that positive bias, and similarly convergence enhances a negative moisture bias. Models forced by prescribing the total moisture forcing, as used in *Fridlind et al.* [2012], do not develop these biases. The ensemble results shown in Figure 8b support the findings of Petch et al. (submitted manuscript, 2012). This model response to bias is not, however, apparent when only the best estimate simulations are considered. GISS and SCAM both have a drier atmosphere during the active period compared to the observations and other SCM which result in reduced precipitation compared to those SCM with a moister atmosphere.

[50] Another important term in the moisture budget is surface evaporation. Figure 8c shows this term for each model and ensemble member as before. Note that the surface evaporation term is an order of magnitude smaller than the moisture convergence contribution. It is evident that there is a fundamentally different relationship between forcing strength and evaporation in the SCMs and the CRMs indicating differences in the physical mechanisms at work in these two classes of models. All SCMs approximate a quasi-linear relationship of evaporation to precipitable water, albeit of varying strength, with larger surface evaporation at lower values of precipitable water and lower surface evaporation when precipitable water is high. This is consistent with the formulation of the SCMs as, given that low level winds and SST are prescribed in all models, evaporation can only change in response to atmospheric moisture. The CRMs on the other hand show a very different response to changes in the forcing. Here, the values of evaporation are independent of precipitable water. This indicates the importance of small-scale wind variability in driving surface evaporation. In the SCMs, this variability is not resolved. Unless it is parametrized, SCM surface fluxes are determined by the mean wind alone. In the CRMs, this wind variability is resolved and hence will enhance the surface fluxes. From the results, it is evident that the SCMs do not deal effectively with the subgrid variability. This result highlights the usefulness of the ensemble approach as this "error" in the SCMs would not have been evident from a set of single best estimate simulations.

[51] By using an ensemble approach, several interesting conclusions about model performance as well as simulation setup could be drawn. Given that strong precipitation in the models (and in nature) is strongly linked to moisture convergence, this exposes some interesting model behavior. By design of the simulations, moisture convergence is calculated by the models. Consequently, those models that develop a dry bias cannot develop large moisture convergence and do not produce as much precipitation, with the opposite effect occurring in models with a moist bias. The SCMs require a drier atmosphere to develop stronger surface evaporation. In contrast, the CRMs develop

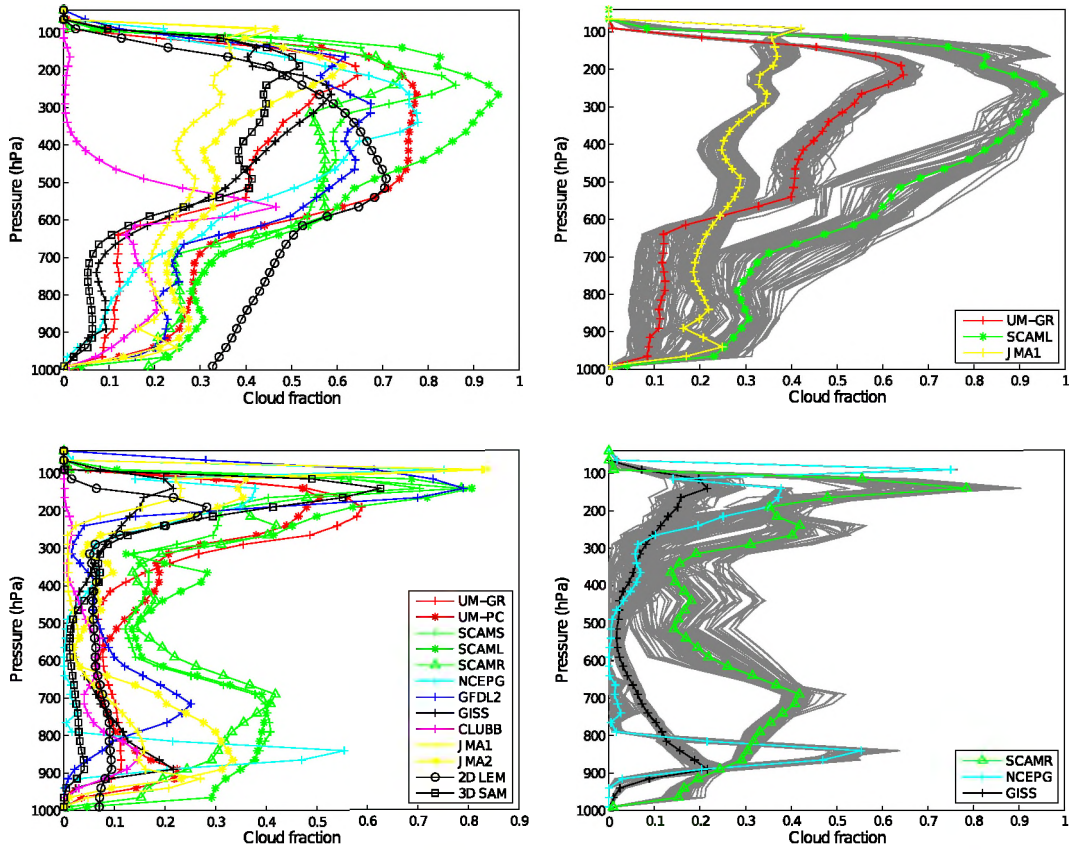

Figure 9. Mean period-averaged cloud fraction (left) for the active period (top) and suppressed period (bottom) for each model. For a limited number of models, the right-hand panels show the period mean together with ensemble members. Colored lines show the average for each model and gray lines ensemble members in the range 10–90. (Note that the CLUBB model does not include ice in cloud fraction and the LEM includes rain in cloud fraction.)

evaporation changes independent of atmospheric moisture likely due to the development of subgrid scale wind variability not present in the SCMs.

3.2. Clouds

[52] This section investigates the simulation of cloud-related variables in the CRMs and SCMs. Initially, the vertical structure of liquid water and ice clouds are discussed in both the active and suppressed monsoon. Following on from this, once again use of the ensemble will be made to investigate relationships between cloud-related variables as the forcing strength changes. This will expose several interesting characteristics of the various model parameterizations.

3.2.1. Profiles of Cloud Properties

[53] Figure 9 shows vertical profiles of the ensemble mean model cloud fraction for all models during the active (top left) and suppressed (bottom left) period as well as selected examples of the full ensemble from three models for the active (top right) and suppressed (bottom right) periods. Cloud fractions generally reflect the meteorological conditions shown in Figure 4 with cloud throughout the troposphere during the more moist, active period and two cloud layers during the suppressed period which are low cloud between 950-750 hPa, and high ice cloud above 200 hPa.

[54] During the active period, there are large differences in CRM cloud fraction of around 30% at all levels, and the SCMs mostly fall within the range of the CRMs. This can largely be explained by the definition of cloud fraction, which in the LEM includes both cloud and precipitating hydrometeors, while in the SAM model it only includes cloud water and ice. All SCMs have cloud fraction less than 30% below 600 hPa and more cloud (with the exception of JMA) above. There are large differences between the models with slightly better agreement in lower levels than in the upper troposphere.

[55] The differences in cloud fraction in the SCMs are also large in the suppressed period. One noticeable feature of the selected full ensembles (right panels) is that the difference of individual ensemble members from their mean tends to be smaller than the differences between models. This indicates that the differences in the simulated cloud structures are dominated by the structural properties of the models, not by the forcing data set, and shows that model representation of cloud is liable to error independent of the meteorological conditions. Best estimate simulations are therefore likely sufficient to expose model differences in this variable. This is investigated in Figure 10, which shows the differences of profiles of cloud cover between the ensemble mean and the best estimate simulation. As for relative humidity, most models show only small differences although with notable

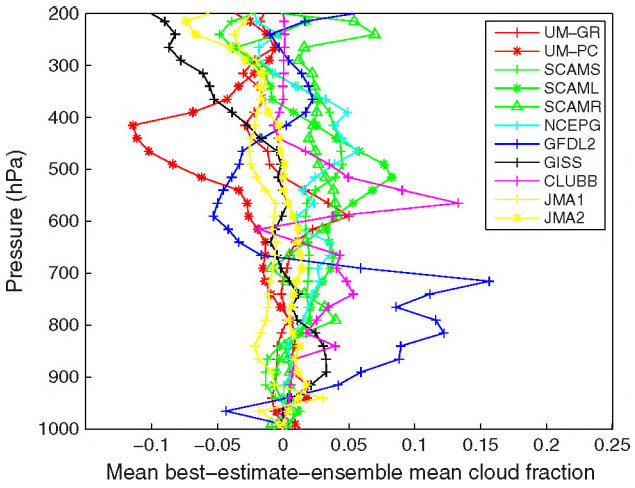

Figure 10. Mean period-averaged difference between the best estimate and ensemble mean cloud fraction for the active period for each SCM.

exceptions, the UM-PC around 400 hPa and GFDL below 700 hPa.

[56] Figure 11 shows profiles of ice water content in all models for the active period. Again, the ensemble means for all models are shown in the left panel, while selected full ensembles are shown in the right panel. The suppressed period is omitted from this Figure as the ice cloud during this period is not linked to local convection and is not well simulated. There are large differences between ice water content in both the CRMs and the SCMs during the active period which will impact on the model radiation budgets. Modeled ice water content differs in terms of both magnitude and vertical structure. Differences in the structural properties can again be noted in modeled ice water content with each SCM clustering around its ensemble mean. Difficulty in representing ice microphysics has been noted in all other TWP-ICE intercomparison studies and has been unanimously suggested as a focus for future model development.

[57] This section has shown that there are substantial differences in the vertical structure of parameterized cloud variables which may be attributable to systematic differences in the representation of clouds between the models. Structure in the cloud variables is clearly identifiable using the ensemble in both the active and suppressed periods. These persistent structures show that the models are not sensitive to changes in the forcing and that for most models best estimate simulations are likely sufficient to expose the mean model behavior in both periods. It is clear from the large differences between them that the CRMs only provide a limited estimate of the truth, especially during the suppressed period, as their representations of clouds are limited themselves [*Fridlind et al.*, 2012].

3.2.2. Ensemble Cloud Characteristics

[58] While the previous section showed that it is likely that the mean cloud properties of each model can be exposed by a single best estimate simulation, the full ensemble results provide a useful tool to investigate how relationships between variables might change within each model as the forcing varies across ensemble members. Representing the correct relationships between variables is a greater challenge for models than representing means, but it is also a necessary condition for applying the models over a wide range of conditions, such as a full GCM. This subsection will investigate how the ensemble developed here can be used to investigate relationships between different variables. Each ensemble member, experiencing different forcing data, can be considered as a separate test case, albeit spaced in controlled manner from all other ensemble members.

[59] Figure 12 shows the mean liquid water path (LWP) as a function of the mean surface precipitation averaged over the active (left) and suppressed (right) periods for all models. Each symbol represents an individual ensemble member. While there are generally different relationships between the two periods (note the change in scale between periods in the Figure), the CRMs show that relationship between LWP and precipitation is linear (with a gradient of approximately 250 kg m^{-3} h in both the active and suppressed period). The CRMs agree very well during the suppressed period but differ at the larger precipitation rates during the active period.

[60] Most, but not all, SCMs also produce a linear relationship between LWP and surface precipitation. Notable exceptions are the GFDL, SCAM, and JMA models. The relationships in the SCMs differ somewhat between the

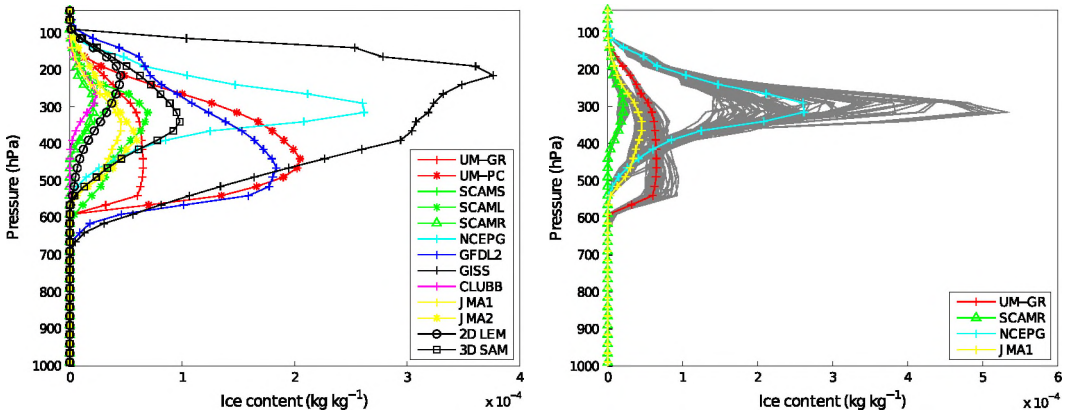

Figure 11. Mean period-averaged ice water content for the active period (left) for each model type. For a limited number of models, the right-hand panels show the period mean together with ensemble members. Colored lines show the average for each model and gray lines ensemble members in the range 10–90.

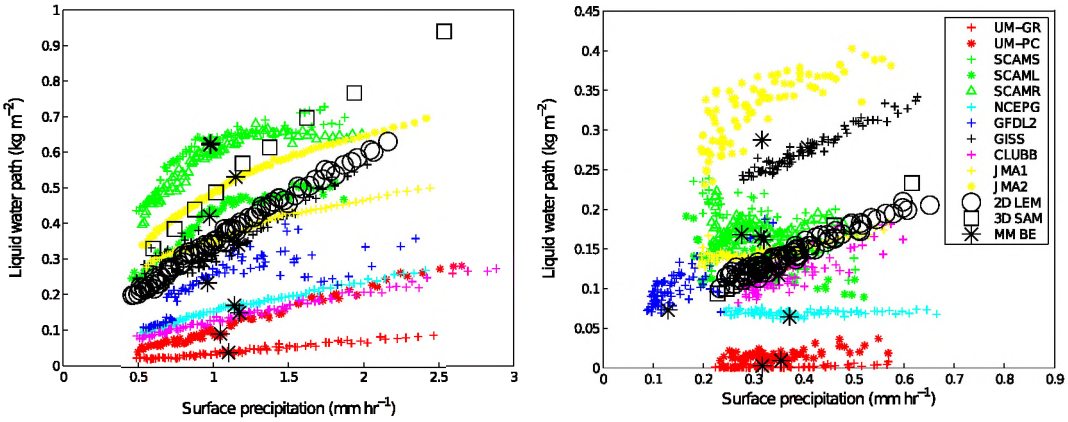

Figure 12. Time-averaged scatter plots of surface precipitation against liquid water path over the active (left) and suppressed (right) periods for ensemble members 10–90. Each model type is represented by a color and each model of a given type by a symbol. The CRM are represented by large open symbols and the multimodel best estimate ensemble by a large asterisk.

active and suppressed periods with a tendency for models to have tighter and more linear relationships during the active period. In the suppressed period when precipitation is small, both the UM and NCEP models tend to have precipitation independent of LWP, which itself is at an almost constant value. The GFDL and SCAM models tend to display significant scatter in LWP with only a weak relationship to precipitation. In fact, only the CLUBB, GISS, and JMA models increase LWP with precipitation as the CRMs suggest during the suppressed period. A linear relationship was observed between LWP and precipitation in *Fridlind et al.* [2012].

[61] The CRMs tend to lie in the middle of the SCM distribution, suggesting that the SCM ensemble mean may approximate the correct values of LWP, although individual models may differ quite considerably from the CRMs. The UM and NCEP models are biased low at all times, whereas the GISS and one of the JMA models have a LWP that is too large during the suppressed period. Unlike for cloud fraction before, the best estimate simulations do not always fall close to the center of the ensemble (note the large asterisks for GFDL and one JMA model to their associated ensemble during the suppressed period). The ensemble results also expose interesting nonlinearities in some of the models. For instance, there is a discontinuity in LWP in the GFDL around 0.15 kg m^{-2} during the active period. This possibly relates to the discontinuity in the convective precipitation fraction in Figure 7. While magnitude differences are apparent in the multimodel ensemble, the relationships between LWP and precipitation are only found in the full ensemble showing a potential usefulness of an ensemble technique when identifying model behavior.

[62] Figure 13a shows the relationship between IWP and precipitation during the active period. It can be seen that similar to LWP, IWP generally has a linear relationship with precipitation. Unlike the relationship of precipitation with LWP, the one with IWP is not consistent between the CRMs. There are very different magnitudes of IWP in the CRMs, and the slope of the relationship to precipitation varies strongly as well. Large differences in the simulation of

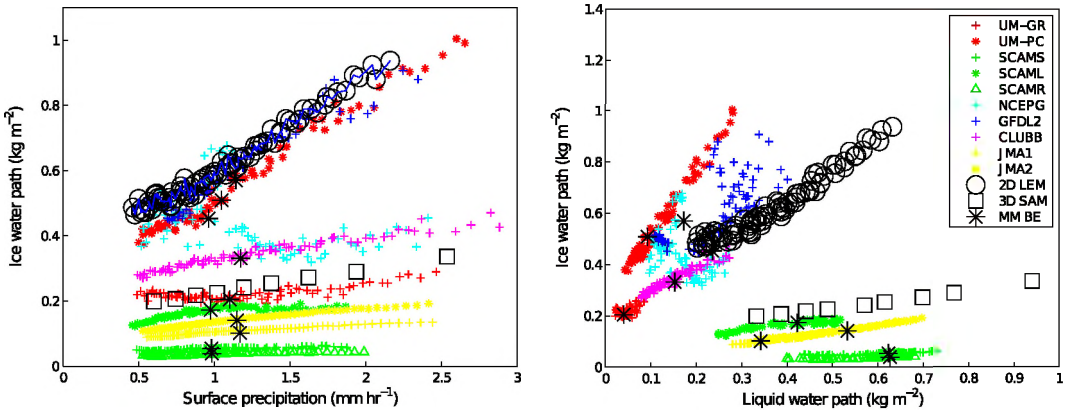

Figure 13. Time-averaged scatter plots of surface precipitation against ice water path (left) and liquid water path against ice water path (right) over the active period for ensemble members 10–90. Each model type is represented by a color and each model of a given type by a symbol. The CRM are represented by large open symbols and the multimodel best estimate ensemble by a large asterisk. Note: GISS model is not shown in these plots. GISS IWP exceeds all other models by a factor of 2.

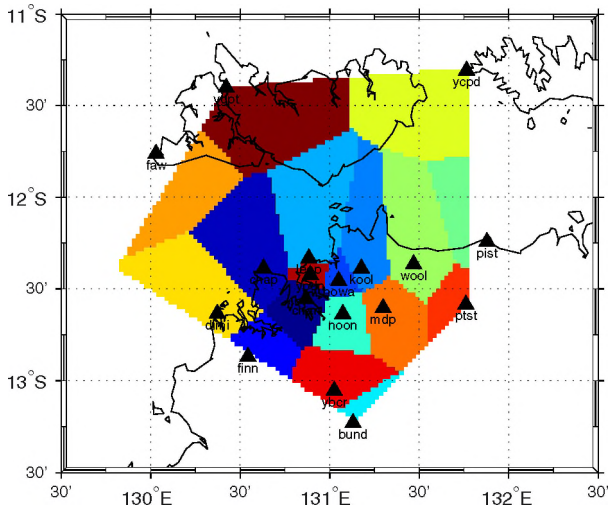

Figure 14. Location of rain gauges used in this study in and around the pentagon-shaped TWP-ICE domain. Comparison of radar-derived rainfall data to gauge rainfall data is conducted at all stations. Representative results are shown for Batchelor station (YBCR, 131.0252W, 13.0545S) and Charles Point (CHAP, 130.6309W, 12.389S). The colored area around each gauge shows the region of the TWP-ICE domain area closest to that gauge.

IWP in CRMs have been identified in other studies [*Fridlind et al.*, 2012]. The existence of those discrepancies makes it difficult to use the CRM results in assessing the SCM behavior. The LEM has approximately double IWP compared to SAM with a gradient of 300 kg m^{-3} h (LEM) compared to 50 kg m^{-3} h in SAM. Most SCM have gradients around this range, although in the NCEP model IWP is relatively insensitive to forcing.

[63] The ensemble enables the comparison not only between models but also of different versions of the same model. For example, SCAMS and SCAMR have very similar IWP, whereas SCAML, using a different microphysics scheme, has twice the IWP of the other SCAM models. There is a more marked difference between the two versions of the UM. UM-PC follows closely the gradient and approximate magnitude of the LEM (which is the UK Met Office's CRM) and which was used in the formulation of the *Plant and Craig* [2008] stochastic convection parameterization scheme. The UM-GR, on the other hand, is close to the SAM CRM which shows that there is complex interplay between the parameterization schemes. The UM SCM only differ in their convection parameterization, but this has a large effect on the IWP produced. In general, there is a split between models that follow the strong slope of the LEM and those closer to the weaker slope of the SAM. It is not possible, however, to attribute the relationship between precipitation and IWP simply based on the model microphysics scheme.

[64] Figure 13b shows the relationship between LWP and IWP and shows different aspects of the relationships between the variables in the models. There is a clear spilt between some models that have larger ranges in LWP (e.g., SCAM and JMA models) and others that have larger ranges in IWP (e.g., UM-PC and CLUBB). *Fridlind et al.* [2012] found that 2-D CRMs have a weaker relationship than 3-D CRMs between IWP and LWP, which is contrary to Figure 13a. However, the 2-D version of the LEM used here was not part of the *Fridlind et al.* [2012] study, and furthermore, the SAM here used a single-moment microphysics scheme, whereas the SAM in *Fridlind et al.* [2012] used a double-moment scheme [*Morrison et al.*, 2009] so a direct comparison is not possible.

[65] Interestingly, considering only the multimodel ensemble (Figure 13b) shows a different relationship between LWP and IWP compared to the relationship shown in the individual ensemble simulations. The ensemble within each model suggests increasing IWP with LWP, whereas the multimodel ensemble would suggest a tendency for IWP to increase with decreasing LWP. This shows the differences and potential limitations of using a multimodel

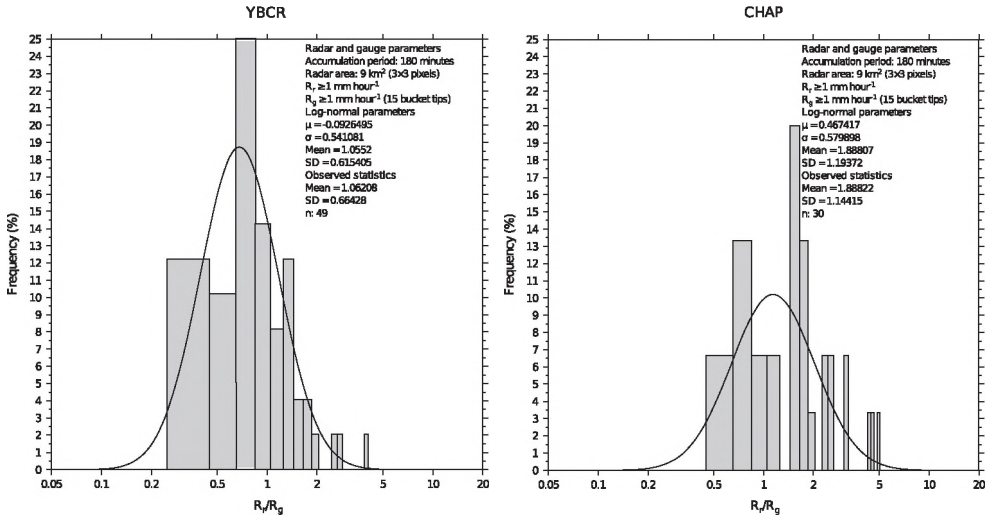

Figure 15. Distributions of radar-derived rainfall normalized by rain gauge rainfall for two rain gauges for TWP-ICE. A log-normal fit is shown in the solid line. Statistics of the observed data and the fit data are given in the top right corner of each panel.

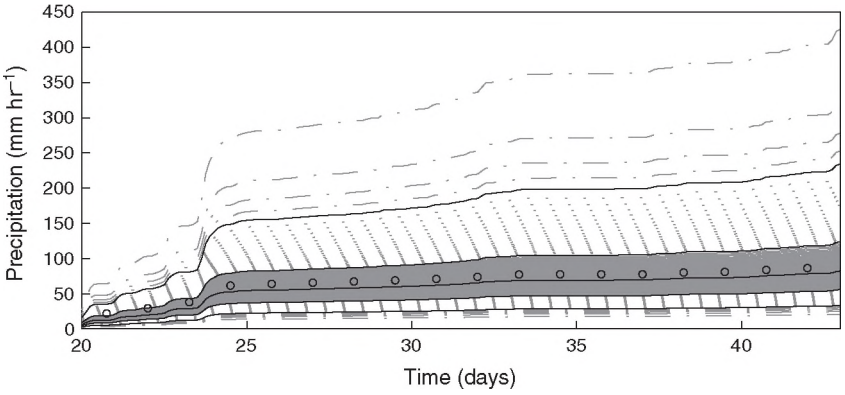

Figure 16. Ensemble cumulative rainfall time series for TWP-ICE derived from error estimates in radar-derived rainfall. Broken and light-colored lines show all ensemble members with key ensemble members (5th, 25th, 50th, 75th, and 95th percentiles) as black continuous lines. The best estimate forcing, used here and in the CRM intercomparison, is shown by small circles.

ensemble. Using a multimodel ensemble would suggest the reverse characteristic relationship between variables to that suggested by CRM and SCM each simulating their own ensemble.

4. Summary and Discussion

[66] This study presents an ensemble of SCM and CRM simulations for the TWP-ICE period. The first purpose of the study was to derive an ensemble of model forcings based on observational uncertainty. This data set was then applied to a variety of models to assess what new information about model behavior and model error might be gleaned from an ensemble approach that could not be attained by a single realization commonly used in CRM and SCM studies. It was found that the overall model behavior in terms of the time evolution of thermodynamic variables or the time-averaged vertical structure of those variables generally changes little between the ensemble mean and a single "best estimate" simulation. However, there were some notable exceptions to that finding. In some model simulations, like those with the UM-PC, ensemble means deviate from the best estimate simulations throughout the troposphere. Given that the ensemble mean forcing is close to that of the best estimate, this indicates nonlinearities in the simulation behavior possibly due to the stochastic component of the model. The ensemble also shows that models have greater sensitivity when weakly forced, and therefore, an ensemble is necessary. Perhaps the main value the ensemble adds to single simulations is the possibility to investigate the changes in model behavior with changes in forcing. This has proved invaluable in highlighting several aspects of model behavior in this study, namely, (i) a distinctly different behavior in the SCMs from that in the CRMs in achieving changes in surface evaporation; (ii) the sensitivity to the particular forcing method applied, (iii) a wide spread in the convective precipitation fraction in models and its sensitivity to forcing strength, and (iv) distinctly different model behavior in the relationships between cloud variables and precipitation.

[67] Examining the terms of the moisture budget using the ensemble enabled interesting conclusions about model behavior for two important terms; the surface evaporation and the moisture convergence. A clear distinction exists between the CRMs and the SCMs. In the CRMs, evaporation increases for constant atmospheric moisture, whereas the SCMs can only increase evaporation by drying the atmosphere. This suggests a role of subgrid variability likely brought about by cold pools in the CRMs that is not parameterized in SCMs. A representation of cold pool dynamics in SCMs would allow surface evaporation to occur in a moist atmosphere. Studying the moisture convergence term as a function of forcing strength revealed an interesting feedback between model error and the particular forcing approach chosen here. As the models are forced with horizontal moisture advection and vertical motion profiles (and hence profiles of mass convergence and divergence), they develop their own vertical moisture advection and moisture convergence terms. In models that develop a moist/dry bias, this bias is reinforced by an increase/decrease of the moisture convergence into the region. This behavior limitation can easily be deduced using the ensemble approach, while it would go largely unnoticed in single simulations with a number of models.

[68] The ensemble was also shown to be useful in investigating cloud variables and their relationships. Ensemble vertical profiles generally highlight structural differences between different models in that all ensemble members of a particular model tend to lie closer to its mean than to that of other models, even with large variations in the forcing. Consistent with the results in the accompanying modeling studies for TWP-ICE [*Lin et al.*, 2012; *Fridlind et al.*, 2012; *Zhu et al.*, 2012], large differences are found in the models' simulation of cloud ice, highlighting this area once again as one warranting further study. The ensemble is used to identify relationships between liquid water, cloud ice, and precipitation. CRM simulations, while varying in magnitude, show clear linear relationships between those variables. This behavior is not reproduced in all SCMs, some of which show strongly nonlinear behavior or even jumps. The ensemble also reveals that the ice water path to liquid water path relationships are very different between models, with one group of models showing a very strong increase of IWP with LWP, while in others IWP is almost independent of LWP. This conclusion applies to both CRMs and SCMs. Using the multimodel best estimate ensemble only,

the important relationship of increasing ice water path with liquid water path in individual models is reversed.

[69] This study shows that the introduction of an ensemble to a modeling study provides more information than might be gathered by simulating only simple best estimate forcing. While the method does not replace the standard best estimate approach to single-column modeling, it complements it by (i) providing an easy framework to study model sensitivities and (ii) increasing confidence in detecting model behavior that is likely due to model, rather than forcing, limitations. Future SCM studies should therefore consider adding ensemble simulations in addition to, rather than instead of, the more conventional best estimate method. Despite the additional information provided by the ensemble, it remains difficult to conclusively link model behavior in an SCM to parameterization assumptions, highlighting the need to embed studies like the one presented here into a larger framework of model evaluation.

Appendix A: Derivation of the Large-Scale Forcing Ensemble

[70] An important part of this study is the use of an ensemble of large-scale forcing data sets. The motivation for doing so is to assess the inherent uncertainty in deriving a single best estimate of the large-scale atmosphere from observations and in its subsequent application to drive model simulations. This appendix describes the construction of the ensemble used in this study, which is based on two steps: (i) estimate errors in the estimate of area-mean rainfall and construct alternative rainfall scenarios and (ii) apply a constrained variational analysis to each of the rainfall scenarios derived in the first step to yield the final ensemble of large-scale atmospheric states.

A1. Deriving an Ensemble of Rainfall Estimates

[71] The main source area-mean rainfall information in this and other TWP-ICE studies [e.g., *Xie et al.*, 2010] are rainfall estimates from a C-band polarimetric radar located near Darwin [*Keenan et al.*, 1998]. The algorithm used to estimate rainfall from radar variables is that of *Bringi and Chandrasekar* [2001]. While the radar provides excellent spatial coverage to estimate area means, deriving rain rates from radar variables will lead to errors in the rainfall estimates. A first step in the ensemble construction is to estimate these errors. To do so, we use rain gauge observations around Darwin and apply a method very similar to that of *Jordan et al.* [2003].

[72] Radar rain rates vary in space and time, and radar errors may vary considerably based on location and timing of rain events. The array of rain gauge data shown in Figure 14 is used as a reference for the radar-derived rainfall data. A grid of 3×3 radar pixels (approximately 9 km^2) are averaged and compared to rain gauge measurements over an accumulated period of 180 min where both rain rates are greater than 1 mm. By performing this analysis at many locations over the TWP-ICE domain, it is anticipated that the differing sources of error may be better accounted for.

[73] Examples of the ratio of radar-derived rainfall data to rain gauge rainfall data are shown in Figure 15 for two rain gauges. Assuming that rain gauge data may be a better estimate of rainfall than radar-derived data, ratios close to 1 suggest small errors in the radar data, with smaller standard deviations showing the clustering of the errors. The statistics in Figure 15 for the observed data show differences in the mean values and standard deviations at the two locations, suggesting that indeed errors have different spatial patterns. As the data tend to cluster about 1, the two observed data sets predominantly agree on the magnitude of rainfall, although the long tails of the error distribution show that on occasions large errors can be identified.

[74] A log-normal distribution is fitted to the errors shown in Figure 15. The log-normal distribution parameters are estimated and used to construct an ensemble of rain rates at each radar pixel as follows. The distribution of radar to gauge rainfall ratios is divided into 100 percentiles. Then the ratio for each percentile is used to multiply the radar rain values, providing 100 rainfall values (one for each percentile) at each radar pixel. For each radar pixel, the error distribution derived at the nearest rain gauge is used. Figure 14 shows the areas (colored) for which error characteristics are assumed constant in space based on the nearest rain gauge behavior.

[75] Having derived rainfall error estimates at each radar pixel, which is expressed as 100 values of rainfall from the lowest to the highest, the next task is to estimate the error in the area-mean rainfall. This requires assumptions about the spatial correlation of the individual pixel errors. As our goal is to span the widest range of possibilities, we will assume the worst case scenario of maximum correlation. In other words, we assume that whenever the largest possible error occurs at 1 pixel, the largest error in the same direction occurs at all radar pixels. This is an extremely simple assumption and will maximize the possible error in the area-mean rainfall, consistent with our goal to maximize ensemble spread. Using this assumption, 100 values of area-mean rainfall are derived by simply averaging the pixel-rainfall rates within each percentile, i.e., the first percentile of the area-mean rainfall distribution is simply the average of all first-percentile values at each pixel and so on stepping through all percentiles. Figure 16 shows the 100 cumulative rainfall time series in this way for TWP-ICE. For comparison, the figure includes the best estimate rainfall time series as derived by *Xie et al.* [2010], which falls close to the 50th percentile as might be anticipated from the method the distribution was constructed. While the error estimates allow for a large range of possible rainfall values, 50% of the distribution falls between the 25th and 75th percentiles of the distribution which has a limited range of rainfall.

A2. Deriving the Large-Scale Atmospheric State

[76] Each of the 100 rainfall scenarios derived above is used separately in the variational analysis algorithm of *Zhang et al.* [2001] (all other observations, such as thermodynamic variables, horizontal winds, and radiation terms, are unchanged and are the same for each scenario) to produce 100 separate forcings that are all equally possible given the uncertainty in area-mean rainfall. The higher (lower) percentile corresponds to stronger (weaker) surface precipitation and generally stronger (weaker) vertical motion. The characteristics of the vertical motion for the active and suppressed periods are discussed in the main text.

[77] Investigations were made into whether the additional variational analysis inputs should be modified in order to

be more physically consistent. For example, an estimate of rainfall error has been used to derive alternative rainfall time series, but increased rainfall may, in the simplest terms, also be associated with more deep cloud and therefore reduced top-of-the-atmosphere longwave radiation, which is also an input to the variational analysis. Sensitivity studies where the radiation was varied in conjunction with rainfall had little impact on the resulting large-scale atmosphere. This supports *Zhang et al.* [2001], who suggested that rainfall provided the largest contribution term in the variational analysis.

[78] The 100 large-scale data sets so derived are used to provide forcing data for SCM and CRM as described in the main text.

[79] **Acknowledgments.** Davies and Jakob are supported by the Office of Science (BER), U.S. Department of Energy, under grant DE-SC0002731. Many of the other coauthors also participated through support from the U.S. Department of Energy Atmospheric System Research Program. V. Larson and B. Nielsen are grateful for financial support from the United States Department of Energy (grants DE-SC0006927 and DE-SC0008668) and the National Science Foundation (grant AGS-0968640). Support for X. Liu was provided by the U.S. Department of Energy (DOE), Office of Science, Atmospheric System Research (ASR) program. The Pacific Northwest National Laboratory is operated for DOE by Battelle Memorial Institute under contract DE-AC06-76RLO 1830. Dr. Weiguo Wang is partly supported by the National Natural Science Foundation of China under Grant No. 41075039. The contributions of S. Xie to this work were performed under the auspices of the U.S. Department of Energy (DOE), Office of Science, Office of Biological and Environmental Research by Lawrence Livermore National Laboratory under contract No. DE-AC52-07NA27344 and supported by the Atmospheric Radiation Measurement Program of the Office of Science at the DOE.

References

Arakawa, A., and W. Schubert (1974), Interaction of a cumulus cloud ensemble with the large-scale environment, Part 1, *J. Atmos. Sci.*, *31*, 674–701, doi:10.1175/1520-0469(1974)031<0674:IOACCE>2.0.CO;2.

Ball, M. A., and R. S. Plant (2008), Comparison of stochastic parameterization approaches in a single-column model, *Phil. Trans. Roy. Soc.*, *366*, 2605–2623, doi:10.1098/rsta.2011.0377.

Bechtold, P., et al. (2000), A GCSS model intercomparison for a tropical squall line observed during TOGA-COARE. II: Intercomparison of single-column models and a cloud-resolving model, *Q. J. R. Meteorolog. Soc.*, *126*(564), 865–888, doi:10.1002/qj.49712656404.

Boville, B. A., P. J. Rasch, J. J. Hack, and J. R. McCaa (2006), Representation of clouds and precipitation processes in the Community Atmosphere Model version 3 (CAM3), *J. Climate*, *19*(11), 2184–2198, doi:10.1175/JCLI3749.1.

Bringi, V. N., and V. Chandrasekar (2001), *Polarimetric Doppler Weather Radar: Principles and Applications*, 636 pp., Cambridge University Press, The Edinburgh Building, Cambridge, CB2 2RU, UK.

Chou, M., M. J. Suarez, C. H. Ho, M. M. H. Yan, and K. T. Lee (1998), Parameterizations for cloud overlapping and shortwave single scattering properties for use in general circulation and cloud ensemble models, *J. Climate*, *11*, 202–214, doi:10.1175/1520-0442(1998)011<0202:PFCOAS>2.0.CO;2.

Collins, W. D., P. J. Rasch, B. A. Boville, J. J. Hack, J. R. McCaa, D. L. W. Williamson, B. P. Briegleb, C. M. Bitz, S.-J. Lin, and M. Zhang (2006), The formulation and atmospheric simulation of the Community Atmosphere Model version 3 (CAM3), *J. Climate*, *19*, 2144–2161, doi:10.1175/JCLI3760.1.

Davies, T., M. J. P. Cullen, A. J. Malcolm, M. H. Mawson, A. Staniforth, A. A. White, and N. Wood (2005), A new dynamical core for the Met Office's global and regional modelling of the atmosphere, *Q. J. R. Meteorol. Soc.*, *131*, 1759–1782, doi:10.1256/qj.04.101.

Del Genio, A., M.-S. Yao, W. Kovari, and K.-W. Lo (1996), A prognostic cloud water parameterization for global climate models, *J. Climate*, *9*, 270–304, doi:10.1175/1520-0442(1996)009<0270:APCWPF>2.0.CO;2.

Del Genio, A., W. Kovari, M.-S. Yao, and J. Jonas (2005), Cumulus microphysics and climate sensitivity, *J. Climate*, *18*, 2376–2387, doi:10.1175/JCLI3413.1.

Derbyshire, S. H., A. V. Maidens, S. F. Milton, R. A. Stratton, and M. R. Willett (2011), Adaptive detrainment in a convective parametrization, *Q. J. R. Meteorolog. Soc.*, *137*(660), 1856–1871, doi:10.1002/qj.875.

Edwards, J., and A. Slingo (1996), Studies with a flexible new radiation code. Part I: Choosing a configuration for a large-scale model, *Q. J. R. Meteorol. Soc.*, *122*, 689–719, doi:10.1002/qj.49712253107.

Emanuel, K., and M. Zivkovic-Rothman (1999), Development and evaluation of a convection scheme for use in climate models, *J. Atmos. Sci.*, *56*(11), 1766–1782, doi:10.1175/1520-0469(1999)056<1766:DAEOAC>2.0.CO;2.

EMC, (2003), The GFS atmospheric model, *Technical report*, National Oceanic and Atmospheric Administration, US Department of Commerce.

Fels, S., and M. Schwarzkopf (1975), The simplified exchange approximation: A new method for radiative transfer calculations, *J. Atmos. Sci.*, *37*, 2265–2297, doi:10.1175/1520-0469(1975)032<1475:TSEAAN>2.0.CO;2.

Freidenreich, S. M., and V. Ramaswamy (1999), A new multiple-band solar radiative parameterization for general circulation models, *J. Geophys. Res.*, *104*(D24), 31389–31409, doi:10.1029/1999JD900456.

Fridlind, A. M., et al. (2012), A comparison of TWP-ICE observational data with cloud-resolving model results, *J. Geophys. Res.*, *117*, D05204, doi:10.1029/2011JD016595.

Fu, Q., and K. N. Liou (1993), Parameterization of the radiative properties of cirrus clouds, *J. Atmos. Sci.*, *50*, 2008–2025, doi:10.1175/1520-0469(1993)050<2008:POTRPO>2.0.CO;2.

GAMDT (2004), The new GFDL global atmosphere and land model AM2-LM2: Evaluation with prescribed SST simulations, *J. Climate*, *17*, 4641–4673, doi:10.1175/JCLI-3223.1.

Ghan, S., et al. (2000), A comparison of single column model simulations of summertime midlatitude continental convection, *J. Geophys. Res.*, *105*(D2), 2091–2124, doi:10.1029/1999JD900971.

Golaz, J.-C., V. Larson, and W. Cotton (2002), A PDF-based model for boundary layer clouds. Part I: Method and model description, *J. Atmos. Sci.*, *59*, 3540–3551, doi:10.1175/1520-0469(2002)059<3540:APBMFB>2.0.CO;2.

Grabowski, W. W., et al. (2006), Daytime convective development over land: A model intercomparison based on LBA observations, *Q. J. Roy. Meteor. Soc.*, *132*, 317–344, doi:10.1256/qj.04.147.

Grant, A. (2001), Cloud-base fluxes in the cumulus-capped boundary layer, *Q. J. Roy. Meteor. Soc.*, *127*(572), 407–421, doi:10.1002/qj.49712757209.

Gray, M. E. B., J. Petch, S. H. Derbyshire, A. R. Brown, A. P. Lock, H. A. Swann, and P. R. A. Brown (2001), Version 2.3 of the Met. Office Large Eddy Model: Part II. Scientific documentation. Met O (APR) Turbulence and Diffusion Note. No. 276.

Gregory, D. (2001), Estimation of entrainment rate in simple models of convective clouds, *Q. J. R. Meteorol. Soc.*, *127*, 53–72, doi:10.1002/qj.49712757104.

Gregory, D., and P. R. Rowntree (1990), A mass flux convection scheme with representation of cloud ensemble characteristics and stability dependent closure, *Mon. Wea. Rev.*, *118*, 1483–1506, doi:10.1175/1520-0493(1990)118<1483:AMFCSW>2.0.CO;2.

Guichard, F., et al. (2004), Modelling the diurnal cycle of deep precipitating convection over land with cloud-resolving models and single-column models, *Q. J. Roy. Meteor. Soc.*, *130*, 3139–3171, doi:10.1256/qj.03.145.

Hack, J. J., and J. A. Pedretti (2000), Assessment of solution uncertainties in single-column modelling frameworks, *J. Climate*, *13*(10), 352–365, doi:10.1175/1520-0442(2000)013<0352:AOSUIS>2.0.CO;2.

Held, I. M., R. S. Hemler, and V. Ramasway (1993), Radiative-convective equilibrium with explicit two-dimensional moist convection, *J. Atmos. Sci.*, *50*, 3909–3927, doi:10.1175/1520-0469(1993)050<3909:RCEWET>2.0.CO;2.

Holtslag, A. A. M., and B. A. Boville (1993), Local versus nonlocal boundary-layer diffusion in a global climate model, *J. Climate*, *6*(10), 1825–1842, doi:10.1175/1520-0442(1993)006<1825:LVNBLD>2.0.CO;2.

Hong, S., and H. Pan (1996), Nonlocal boundary layer vertical diffusion in a medium-range forecast model, *Mon. Wea. Rev.*, *124*(10), 2322–2339, doi:10.1175/1520-0493(1996)124<2322:NBLVDI>2.0.CO;2.

Hume, T., and C. Jakob (2005), Ensemble Single Column Modelling (ESCM) in the tropical western Pacific: Forcing datasets and uncertainty analysis, *J. Geophys. Res.*, *110*, D13109, doi:10.1029/2004JD005704.

Hume, T., and C. Jakob (2007), Ensemble Single Column Model (ESCM) validation in the tropical western Pacific, *J. Geophys. Res.*, *112*, D10206, doi:10.1029/2006JD008018.

JMA (2007), Outline of the Operational Forecast and Analysis System of the Japan Meteorological Agency. http://www.jma.go.jp/jma/jma-eng/jma-center/nwp/outline-nwp/index.htm.

Jordan, P., A. Seed, and P. Weinmann (2003), A stochastic model of radar measurement errors in rainfall accumulations at catchment

scale, *J. Hydro.*, *4*, 841–855, doi:10.1175/1525-7541(2003)004<0841:ASMORM>2.0.CO;2.

Joss, J., and A. Waldvogel (1990), *Precipitation Measurement and Hydrology. Radar in Meteorology*, chapter 29a, pp. 577–606, Academic Press, Boston, MA, USA.

Keenan, T. D., K. Glasson, F. Cummings, T. S. Bird, J. Keller, and J. Lutz (1998), The BMRC/NCAR C-band polarimetric (CPOL) radar system, *J. Atmos. Oceanic Technol.*, *15*, 871–886, doi:10.1175/1520-0426(1998)015<0871:TBNCBP>2.0.CO;2.

Khairoutdinov, M., and D. Randall (2003), Cloud resolving modeling of the ARM summer 1997 IOP: Model formulation, results, uncertainties, and sensitivities, *J. Atmos. Sci.*, *60*, 607–625, doi:10.1175/1520-0469(2003)060<0607:CRMOTA>2.0.CO;2.

Khairoutdinov, M. F., and Y. L. Kogan (1999), A large eddy simulation model with explicit microphysics: Validation against aircraft observations of a stratocumulus-topped boundary layer, *J. Atmos. Sci.*, *56*(13), 2115–2131, doi:10.1175/1520-0469(1999)056<2115:ALESMW>2.0.CO;2.

Kiehl, J., J. J. Hack, G. B. Bonan, B. A. Boville, D. L. Williamson, and P. J. Rasch (1998), The national center for atmospheric research community climate model: CCM3*, *J. Climate*, *11*(6), 1131–1149, doi:10.1175/1520-0442(1998)011<1131:TNCFAR>2.0.CO;2.

Larson, V. E., and J.-C. Golaz (2005), Using probability density functions to derive consistent closure relationships among higher-order moments, *Mon. Wea. Rev.*, *133*, 1023–1042, doi:10.1175/MWR2902.1.

Larson, V. E., D. P. Schanen, M. Wang, M. Ovchinnikov, and S. Ghan (2012), PDF parameterization of boundary layer clouds in models with horizontal grid spacings from 2 to 16 km, *Mon. Wea. Rev.*, *140*, 285–306, doi:10.1175/MWR-D-10-05059.1.

Lin, Y., et al. (2012), TWP-ICE global atmospheric model intercomparison: Convection responsiveness and resolution impact, *J. Geophys. Res.*, *117*, D09111, doi:10.1029/2011JD017018.

Liu, X., and J. Penner (2005), Ice nucleation parameterization for global models, *Meteorol. Z.*, *14*(4), 499–514, doi:10.1127/0941-2948/2005/0059.

Liu, X., J. E. Penner, S. J. Ghan, and M. Wang (2007), Inclusion of ice microphysics in the NCAR community atmospheric model version 3 (CAM3), *J. Climate*, *20*, 4526–4547, doi:10.1175/JCLI4264.1.

Lock, A. P., A. R. Brown, M. R. Bush, G. M. Martin, and R. N. B. Smith (2000), A new boundary layer mixing scheme. Part I: Scheme description and single-column model tests, *Mon. Wea. Rev.*, *128*, 3187–3199, doi:10.1175/1520-0493(2000)128<3187:ANBLMS>2.0.CO;2.

Lowe, P. (1977), An approximating polynomial for the computation of saturation vapor pressure, *J. Appl. Meteorol.*, *16*, 100–102, doi:10.1175/1520-0450(1977)016<0100:AAPFTC>2.0.CO;2.

MacVean, M., and P. Mason (1990), Cloud-top entrainment instability through small-scale mixing and its parameterization in numerical models, *J. Atmos. Sci.*, *47*(8), 1012–1030, doi:10.1175/1520-0469(1990)047<1012:CTEITS>2.0.CO;2.

Martin, G. M., M. A. Ringer, V. D. Pope, A. Jones, C. Dearden, and T. J. Hinton (2006), The physical properties of the atmosphere in the new Hadley Centre Global Environmental Model (HadGEM1). Part I: Model description and global climatology, *J. Climate*, *19*(7), 1274–1301, doi:10.1175/JCLI3636.1.

May, P. T., J. H. Mather, G. Vaughan, C. Jakob, G. M. McFarquhar, K. N. Bower, and G. G. Mace (2008), The tropical warm pool international cloud experiment, *Bull. Amer. Meteor. Soc.*, *89*, 629–645, doi:10.1175/BAMS-89-5-629.

McClatchey, R. A., R. W. Fenn, J. Selby, F. E. Volz, and J. S. Garing, (1972), The Tropical Warm Pool International Cloud Experiment, *Technical Report 411*, Air Force Cambridge Research Laboratory Environmental Research Paper.

Mellor, G. L., and T. Yamada (1974), A hierarchy of turbulence closure models for planetary boundary layers, *J. Atmos. Sci.*, *31*, 1791–1806, doi:10.1175/1520-0469(1974)031<1791:AHOTCM>2.0.CO;2.

Moorthi, S., and M. J. Suarez (1992), Relaxed Arakawa-Schubert: A parameterization of moist convection for general circulation models, *Mon. Wea. Rev.*, *120*, 978–1002, doi:10.1175/1520-0493(1992)120<0978:RASAPO>2.0.CO;2.

Morrison, H., G. Thompson, and V. Tatarskii (2009), Impact of cloud microphysics on the development of trailing stratiform precipitation in a simulated squall line: Comparison of one-and two-moment schemes, *Mon. Wea. Rev.*, *137*(3), 991–1007, doi:10.1175/2008MWR2556.1.

Nakagawa, M., (2009), Outline of the high resolution global model at the Japan meteorological agency, *RSMC Tokyo-Typhoon Center Technical Review, 11(1-13)*, Available from http://www.jma.go.jp/jma/jma--eng/jma--center/rsmc--hp--pub--eg/techrev/text11--1.pdf.

Pan, H., and W. Wu (1995), Implementing a mass flux convection parameterization package for the NMC medium-range forecast model. *NMC Office Note,* No. 409, 40 pp. [Available from NCEP, 5200 Auth Road, Washington, DC 20233].

Plant, R. S., and G. C. Craig (2008), A stochastic parameterization for deep convection based on equilibrium statistics, *J. Atmos. Sci.*, *65*, 87–105, doi:10.1175/2007JAS2263.1.

Randall, D., and D. M. Pan (1993), Implementation of the Arakawa-Schubert cumulus parameterization with a prognostic closure, *Meteorol. Monogr.*, *46*, 137–144.

Randall, D., et al. (2003), Confronting models with data: The GEWEX cloud systems study, *Bull. Amer. Meteor. Soc.*, *84*, 455–469, doi:10.1175/BAMS-84-4-455.

Rasch, P. J., and J. E. Kristjánsson (1998), A comparison of the CCM3 model climate using diagnosed and predicted condensate parameterizations, *J. Climate*, *11*(7), 1587–1614, doi:10.1175/1520-0442(1998)011<1587:ACOTCM>2.0.CO;2.

Rotstayn, L. D. (1979), A physically based scheme for the treatment of stratiform clouds and precipitation in large-scale models. I: Description and evaluation of the microphysical processes, *Q. J. Roy. Meteor. Soc.*, *123*, 1227–1282, doi:10.1002/qj.49712354106.

Schmidt, G. A., et al. (2006), Present day atmospheric simulations using GISS Model E: Comparison to in-situ, satellite and reanalysis data, *J. Climate*, *19*, 153–192, doi:10.1175/JCLI3612.1.

Schwarzkopf, M. D., and S. B. Fels (1991), The simplified exchange method revisited: An accurate, rapid method for computation of infrared cooling rates and fluxes, *J. Geophys. Res.*, *96*(D5), 9075–9096, doi:10.1029/89JD01598.

Schwarzkopf, M. D., and V. Ramaswamy (1999), Radiative effects of CH_4, N_2O, halocarbons and the foreign-broadened H_2O continuum: A GCM experiment, *J. Geophys. Res.*, *104*(D8), 9467–9488, doi:10.1029/1999JD900003.

Slingo, A. (1989), A GCM parameterization for the shortwave radiative properties of water clouds, *J. Atmos. Sci.*, *46*, 1419–1427, doi:10.1175/1520-0469(1989)046<1419:AGPFTS>2.0.CO;2.

Smith, R. N. B. (1990), A scheme for predicting layer clouds and their water content in a general circulation model, *Q. J. R. Meteorol. Soc.*, *116*, 435–460, doi:10.1002/qj.49711649210.

Stephens, G. L., P. M. Gabriel, and P. T. Partain (2001), Parameterization of atmospheric radiative transfer. Part I: Validity of simple models, *J. Atmos. Sci.*, *58*, 3391–3409, doi:10.1175/1520-0469(2001)058<3391:POARTP>2.0.CO;2.

Sundqvist, H., E. Berge, and J. E. Kristjansson (1989), Condensation and cloud parameterization studies with a mesoscale numerical weather prediction model, *Mon. Wea. Rev.*, *117*, 1641–1657, doi:10.1175/1520-0493(1989)117<1641:CACPSW>2.0.CO;2.

Tiedtke, M. (1983), The sensitivity of the time-mean large-scale flow to cumulus convection in the ECMWF model, in *Workshop on Convection in Large-scale Numerical Models*, vol. *28*, Shinfield Park, Reading, pp. 297–316.

Tiedtke, M. (1993), Representation of clouds in large-scale models, *Mon. Wea. Rev.*, *121*(11), 3040–3061, doi:10.1175/1520-0493(1993)121<3040:ROCILS>2.0.CO;2.

Wang, W., X. Liu, S. Xie, J. Boyle, and S. A. McFarlane (2009), Testing ice microphysics parameterizations in the NCAR community atmospheric model version 3 using tropical warm pool–International Cloud Experiment data, *J. Geophys. Res.*, *114*, D14107, doi:10.1029/2008JD011220.

Webster, P., and R. Lukas (1992), TOGA-COARE: The Coupled Ocean-Atmosphere Response Experiment, *Bull. Amer. Meteor. Soc*, *73*, 1377–1416, doi:10.1175/1520-0477(1992)073<1377:TCTCOR>2.0.CO;2.

Wilson, D., and R. Forbes, (2004), Unified model documentation paper 26: The large-scale precipitation parametrization scheme, *Technical Report 26*, Met Office R&D.

Wilson, D. R., and S. P. Ballard (1999), A microphysically based precipitation scheme for the UK Meteorological Office Unified Model, *Q. J. R. Meteorol. Soc.*, *125*, 1607–1636, doi:10.1002/qj.49712555707.

Woolnough, S. J., P. Blossey, K. M. Xu, P. Bechtold, J. C. T. Hosomi, S. Iacobellis, Y. Luo, J. Petch, R. Wong, and S. Xie (2010), Modelling convective processes during the suppressed phase of a Madden–Julian oscillation: Comparing single-column models with cloud-resolving models, *Q. J. R. Meteorol. Soc.*, *136*(647), 333–353, doi:10.1002/qj.568.

Xie, S., et al. (2002), Intercomparison and evaluation of cumulus parametrizations under summertime midlatitude continental conditions, *Quart. J. Roy. Meteor. Soc.*, *128*, 1095–1136, doi:10.1256/003590002320373229.

Xie, S., R. T. Cederwall, and M. Zhang (2004), Developing long-term single-column model/cloud system—resolving model forcing data using numerical weather prediction products constrained by surface and

top of the atmosphere observations, *J. Geophys. Res.*, *109*, D01104, doi:10.1029/2003JD004045.

Xie, S., et al. (2005), Simulations of midlatitude frontal clouds by single-column and cloud-resolving models during the Atmospheric Radiation Measurement March 2000 cloud intensive operational period, *J. Geophys. Res.*, *110*, D15S03, doi:10.1029/2004JD005119.

Xie, S., T. Hume, C. Jakob, S. A. Klein, R. B. McCoy, and M. Zhang (2010), Observed large-scale structures and diabatic heating and drying profiles during TWP-ICE, *J. Climate*, *23*, 57–79, doi:10.1175/2009JCLI3071.1.

Xie, S., and M. Zhang (2000), Impact of the convection triggering function on single-column model simulations, *J. Geophys. Res.*, *105*(D11), 14983–14996, doi:10.1029/2000JD900170.

Xu, K. M., et al. (2002), An intercomparison of cloud-resolving models with the atmospheric radiation measurement summer 1997 intensive observation period data, *Quart. J. Roy. Meteor. Soc.*, *580*, 593–624, doi:10.1256/003590002321042117.

Zhang, G., and N. A. McFarlane (1995), Sensitivity of climate simulations to the parameterization of cumulus convection in the Canadian climate centre general circulation model, *Atmos. Ocean*, *33*, 407–446, doi:10.1080/07055900.1995.9649539.

Zhang, G. J. (2002), Convective quasi-equilibrium in midlatitude continental environment and its effect on convective parameterization, *J. Geophys. Res.*, *107*(D14), 4220, doi:10.1029/2001JD001005.

Zhang, M., W. Lin, C. S. Bretherton, J. J. Hack, and P. J. Rasch (2003), A modified formulation of fractional stratiform condensation rate in the NCAR Community Atmospheric Model (CAM2), *J. Geophys. Res.*, *108*(D1), 4035, doi:10.1029/2002JD002523.

Zhang, M. H., and J. L. Lin (1997), Constrained variational analysis of sounding data based on column integrated budgets of mass, heat, moisture, and momentum: Approach and application to ARM measurements, *J. Atmos. Sci.*, *54*, 1503–1524, doi:10.1175/1520-0469(1997)054<1503:CVAOSD>2.0.CO;2.

Zhang, M. H., J. L. Lin, R. T. Cederwall, J. J. Yio, and S. C. Xie (2001), Objective analysis of ARM IOP data: Method and sensitivity, *Mon. Wea. Rev.*, *129*, 295–311, doi:10.1175/1520-0493(2001)129<0295:OAOAID>2.0.CO;2.

Zhao, Q. Y., and F. H. Carr (1997), A prognostic cloud scheme for operational NWP models, *Mon. Wea. Rev.*, *125*, 1931–1953, doi:10.1175/1520-0493(1997)125<1931:APCSFO>2.0.CO;2.

Zhu, P., J. Dudhia, P. Field, K. Wapler, A. Fridlind, A. Varble, E. Zipser, J. Petch, M. Chen, and Z. Zhu (2012), A limited area model (LAM) intercomparison study of a TWP-ICE active monsoon mesoscale convective event, *J. Geophys. Res.*, *117*, D11208, doi:10.1029/2011JD016447.